

Coherent phenomena in the interaction of pulsed particle beams and radiation

Citation for published version (APA):

Smorenburg, P. W. (2013). *Coherent phenomena in the interaction of pulsed particle beams and radiation*. [Phd Thesis 1 (Research TU/e / Graduation TU/e), Applied Physics and Science Education]. Technische Universiteit Eindhoven. <https://doi.org/10.6100/IR749400>

DOI:

[10.6100/IR749400](https://doi.org/10.6100/IR749400)

Document status and date:

Published: 01/01/2013

Document Version:

Publisher's PDF, also known as Version of Record (includes final page, issue and volume numbers)

Please check the document version of this publication:

- A submitted manuscript is the version of the article upon submission and before peer-review. There can be important differences between the submitted version and the official published version of record. People interested in the research are advised to contact the author for the final version of the publication, or visit the DOI to the publisher's website.
- The final author version and the galley proof are versions of the publication after peer review.
- The final published version features the final layout of the paper including the volume, issue and page numbers.

[Link to publication](#)

General rights

Copyright and moral rights for the publications made accessible in the public portal are retained by the authors and/or other copyright owners and it is a condition of accessing publications that users recognise and abide by the legal requirements associated with these rights.

- Users may download and print one copy of any publication from the public portal for the purpose of private study or research.
- You may not further distribute the material or use it for any profit-making activity or commercial gain
- You may freely distribute the URL identifying the publication in the public portal.

If the publication is distributed under the terms of Article 25fa of the Dutch Copyright Act, indicated by the "Taverne" license above, please follow below link for the End User Agreement:

www.tue.nl/taverne

Take down policy

If you believe that this document breaches copyright please contact us at:

openaccess@tue.nl

providing details and we will investigate your claim.

Coherent phenomena in the interaction of pulsed particle beams and radiation

PROEFSCHRIFT

ter verkrijging van de graad van doctor aan de Technische
Universiteit Eindhoven, op gezag van de rector magnificus,
prof.dr.ir. C.J. van Duijn, voor een commissie aangewezen
door het College voor Promoties in het openbaar te
verdedigen op donderdag 25 april 2013 om 14.00 uur

door

Petrus Wilhelmus Smorenburg

geboren te Utrecht

Dit proefschrift is goedgekeurd door de promotor:

prof.dr.ir. O.J. Luiten

Copromotor:

dr.ir. L.P.J. Kamp

Printed by Universiteitsdrukkerij Technische Universiteit Eindhoven.

A catalogue record is available from the Eindhoven University of Technology Library.

ISBN: 978-90-386-3332-9

NUR: 924

The front cover has been designed by P. W. Smorenburg inspired by D. R. Hofstadter's "Gödel, Escher, Bach: An Eternal Golden Braid" (Basic Books, 1979). The figure symbolizes the interwovenness of electromagnetic fields (E and B) and motion (F) that lies at the core of the dynamics of charged particles (sphere).

The research described in this thesis has been carried out in the group Coherence and Quantum Technology at the Department of Applied Physics of the Eindhoven University of Technology. This work is part of the research program of the Stichting Fundamenteel Onderzoek der Materie (FOM), which is financially supported by the Nederlandse Organisatie voor Wetenschappelijk Onderzoek (NWO).

Contents

1	Introduction	1
1.1	Electron theory	1
1.2	Coherently enhanced radiation reaction	2
1.3	The ponderomotive force	4
1.4	Finite-sized plasmas	5
1.5	Coherent generation of terahertz waves	8
2	Classical formulations of the electromagnetic self-force	15
2.1	Introduction	16
2.2	Existing self-force derivations	17
2.3	Equivalence of the self-force expressions	23
2.4	Charged particle theories	30
2.5	Discussion	32
3	Coherently enhanced radiation reaction effects	37
3.1	Introduction	38
3.2	Averaged radiation reaction force	40
3.3	Radiation reaction in a laser pulse	43
3.4	Realistic electron bunches	47
3.5	The radiation reaction dominated regime	50
3.6	Conclusion	55
3.A	Laser field representations	56
4	Polarization-dependent ponderomotive gradient force	61
4.1	Introduction	62
4.2	The polarization-dependent ponderomotive force	65
4.3	Wiggling motion in a standing wave	70
4.4	Comparison with simulations	72
4.5	Conclusion	76
4.A	Order equations	77
4.B	General field strength	78

4.C	Fields used in numerical calculations	79
5	Heating mechanisms in rf-driven ultracold plasmas	85
5.1	Introduction	86
5.2	Collisional absorption	88
5.3	Three-body recombination	91
5.4	Collisionless absorption	96
5.5	Discussion and conclusions	104
5.A	Effective collision frequency	106
5.B	TBR rate for arbitrary ratio U_p/U_{ion}	107
5.C	Decay rate of ν_p for UCPs	108
6	Ponderomotive manipulation of cold subwavelength plasmas	117
6.1	Introduction	118
6.2	Fields	120
6.3	Forces	124
6.4	Homogeneous plasma	126
6.5	Inhomogeneous plasmas	131
6.6	Acceleration of ultracold plasmas	137
6.7	Conclusions	141
6.A	Quasistatic limit from general field expressions	142
6.B	Explicit expressions for ponderomotive forces	143
6.C	Radial functions for homogeneous sphere	145
7	Direct generation of THz SPPs on a wire using electron bunches	153
7.1	Introduction	154
7.2	SPPs as perturbation of radiation field at ideal conductor	157
7.3	Radiation field calculation	159
7.4	Numerical results	164
7.5	Validation	168
7.6	Extension to electron bunches	173
7.7	Obtainable SPPs in the time domain	179
7.8	Experimental verification	182
7.9	Conclusion	183
7.A	SPP field in conical geometry	184
7.B	Derivation of Eq. (7.13)	185
7.C	Green's function for conical geometry	186
7.D	Electric field in the far zone	188
7.E	Analysis of Q_σ in Eq. (7.52)	188
7.F	Peak field and pulse duration	191
8	Concluding remarks	199

Summary	205
Samenvatting	209
Publications	213
Curriculum Vitae	215
Dankwoord	217

This thesis is partially based on the following publications:

- Chapter 2: P. W. Smorenburg, L. P. J. Kamp, and O. J. Luiten (submitted 2013).
- Chapter 3: P. W. Smorenburg, L. P. J. Kamp, G. A. Geloni, and O. J. Luiten, Laser Part. Beams **28**, 553-562 (2010).
- Chapter 4: P. W. Smorenburg, J. H. M. Kanters, A. Lassise, G. J. H. Brussaard, L. P. J. Kamp, and O. J. Luiten, Phys. Rev. A **83**, 063810 (2011).
- Chapter 5: P. W. Smorenburg, L. P. J. Kamp, and O. J. Luiten, Phys. Rev. A **85**, 063413 (2012).
- Chapter 6: P. W. Smorenburg, L. P. J. Kamp, and O. J. Luiten, Phys. Rev. E **87**, 023101 (2013).
- Chapter 7: P. W. Smorenburg, W. P. E. M. op 't Root, and O. J. Luiten, Phys. Rev. B **78**, 115415 (2008).



1

Introduction

This thesis concerns a conceptually very simple physical system: a well-defined bunch of charged particles subjected to an electromagnetic wave. To delineate this even more: we consider bunches that are smaller than the wavelength of the radiation. Despite its simplicity, however, this elementary system gives rise to a multitude of interesting phenomena. In this thesis, we will study such phenomena analytically from multiple perspectives, identifying new physical effects and emphasizing technological possibilities to take advantage of them. Our system of a subwavelength body of charge emerges in a variety of contexts, ranging from pre-quantum classical electron theory (section 1.1) to modern high-power laser experiments (section 1.2) and from classical Mie theory to modern ultracold plasmas (section 1.4). Across these contexts an important part is played by the ponderomotive force experienced by charges in an oscillating, inhomogeneous electromagnetic field (section 1.3). While these topics emphasize the role of subwavelength charged bunches as passive objects *subjected* to radiation, they can also act as a coherent radiation *source* of, for example, terahertz waves on a metal wire (section 1.5).

1.1 Electron theory

The structure of matter has always been one of the prime issues in theoretical physics. Before the advent of quantum mechanics and the standard model, attempts were made to describe elementary particles as small rigid charged bodies. Evidently, to a certain extent a macroscopic bunch of charged particles may be viewed as a scaled-up version of such a classical elementary particle, albeit one with much more charge and mass than a single classical electron. The results of these classical studies, or 'electron theories', are therefore directly relevant to the bunches studied in this thesis. Central to the electron theories were the Lorentz forces as experienced by the parts of the charged particle, and caused by the electromagnetic fields generated by all the other parts. The formulation in terms of such electromagnetic self-forces, most notably by Abraham [1] and Lorentz [2], led to some partial successes. First of all, it was

found that part of the total self-force is proportional and oppositely directed to the acceleration of the particle, which suggested an electromagnetic explanation of inertia. Second, a contribution to the self-force was identified that could account for the momentum that is lost by a charged particle in the form of Larmor radiation when the particle is accelerated. The latter force is known as the radiation reaction force. While radiation reaction for a long time has been considered experimentally irrelevant due to the smallness of the effect, it has recently regained interest because available laser intensities and the associated accelerations of electrons have almost increased to the point where radiation reaction effects may become observable [3]. The classical electron theories, however, were not without conceptual difficulties. A well-known example is the so-called 4/3-problem related to the absence of relativistic covariance, which is partially resolved by assuming the presence of non-electromagnetic "Poincaré stresses" within the particle. The classical description of charged particles, initiated in pre-relativistic times, is still being actively pursued in literature [4–7], which makes it the most long-standing unfinished issue in electrodynamics. The consensus is that the motion of a charged particle, under the influence of both external forces and its self-force, is most correctly described by the so-called Lorentz-Abraham-Dirac equation of motion [8]. This covariant equation also takes full account of relativistic effects.

In *chapter 2*, we review a number of approaches that have been taken to evaluate the self-force of a charged sphere. Although the resulting self-force representations have been known for a long time, it has never been shown how these results can be derived directly from one another. In *chapter 2*, we establish these interrelations.

1.2 Coherently enhanced radiation reaction

The recent availability of ultra-intense laser pulses has led to increased efforts to develop novel compact acceleration schemes for electron beams. These include wakefield accelerators [9–12], thin foil irradiation schemes [13, 14] and laser-vacuum acceleration concepts [15, 16]. Most studies so far have concentrated on the dynamics of the individual electrons in the considered electron bunches under the action of the externally applied electromagnetic fields. Incorporation of the collective interactions in the bunches is usually limited to space-charge effects, while the radiation reaction force is usually neglected, which is well justified if the electron density is not too high and the electron bunch size exceeds the laser wavelength used. However, in recent years the interaction of intense laser light with nanometer to micrometer sized atomic clusters of near solid state density has become the subject of thorough investigation [17, 18]. This has led to the observation of large numbers of electrons emitted from such clusters [19–22]. In particular, under suitable conditions the production of dense, attosecond electron bunches from laser-irradiated clusters has been observed both numerically [23] and experimentally [21, 24]. Also the creation of ultrashort

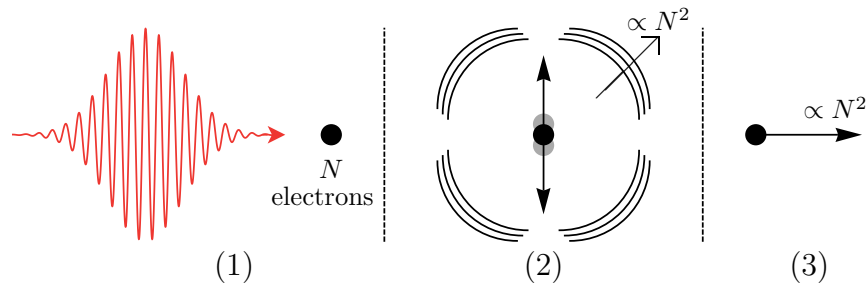


Figure 1.1: Principle of acceleration due to coherent Thomson scattering, showing (1) arrival of a laser pulse (red) at a subwavelength electron bunch (black disk), (2) emission of coherently enhanced dipole radiation, and (3) forward resultant force on the electron bunch due to conservation of momentum.

bunches from laser-irradiated foils is actively studied [25–27]. Such experiments in which powerful laser pulses irradiate solid-state targets constitute a second important context where subwavelength charged bunches interact with an electromagnetic wave, next to classical electron theories.

Bearing on the results from electron theory, we consider in *chapter 3* the effect of radiation reaction on relativistic electron bunches in interaction with a laser pulse. It is shown that the interaction can be modeled by a particularly simple picture of radiation pressure in the direction of the laser beam on a coherently enhanced effective cross section, in combination with a viscous force perpendicular to the laser propagation direction. This suggests that laser-vacuum acceleration schemes, which normally exhibit a transverse instability due to a radially outward ponderomotive force, may be partially stabilized by the presence of radiation reaction. The mechanism by which radiation reaction may become significant in electron bunches, in contrast to virtually all experiments where single electrons interact with laser pulses, is that of coherent enhancement. Here, coherence means that the fields produced by the individual electrons in the bunch add constructively. This happens because the externally applied fields of the incident radiation are more or less uniform over the extent of a subwavelength bunch, so that all electrons move in roughly the same way. As the electromagnetic self-force is a direct consequence of the self-generated fields, coherent fields therefore lead to a coherently enhanced self-force. This is apparent from the fact that the part of the Lorentz-Abraham-Dirac equation that represents radiation reaction is proportional to the charge of the bunch squared.

In the present context, coherent enhancement and the average effect of radiation reaction are best exhibited in terms of the phenomenon of Thomson scattering, as is illustrated by Fig. 1.1. Thomson scattering is the production of secondary dipole radiation by charges that oscillate due to the electric field of the incident radiation

wave, which can be seen as scattering of part of the incident radiation by the charges. In case of a subwavelength electron bunch consisting of N electrons, the fields within the scattered radiation add constructively to N times the field that a single electron would produce, so that an N^2 times larger power is scattered from the incident wave. In the scattering process, directed radiation with net momentum is converted into dipole radiation that has less net momentum, so that the momentum difference must be absorbed by the electron bunch. Since this momentum difference is enhanced N^2 times, Thomson scattering thus leads to a coherently enhanced force on the bunch in the direction of the wave. The technological possibility to accelerate bunches with this force was first articulated by Veksler [28]. In *chapter 3*, we show how this force follows from the Lorentz-Abraham-Dirac equation, and how it generalizes to relativistic velocities.

1.3 The ponderomotive force

The ponderomotive force is a time-averaged force experienced by a charged particle in an oscillating electromagnetic (EM) field that is spatially inhomogeneous. In the conventional treatment [29, 30], it is shown that this force is the gradient of a ponderomotive potential, and that it is always directed toward regions of low field strength. Whenever field gradients are involved, the ponderomotive force should be taken into account. Indeed in *chapter 3*, this force significantly influences the calculated electron trajectories, and proves to be essential for a correct interpretation of the numerical results. In physics, the ponderomotive force is observed and exploited in a wide range of contexts. In laser-plasma physics, this force drives the formation of laser wakefields that are used for next generation electron accelerators [9–12]. Ion beams are produced by intense laser irradiation of thin foils, in which the ponderomotive force plays an essential role [31, 32]. Schemes have been proposed for ponderomotive laser-vacuum acceleration of electrons [33, 34]. In Paul traps, ions are confined by a ponderomotive potential [35]. In electron beam diagnostics, the length of electron bunches is measured by sequentially scattering different sections of the bunch using the ponderomotive force of a laser pulse [36, 37].

The ponderomotive force that can be produced by a single laser pulse is limited by the minimum pulse duration and focal spot that can be reached at a given laser intensity. For many applications of the ponderomotive force this means that, in order to obtain a sufficiently strong force, very large field intensities are required. An attractive alternative is the use of a standing wave. In this configuration, the nodes and antinodes are spaced on the scale of the wavelength, which is much smaller than the laser pulse length or focal spot. This results in correspondingly larger field gradients and ponderomotive forces, which may be used to deflect charged particles, as is illustrated in Fig. 1.2. A number of applications have been proposed that take advantage

of the large standing wave ponderomotive forces. These include a table-top standing wave version of the bunch length measurement setup mentioned previously [38], a novel x-ray free electron laser based on the wiggling of electrons in the ponderomotive potential of a standing wave [39], use of a standing wave formed by colliding laser pulses to pre-accelerate electrons ponderomotively in a laser-wakefield setup [40], and creation of attosecond electron pulse trains by bunching of an electron beam due to a co-moving ponderomotive beat potential between laser pulses of different frequencies [41]. However, we discovered that the ponderomotive force is no longer correctly described by the classical ponderomotive potential when applied to a standing wave. A similar conclusion was drawn by Kaplan and Pokrovsky [42] for certain special field configurations. In *chapter 4*, the ponderomotive force is derived for a relativistic particle entering a nonrelativistic standing wave with a general three-dimensional field distribution. It is shown that the force is polarization-dependent, and may in some cases even be directed toward high field intensities. This may have important implications for experiments and proposals based on the standing wave ponderomotive force.

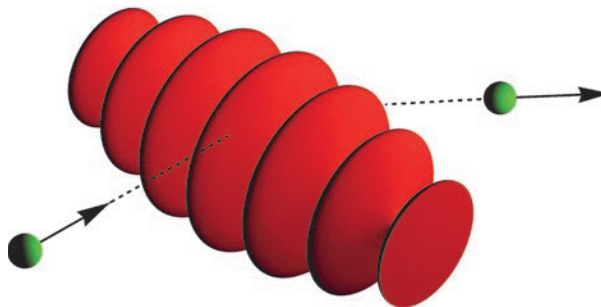


Figure 1.2: Charged particle that is deflected by the ponderomotive force of a standing EM wave.

1.4 Finite-sized plasmas

Dense bunches consisting of only electrons are inherently unstable systems: they will expand rapidly due to the Coulomb repulsion, and they will do so more forcefully the higher the charge density. This property directly conflicts with the requirements for pronounced coherent interactions, that is, with a large amount of charge that is localized within a subwavelength volume for a long time. This suggests that neutralized bunches, consisting of both electrons and ions so that Coulomb forces are compensated, have more chance to exhibit significant coherent effects. Such finite-sized plasmas, when driven by radiation, constitute a third context in which bunches of charged particles interact with an electromagnetic wave.

Considering irradiated subwavelength plasmas rather than electron bunches, however, introduces all kinds of processes studied in the very rich field of plasma physics, such as ionization and recombination, radiative processes, and various types of plasma waves. These processes are not within the scope of this thesis. Nevertheless, being interested in coherent effects, it should be realized that plasma bunches too expand and hence become larger than the applied wavelength after some time. The expansion in this case is driven by the hydrodynamic pressure rather than Coulomb forces. It is therefore of direct relevance to at least assess the evolution of the pressure, or what amounts to the same, the plasma temperature. In *chapter 5*, we consider mechanisms by which the applied electromagnetic wave may lead to plasma heating and an associated acceleration of the plasma expansion towards incoherent sizes.

Evidently, the slower the expansion of a subwavelength plasma, the more possibilities there are for coherent interactions to induce significant physical effects. This suggests the use of plasmas that are preferably as cold as possible. Recently, it has become possible to produce so-called ultracold plasmas [43], in which the electron temperature can be less than 10 K. Ultracold plasmas are created by photo-ionization of a cloud of laser-cooled atoms, as is illustrated by Fig 1.3, resulting in a low-density plasma less than a millimeter in size. The combination of low temperature and low density makes ultracold plasmas exotic systems that are close to the strongly-coupled regime where the Coulomb interaction energy between the particles exceeds the thermal energy. For such systems, standard descriptions of plasma processes that are commonly applied to conventional plasmas need to be reconsidered. *chapter 5* on heating mechanisms is therefore specialized to ultracold plasmas, and it is indeed found that the combination of a very low temperature and an applied electromagnetic wave leads to some unexpected results. The latter are also directly relevant for current experiments in which ultracold plasmas are probed with radiofrequency and microwave fields, enabling the observation of phenomena such as plasma oscillations [44, 45], Tonks-Dattner resonances [46], and modes associated with nonneutral plasmas [47, 48]. These experiments in turn yield valuable fundamental insights into the plasma dynamics in the ultracold and strongly-coupled regime.

A crude but fruitful description of a plasma bunch is the so-called nanoplasma model [49], which pictures the plasma as a rigid sphere of electrons overlapping with an equally sized rigid sphere of ions. Accordingly, the coherent interaction of the plasma electrons with electromagnetic radiation may to some extent be described within the framework of electron theory and radiation reaction, as it is done in *chapter 3* on relativistic electron bunches. However, in a realistic plasma the electrons do not form a rigid sphere, and due to self-produced polarization fields they may oscillate with an amplitude that depends on the position in the plasma. A formalism that is better suited to describe such effects, and which in particular enables the self-consistent calculation of position-dependent fields and electron oscillation ampli-

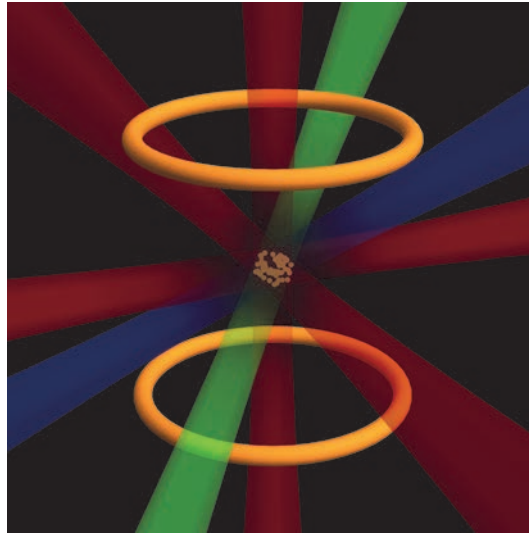


Figure 1.3: Creation of an ultracold plasma in a magneto-optical trap, involving a cloud of atoms (center) that are subsequently cooled and confined by three pairs of counterpropagating lasers (red) and a pair of coils (yellow), excited by a resonant laser (blue) and ionized by another laser (green). Colors do not represent the laser wavelengths.

tudes, are the macroscopic Maxwell equations. In *chapter 6*, plasma bunches in interaction with an electromagnetic wave are therefore modeled as inhomogeneous dielectric media, and the internal fields are calculated self-consistently. Such a dielectric formulation is commonplace in the description of far-field radiation patterns resulting from Mie scattering by homogeneous solid objects. We will use the formalism to study internal fields and forces in inhomogeneous plasmas, and show that the radiation reaction effects emphasized in classical electron theory are still exhibited.

In addition to resultant forces that act on the electromagnetically driven plasma as a whole, any inhomogeneities in the self-consistent fields within the plasma give rise to local ponderomotive forces. Detailed knowledge of the fields, as provided by the dielectric plasma description, enables an assessment of these forces, which is given in *chapter 6* as well. Since the dielectric description is not particular to plasmas, the results suggest possibilities for the ponderomotive manipulation of other dielectric media as well. The latter include solid state spheres and droplets in scattering experiments [50–52], and levitated droplets that are needed for contact-free observation of processes such as surface vibrations [53], ice nucleation [54], and crystallization of salts [55].

1.5 Coherent generation of terahertz waves

Up to now we have been introducing the topics of this thesis by discussing subwavelength bunches of charged particles in the contexts of electron theory, laser-driven electron bunches, plasma physics, and dielectric media. In the systems and applications mentioned so far, one could say that the charged particles play a passive part, reacting to an electromagnetic field that is externally applied. As a final topic of this thesis, we consider an application in which the roles of the particles and the radiation field are reversed, the particles acting as a source of coherent electromagnetic waves rather than a receiver. In *chapter 7*, we consider the generation of terahertz surface waves on a metal wire by launching electron bunches onto a tapered end of the wire.

Terahertz surface waves on a wire are of current technological interest because these waves can efficiently be focused below the diffraction limit [56–58]. This leads to electromagnetic pulses that are both very strong and highly localized, making it possible to study materials at terahertz frequencies with sub-wavelength spatial resolutions [59, 60], with applications in near-field microscopy [61, 62], imaging [63–66], single particle sensing [67, 68] and terahertz spectroscopy [69, 70]. However, it is still a challenge to generate wire-carried terahertz waves of appreciable amplitude. Currently, these waves are generated by scattering linearly polarized free-space terahertz waves into a radially polarized wave, which is then coupled onto the wire [71]. However, the coupling efficiency of this scheme is very low [72], although some methods exist to increase this efficiency somewhat [72–75].

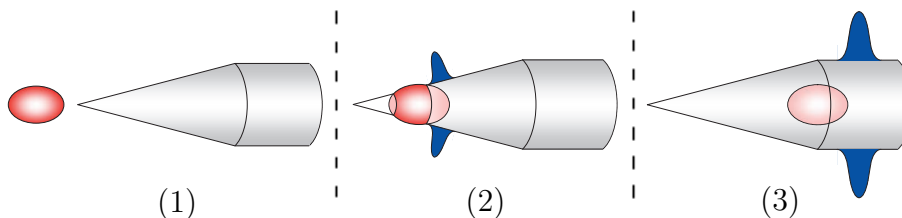


Figure 1.4: Principle of terahertz surface wave (blue pulse) generation on a wire by launching electron bunches (red) onto a conical metal tip.

In *chapter 7*, it is proposed to use the coherent properties of electron bunches to produce terahertz waves on a wire, rather than trying to convert free-space terahertz radiation. Our novel method is based on the phenomenon of transition radiation, which is generated when charged particles pass a boundary between different media. By letting an electron bunch pass the conical vacuum-metal boundary of the tapered tip of a wire, transition radiation is generated that partly consists of electromagnetic surface waves propagating along the boundary. This process is illustrated in Fig.

1.4. We will show that the surface waves can become very strong for sharp wire tips, and will add coherently for wavelengths larger than the electron bunch, that is, at terahertz frequencies.

Bibliography

- [1] M. Abraham, “Principien der Dynamik des Elektrons,” *Ann. Phys. (Leipzig)* **315**, 105–179 (1902).
- [2] H. A. Lorentz, *The theory of electrons* (Teubner, Leipzig, 1916) 2nd ed.
- [3] M. Tamburini, F. Pegoraro, A. Di Piazza, C. H. Keitel, and A. Macchi, “Radiation reaction effects on radiation pressure acceleration,” *New J. Phys.* **12**, 123005 (2010).
- [4] J. A. E. Roa-Neri and J. L. Jiménez, “On the classical dynamics of non-rotating extended charges,” *Nuovo Cimento B* **108**, 853–869 (1993).
- [5] S. E. Gralla, A. I. Harte, and R. M. Wald, “Rigorous derivation of electromagnetic self-force,” *Phys. Rev. D* **80**, 024031 (2009).
- [6] F. Rohrlich, “Dynamics of a charged particle,” *Phys. Rev. E* **77**, 046609 (2008).
- [7] A. D. Yaghjian, *Relativistic dynamics of a charged sphere* (Springer, New York, 2006) 2nd ed.
- [8] P. A. M. Dirac, “Classical theory of radiating electrons,” *Proc. Royal Soc. London A* **167**, 148–169 (1938).
- [9] T. Tajima and J. M. Dawson, “Laser electron accelerator,” *Phys. Rev. Lett.* **43**, 267–270 (1979).
- [10] S. P. D. Mangles, C. D. Murphy, Z. Najmudin, A. G. R. Thomas, J. L. Collier, A. E. Dangor, E. J. Divall, P. S. Foster, J. G. Gallacher, C. J. Hooker, D. A. Jaroszynski, A. J. Langley, W. B. Mori, P. A. Norreys, F. S. Tsung, R. Viskup, B. R. Walton, and K. Krushelnick, “Monoenergetic beams of relativistic electrons from intense laser-plasma interactions,” *Nature (London)* **431**, 535–538 (2004).
- [11] C. G. R. Geddes, Cs. Toth, J. van Tilborg, E. Esarey, C. B. Schroeder, D. Bruhwiler, C. Nieter, J. Cary, and W. P. Leemans, “High-quality electron beams from a laser wakefield accelerator using plasma-channel guiding,” *Nature (London)* **431**, 538–541 (2004).
- [12] J. Faure, Y. Glinec, A. Pukhov, S. Kiselev, S. Gordienko, E. Lefebvre, J.-P. Rousseau, F. Burgy, and V. Malka, “A laser-plasma accelerator producing monoenergetic electron beams,” *Nature (London)* **431**, 541–544 (2004).

- [13] A. Maksimchuk, S. Gu, K. Flippo, and D. Umstadter, “Forward ion acceleration in thin films driven by a high-intensity laser,” *Phys. Rev. Lett.* **84**, 4108–4111 (2000).
- [14] M. Borghesi, J. Fuchs, S. V. Bulanov, A. J. Mackinnon, and P. K. Patel, “Fast ion generation by high-intensity laser irradiation of solid targets and applications,” *Fusion Sci. Technol.* **49**, 412–439 (2006).
- [15] G. V. Stupakov and M. S. Zolotarev, “Ponderomotive laser acceleration and focusing in vacuum for generation of attosecond electron bunches,” *Phys. Rev. Lett.* **86**, 5274–5277 (2001).
- [16] H. F. Wang, L. P. Shi, B. Lukyanchuk, C. Sheppard, and C. T. Chong, “Creation of a needle of longitudinally polarized light in vacuum using binary optics,” *Nature Photonics* **2**, 501–505 (2008).
- [17] U. Saalmann, Ch. Siedschlag, and J. M. Rost, “Mechanisms of cluster ionization in strong laser pulses,” *J. Phys. B* **39**, R39–R77 (2006).
- [18] V. P. Krainov and M. B. Smirnov, “Cluster beams in the superintense femtosecond laser pulse,” *Phys. Reports* **370**, 237–331 (2002).
- [19] Y. L. Shao, T. Ditmire, J. W. G. Tisch, E. Springate, J. P. Marangos, and M. H. R. Hutchinson, “Multi-keV electron generation in the interaction of intense laser pulses with Xe clusters,” *Phys. Rev. Lett.* **77**, 3343–3346 (1996).
- [20] E. Springate, S. A. Aseyev, S. Zamith, and M. J. J. Vrakking, “Electron kinetic energy measurements from laser irradiation of clusters,” *Phys. Rev. A* **68**, 053201 (2003).
- [21] T. Fennel, T. Döppner, J. Passig, C. Schaal, J. Tiggesbäumker, and K.-H. Meiwes-Broer, “Plasmon-enhanced electron acceleration in intense metal-cluster interactions,” *Phys. Rev. Lett.* **98**, 143401 (2007).
- [22] L. M. Chen, J. J. Park, K.-H. Hong, I. W. Choi, J. L. Kim, J. Zhang, and C. H. Nam, “Measurement of energetic electrons from atomic clusters irradiated by intense femtosecond laser pulses,” *Phys. Plasmas* **9**, 3595–3599 (2002).
- [23] T. V. Liseykina, S. Pirner, and D. Bauer, “Relativistic attosecond electron bunches from laser-illuminated droplets,” *Phys. Rev. Lett.* **104**, 095002 (2010).
- [24] Y. Fukuda, Y. Akahane, M. Aoyama, Y. Hayashi, T. Homma, N. Inoue, M. Kando, S. Kanazawa, H. Kiriya, S. Kondo, H. Kotaki, S. Masuda, M. Mori, A. Yamazaki, K. Yamakawa, E. Yu. Echkina, I. N. Inovenkov, J. Koga, and S. V. Bulanov, “Ultrarelativistic electron generation during the intense, ultrashort laser pulse interaction with clusters,” *Phys. Lett. A* **363**, 130–135 (2007).

-
- [25] J. Meyer-ter-Vehn and H.-C. Wu, “Coherent Thomson backscattering from laser-driven relativistic ultra-thin electron layers,” *Eur. Phys. J. D* **55**, 433–441 (2009).
- [26] H.-C. Wu and J. Meyer-ter-Vehn, “The reflectivity of relativistic ultra-thin electron layers,” *Eur. Phys. J. D* **55**, 443–449 (2009).
- [27] B. Qiao, M. Zepf, M. Borghesi, B. Dromey, and M. Geissler, “Coherent x-ray production via pulse reflection from laser-driven dense electron sheets,” *New J. Phys.* **11**, 103042 (2009).
- [28] V. I. Veksler, “The principle of coherent acceleration of charged particles,” *Sov. Atom. Energy* **2**, 525–528 (1957).
- [29] H. A. H. Boot and R. B. R. S. Harvie, “Charged particles in a non-uniform radio-frequency field,” *Nature (London)* **180**, 1187 (1957).
- [30] A. V. Gaponov and M. A. Miller, “Potential wells for charged particles in a high-frequency electromagnetic field,” *Sov. Phys. JETP* **7**, 168–169 (1958).
- [31] J. Denavit, “Absorption of high-intensity subpicosecond lasers on solid density targets,” *Phys. Rev. Lett.* **69**, 3052–3055 (1992).
- [32] J. Badziak, S. Glowacz, S. Jablonski, P. Parys, J. Wolowski, and H. Hora, “Laser-driven generation of high-current ion beams using skin-layer ponderomotive acceleration,” *Laser and Particle Beams* **23**, 401–409 (2005).
- [33] E. Esarey, P. Sprangle, and J. Krall, “Laser acceleration of electrons in vacuum,” *Phys. Rev. E* **52**, 5443–5453 (1995).
- [34] J. L. Chaloupka and D. D. Meyerhofer, “Observation of electron trapping in an intense laser beam,” *Phys. Rev. Lett.* **83**, 4538–4541 (1999).
- [35] W. Paul, “Electromagnetic traps for charged and neutral particles,” *Rev. Mod. Phys.* **62**, 531–540 (1990).
- [36] B. J. Siwick, A. A. Green, C. T. Hebeisen, and R. J. D. Miller, “Characterization of ultrashort electron pulses by electron-laser pulse cross correlation,” *Opt. Lett.* **30**, 1057–1059 (2005).
- [37] C. T. Hebeisen, R. Ernstorfer, M. Harb, T. Dartigalongue, R. E. Jordan, and R. J. D. Miller, “Femtosecond electron pulse characterization using laser ponderomotive scattering,” *Opt. Lett.* **31**, 3517–3519 (2006).
- [38] C. T. Hebeisen, G. Sciaini, M. Harb, R. Ernstorfer, T. Dartilongue, S. G. Kruglik, and R. J. D. Miller, “Grating enhanced ponderomotive scattering for visualization and full characterization of femtosecond electron pulses,” *Opt. Express* **16**, 3334–3341 (2008).

- [39] P. Balcou, “Proposal for a Raman X-ray free electron laser,” *Eur. Phys. J. D* **59**, 525–537 (2010).
- [40] J. Faure, C. Rechatin, A. Norlin, A. Lifschitz, Y. Glinec, and V. Malka, “Controlled injection and acceleration of electrons in plasma wakefields by colliding laser pulses,” *Nature (London)* **444**, 737–739 (2006).
- [41] P. Baum and A. H. Zewail, “Attosecond electron pulses for 4D diffraction and microscopy,” *Proc. Nat. Acad. Sci. USA* **104**, 18409–18414 (2007).
- [42] A. E. Kaplan and A. L. Pokrovsky, “Fully relativistic theory of the ponderomotive force in an ultraintense standing wave,” *Phys. Rev. Lett.* **95**, 053601 (2005).
- [43] T. C. Killian, T. Pattard, T. Pohl, and J. M. Rost, “Ultracold neutral plasmas,” *Phys. Reports* **449**, 77–130 (2007).
- [44] S. Kulin, T. C. Killian, S. D. Bergeson, and S. L. Rolston, “Plasma oscillations and expansion of an ultracold neutral plasma,” *Phys. Rev. Lett.* **85**, 318–321 (2000).
- [45] S. D. Bergeson and R. L. Spencer, “Neutral-plasma oscillations at zero temperature,” *Phys. Rev. E* **67**, 026414 (2003).
- [46] R. S. Fletcher, X. L. Zhang, and S. L. Rolston, “Observation of collective modes of ultracold plasmas,” *Phys. Rev. Lett.* **96**, 105003 (2006).
- [47] K. A. Twedt and S. L. Rolston, “Electronic detection of collective modes of an ultracold plasma,” *Phys. Rev. Lett.* **108**, 065003 (2012).
- [48] A. Lyubonko, T. Pohl, and J. M. Rost, “Collective energy absorption of ultracold plasmas through electronic edge-modes,” *New J. Phys.* **14**, 053039 (2012).
- [49] T. Ditmire, T. Donnelly, A. M. Rubenchik, R. W. Falcone, and M. D. Perry, “Interaction of intense laser pulses with atomic clusters,” *Phys. Rev. A* **53**, 3379–3402 (1996).
- [50] D. Duft and T. Leisner, “The index of refraction of supercooled solutions determined by the analysis of optical rainbow scattering from levitated droplets,” *Int. J. Mass Spectrosc.* **233**, 61–65 (2004).
- [51] A. D. Ward, M. Zhang, and O. Hunt, “Broadband Mie scattering from optically levitated aerosol droplets using a white LED,” *Opt. Express* **16**, 16390–16403 (2008).
- [52] T. R. Lettieri, W. D. Jenkins, and D. A. Swyt, “Sizing of individual optically levitated evaporating droplets by measurement of resonances in the polarization-ratio,” *Appl. Opt.* **20**, 2799–2805 (1981).

-
- [53] R. J. A. Hill and L. Eaves, “Vibrations of a diamagnetically levitated water droplet,” *Phys. Rev. E* **81**, 056312 (2010).
- [54] P. Stockel, I. M. Weidinger, H. Baumgartel, and T. Leisner, “Rates of homogeneous ice nucleation in levitated H₂O and D₂O droplets,” *J. Phys. Chem. A* **109**, 2540–2546 (2005).
- [55] S. E. Wolf, J. Leiterer, M. Kappl, F. Emmerling, and W. Tremel, “Early homogeneous amorphous precursor stages of calcium carbonate and subsequent crystal growth in levitated droplets,” *J. Am. Chem. Soc.* **130**, 12342–12347 (2008).
- [56] S. A. Maier, S. R. Andrews, L. Martín-Moreno, and F. J. García-Vidal, “Terahertz surface plasmon-polariton propagation and focusing on periodically corrugated metal wires,” *Phys. Rev. Lett.* **97**, 176805 (2006).
- [57] L. Shen, X. Chen, Y. Zhong, and K. Agarwal, “Effect of absorption on terahertz surface plasmon polaritons propagating along periodically corrugated metal wires,” *Phys. Rev. B* **77**, 075408 (2008).
- [58] M. I. Stockman, “Nanofocusing of optical energy in tapered plasmonic waveguides,” *Phys. Rev. Lett.* **93**, 137404 (2004).
- [59] W. L. Barnes, A. Dereux, and T. W. Ebbesen, “Surface plasmon subwavelength optics,” *Nature* **424**, 824–830 (2003).
- [60] M. S. Sherwin, C. A. Schmuttenmaer, and P. H. Bucksbaum, Proc. DOE-NSF-NIH Workshop on opportunities in THz science, Arlington, VA. (2004).
- [61] F. Keilmann, “Surface-polariton propagation for scanning near-field optical microscopy application,” *J. Microsc.* **194**, 567–570 (1999).
- [62] R. Hillenbrand and F. Keilmann, “Optical oscillation modes of plasmon particles observed in direct space by phase-contrast near-field microscopy,” *Appl. Phys. B* **73**, 239–243 (2001).
- [63] H.-T. Chen, R. Kersting, and G. C. Cho, “Terahertz imaging with nanometer resolution,” *Appl. Phys. Lett.* **83**, 3009–3011 (2003).
- [64] F. Buersegens, R. Kersting, and H.-T. Chen, “Terahertz microscopy of charge carriers in semiconductors,” *Appl. Phys. Lett.* **88**, 112115 (2006).
- [65] D. Crawley, C. Longbottom, V. P. Wallace, B. Cole, D. Arnone, and M. Pepper, “Three-dimensional terahertz pulse imaging of dental tissue,” *J. Biomed. Opt.* **8**, 303–307 (2003).
- [66] R. M. Woodward, V. P. Wallace, D. D. Arnone, E. H. Linfield, and M. Pepper, “Terahertz pulsed imaging of skin cancer in the time and frequency domain,” *J. Biol. Phys.* **29**, 257–261 (2003).

- [67] K. Kneipp, Y. Wang, H. Kneipp, L. T. Perelman, I. Itzkan, R. Dasari, and M. S. Feld, “Single molecule detection using surface-enhanced Raman scattering (SERS),” *Phys. Rev. Lett.* **78**, 1667–1670 (1997).
- [68] S. Nie and S. R. Emory, “Probing single molecules and single nanoparticles by surface-enhanced Raman scattering,” *Science* **275**, 1102–1106 (1997).
- [69] R. H. Jacobsen, D. M. Mittleman, and M. C. Nuss, “Chemical recognition of gases and gas mixtures with terahertz waves,” *Opt. Lett.* **21**, 2011–2013 (1996).
- [70] M. Walther, M. R. Freeman, and F. A. Hegmann, “Metal-wire terahertz time-domain spectroscopy,” *Appl. Phys. Lett.* **87**, 261107 (2005).
- [71] K. Wang and D. M. Mittleman, “Metal wires for terahertz wave guiding,” *Nature* **432**, 376–379 (2004).
- [72] J. A. Deibel, K. Wang, M. D. Escarra, and D. M. Mittleman, “Enhanced coupling of terahertz radiation to cylindrical wire waveguides,” *Opt. Express* **14**, 279–290 (2006).
- [73] T.-I. Jeon, J. Zhang, and D. Grischkowsky, “THz Sommerfeld wave propagation on a single metal wire,” *Appl. Phys. Lett.* **86**, 161904 (2005).
- [74] A. Agrawal and A. Nahata, “Coupling terahertz radiation onto a metal wire using a subwavelength coaxial aperture,” *Opt. Express* **15**, 9022–9028 (2007).
- [75] R. Adam, L. Chusseau, T. Grosjean, A. Penarier, J.-P. Guillet, and D. Charraut, “Near-field wire-based passive probe antenna for the selective detection of the longitudinal electric field at terahertz frequencies,” *J. Appl. Phys.* **106**, 073107 (2009).

2

Classical formulations of the electromagnetic self-force of extended charged bodies

Abstract - Derivations of the electromagnetic self-force of rigid charged objects, as developed in the context of classical models of charged particles, are reviewed. The mathematical equivalence of the various dissimilar self-force expressions is demonstrated explicitly. The position of the presented self-force calculations in the wider context of classical electrodynamic descriptions of charged particles is discussed, as well as their relevance to the description of macroscopic bunches of charged particles.

Publication status - The work described in this chapter has been submitted as an article for publication by P. W. Smorenburg, L. P. J. Kamp, and O. J. Luiten (2013).

2.1 Introduction

The origin of mass has always been a most important issue in physics, as exemplified by the extreme efforts culminating in the recent observation of the Higgs particle. Before the invention of the Higgs mechanism, and indeed before the advent of quantum mechanics and the standard model, attempts were made to explain the mass of elementary particles in terms of electromagnetic fields. As was first articulated by Thomson [76], the acceleration of a charged body increases the energy of the electromagnetic field associated with the charge. This implies a resistance to accelerations, or a electromagnetic contribution to the inertia of the body. On this basis, Abraham [77], Lorentz [78], and others developed models for the electron in which the latter was thought of as an extended charged body, possibly with zero non-electromagnetic mass, that interacted with both externally applied and self-produced electromagnetic fields. Classical electromagnetic electron models are still being actively pursued in literature [79–82].

While electromagnetic descriptions of inertia relate to the fields that are inseparably connected to the charge, that is, the Coulomb or near fields, the acceleration of charged particles also gives rise to radiation fields, which too have their mechanical effect on the motion of the accelerated particle. The latter influence is known as radiation reaction, and its existence was recognized from the outset [77, 78]. While radiation reaction for a long time has been considered experimentally irrelevant due to the smallness of the effect, it has recently regained interest because available laser intensities and the associated accelerations of electrons have almost increased to the point where radiation reaction effects may become observable [83, 84]. Moreover, we will show in chapter 5 that coherent enhancement of radiation reaction may lead to observable effects already at moderate laser intensities.

Central to the classical electromagnetic description of inertia and radiation reaction is the resultant Lorentz force \mathbf{F} that is experienced by the charged particle, and caused by the self-produced electromagnetic fields. In extended electron models where the particle is assumed to have a finite size, this self-force reads

$$\mathbf{F} = \int (\rho \mathbf{E} + \mathbf{J} \times \mathbf{B}) d^3 \mathbf{x} = \int \left[-\rho \left(\nabla \phi + \frac{\partial \mathbf{A}}{\partial t} \right) + \mathbf{J} \times (\nabla \times \mathbf{A}) \right] d^3 \mathbf{x}, \quad (2.1)$$

where ρ is the charge density, \mathbf{J} is the current density, \mathbf{E} is the electric field, \mathbf{B} is the magnetic field, ϕ and \mathbf{A} are the electromagnetic potentials, and the integration is over the extent of the particle. Eq. (2.1) is the starting point of any explicit calculation of the electromagnetic self-force of a rigid charged body. In the past, several approaches have been adopted to carry out this evaluation. In the special case of a homogeneously charged sphere, this has yielded results in a variety of forms such as series expansions [85, 86], definite integrals over time [87, 88], and Fourier integrals [89, 90]. Although

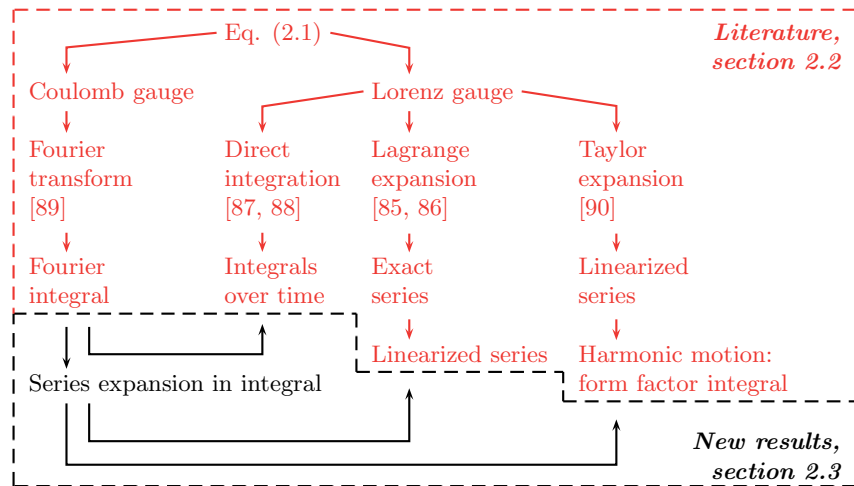


Figure 2.1: The content of this chapter in relation to existing results in literature.

these results have been cited many times and have been extensively reviewed [91], it has never been shown how the various dissimilar expressions for the self-force can be derived directly from each other, rather than starting from Eq. (2.1) for each method separately. In this chapter, we establish these interrelations by deriving the mentioned series expansions [85, 86] and integral expressions [87, 88, 90] from the result of Bohm and Weinstein [89].

Figure 2.1 shows schematically the content of this chapter in relation to the results available in literature. In section 2.2, a number of existing self-force derivations are reviewed. In section 2.3, the mathematical equivalence of the resulting self-force expressions is demonstrated. The derivations of section 2.3 constitute new results that have not been given previously. Section 2.4 sketches the position of the presented self-force calculations in the wider context of classical electrodynamic descriptions of charged particles. In section 2.5, we conclude by discussing the relevance of classical electron models to the description of macroscopic bunches of charged particles, which are the main subject of this thesis.

2.2 Existing self-force derivations

The derivation of the self-force of a rigid charged body requires the evaluation of Eq. (2.1) by some method. This involves a calculation of the electromagnetic potentials appearing in Eq. (2.1), which necessitates a choice of gauge. The potentials $\phi^{(L)}$ and $\mathbf{A}^{(L)}$ in the Lorenz gauge and the vector potential $\mathbf{A}^{(C)}$ in the Coulomb gauge satisfy

the wave equations

$$\left(\frac{1}{c^2}\frac{\partial^2}{\partial t^2} - \nabla^2\right)\Psi(\mathbf{x}, t) = \mu_0 c \Pi(\mathbf{x}, t). \quad (2.2)$$

Here, $\Psi \equiv \{\phi^{(L)}, c\mathbf{A}^{(L)}, c\mathbf{A}^{(C)}\}$ and $\Pi \equiv \{c\rho, \mathbf{J}, \mathbf{J}_T\}$, with \mathbf{J}_T the divergenceless part of the current density [90]. The scalar potential in the Coulomb gauge is not relevant here, as will be discussed below. In terms of the causal Green's function for the wave equation, which equals [90]

$$G(\mathbf{x}, \mathbf{x}', t, t') = \frac{\delta(t - t' - |\mathbf{x} - \mathbf{x}'|/c)}{|\mathbf{x} - \mathbf{x}'|} \quad (2.3)$$

with δ the Dirac delta function, the relevant particular solution of Eq. (2.2) is given by

$$\Psi(\mathbf{x}, t) = \frac{\mu_0 c}{4\pi} \iint G(\mathbf{x}, \mathbf{x}', t, t') \Pi(\mathbf{x}', t') d^3\mathbf{x}' dt'. \quad (2.4)$$

For any given charge distribution and given history of the motion of the charged body, $\Pi(\mathbf{x}', t')$ is known, so that in principle the potentials can be evaluated with Eq. (2.4), after which the self-force can be determined via Eq. (2.1). The calculations available in literature where this program is followed differ in the order in which the integrations in Eq. (2.4) are carried out. In view of the delta function in Eq. (2.3), it is tempting to start with the integration with respect to t' . This immediately yields the well-known retarded integral expressions [90] for the potentials, which indeed are the starting point for the self-force calculations presented in sections 2.2.1 and 2.2.2 below. However, integrating first with respect to t' in Eq. (2.4) is not the only possibility. For certain charge distributions, it is advantageous to start with the integration over \mathbf{x}' , as will be described in section 2.2.3. Still another possibility is to Fourier transform Eq. (2.4), that is, to integrate with respect to the coordinates \mathbf{x} ; this is shown in section 2.2.4.

2.2.1 Taylor expansion

Adopting the Lorenz gauge, integration of Eq. (2.4) with respect to t' yields the retarded integral expressions

$$\Psi(\mathbf{x}, t) = \frac{\mu_0 c}{4\pi} \int \frac{\Pi(\mathbf{x}', t_{ret})}{|\mathbf{x} - \mathbf{x}'|} d^3\mathbf{x}', \quad (2.5)$$

where now $\Psi \equiv \{\phi, c\mathbf{A}\}$ and $\Pi \equiv \{c\rho, \mathbf{J}\}$. In Eq. (2.5), the integration is complicated by the fact that Π must be evaluated at the retarded time $t_{ret} \equiv t - |\mathbf{x} - \mathbf{x}'|/c$, which is different for each volume element $d^3\mathbf{x}'$. Jackson [90] approaches this problem by expanding Π in a Taylor series around the current time t ,

$$\Pi(\mathbf{x}', t_{ret}) = \sum_{n=0}^{\infty} \frac{1}{n!} \left(-\frac{|\mathbf{x} - \mathbf{x}'|}{c} \right)^n \frac{\partial^n \Pi(\mathbf{x}, t)}{\partial t^n}. \quad (2.6)$$

Substitution of Eq. (2.6) in Eq. (2.5) expresses the potential in terms of quantities evaluated at the current time only. Using the result in Eq. (2.1) gives, after some manipulations [90], the electric component of the self-force

$$\mathbf{F} = \int d^3 \mathbf{r} \rho(\mathbf{r}, t) \left[\frac{\mu_0}{4\pi} \sum_{n=0}^{\infty} \frac{(-1)^n}{n! c^n} \int R^{n-1} \frac{\partial^{n+1}}{\partial t^{n+1}} \left(\frac{n+1}{n+2} \mathbf{J} - \frac{n-1}{n+2} \frac{(\mathbf{J} \cdot \mathbf{R}) \mathbf{R}}{R^2} \right) d^3 \mathbf{r}' \right], \quad (2.7)$$

where the integration variables have been changed to $\mathbf{r} = \mathbf{x} - \boldsymbol{\xi}(t)$, $\mathbf{r}' = \mathbf{x}' - \boldsymbol{\xi}(t)$, and $\mathbf{R} = \mathbf{r} - \mathbf{r}'$. For a spherically symmetric rigid charge distribution, Eq. (2.7) simplifies to

$$\mathbf{F} = \frac{\mu_0}{6\pi} \sum_{n=0}^{\infty} \frac{(-1)^n}{n! c^n} \frac{d^{n+2} \boldsymbol{\xi}}{dt^{n+2}} \iint \rho(\mathbf{r}) \rho(\mathbf{r}') |\mathbf{r} - \mathbf{r}'|^{n-1} d^3 \mathbf{r} d^3 \mathbf{r}', \quad (2.8)$$

in which $\boldsymbol{\xi}(t)$ is the trajectory of the center of the charged body. In Eq. (2.8), the magnetic component corresponding to the last term in square brackets in Eq. (2.1) has been neglected, so that Eq. (2.8) is only correct up to terms linear in $\boldsymbol{\xi}$ and its time derivatives. In case of harmonic motion $\boldsymbol{\xi} = \boldsymbol{\xi}_0 \exp(-i\omega t) \equiv \tilde{\boldsymbol{\xi}}$, the series in Eq. (2.8) can be readily summed, and is proportional to $\exp(i\omega |\mathbf{r} - \mathbf{r}'|/c)$. Furthermore, writing in Eq. (2.8) the charge distributions ρ in terms of their spatial Fourier transforms, and integrating the resulting expression, it is found that [90]

$$\mathbf{F} = \frac{8\pi\omega^2}{3\epsilon_0 c^2} \tilde{\boldsymbol{\xi}} \lim_{\lambda \downarrow 0} \int_0^{\infty} \frac{k^2 |\rho_k|^2}{k^2 - (\omega/c + i\lambda)^2} dk. \quad (2.9)$$

Here, the symmetrical convention for Fourier transformed quantities

$\mathbf{Y}_k \equiv (2\pi)^{-3/2} \int \mathbf{Y}(\mathbf{r}) \exp(-i\mathbf{k} \cdot \mathbf{r}) d^3 \mathbf{r}$ is adopted. The quantity ρ_k is often called the form factor of the charge distribution.

2.2.2 Lagrange expansion

As mentioned above, Eq. (2.8) is a linearized approximation to the exact self-force due to the neglect of the magnetic term in Eq. (2.1). However, the derivation in section 2.2.1 is inexact for another reason. Namely, by making use of a predefined rigid charge distribution ρ throughout the derivation (or more precisely, using the distribution in the proper frame), it is implied that the potentials are generated by a total charge $\int \rho(\mathbf{x}', t_{ret}) d^3 \mathbf{x}'$. The latter is in general not equal to the true charge of the body $\int \rho(\mathbf{x}', t) d^3 \mathbf{x}' \equiv q$, but rather depends on the body's state of motion. To correct for this inconsistency, either the quantity Π should be defined in a relativistically

covariant way, or else the integral (2.5) should be modified to leave the total charge invariant. The latter, however, is precisely how the Liénard-Wiechert potentials for a moving point charge were devised, as is explained clearly in Ref. [92]. Accordingly, the charged body may be regarded as a collection of infinitesimal particles moving with the trajectory $\boldsymbol{\xi}(t) + \mathbf{r}'$ and having a fixed charge $\rho(\mathbf{r}')d^3\mathbf{r}'$ with ρ the proper frame distribution. The corresponding potentials are thus given by

$$\Psi(\mathbf{x}, t) = \frac{\mu_0 c}{4\pi} \int \frac{\{c, \mathbf{v}\}}{R - \mathbf{R} \cdot \mathbf{v}/c} \Big|_{t=t_{ret}} \rho(\mathbf{r}') d^3\mathbf{r}', \quad (2.10)$$

where $\mathbf{v}(t) = d\boldsymbol{\xi}/dt$ is the velocity of the charged body, and $\mathbf{R}(t) \equiv \mathbf{x} - \boldsymbol{\xi}(t) - \mathbf{r}'$. An important difference between Eq. (2.5) and the Liénard-Wiechert formulation Eq. (2.10), apart from the different denominator, is that in the former the retarded time was known explicitly in terms of the coordinates \mathbf{x} and \mathbf{x}' , while in the latter it is only defined implicitly by the retardation condition $t_{ret} = t - R(t_{ret})/c$. This complicates the derivation of the self-force significantly. Herglotz [85] and Schott [86] proceeded by expanding retarded quantities Y in series using Lagrange's reversion theorem [93],

$$Y(t_{ret}) = Y(t) + \sum_{n=1}^{\infty} \frac{(-1)^n}{n! c^n} \frac{d^{n-1}}{dt^{n-1}} \left[R(t)^n \frac{dY(t)}{dt} \right]. \quad (2.11)$$

Note that differentiation of the quantity R^n in Eq. (2.11) produces factors of the velocity \mathbf{v} and derivatives thereof, so that the Taylor series Eq. (2.6) is in fact a linearization of Eq. (2.11) in which all terms nonlinear in \mathbf{v} and its derivatives have been neglected. Likewise, the potentials Eq. (2.5) are linearizations of the Liénard-Wiechert potentials Eq. (2.10). On working out the first few terms of Eq. (2.11), and noting that $R \sim b$ for relevant field points \mathbf{x} , it becomes apparent that these linearizations are good approximations provided that

$$\left| \frac{b^n}{c^n} \frac{d^n}{dt^n} \mathbf{v} \right| \ll |\mathbf{v}| \quad (2.12)$$

for $n \geq 1$. Roughly speaking, this means that the motion of the body should not change significantly on the time scale necessary for light to travel across the body, which is the time scale at which self-forces are communicated. This condition is known as quasi-stationary motion [91]. It indicates the range of validity of the form factor integral Eq. (2.9), in addition to the condition $|\mathbf{v}| \ll c$ associated with the neglect of magnetic forces.

Substitution of Eq. (2.11) in Eq. (2.10) expresses the potentials in terms of quantities evaluated at the current time only. Using the result in Eq. (2.1), and performing all integrations, gives a series expansion for the self-force. This series has been evaluated explicitly up to cubic terms in the velocity for a homogeneously

charged sphere of radius b by Herglotz [85]. The linear terms are

$$\mathbf{F} = -\frac{6\mu_0 q^2}{\pi b} \sum_{n=0}^{\infty} \frac{(n+1)(n+4)(-2b/c)^n}{(n+5)!} \frac{d^{n+2}\boldsymbol{\xi}}{dt^{n+2}}, \quad (2.13)$$

and dominate the nonlinear terms in case of quasi-stationary motion Eq. (2.12). For a homogeneously charged sphere in rectilinear motion $\boldsymbol{\xi}(t) = \xi(t)\mathbf{e}_z$, Schott [86] derived the following closed-form expression including terms up to arbitrary order:

$$\begin{aligned} \mathbf{F} = & -\frac{36q^2}{\pi\epsilon_0 b} \mathbf{e}_z \sum_{n=0}^{\infty} \sum_{m=0}^{\infty} \frac{(m+1)(n+1)(n+4)(-2b)^n}{(2m+1)(2m+3)!(n+5)!} \\ & \times \frac{\partial^{2m+n+2}}{\partial u^{2m+n+2}} [\xi(t+u/c) - \xi(t)]^{2m+1} \Big|_{u=0}, \end{aligned} \quad (2.14)$$

which reduces to Eq. (2.13) when truncated at $m = 0$.

2.2.3 Direct evaluation

Sommerfeld [87, 88] has evaluated the self-generated potentials of a charged body by integrating Eq. (2.4) with respect to \mathbf{x}' . For a homogeneously charged sphere, this leaves a one-dimensional integral over t' [88]:

$$\Psi(\mathbf{x}, t) = -\frac{3q}{16\pi^2 b^3} \int_{-\infty}^t \frac{\{c, \mathbf{v}(t')\}}{R_c(t')} \chi dt', \quad (2.15)$$

where $R_c(t') = |\mathbf{x} - \boldsymbol{\xi}(t')|$ is the distance to the center of the sphere, and

$$\chi = \begin{cases} 4c(t-t')R_c & c(t-t') < b - R_c \\ b^2 - [c(t-t') - R_c]^2 & b - R_c < c(t-t') < b + R_c \\ 0 & c(t-t') > b + R_c. \end{cases} \quad (2.16)$$

In virtue of the delta function in Eq. (2.4), times between t' and $t' + dt'$ in Eq. (2.15) correspond to the contribution to the potentials $\Psi(\mathbf{x}, t)$ generated by the charge located within a shell with radius $c(t-t')$ and thickness cdt' centered around the field point \mathbf{x} . Depending on R_c and t' , this shell may fall completely within the charged sphere, or only partially, or not at all, each case leading to a different factor χ as given by Eq. (2.16). Using the potentials Eq. (2.15) in Eq. (2.1) results in the self-force [87]

$$\mathbf{F} = -\frac{3q^2}{32\pi\epsilon_0 b^4 c} \left(\int_0^{\tau^+} G^+(\tau) d\tau + \int_0^{\tau^-} G^-(\tau) d\tau \right), \quad (2.17)$$

in which the integrations are over the time difference $\tau \equiv t - t'$, and

$$G^\pm(\tau) = [c^2 - \mathbf{v}(t) \cdot \mathbf{v}(t - \tau)] \frac{\mathbf{s}}{s} \frac{\partial}{\partial s} \frac{g(c\tau \pm s)}{s} + \frac{\partial}{\partial t} \frac{\mathbf{v}(t - \tau)g(c\tau \pm s)}{s}; \quad (2.18)$$

$$g(y) = \frac{y^5}{20b^5} - y^3 + 2by^2 - \frac{8b^3}{5}. \quad (2.19)$$

Here, $\mathbf{s} = \boldsymbol{\xi}(t) - \boldsymbol{\xi}(t - \tau)$ is the displacement of the charged sphere during the time interval τ . The upper integration limits in Eq. (2.17) are the roots of the equations $c\tau^\pm \pm s(\tau^\pm) = 2b$. These limits demarcate different stages in the communication of electromagnetic signals between the parts of the charged sphere that lead to the self-force at the current time t . For subluminal motion, the trailing end of the sphere receives electromagnetic signals at time t that were emitted by the other parts of the sphere at times between $t - \tau^+$ and t . The signals received by the leading end at time t were emitted by the other parts during the slightly longer interval between $t - \tau^-$ and t . Signals emitted at still earlier at times before $t - \tau^-$ do not arrive at any other part of the sphere at time t , so that the domain $\tau > \tau^-$ does not contribute to the self-force Eq. (2.17) at all.

2.2.4 Fourier transform

Bohm and Weinstein [89] have adopted the Coulomb gauge to evaluate Eq. (2.1). The benefit of this gauge choice for the calculation of the self-force of a rigid charged body is that the scalar potential ϕ equals the electrostatic potential corresponding to the instantaneous distribution of charge. Since for any pair of charge elements de_1 and de_2 the instantaneous electrostatic force on de_1 due to de_2 is the negative of the electrostatic force on de_2 due to de_1 , the contribution of ϕ to the self-force \mathbf{F} integrates to zero identically. Therefore only the vector potential has to be taken into account, which is given by Eq. (2.4) as before. It can be shown [89] that a Fourier transformation of this equation from the spatial domain \mathbf{x} to the wave vector domain \mathbf{k} yields the potential

$$\mathbf{A}_k(\mathbf{k}, t) = \frac{\mu_0 c}{k} \int_{-\infty}^t \mathbf{J}_{T,k}(\mathbf{k}, t) \sin[ck(t - t')] dt'. \quad (2.20)$$

Notice that the integration in Eq. (2.20) extends to the upper boundary t , so that the potential at time t depends only on currents at past times $t' < t$, that is, Eq. (2.20) is causal as it should be. Using in the self-force Eq. (2.1) the inverse Fourier transform $\mathbf{A} \equiv (2\pi)^{-3/2} \int \mathbf{A}_k \exp(i\mathbf{k} \cdot \mathbf{x}) d^3\mathbf{k}$, and substituting Eq. (2.20), gives [89]

$$\mathbf{F} = \frac{1}{\epsilon_0} \int_{-\infty}^t dt' \int d^3\mathbf{k} |\rho_k|^2 \exp(i\mathbf{k} \cdot \mathbf{s}) \quad (2.21)$$

$$\times \left(\frac{\mathbf{k} \times [\mathbf{v}(t') \times \mathbf{k}]}{k^2} \cos ck\tau - \frac{\mathbf{v}(t) \times [\mathbf{k} \times \mathbf{v}(t')]}{ck} i \sin ck\tau \right).$$

Note that the second term in large braces is proportional to and perpendicular to the current velocity $\mathbf{v}(t)$ of the charged body, and therefore represents the magnetic component of the self-force. The first term gives the electric component. For a spherically symmetric charge distribution, $\rho_k(\mathbf{k})$ is a function of the magnitude of \mathbf{k} but not of its direction. In this case, Eq. (2.21) can be straightforwardly integrated over angles in \mathbf{k} -space. This reduces Eq. (2.21) to

$$\mathbf{F} = -\frac{4\pi}{\epsilon_0} \int_{-\infty}^t dt' \int_0^\infty dk k^2 |\rho_k|^2 \left[\left(\mathbf{v}(t') - \frac{3[\mathbf{v}(t') \cdot \mathbf{s}]\mathbf{s}}{s^2} \right) \frac{j_1(ks)}{ks} \cos ck\tau \right.$$

$$\left. - \left(\mathbf{v}(t') - \frac{[\mathbf{v}(t') \cdot \mathbf{s}]\mathbf{s}}{s^2} \right) j_0(ks) \cos ck\tau - \frac{\mathbf{v}(t) \times [\mathbf{s} \times \mathbf{v}(t')]}{cs} j_1(ks) \sin ck\tau \right], \quad (2.22)$$

where j_n denotes the spherical Bessel function of the first kind and order n [94]. In Eq. (2.22), the first two terms in large square brackets represent the electric component of the force and are given in Ref. [89]; the last term gives the magnetic component. The integral over k containing Bessel function kernels has the typical form of an inverse Fourier transform in spherical coordinates [95]. In section 2.3, we will derive the other self-force representations given in sections 2.2.1 to 2.2.3 from this Fourier integral.

2.3 Equivalence of the self-force expressions

2.3.1 Fourier integral and integral over time

Sommerfeld derived for the piecewise function χ given by Eq. (2.16) the integral representation [88]

$$\chi = \frac{8b^2}{\pi} \int_0^\infty \frac{j_1(kb) \sin(kR_c) \sin[ck(t-t')]}{k} dk. \quad (2.23)$$

Substituting this representation in Eq. (2.15), and using the result in Eq. (2.1), gives the self-force [88]

$$\mathbf{F} = -\frac{9q^2}{2\pi^2 \epsilon_0 b^2 c} \int_0^\infty d\tau \int_0^\infty dk [j_1(kb)]^2 \quad (2.24)$$

$$\times \left(\frac{1}{k} \frac{\partial}{\partial t} [\mathbf{v}(t-\tau) j_0(ks) \sin ck\tau] - [c^2 - \mathbf{v}(t) \cdot \mathbf{v}(t-\tau)] \frac{\mathbf{s}}{s} j_1(ks) \sin ck\tau \right).$$

Performing the integration over k indeed yields the force Eq. (2.17). We now show that Eq. (2.24) is equivalent to Eq. (2.22) that was derived by Fourier analysis of the potentials in the Coulomb gauge. Note that the integrands of both equations already have a similar structure due to the form of the integral representation Eq. (2.23). Performing the differentiation $\partial/\partial t$ in Eq. (2.24) using the property

$$\frac{\partial j_0(ks)}{\partial t} = -kj_1(ks) \frac{\partial s}{\partial t} = -kj_1(ks) \frac{[\mathbf{v}(t) - \mathbf{v}(t - \tau)] \cdot \mathbf{s}}{s}$$

gives, after changing the integration variable back to t' and rearranging,

$$\begin{aligned} \mathbf{F} = & -\frac{9q^2}{2\pi^2\epsilon_0 b^2 c} \int_{-\infty}^t dt' \int_0^\infty dk [j_1(kb)]^2 \sin ck(t-t') \left[\frac{c^2 \mathbf{s}}{s} j_1(ks) \right. \\ & \left. - \frac{1}{k} \frac{d\mathbf{v}(t')}{dt'} j_0(ks) + \left(\frac{[\{\mathbf{v}(t) - \mathbf{v}(t')\} \cdot \mathbf{s}] \mathbf{v}(t')}{s} - \frac{[\mathbf{v}(t) \cdot \mathbf{v}(t')] \mathbf{s}}{s} \right) j_1(ks) \right]. \end{aligned} \quad (2.25)$$

Next we integrate by parts the first two terms in large square brackets in Eq. (2.25) with respect to t' , choosing for the differentiated factors respectively $f_1(t') = \mathbf{s}j_1(ks)/s$ and $f_2(t') = j_0(ks) \sin ck\tau$. To carry out this integration unambiguously, it is necessary to replace the lower integration limit $t' = -\infty$ by $t' = -a$, and take the limit $a \rightarrow \infty$ afterwards. With the help of the relations

$$\begin{aligned} \frac{\partial f_1}{\partial t'} &= \left(\frac{3j_1(ks)}{ks} - j_0(ks) \right) \frac{k[\mathbf{v}(t') \cdot \mathbf{s}] \mathbf{s}}{s^2} - \frac{\mathbf{v}(t')}{s} j_1(ks); \\ \frac{\partial f_2}{\partial t'} &= \frac{k\mathbf{v}(t') \cdot \mathbf{s}}{s} j_1(ks) \sin ck\tau - ckj_0(ks) \cos ck\tau, \end{aligned}$$

the resulting self-force is

$$\mathbf{F} = \frac{9q^2}{2\pi^2\epsilon_0 b^2} \lim_{a \rightarrow \infty} \int_0^\infty [j_1(kb)]^2 (B + I) dk, \quad (2.26)$$

where

$$\begin{aligned} B &= \left[\frac{\mathbf{v}(t')}{ck} j_0(ks) \sin ck\tau - \frac{\mathbf{s}}{ks} j_1(ks) \cos ck\tau \right]_{t'=-a}^t; \\ I &= - \int_{-a}^t dt' \left[\left(\mathbf{v}(t') - \frac{3[\mathbf{v}(t') \cdot \mathbf{s}] \mathbf{s}}{s^2} \right) \frac{j_1(ks)}{ks} \cos ck\tau \right. \\ &\quad \left. - \left(\mathbf{v}(t') - \frac{[\mathbf{v}(t') \cdot \mathbf{s}] \mathbf{s}}{s^2} \right) j_0(ks) \cos ck\tau - \frac{\mathbf{v}(t) \times [\mathbf{s} \times \mathbf{v}(t')]}{cs} j_1(ks) \sin ck\tau \right]. \end{aligned}$$

Taking in Eq. (2.26) the limit $a \rightarrow \infty$ of I presents no difficulties, and yields precisely Eq. (2.22), specialized to a homogeneous sphere that has the form factor

$$\rho_k = \frac{3q}{(2\pi)^{3/2}} \frac{j_1(kb)}{kb}. \quad (2.27)$$

Therefore Eq. (2.26) is equivalent to Eq. (2.22), provided that the boundary term B vanishes. This can be shown to be the case as follows. B evaluated at $t' = t$ vanishes since $\sin ck\tau = 0$ and $s(t') = 0$ at $t' = t$. In the limit $t' \rightarrow -\infty$, the first term of B is zero trivially when $\mathbf{v}(-\infty) = \mathbf{0}$. When $\mathbf{v}(-\infty) \neq \mathbf{0}$, it must be that $s(t') \rightarrow \infty$ and hence $j_0(ks) \rightarrow 0$ as $t' \rightarrow -\infty$, so that the first term does not contribute in this case either. The second term of B , on the other hand, vanishes at $t \rightarrow -\infty$ only when $\mathbf{v}(-\infty) \neq \mathbf{0}$. Namely, when $\mathbf{v}(-\infty) = \mathbf{0}$ it is possible that $s(-\infty) \equiv S$ has a finite value. In that case, the boundary term makes a contribution to Eq. (2.26) proportional to

$$\lim_{a \rightarrow \infty} \int_0^\infty h(k) \cos ck(t-a) dk, \quad (2.28)$$

where $h(k) = [j_1(kb)]^2 j_1(kS)/k$. However, Eq. (2.28) evaluates to zero by the Riemann-Lebesgue lemma [93]. Hence $B = 0$ for all possible $\mathbf{v}(-\infty)$, so that the force Eq. (2.26) is indeed identical to the force Eq. (2.22) that was derived by Fourier analysis of the potentials in the Coulomb gauge.

2.3.2 Fourier integral and form factor integral

As discussed above, the self-force Eq. (2.9) in terms of a form factor integral is valid for quasi-stationary motion Eq. (2.12) and $|\mathbf{v}| \ll c$, and for the special case of harmonic motion. In order to compare Eq. (2.9) with the self-force derived in section 2.2.4, the latter should be specialized accordingly. This may be effected by expanding the integrand of Eq. (2.21) in a Taylor series around $t' = t$, and linearizing the result by neglecting all terms nonlinear in \mathbf{v} and its derivatives. The extremely involved full expansion, in which all nonlinear terms have been kept, is given in Ref. [79]. Formally, such use of a Taylor series to describe the integrand on the infinite interval $-\infty < t' < t$ is questionable because the series may have a finite radius of convergence. However, for subrelativistic motion electromagnetic signals are communicated between parts of the charged body on a time scale $\sim b/c$, so that only the small interval $t - b/c \lesssim t' < t$ significantly contributes to the integral in Eq. (2.21). This can be seen by noting in Eq. (2.21) that the integrand only contributes in the domain $|\mathbf{k}| \lesssim b^{-1}$ because the form factor $|\rho_k|^2 \approx 0$ elsewhere, and that the integral over this domain averages out due to the sinusoidal functions unless $ck\tau \lesssim \pi/2$, that is, unless $t - b/c \lesssim t' < t$. Proceeding on this basis by Taylor-expanding, neglecting nonlinear terms, and integrating over angles in \mathbf{k} -space, yields

$$\mathbf{F} = -\frac{8\pi}{3\epsilon_0} \sum_{n=0}^{\infty} \frac{(-1)^n}{n!} \frac{d^n \mathbf{v}}{dt^n} \int_0^\infty \int_0^\infty k^2 |\rho_k|^2 \tau^n \cos ck\tau d\tau dk. \quad (2.29)$$

Writing in Eq. (2.29)

$$\begin{aligned}\tau^{2n} \cos ck\tau &= (-1)^n c^{-2n} (d/dk)^{2n} \cos ck\tau; \\ \tau^{2n+1} \cos ck\tau &= (-1)^n c^{-2n-1} (d/dk)^{2n+1} \sin ck\tau,\end{aligned}$$

as is also done in Ref. [79], and integrating by parts with respect to k repeatedly, gives

$$\begin{aligned}\mathbf{F} &= -\frac{8\pi}{3\epsilon_0} \sum_{n=0}^{\infty} \frac{(-1)^n}{c^{2n} (2n)!} \frac{d^{2n} \mathbf{v}}{dt^{2n}} \int_0^{\infty} \left(B_n^{(e)} + I_n^{(e)} \right) d\tau \\ &\quad - \frac{8\pi}{3\epsilon_0} \sum_{n=0}^{\infty} \frac{(-1)^n}{c^{2n+1} (2n+1)!} \frac{d^{2n+1} \mathbf{v}}{dt^{2n+1}} \int_0^{\infty} \left(B_n^{(o)} + I_n^{(o)} \right) d\tau,\end{aligned}\tag{2.30}$$

in which

$$\begin{aligned}B_n^{(e)} &= \sum_{m=0}^{2n-1} (-1)^m \frac{d^m}{dk^m} k^2 |\rho_k|^2 \frac{d^{2n-m-1}}{dk^{2n-m-1}} \cos ck\tau \Big|_{k=0}^{\infty}; \\ B_n^{(o)} &= \sum_{m=0}^{2n} (-1)^{m+1} \frac{d^m}{dk^m} k^2 |\rho_k|^2 \frac{d^{2n-m}}{dk^{2n-m}} \sin ck\tau \Big|_{k=0}^{\infty}; \\ I_n^{(e)} &= \int_0^{\infty} \frac{d^{2n}}{dk^{2n}} \left(k^2 |\rho_k|^2 \right) \cos ck\tau dk; \\ I_n^{(o)} &= \int_0^{\infty} \frac{d^{2n+1}}{dk^{2n+1}} \left(k^2 |\rho_k|^2 \right) \sin ck\tau dk.\end{aligned}$$

All boundary terms $B_n^{(e)}$ and $B_n^{(o)}$ vanish identically. At $k = \infty$, this is because $\rho_k(\infty) = 0$ for any finite charge distribution. At $k = 0$, the terms with odd m are zero because $k^2 |\rho_k|^2$ is an even function, and those with even m vanish because they contain $\sin ck\tau$ as a factor. The quantity $\sqrt{2/\pi} I_n^{(e)} \equiv J_n^{(e)}$ can be interpreted as the symmetric cosine transform of the function $j_{2n}(k) = (d/dk)^{2n} k^2 |\rho_k|^2$; likewise, $\sqrt{2/\pi} I_n^{(o)} \equiv J_n^{(o)}$ is the symmetric sine transform of $j_{2n+1}(k)$. Therefore the double integrals in Eq. (2.30) reduce to the single integrals

$$\int_0^{\infty} I_n^{(e)} d\tau = \frac{\pi}{2c} \left(\sqrt{\frac{2}{\pi}} \int_0^{\infty} J_n^{(e)} \cos kx dx \right)_{k=0} = \frac{\pi}{2c} j_{2n}(0); \tag{2.31}$$

$$\begin{aligned}\int_0^{\infty} I_n^{(o)} d\tau &= \frac{1}{c} \sqrt{\frac{2}{\pi}} \left(\int_0^{\infty} \frac{\sin kx}{k} dk \right) \left(\int_0^{\infty} J_n^{(o)} dx \right) \\ &= \int_0^{\infty} \left(\sqrt{\frac{2}{\pi}} \int_0^{\infty} J_n^{(o)} \sin kx dx \right) \frac{dk}{ck} = \int_0^{\infty} \frac{j_{2n+1}(k)}{ck} dk.\end{aligned}\tag{2.32}$$

Here, the identity $\int_0^\infty k^{-1} \sin kx dk = \pi/2$ and the variable $x = c\tau$ have been used. With the help of Eqs. (2.31)-(2.32), the force Eq. (2.30) reduces to

$$\mathbf{F} = \frac{8\pi}{3\epsilon_0 c} \sum_{n=0}^{\infty} \frac{(-1)^{n+1}}{c^{2n}(2n)!} \left[\frac{\pi}{2} \left(\frac{d^{2n}}{dk^{2n}} k^2 |\rho_k|^2 \right)_{k=0} \frac{d^{2n} \mathbf{v}}{dt^{2n}} \right. \\ \left. + \frac{1}{(2n+1)c} \left(\int_0^\infty \frac{d^{2n+1}}{dk^{2n+1}} k^2 |\rho_k|^2 \frac{dk}{k} \right) \frac{d^{2n+1} \mathbf{v}}{dt^{2n+1}} \right]. \quad (2.33)$$

This expression now has the manageable form of a series in terms of the derivatives of the current velocity, with coefficients that are readily calculated from the form factor of the charge distribution. In the next section, we will specialize this result to a homogeneously charged sphere, and show that it is equivalent to the series expansion Eq. (2.13) obtained by application of Lagrange's reversion theorem. Here, we apply Eq. (2.33) to the case of harmonic motion, for which $\mathbf{v} = -i\omega \boldsymbol{\xi}_0 \exp(-i\omega t) \equiv -i\omega \tilde{\boldsymbol{\xi}}$. Since $(d/dt)^n \mathbf{v} = (-i\omega)^n \mathbf{v}$, Eq. (2.33) then becomes the sum of two ordinary power series in the quantity ω/c . The series corresponding to the first line of Eq. (2.33) may be interpreted as the even part of the Taylor series of the function $p(\kappa) = \kappa^2 |\rho_k(\kappa)|^2$ around $\kappa = 0$, evaluated at $\kappa = \omega/c$. Similarly, the series in the second line may be identified with the odd part of the Taylor series of $p(\kappa)$ around $\kappa = k$, evaluated at $\kappa = k + \omega/c$. Summing these two series therefore results in

$$\mathbf{F} = \frac{4\pi\omega}{3\epsilon_0 c} \tilde{\boldsymbol{\xi}} \left(\int_0^\infty \frac{p(k + \omega/c) - p(k - \omega/c)}{k} dk + \frac{i\pi}{2} [p(\omega/c) + p(-\omega/c)] \right). \quad (2.34)$$

Noting that $p(k)$ is an even function, the integral in Eq. (2.34) may be recognized as the Hilbert transform of $p(k)$ in a less common notation [96]. Accordingly, by changing variables it may be shown [96] that

$$\mathbf{F} = \frac{8\pi\omega^2}{3\epsilon_0 c^2} \tilde{\boldsymbol{\xi}} \left(\int_0^\infty \frac{k^2 |\rho_k(k)|^2}{k^2 - \omega^2/c^2} dk + i\pi \operatorname{Res}_{k=\omega/c} \frac{k^2 |\rho_k(k)|^2}{k^2 - \omega^2/c^2} \right), \quad (2.35)$$

where f denotes the Cauchy principal value. Here, the second line of Eq. (2.34) has been interpreted as a residue. Eq. (2.35) is identical to the force Eq. (2.9) derived from a Taylor expansion of the retarded integrals for the potentials.

2.3.3 Fourier integral and Lagrange expansion

In the previous section, we derived the series expansion Eq. (2.33) that expresses the linearized self-force in terms of the derivatives of the current velocity of the charged body, for a general spherically symmetric charge distribution. We will now specialize this result to a homogeneously charged sphere, and show that this yields the self-force Eq. (2.13) that was obtained from series expansion of the retarded potentials. Evaluation of Eq. (2.33) using the form factor of a homogeneous sphere Eq. (2.27)

requires determination of the quantities

$$S_n = \left. \frac{d^{2n} [j_1(x)]^2}{dx^{2n}} \right|_{x=0}; \quad T_n = \int_0^\infty \frac{d^{2n+1} [j_1(x)]^2}{dx^{2n+1}} \frac{dx}{x}. \quad (2.36)$$

The first of these equals $(2n)!$ times the coefficient of x^{2n} in the Taylor series of $[j_1(x)]^2$ around $x = 0$. By squaring the ascending power series of the Bessel function [94], it is thus found that

$$S_n = \sum_{m=0}^{n-1} \frac{(2n)! \left(-\frac{1}{2}\right)^{n-1}}{m!(n-m-1)!(2m+3)!(2n-2m+1)!}. \quad (2.37)$$

Writing factorials in terms of Pochhammer symbols $(p)_q \equiv \Gamma(p+q)/\Gamma(p)$ with Γ the Gamma function [94], Eq. (2.37) becomes

$$S_n = \frac{\pi(2n)! \left(-\frac{1}{4}\right)^{n+1}}{\Gamma\left(\frac{5}{2}\right) \Gamma(n) \Gamma\left(n + \frac{3}{2}\right)} \sum_{m=0}^{n-1} \frac{(1-n)_m \left(-\frac{1}{2} - n\right)_m}{m! \left(\frac{5}{2}\right)_m}. \quad (2.38)$$

Here, it has been used that $(p)_{-q} = (-1)^q/(1-p)_q$ [97]. The series in Eq. (2.38) defines a Gauss hypergeometric function with unit argument [94]. Evaluating this hypergeometric function, and converting Gamma functions to factorials, results in

$$S_n = -\frac{n(-4)^n}{(n+1)(n+2)(2n+1)}. \quad (2.39)$$

Establishing T_n is more involved. The squared Bessel function $[j_1(x)]^2$ can be expanded in a series of Bessel functions with doubled argument [98]. This gives

$$[j_1(x)]^2 = \sum_{m=0}^{\infty} \frac{2m+2}{(2m+1)(2m+3)} \frac{J_{4m+3}(2x) + J_{4m+5}(2x)}{x}, \quad (2.40)$$

where J denotes the cylindrical Bessel function of the first kind [94]. The factor x in the denominator can be removed with the help of the recurrence relation $2pJ_p(z)/z = J_{p-1}(z) + J_{p+1}(z)$. Subsequently, the integrand of T_n in Eq. (2.36) is found by applying the expansion [99]

$$\frac{d^p J_q(z)}{dz^p} = \frac{1}{2^p} \sum_{u=0}^p (-1)^u \binom{p}{u} J_{q-p+2u}(z). \quad (2.41)$$

This gives

$$\frac{1}{x} \frac{d^{2n+1} [j_1(x)]^2}{dx^{2n+1}} = \sum_{m=0}^{\infty} \sum_{u=0}^{2n+1} \frac{(2m+2)(-1)^u}{(2m+1)(2m+3)} \binom{2n+1}{u} \quad (2.42)$$

$$\times [C_0 J_v(2x) + C_2 J_{v+2}(2x) + C_4 J_{v+4}(2x) + C_6 J_{v+6}(2x)],$$

where $v \equiv 4m - 2n + 2u$, and

$$C_0 = \frac{1}{(4m+3)(4m-2n+2u+1)};$$

$$C_6 = \frac{1}{(4m+5)(4m-2n+2u+5)};$$

$$C_2 = C_0 + \frac{2(4m+4)}{(4m+3)(4m+5)(4m-2n+2u+3)};$$

$$C_4 = C_6 + \frac{2(4m+4)}{(4m+3)(4m+5)(4m-2n+2u+3)}.$$

Substituting this expansion in Eq. (2.36), the integral T_n can be evaluated trivially because $\int_0^\infty J_p(z) dz = 1$ for arbitrary $p > -1$ [94]. Therefore T_n is given by Eq. (2.42) if each Bessel function is replaced by $1/2$. The remaining double series can be summed in closed form. The sums over u of the various terms have been tabulated [97]; together they evaluate to

$$T_n = \frac{\pi(-1)^n(2n+1)!}{4\Gamma(n+\frac{1}{2})\Gamma(n+\frac{9}{2})} \quad (2.43)$$

$$\times \sum_{m=0}^{\infty} \left(4 + \frac{1}{m+\frac{1}{2}} - \frac{1}{m+\frac{3}{2}} \right) \frac{(1)_m (\frac{1}{4} - \frac{n}{2})_m (\frac{3}{4} - \frac{n}{2})_m}{m! (\frac{9}{4} + \frac{n}{2})_m (\frac{11}{4} + \frac{n}{2})_m}.$$

The series in the second line of Eq. (2.43) is derivable from the series

$$U_n(z) = \sum_{m=0}^{\infty} \frac{(1)_m (\frac{1}{4} - \frac{n}{2})_m (\frac{3}{4} - \frac{n}{2})_m z^m}{m! (\frac{9}{4} + \frac{n}{2})_m (\frac{11}{4} + \frac{n}{2})_m}, \quad (2.44)$$

which defines the generalized hypergeometric function [100]

$$U_n(z) = {}_3F_2 \left(1, \frac{1-2n}{4}, \frac{3-2n}{4}; \frac{11+2n}{4}, \frac{9+2n}{4}; z \right). \quad (2.45)$$

Comparing Eqs. (2.43) and (2.44), it is found that

$$T_n = \frac{\pi(-1)^n(2n+1)!}{4\Gamma(n+\frac{1}{2})\Gamma(n+\frac{9}{2})} \left(4U_n(1) + \int_0^1 U_n(z) D(z) dz \right), \quad (2.46)$$

with $D(z) = z^{-1/2} - z^{1/2}$. The integral in Eq. (2.46) is equal to [101]

$$\int_0^1 U_n D dz = \frac{4}{3} {}_4F_3\left(1, \frac{1}{2}, \frac{1-2n}{4}, \frac{3-2n}{4}; \frac{5}{2}, \frac{11+2n}{4}, \frac{9+2n}{4}; 1\right). \quad (2.47)$$

Eqs. (2.45)-(2.47) define T_n in terms of two generalized hypergeometric functions of unit argument; for both functions closed form expressions in terms of Gamma functions exist [102]. Writing these expressions in terms of factorials yields, after considerable reduction,

$$T_n = \frac{\pi(2n+1)(-4)^n}{(n+1)(2n+3)(2n+5)}. \quad (2.48)$$

Finally, having the quantities S_n and T_n at our disposal, the self-force Eq. (2.33) can be evaluated. Combining Eqs. (2.33), (2.27), (2.40) and (2.48) gives

$$\mathbf{F} = \frac{3q^2}{\pi\epsilon_0 cb^2} \sum_{n=0}^{\infty} \left(\frac{(2n)(2n+3)(-2b)^{2n}}{(2n+4)!} \frac{1}{c^{2n}} \frac{d^{2n}\mathbf{v}}{dt^{2n}} + \frac{(2n+1)(2n+4)(-2b)^{2n+1}}{(2n+5)!} \frac{1}{c^{2n+1}} \frac{d^{2n+1}\mathbf{v}}{dt^{2n+1}} \right). \quad (2.49)$$

Taking the two terms in large braces together by relabeling the summation index gives precisely Eq. (2.13). It has thus been shown that the self-force obtained by Fourier analysis of the potentials in the Coulomb gauge is equivalent to the force derived by Lagrange expansion of the potentials in the Lorenz gauge.

2.4 Charged particle theories

In the previous sections we have given an overview of classical derivations of the self-force of an extended rigid charged object, and we established the equivalence of the various approaches by deriving the resulting self-force expressions from one another. This body of research, symbolized by Fig. 2.1 as a whole, has been termed 'extended electron theories' [91]. It is useful to indicate the position of these theories within the wider scope of the classical electrodynamic description of charged particles. First of all, classical formulations in general were largely abandoned with the advent of quantum electrodynamics. However, on a small scale classical descriptions have continued to attract interest, partly motivated by the unsatisfactory need of renormalization procedures in quantum electrodynamics. Descriptions that are based on extended electron theories may be classified by their assumption regarding the size of the electron, which may be illustrated with reference to the self-force expressions Eqs. (2.13)-(2.14). In theories where the electron is supposed to have a finite size b , the force can be represented by a series of derivatives of the velocity, which may

be linearized or truncated depending on the approximations made. Truncation of the series, however, leads to an equation of motion of the electron that has the form of a finite-order differential equation, and it can be shown [103] that this equation always admits unphysical runaway solutions in which the electron keeps accelerating without the application of an external force. Such runaway solutions can be circumvented by keeping all terms of the linearized series, which leads to a better behaved differential equation of motion of infinite-order, or finite-difference equation [89, 104, 105]. Nevertheless, theories in which the electron is considered to be of finite size are plagued by other inconsistencies as well, in particular in connection with relativistic covariance and with a meaningful formulation of rigidity of extended relativistic objects [106]. These problems are avoided altogether in models which assume that the electron has vanishing extent. However, when formulating such models as the limit $b \rightarrow 0$ of extended electron theories, self-force divergences are encountered, as is apparent from Eqs. (2.13)-(2.14). Although these divergences could be handled by appropriate renormalization procedures [91], such procedures involve the unattractive assumption of a negative non-electromagnetic mass, which inherently leads again to an equation of motion that admits runaway solutions [107].

An alternative approach to the dynamics of classical charged particles is to assume a point particle from the outset, thereby dispensing with any problematic implications from extended electron theories, and base oneself on conservation laws only. Dirac [108] showed that it is possible to formulate a consistent covariant equation of motion in this way, which reads

$$\dot{p}^\mu = \frac{q}{m} F^{\mu\nu} p_\nu + \tau_e \left[\frac{\dot{p}^\lambda \dot{p}_\lambda}{(mc)^2} p^\mu + \ddot{p}^\mu \right], \quad (2.50)$$

where p^μ is the four momentum of the charged particle, $F^{\mu\nu}$ is the electromagnetic field tensor of the applied field, m and q are the mass and charge of the particle, and $\tau_e \equiv q^2/(6\pi\epsilon_0 mc^3)$. Eq. (2.50), together with some approximating versions, is presently the most widely accepted classical equation of motion of a charged particle. However, due to the presence of the second derivative \ddot{p}^μ , this equation too admits runaway solutions. To select the physically admissible solutions, auxiliary conditions must be made (such as $\dot{p}^\mu \equiv 0$ in the distant future). Alternatively, these conditions may be implied automatically by approximating $\dot{p}^\mu \approx (q/m)F^{\mu\nu}p_\nu$ in the bracketed term in Eq. (2.50), which is equivalent to demanding that this term remain small compared to the other terms. Both techniques to select physical solutions are equivalent [109]. The so-called Landau-Lifshitz equation of motion [110] resulting from the latter technique is at present commonly used [83, 84] as a numerically stable alternative to Eq. (2.50).

2.5 Discussion

From the previous section, it may be concluded that the present emphasis in classical descriptions of charged particles is on conservation laws and relativistic covariance. Although extended electron theories preceded and inspired currently used descriptions, the fields and forces within the particle presently play a subsidiary role. Nevertheless, in the context of this thesis, where our subject is macroscopic charged bunches rather than point particles, self-generated internal fields and forces are more than relevant. Extended electron theories therefore offer direct information about physical effects that can be expected in macroscopic bunches, insofar these bunches move in a more or less rigid manner. For example, the quantity in square brackets in Eq. (2.7) represents the self-generated retarded electric field $\mathbf{E}(\mathbf{r}, t)$ minus the electrostatic field $\mathbf{E}_{es}(\mathbf{r}, t)$ [90]. Assuming a homogeneous bunch in harmonic motion and evaluating the lowest order term $n = 0$, yields

$$\mathbf{E} - \mathbf{E}_{es} \approx -\frac{\mu_0 q \omega^2}{20\pi b^3} \left[(5b^2 - 2r^2) \tilde{\boldsymbol{\xi}} + (\mathbf{r} \cdot \tilde{\boldsymbol{\xi}}) \mathbf{r} \right]. \quad (2.51)$$

In practice the harmonic motion is caused by the electric field $\tilde{\mathbf{E}}$ of an applied electromagnetic wave, such that $\tilde{\boldsymbol{\xi}} = e\tilde{\mathbf{E}}/(m\omega^2)$; hence the total field in the bunch is $\tilde{\mathbf{E}} + \mathbf{E}$. Now, this total field is inhomogeneous, and therefore the time-average of the Lorentz force experienced by the electrons oscillating in this field is the ponderomotive force $\mathbf{F}_p = -e^2 \nabla |\tilde{\mathbf{E}} + \mathbf{E}|^2 / (4m\omega^2)$. For linear polarization in the z -direction, the cartesian components of \mathbf{F}_p evaluate to

$$\mathbf{F}_p \approx -\frac{e^2}{2m\omega^2} \nabla (\mathbf{E} \cdot \tilde{\mathbf{E}}) = -\frac{\mu_0 q e \omega^2 \tilde{\xi}^2}{20\pi b^3} \begin{pmatrix} 2x \\ 2y \\ z \end{pmatrix}. \quad (2.52)$$

Eq. (2.52) shows that coherently oscillating homogenous bunches self-generate a linearly compressive ponderomotive force.

Although the previous example already indicates the relevance of extended electron theories for the coherent interaction of macroscopic bunches, an important aspect of the latter is completely lacking from these theories: bunches of charged particles are not rigid. In case of electron bunches, electrostatic forces dominate any ponderomotive forces, leading to a rapid Coulomb explosion unless the bunch is accelerated to relativistic velocities. At relativistic velocities, however, all of the self-force expressions in this chapter lose their meaning, because no proper account has been taken of the relativistic consequences of assuming a rigid object [106]. To still make quantitative predictions about effects caused by the self-force of relativistic electron bunches, the best available result is the equation of motion Eq. (2.51), which at least is fully consistent with both relativity and conservation laws. In chapter 3, we therefore base

ourselves on Eq. (2.51) to calculate trajectories of subwavelength electron bunches interacting with a strong laser pulse. It is shown that the coherently enhanced self-force of the bunch may lead to observable effects, which may be tentatively extrapolated to significant acceleration in the regime of highly charged electrons bunches.

In case of quasi-neutral plasma bunches, electrostatic forces that drive the Coulomb explosion are largely absent. For such bunches, however, the lack of rigidity presents itself in the fact that the plasma electrons may oscillate with different amplitudes. Indeed, it is well known that the field strength of an electromagnetic wave traveling through an inhomogeneous plasma may vary substantially. Therefore, rather than calculating the self-force based on a presupposed rigid motion, the electromagnetic fields in a plasma bunch are more appropriately determined self-consistently by considering the plasma as a dielectric medium, and solving the macroscopic Maxwell equations. This is done in chapter 6. Note that such a dielectric description is valid only for nonrelativistic motion; however, in absence of a Coulomb explosion there is no urgent experimental need to invoke relativistic velocities. It is shown in chapter 6 that a dielectric description of the plasma bunch still exhibits the total self-force on the bunch. In addition, knowledge of the self-consistent motion is employed to study in detail the ponderomotive effects in the plasma.

Bibliography

- [76] J. J. Thomson, “On the electric and magnetic effects produced by the motion of electrified bodies,” *London Edinburgh Dublin Phil. Mag. J. Sci.* **11**, 229–249 (1881), 5th series.
- [77] M. Abraham, “Principien der Dynamik des Elektrons,” *Ann. Phys. (Leipzig)* **315**, 105–179 (1902).
- [78] H. A. Lorentz, *The theory of electrons* (Teubner, Leipzig, 1916) 2nd ed.
- [79] J. A. E. Roa-Neri and J. L. Jiménez, “On the classical dynamics of non-rotating extended charges,” *Nuovo Cimento B* **108**, 853–869 (1993).
- [80] S. E. Gralla, A. I. Harte, and R. M. Wald, “Rigorous derivation of electromagnetic self-force,” *Phys. Rev. D* **80**, 024031 (2009).
- [81] F. Rohrlich, “Dynamics of a charged particle,” *Phys. Rev. E* **77**, 046609 (2008).
- [82] A. D. Yaghjian, *Relativistic dynamics of a charged sphere* (Springer, New York, 2006) 2nd ed.
- [83] A. Di Piazza, K. Z. Hatsagortsyan, and C. H. Keitel, “Strong signatures of radiation reaction below the radiation-dominated regime,” *Phys. Rev. Lett.* **102**, 254802 (2009).

- [84] M. Tamburini, F. Pegoraro, A. Di Piazza, C. H. Keitel, and A. Macchi, “Radiation reaction effects on radiation pressure acceleration,” *New J. Phys.* **12**, 123005 (2010).
- [85] G. Herglotz, “Zur Elektronentheorie,” *Nachr. Ges. Wissenschaften Göttingen* **1903**, 357–382 (1903).
- [86] G. A. Schott, “Über den Einfluß von Unstetigkeiten bei der Bewegung von Elektronen,” *Ann. Phys. (Leipzig)* **330**, 63–91 (1908).
- [87] A. Sommerfeld, “Zur Elektronentheorie,” *Nachr. Ges. Wissenschaften Göttingen* **1904**, 99–439 (1904).
- [88] A. Sommerfeld, “Simplified deduction of the field and forces of an electron moving in any given way,” *Proc. K. Akad. Wetenschappen Amsterdam, Section of Sciences* **7**, 346–367 (1904), (English translation).
- [89] D. Bohm and M. Weinstein, “The self-oscillations of a charged particle,” *Phys. Rev.* **74**, 1789–1798 (1948).
- [90] J. D. Jackson, *Classical electrodynamics* (Wiley, New York, 1999) 3rd ed.
- [91] T. Erber, “The classical theories of radiation reaction,” *Fortschr. Phys.* **9**, 343–392 (1961).
- [92] W. K. H. Panofsky and M. Phillips, *Classical electricity and magnetism* (Dover, Mineola, 2005) 2nd ed., sec. 19.1.
- [93] E. T. Whittaker and G. N. Watson, *A course of modern analysis* (Cambridge university press, Cambridge, 1962) 4th ed.
- [94] M. Abramowitz and I. A. Stegun, *Handbook of mathematical functions* (Dover, New York, 1965).
- [95] J. A. Stratton, *Electromagnetic theory* (McGraw-Hill, London, 1941) sec. 7.8.
- [96] A. Zygmund, *Trigonometric series* (Cambridge university press, Cambridge, 1968) 2nd ed., vol. 2, p. 243.
- [97] E. R. Hansen, *A table of series and products* (Prentice-Hall, Englewood Cliffs, 1975) pp. 5 and 124.
- [98] G. N. Watson, *A treatise on the theory of Bessel functions* (Cambridge university press, Cambridge, 1966) 2nd ed., p. 528.
- [99] Y. L. Luke, *Integrals of Bessel functions* (McGraw-Hill, London, 1962) p. 28.
- [100] L. J. Slater, *Generalized hypergeometric functions* (Cambridge university press, Cambridge, 1966).

- [101] [http://functions.wolfram.com/HypergeometricFunctions/
/Hypergeometric3F2/21/01/02/01/01/01/
and .../Hypergeometric4F3/17/02/01/0002/](http://functions.wolfram.com/HypergeometricFunctions/Hypergeometric3F2/21/01/02/01/01/01/Hypergeometric4F3/17/02/01/0002/).
(accessed 12 November 2012).
- [102] [http://functions.wolfram.com/HypergeometricFunctions/
/Hypergeometric3F2/03/02/03/0003/
and .../Hypergeometric4F3/03/02/05/0002/](http://functions.wolfram.com/HypergeometricFunctions/Hypergeometric3F2/03/02/03/0003/Hypergeometric4F3/03/02/05/0002/).
(accessed 12 November 2012).
- [103] C. J. Eliezer, “The interaction of electrons and an electromagnetic field,” *Rev. Mod. Phys.* **19**, 147–184 (1947).
- [104] L. Page, “Is a moving mass retarded by the reaction of its own radiation?” *Phys. Rev.* **11**, 376–400 (1918).
- [105] C. J. Eliezer, “A note on electron theory,” *Math. Proc. Cambridge Phil. Soc.* **46**, 199–201 (1950).
- [106] S. N. Lyle, *Self-force and inertia* (Springer, Berlin, 2010) chap. 12.
- [107] K. Wildermuth, “Zur physikalischen Interpretation der Elektronenselbstbeschleunigung,” *Z. Naturforsch. A* **10**, 450–459 (1955).
- [108] P. A. M. Dirac, “Classical theory of radiating electrons,” *Proc. Royal Soc. London A* **167**, 148–169 (1938).
- [109] H. Spohn, “The critical manifold of the Lorentz-Dirac equation,” *Europhys. Lett.* **50**, 287–292 (2000).
- [110] L. D. Landau and E. M. Lifshitz, *Classical theory of fields* (Pergamon, Oxford, 1975) 4th rev. ed., sec. 76.

3

Coherently enhanced radiation reaction effects in laser-vacuum acceleration of electron bunches

Abstract - The effects of coherently enhanced radiation reaction on the motion of subwavelength electron bunches in interaction with intense laser pulses are analyzed. The radiation reaction force behaves as a radiation pressure in the laser beam direction, combined with a viscous force in the perpendicular direction. Due to Coulomb expansion of the electron bunch, coherent radiation reaction takes effect only in the initial stage of the laser-bunch interaction while the bunch is still smaller than the wavelength. It is shown that this initial stage can have observable effects on the trajectory of the bunch. By scaling the system to larger bunch charges, the radiation reaction effects are strongly increased. On the basis of the usual equation of motion, this increase is shown to be such that radiation reaction may suppress the radial instability normally found in ponderomotive acceleration schemes, thereby enabling the full potential of laser-vacuum electron bunch acceleration to GeV energies. However, the applicability of the used equation of motion still needs to be validated experimentally, which becomes possible using the presented experimental scheme.

Publication status - The work described in this chapter has been published by P. W. Smorenburg, L. P. J. Kamp, G. A. Geloni, and O. J. Luiten in *Laser Part. Beams* **28**, 553-562 (2010).

3.1 Introduction

The recent availability of ultra-intense laser pulses has led to increased efforts to develop novel compact acceleration schemes for electron beams. These include wakefield accelerators [111–114], thin foil irradiation schemes [115, 116] and laser-vacuum acceleration concepts [117, 118]. Most studies so far have concentrated on the dynamics of the individual electrons in the considered electron bunches under the action of the externally applied electromagnetic fields, while consideration of the self-interaction of the bunches is limited to space-charge effects. Self-interaction due to the radiation emitted by the bunch itself is often ignored. Neglect of this collective radiation reaction is well-justified if the electron density is not too high and the electron bunch size exceeds the laser wavelength used.

In recent years, however, the interaction of intense laser light with nanometer to micrometer sized atomic clusters of near solid state density has become the subject of thorough investigation [119, 120]. This has led to the observation of large numbers of electrons emitted from such clusters [121–124]. In particular, under suitable conditions the production of dense, attosecond electron bunches from laser-irradiated clusters has been observed both numerically [125] and experimentally [123, 126]. Also the creation of ultrashort bunches from laser-irradiated foils is actively studied [127–129]. In view of these developments, collective radiation reaction effects may become an important factor in the dynamics of dense electron bunches and should be taken into account. It was realized already many years ago [130] that these effects can even dominate the bunch dynamics and may be exploited as a collective acceleration mechanism. More recently, the ultra-intense field regime in which radiation reaction effects become dominant has been analyzed [131] and the acceleration of plasma sheets assisted by radiation reaction has been considered [132, 133] in the context of current technological possibilities.

In the present chapter, we consider the effect of collective radiation reaction on a dense subwavelength electron bunch in interaction with a laser pulse. It is shown that the interaction can be modeled by a particularly simple picture of radiation pressure in the direction of the laser beam on a coherently enhanced effective cross section, in combination with a viscous force perpendicular to the laser propagation direction. Thus collective radiation reaction may be exploited in acceleration schemes as an additional accelerating force as well as a stabilizing force in the transverse direction.

Classically, the net radiative effect of the interaction of charged particles with an electromagnetic wave is described by Thomson scattering. This is the production of secondary dipole radiation by charges that oscillate due to the electric field of an incident radiation wave, which can be seen as scattering of part of the incident radiation by the charges. In case of an electron bunch of charge $q = Ne$ and radius $R = R_0$ much smaller than the wavelength λ of the incident radiation, the N electrons in the bunch will essentially perform an identical oscillation, yielding coherently amplified

secondary radiation that is identical to the radiation a point charge of magnitude q would produce. Hence the dynamics of the bunch as a whole can be modeled by such a point charge, as long as $R \ll \lambda$ is fulfilled. The classical Thomson cross section, defined as the ratio of scattered power to incident intensity I in the non-relativistic limit, is $\sigma_T = N^2(8\pi/3)r_0^2$, with $r_0 = e^2/(4\pi\epsilon_0 m_e c^2)$ the classical electron radius [134]. The factor N^2 shows the coherent enhancement of the cross section compared to that of a single electron. Since directed momentum of the incident radiation is scattered into dipole radiation with zero net momentum, momentum is transferred to the electron bunch at a rate $\sigma_T I/c \equiv F_T$. This means that the effective force per electron F_T/N is proportional to N , and can therefore become significant for dense bunches. It is instructive to compare F_T to the ponderomotive force $\mathbf{F}_P = -Ne^2\nabla I/(2\epsilon_0 m_e c\omega^2)$ in a laser pulse, which is conventionally used to accelerate charges in laser-vacuum acceleration schemes. Using a typical laser pulse with $\lambda = 1 \mu\text{m}$ and 100 fs pulse length, the ratio F_T/F_P becomes of the order of unity for a bunch of $N = 10^6$ electrons. Assuming a laser intensity of $I = 1 \cdot 10^{19} \text{ W/cm}^2$, this corresponds to a force of $F_T = 22 \text{ mN}$, which is equivalent to an electric field of $F_P/(Ne) = 0.14 \text{ TV/m}$ in the laser propagation direction. This field already compares to the accelerating fields produced in wakefield accelerators, and increases to well above 1 TV/m for larger numbers of electrons.

Hence, radiation reaction is important for bunches containing $\gtrsim 10^6$ electrons within a size $\ll \lambda$, that is, for bunches with a charge density close to solid state density. These electron bunches could only recently be extracted from atomic clusters by irradiation with an intense laser pulse. Of course, such dense electron bunches quickly expand beyond $R = \lambda$ due to the strong Coulomb repulsion, so that they will scatter radiation coherently only for a brief period of time after creation. Therefore coherent Thomson scattering will not in itself be an efficient driving mechanism for electron bunch acceleration. However, it will be shown in this chapter that even a short initial period of radiation reaction dominated interaction can have observable effects.

Collective radiation reaction of subwavelength electron bunches is, in some respects, the coherently enhanced version of the radiation reaction of a point charge. The latter has been a subject fundamental to the understanding of elementary particles and early electron theory and played a role in the development of quantum theory [135–138]. It has always been a purely academic subject due to the smallness of the effect, however, and is only now coming within experimental reach due to the availability of ultra-intense fields [131]. We suggest that an interesting alternative may now be offered by electron bunches of subwavelength size. As explained above, for bunches the enhanced radiation reaction effects are much stronger so that they are accessible already using moderate laser intensities. Furthermore, also the characteristic time scale on which radiation reaction effects play a role (as measured by the quantity τ_e introduced below) is coherently prolonged, bringing these effects into the experimental attosecond regime. Thus the coherent enhancement of radiation reac-

tion by electron bunches yields interesting possibilities to investigate this fundamental subject by experimental techniques.

In sections 3.2-3.4, the bunch dynamics are analyzed treating the radiation reaction force in a perturbative way. In section 3.2, multiple-scale analysis and averaging over the laser optical time scale are applied to the equation of motion including radiation reaction, yielding a cycle-averaged description of the bunch dynamics. The results are applied to the case of a laser pulse in section 3.3, validating the averaged description and our numerical calculations. Subsequently, in section 3.4 the theoretical results are placed in an experimental context by exploring the possibility of having subwavelength electron bunches in the first place. Both the time in which electron bunches Coulomb expand beyond the wavelength and the production of dense bunches in laser-cluster interactions are addressed. Using accordingly realistic electron bunches, the observable effects of coherent radiation reaction on the bunch trajectory are calculated. Finally, in section 3.5 the theoretical and numerical results are tentatively extrapolated to the non-perturbative regime of highly charged electron bunches. It is shown that ponderomotive acceleration of electron bunches by laser pulses may be stabilized by radiation reaction.

3.2 Averaged radiation reaction force

Suppose that an electron bunch of charge $q = Ne$, mass $m = Nm_e$ and radius $R_0 \ll \lambda$ oscillates due to the Lorentz force \mathbf{F}_L of plane wave radiation propagating in the z -direction with electric field $\mathbf{E} = E_0 \sin(\omega t - kz) \mathbf{e}_x$. The oscillatory quiver motion of the bunch (henceforth modeled by a point charge q) is a 'figure-of-eight'-cycle in the (x, z) -plane in the Lorentz frame in which the charge is at rest on average [139]. In the course of each cycle, the accelerating charge continuously radiates and exchanges energy with its periodically changing Coulomb field, thereby experiencing an additional radiation reaction force \mathbf{F}_R . The detailed description of \mathbf{F}_R has been discussed intensively in the literature [135], in which the covariant equation of motion for a point charge [136–138],

$$\dot{p}^\mu = F_L^\mu + F_R^\mu = qF^{\mu\nu} \frac{p_\nu}{m} + \tau_e (\dot{p}^\lambda \dot{p}_\lambda p^\mu / (mc)^2 + \ddot{p}^\mu), \quad (3.1)$$

has played a central role. In Eq. (3.1), dots denote differentiation with respect to proper time, $F^{\mu\nu}$ is the electromagnetic field tensor of the incident radiation, $\tau_e = N(2r_0)/(3c)$ is the characteristic time for radiation reaction, and the metric signature $(+, -, -, -)$ has been adopted. The first term in brackets equals the covariant Larmor power and represents the recoil of the charge caused by emission of radiation, that is, by the irreversible loss of four-momentum detaching from the charge and propagating towards infinity. The second term is referred to as the 'Schott term' and

is associated with the reversible exchange of four-momentum with the Coulomb or velocity field, that is, with the part of the electromagnetic field bound to the charge that does not give rise to radiation [140, 141]. In the usual incoherent case $N = 1$, the bracketed terms can be neglected because of the smallness of τ_e . However, in the present case τ_e is N times larger and $p^\mu \propto m \equiv Nm_e$, so that $F_R^\mu \propto N^2$. This shows again that the radiation reaction force is coherently enhanced and can become very relevant. Two regimes may be identified: the perturbative regime in which $\omega\tau_e \ll 1$ and the radiation reaction dominated regime in which $\omega\tau_e \gtrsim 1$ [131]. In the perturbative regime, the Thomson cross section is by definition much smaller than the physical bunch size, and $F_R \ll F_L$. This is the regime studied in this and the next two sections. In section 3.5, laser-vacuum acceleration in the radiation reaction dominated regime is considered.

The two-dimensional 'figure-of-eight'-motion in the (x, z) -plane due to the linearly polarized incident radiation does not induce any y -component of acceleration in Eq. (3.1), so that the motion of the charge remains two-dimensional throughout. Assuming $F_R \ll F_L$, the radiation reaction force \mathbf{F}_R affects the quiver motion negligibly on time scales $\sim \omega^{-1}$. However, its cumulative effect over many cycles is to accelerate the charge, so that it gains a slowly varying average momentum $\bar{\mathbf{p}}$ superimposed on the quiver motion. To study $\bar{\mathbf{p}}$, it is instructive to derive averaged equations of motion from Eq. (3.1) by means of a multiple-scale expansion. For this purpose, define a fast dimensionless time scale $T \equiv \omega t$ and a slow dimensionless time scale $\epsilon T \equiv (\omega\tau_e)T$. The latter equals the time scale of radiative damping of a charged harmonic oscillator [134] so that this is the time scale on which $\bar{\mathbf{p}}$ will change appreciably. Hence, the dimensionless momentum $(\gamma, P_x, P_y, P_z) = P^\mu \equiv p^\mu/(mc)$ may be written as the sum of a slowly varying part $\bar{P}^\mu(\epsilon T) \equiv \langle P^\mu \rangle$ and a rapidly varying part $\tilde{P}^\mu(\epsilon T, T) = P^{(0)\mu}(\epsilon T, T) + \epsilon P^{(1)\mu}(\epsilon T, T) + O(\epsilon^2)$, where $\langle \cdot \rangle$ denotes the average over an optical period. Incidentally, the quiver motion in a plane wave turns out to be more easily described in terms of the laser phase $\eta \equiv T - kz$ rather than the time T explicitly [139]. Anticipating this fact by changing the fast coordinate from T to η , time-differentiation takes the form

$$\gamma \frac{d}{dT} P^\mu(\epsilon T, \eta) = \left(\epsilon \gamma \frac{\partial}{\partial(\epsilon T)} + (\gamma - P_z) \frac{\partial}{\partial \eta} \right) P^\mu(\epsilon T, \eta), \quad (3.2)$$

where $\gamma^2 \equiv 1 + P_x^2 + P_z^2$ is the usual Lorentz factor. Substituting the sum $P^\mu = \bar{P}^\mu + \tilde{P}^\mu$ in the space and time components of Eq. (3.1), using Eq. (3.2), and collecting equal powers of ϵ , yields the zeroth-order equations

$$P_x^{(0)} = -a \cos \eta; \quad (3.3)$$

$$P_z^{(0)} = \gamma^{(0)} = -\frac{a\bar{P}_x \cos \eta}{\bar{\gamma} - \bar{P}_z} + \frac{a^2 \cos 2\eta}{4(\bar{\gamma} - \bar{P}_z)}; \quad (3.4)$$

$$\bar{\gamma}^2 = 1 + a^2/2 + \bar{P}_x^2 + \bar{P}_z^2, \quad (3.5)$$

where $a \equiv (eE_0)/(m_e c \omega)$ is the dimensionless field strength. Eqs. (3.3)-(3.4) give the well-known plane wave quiver motion with average momentum $\bar{\mathbf{p}}$ [142]. Eq. (3.5) shows that the oscillating charge behaves like a particle with effective mass $m\sqrt{1 + a^2/2}$ due to the energy contained in the quiver motion [143]. Expanding next the components of Eq. (3.1) to first order in ϵ , substituting the zeroth-order results Eqs. (3.3)-(3.5), and averaging over the fast time scale, one finally obtains

$$\frac{d\bar{P}_x}{dT} = -\frac{\omega\tau_e a^2}{2}(\bar{\gamma} - \bar{P}_z)^2 \frac{\bar{P}_x}{\bar{\gamma}}; \quad (3.6)$$

$$\frac{d\bar{P}_z}{dT} = \frac{\omega\tau_e a^2}{2}(\bar{\gamma} - \bar{P}_z)^2 \left(1 - \frac{\bar{P}_x^2}{\bar{\gamma}(\bar{\gamma} - \bar{P}_z)}\right). \quad (3.7)$$

The averaged dimensionless position $\bar{\mathbf{X}} \equiv k\bar{\mathbf{x}}$ is calculated from

$$\frac{d\bar{\mathbf{X}}}{dT} \equiv \bar{\boldsymbol{\beta}} = \frac{\bar{\mathbf{P}}}{\bar{\gamma}}, \quad (3.8)$$

Eqs. (3.5)-(3.8) now give the evolution of the averaged position $\bar{\mathbf{X}}$ and momentum $\bar{\mathbf{P}}$ of the charge in the plane wave. First, consider the special case $\bar{P}_x = 0$. Then Eqs. (3.6)-(3.7) reduce, after multiplication by $m_e c \omega$, to

$$\frac{d\bar{\mathbf{p}}}{dt} = \sigma_T \frac{I}{c} \bar{\gamma}^2 (1 - \bar{\beta}_z)^2 \mathbf{e}_z, \quad (3.9)$$

where $I = \epsilon_0 c E_0^2/2$ is the intensity of the incident plane wave. This clearly shows that the averaged reaction force takes the classical form of a radiation pressure I/c on an effective cross section σ_T , corrected by a Doppler factor $\bar{\gamma}^2 (1 - \bar{\beta}_z)^2$. This Doppler factor reflects the fact that plane wave appears Doppler-shifted in the frame of the charge, with a corresponding change in radiation pressure. Eq. (3.9) may also be obtained by Lorentz-transformation of the non-relativistic force $\sigma_T I/c$ [139]. In the more general case $\bar{P}_x \neq 0$, the direction of the radiation pressure is no longer along the propagation direction of the incident wave. This is because the secondary, scattered radiation produced by the charge is Lorentz boosted along $\bar{\mathbf{P}}$, so that the recoil from this radiation has a net transverse component when $\bar{P}_x \neq 0$. The latter appears in Eqs. (3.6)-(3.7) as the additional factors involving \bar{P}_x on the very right. Effectively, in the transverse direction the averaged reaction force appears as a frictional force proportional to the velocity, which will be important below. Effective forces similar

to Eqs. (3.6)-(3.7) have been obtained earlier for a one-dimensional plasma sheet [132].

A typical experiment will involve the use of a high-intensity laser pulse of length τ_L focused to a waist of size w_0 . Due to the intensity gradients in such a pulse, on average the electron bunch will experience ponderomotive forces in addition to the radiation reaction forces. In absence of the latter, the ponderomotive force takes the simple form

$$\frac{\mathbf{F}_P}{m_e c \omega} = -\frac{(k^{-1} \nabla)[a^2(\overline{\mathbf{X}}, T)]}{4\bar{\gamma}}, \quad (3.10)$$

which can be derived by means of a separate multiple-scale analysis, using the small parameters $\lambda/(c\tau_L)$ and $(kw_0)^{-1}$ [144]. The combined effect of radiation reaction and gradients may be derived formally using a multiple-scale analysis in terms of all three small parameters $\omega\tau_e$, $\lambda/(c\tau_L)$, and $(kw_0)^{-1}$. This is possible provided that these parameters are all of the same order of magnitude. However, mixed expansion terms that involve products of the parameters appear only from the second order onwards, so that to first order the radiation reaction and ponderomotive effects remain separated throughout the analysis. Hence, the averaged reaction force is still given by Eqs. (3.6)-(3.7), but now with the dimensionless field strength $a(\overline{\mathbf{X}}, T)$ evolving according to the laser pulse shape. Furthermore, Eqs. (3.6)-(3.7) are supplemented with the effects of intensity gradients by simply adding the ponderomotive force Eq. (3.10) to the right hand sides. Carrying out the full three-parameter multiple-scale analysis to first order confirms these results. In the numerical calculations below, Eqs. (3.6)-(3.7) will always be used with the force Eq. (3.10) included.

Rather than using averaged equations, the detailed trajectory of the electron bunch may be calculated by direct integration of Eq. (3.1). However, it is well-known that this equation yields unphysical runaway solutions, which may be disposed of by substituting the applied Lorentz force $\dot{p}^\mu \approx F_L^\mu$ in the right hand side of Eq. (3.1). This yields the space component [139, 145, 146]

$$\frac{d\mathbf{p}}{dt} = \mathbf{F}_L + \tau_e \left[\gamma \frac{d\mathbf{F}_L}{dt} - \frac{\gamma^3}{c^2} \left(\frac{d\mathbf{v}}{dt} \times (\mathbf{v} \times \mathbf{F}_L) \right) \right]. \quad (3.11)$$

This expression can also be derived from quantum mechanical arguments [146, 147].

3.3 Radiation reaction in a laser pulse

In this section the results of the previous section will be applied to concrete examples of laser-vacuum experiments. First, however, it should be stressed that an accurate calculation of the detailed charge trajectory in a laser pulse requires the field of the pulse to be described in more detail than the usual paraxial approximations [148], even

in the absence of radiation reaction forces. Quesnel and Mora [144] use a laser field representation in terms of Fresnel-type integrals to calculate detailed charge trajectories in a laser pulse, which are then compared with averaged trajectories calculated from the ponderomotive force Eq. (3.10) using the laser field in paraxial approximation. The agreement between the two results was found to be excellent except for highly relativistic initial velocities. In this chapter we will adopt the same approach, using the detailed field representation of Quesnel and Mora [144] when evaluating the Lorentz force \mathbf{F}_L in Eq. (3.11), while taking the simpler paraxial approximation to evaluate the field intensity a^2 in the averaged equations (3.5-3.10). As a reference, both field representations are shown in Appendix 3.A.

To validate the results of the previous section and to illustrate the effect of the effective radiation pressure produced by radiation reaction, we consider an intense laser pulse propagating in the z -direction and polarized in the x -direction, which has wavelength $\lambda = 1 \mu\text{m}$, peak intensity $I = 1 \cdot 10^{19} \text{ W/cm}^2$ and pulse length $\tau_L = 200 \text{ fs}$, focused to a relatively large waist of size $w_0 = 10\lambda$. This pulse contains 2.3 J of energy and has a peak dimensionless field strength $a_{\text{max}} = 2.7$. An electron bunch of radius $R_0 \ll \lambda$ and radiation reaction parameter $\omega\tau_e = 0.03$ is considered, corresponding to a bunch charge of $q = 0.4 \text{ pC}$. For these parameters, $\lambda/(c\tau_L) \sim (kw_0)^{-1} \sim \omega\tau_e$ so that the averaged description is valid. The electron bunch is placed at rest at the initial position $\mathbf{x}_0 \equiv (x_0, z_0) = (\lambda, 0)$ prior to arrival of the laser pulse, deliberately at an off-axis position arbitrarily set to one wavelength, in order to study the radial acceleration as well. In this (unrealistic) first example, we disregard the Coulomb expansion of the bunch and assume that it retains its coherent Thomson cross section during the entire interaction.

Fig. 3.1 shows the trajectory of the bunch and its momentum as a function of time as it is overtaken by the laser pulse, calculated using both the averaged description Eqs. (3.5)-(3.10) and the detailed description Eq. (3.11). Clearly, the agreement between the averaged and the detailed description is excellent, validating the multiple-scale analysis, the applicability of Eq. (3.11), and our numerical calculations. The figure also shows the trajectory and the momentum in the absence of radiation reaction, that is, in case of conventional ponderomotive acceleration. In the latter case the charge is quickly expelled in the radial direction because of the large radial intensity gradient, which is a well-known instability that so far has limited the applicability of ponderomotive acceleration schemes [117].

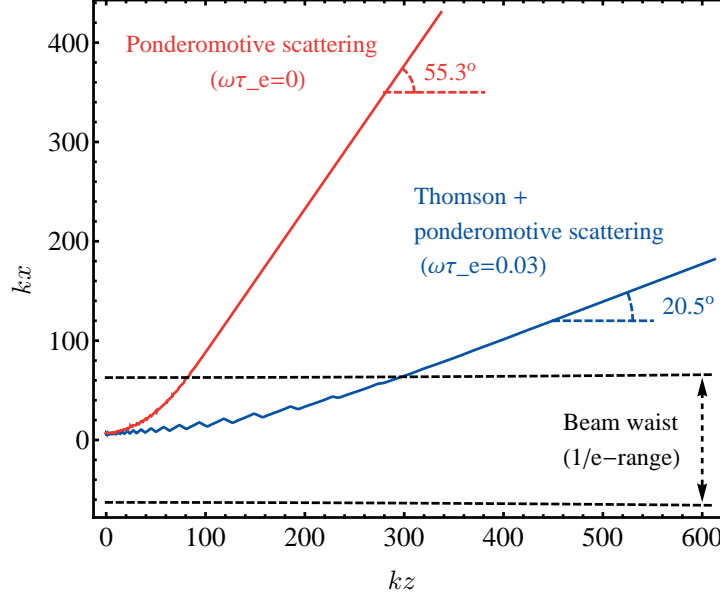


Figure 3.1: a) Trajectory of an electron bunch accelerated by a laser pulse with parameters $\lambda = 1 \mu\text{m}$, $I = 1 \cdot 10^{19} \text{ W/cm}^2$, $\tau_L = 200 \text{ fs}$, and $w_0 = 10\lambda$, calculated for the case including radiation reaction (Thomson + ponderomotive scattering, $\omega\tau_e = 0.03$) and for the case without radiation reaction (ponderomotive scattering, $\omega\tau_e = 0$). The trajectories have been calculated using Eq. (3.11) with $\mathbf{F}_L = q(\mathbf{E} + \mathbf{v} \times \mathbf{B})$, taking for \mathbf{E} and \mathbf{B} Eqs. (3.17)-(3.20). The initial position was $\mathbf{x}_0 = (\lambda, 0)$ and the initial velocity was zero. (Continued on next page)

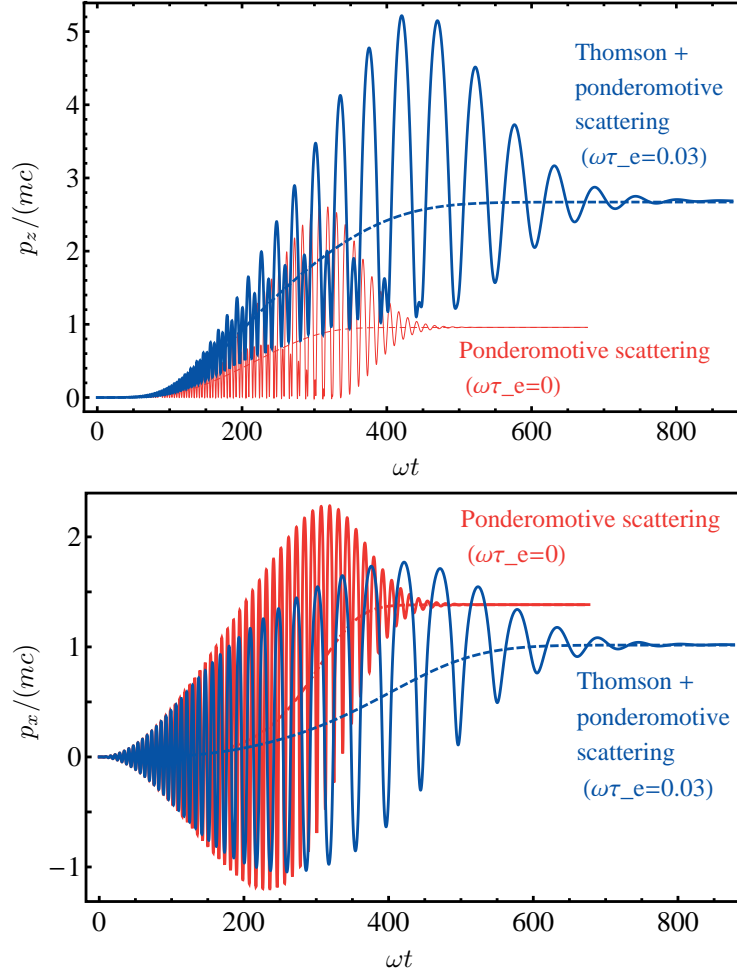


Figure 3.1: (continued from previous page)

b) Longitudinal momentum of the bunch as a function of time;
c) Transverse momentum of the bunch as a function of time, calculated for the case including radiation reaction (Thomson + ponderomotive scattering, $\omega\tau_e = 0.03$) and for the case without radiation reaction (ponderomotive scattering, $\omega\tau_e = 0$). The solid lines have been calculated using Eq. (3.11) with $\mathbf{F}_L = q(\mathbf{E} + \mathbf{v} \times \mathbf{B})$, taking for \mathbf{E} and \mathbf{B} Eqs. (3.17)-(3.20). The dashed lines have been calculated using Eqs. (3.5)-(3.10), taking a^2 according to Eq. (3.21). The initial position was $\mathbf{x}_0 = (\lambda, 0)$ and the initial velocity was zero.

The theoretical escape angle θ for ponderomotive acceleration of a charge initially at rest by a radiation pulse, is related to the final Lorentz factor γ_f by [149]

$$\theta = \arccos \sqrt{\frac{\gamma_f - 1}{\gamma_f + 1}}. \quad (3.12)$$

In the present example $\gamma_f = 1.96$, yielding a theoretical escape angle of 55.3° in excellent agreement with the numerically calculated result. In contrast to the purely ponderomotive case, in the case including coherent Thomson scattering the acceleration in the radial direction is markedly suppressed. This stabilizing effect is due to the average frictional force shown by Eq. (3.6), which opposes the tendency to radial acceleration. Meanwhile, the charge stays in the beam longer and is accelerated in the forward direction for a longer time by both the radiation reaction pressure and ponderomotive forces, leading to a higher final energy and a smaller escape angle.

3.4 Realistic electron bunches

We now consider the more realistic case of an electron bunch that expands due to Coulomb repulsion. The time after which the Thomson cross section fails to be coherent, that is, the time it takes the bunch to expand to $R = \lambda$, depends on the charge and the initial size of the bunch. To obtain realistic values for these initial parameters, we first make some estimates concerning the method to produce dense electron bunches mentioned in the introduction.

Rather than irradiating a pre-existing electron bunch, an electron bunch may be created in practice by irradiating a subwavelength atomic cluster. When the laser pulse is sufficiently strong, the electron bunch will be emitted from the cluster somewhere in the leading edge of the pulse, after which it is available to be accelerated by the remainder of the pulse as has been analyzed in the previous section. Many different mechanisms play a role in laser-cluster interaction [119, 120] and it is beyond the scope of this thesis to analyze this interaction in detail. Instead, we use a strongly simplified model of the cluster suggested by Parks *et al.* [150] to obtain order-of-magnitude estimates for the initial parameters of the electron bunch. Accordingly, at some point in the leading edge of the pulse the field strength becomes such that all atoms in the cluster are ionized almost instantaneously, changing the neutral cluster into a dense plasma ball. Subsequently, this plasma ball is modeled as a spherical rigid electron bunch, interpenetrating with and moving through a practically immobile oppositely charged ion bunch, under the action of both the driving laser electric field and the restoring Coulomb force of the ion cloud. As the rising edge of the laser pulse advances, the electron bunch oscillates around the ion bunch center with increasing amplitude. At a critical laser field strength the electron bunch breaks free and escapes the ion bunch within a fraction of an optical period, yielding the free, dense electron bunch we will now use as an input for our calculation.

The critical dimensionless field strength at which the electron bunch is liberated may be estimated as [150]

$$a_{\text{crit}} = \frac{15}{96} \left(\frac{\omega_p}{\omega} \right)^2 kR_0, \quad (3.13)$$

where $\omega_p = \sqrt{3Ne^2/(4\pi\epsilon_0 m_e R_0^3)}$ is the electron plasma frequency of the ionized cluster consisting of N atoms. The electron bunch leaves the cluster at the maximum of an optical cycle. The time this takes is of the order $t_{\text{esc}} \sim \omega_p^{-1}$ [150], so that the escaping electron bunch will have a velocity of approximately

$$\beta_{\text{esc}} c \approx \omega_p R_0 \quad (3.14)$$

in the direction of the laser polarization. Incidentally, note that the coherent radiation reaction parameter can be expressed in terms of the cluster parameters as $\omega\tau_e = (2/9)(\omega_p/\omega)^2(kR_0)^3$, by which the validity condition $\omega\tau_e \ll kR_0$ of section 3.2 automatically implies that $\beta_{\text{esc}} < 1$. After leaving the cluster, the electron bunch will start to expand. It can be shown straightforwardly that, after a short period of slow expansion, the expansion rate increases to the constant value [151]

$$\frac{dR}{dt} \approx \frac{\sqrt{\frac{2}{3}}\omega_p R_0}{\sqrt{1 + P_{\text{esc}}^2 + \frac{a_{\text{crit}}^2}{2}}}. \quad (3.15)$$

In Eq. (3.15), it has been used that the expanding electron bunch will be in quiver motion immediately after leaving the cluster, so that it will move with an average Lorentz factor according to Eq. (3.5). This reduces the expansion rate by a factor $\bar{\gamma} = \sqrt{1 + P_{\text{esc}}^2 + a_{\text{crit}}^2/2}$.

As an example we take an $R_0 = 16$ nm cluster with an electron density of $5 \cdot 10^{28}$ m⁻³, which can be routinely made using a supersonic gas jet [120], irradiated by the same laser pulse as in the previous example. With these numbers the other parameters are $kR_0 = 0.1$, $\omega_p/\omega = 6.6$, $\omega\tau_e = 0.01$, and $a_{\text{crit}} = 0.68$ and $\beta_{\text{esc}} = 0.66$ according to Eqs. (3.13)-(3.14). The last two numbers roughly compare to the field strengths used and electron velocities obtained by Liseykina *et al.* [125] and Fukuda *et al.* [126]. Assuming the expansion rate Eq. (3.15), the bunch grows larger than the wavelength after a time $8.3\omega^{-1}$, that is, after no more than 1.3 optical cycles following the moment of escape from the cluster. Thus coherent Thomson scattering will only occur for a brief initial period. Nevertheless, even such a brief period can have an observable effect on the trajectory of the electron bunch in interaction with the laser pulse.

Fig. 3.2 shows the trajectory of the bunch in interaction with the laser pulse, both for the case without the radiation reaction force ($\omega\tau_e = 0$) and for the case including the radiation reaction force ($\omega\tau_e = 0.01$) during the initial period $0 \leq \omega t \leq 8.3$. In

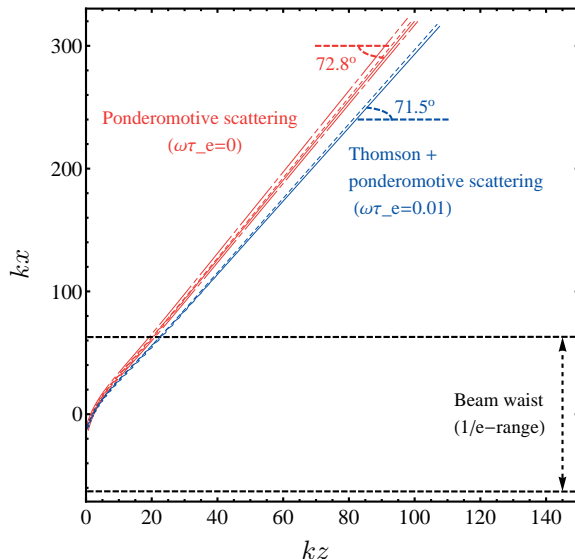


Figure 3.2: Trajectory of an electron bunch accelerated by a laser pulse, calculated for the case including radiation reaction (Thomson + ponderomotive scattering, $\omega\tau_e = 0.01$) during the initial period $0 \leq T \leq 8.3$, and for the case without radiation reaction (ponderomotive scattering, $\omega\tau_e = 0$). See Fig. (3.1) for details about the calculation and laser parameters. The dash-dotted lines show the error margins for the case $\omega\tau_e = 0$ corresponding to an hypothetical uncertainty of magnitude λ in the initial position, calculated using the averaged description. The initial position was $\mathbf{x}_0 = (-\lambda, 0)$ and the initial velocity was according to Eq. (3.14).

the latter case, the decrease in coherent radiation reaction was modeled by a sudden switch-off, setting $\omega\tau_e = 0$ at the somewhat arbitrary point $\omega t = 8.3$. Again, the results of Fig. 3.2 were calculated both using the averaged description Eqs. (3.5)-(3.10) and the detailed description Eq. (3.11). In both cases the initial position was $\mathbf{x}_0 = (-\lambda, 0)$ and the initial velocity was $\beta_{\text{esc}} c \mathbf{e}_x$. The initial position of the laser pulse along the z -axis was chosen such that $a = a_{\text{crit}}$ at \mathbf{x}_0 , and the optical phase offset ϕ_0 was chosen such that the optical cycle was at its maximum at $t = 0$. This time, the escape angle for the case without radiation reaction does no longer agree with Eq. (3.12) or its generalization for a nonzero initial velocity [149]. This may be caused by the sudden injection into the radiation field at $t = 0$, which is not considered in the derivation of Eq. (3.12). The good agreement between the averaged and detailed descriptions is remarkable here, considering the fact that the concept of averaging the equation of motion over the optical time scale is not a priori valid when applied during the initial period, which is as short as the optical period itself. From the figure it is clear that the initial period of radiation reaction still reduces the escape angle observably, but much less than in the previous example because the

radiation reaction force is switched off at an early stage. To put the 1.3 degrees of reduction in angle in perspective, the figure also shows the error margins around the trajectory without radiation reaction which would be caused by an uncertainty of magnitude λ in the initial position \mathbf{x}_0 . The deviation caused by radiation reaction is clearly outside these error margins.

As another example we show how the initial period of coherent Thomson scattering may even change the behavior of the bunch completely. Fig. 3.3 shows the trajectory of the bunch, using the same laser parameters and initial conditions as in the previous example, only now with the initial position changed to $\mathbf{x}_0 = (-7.1\lambda, 0)$. This time the effect of radiation reaction is such that the bunch is deflected by the laser pulse in the negative x -direction instead of the positive x -direction. Under the initial conditions of this example, the bunch is produced much further from the laser beam axis and is therefore decelerated in the negative x -direction by the radial ponderomotive force of Eq. (3.10) for a longer time. Without the action of the radiation reaction force, the bunch just makes it across the laser axis (where the ponderomotive potential is maximum), after which it is accelerated in the positive x -direction. Including radiation reaction, however, in the initial stage the bunch is additionally decelerated by the frictional force of Eq. (3.6). Furthermore it is additionally accelerated in the positive z -direction by the radiation pressure of Eq. (3.7), so that it keeps up with the laser pulse and is under the action of the decelerating radial ponderomotive force for a somewhat longer time. Both effects are only small, but in this case just enough to prevent the bunch from passing the beam axis. It is to be noted that in this example whether or not the bunch will pass the beam axis is very sensitive to the initial parameters. This is an additional reason why the averaged description cannot be used here to reproduce the trajectories of Fig. (3.3), since the small differences between the two descriptions in the initial part of the trajectory affect the final behavior strongly. Still, it is clear that radiation reaction can play an important role in laser-vacuum experiments.

3.5 The radiation reaction dominated regime

In the previous section, relatively small electron bunches were considered leading to modest values for the bunch charge and for the radiation reaction parameter ($\omega\tau_e \ll 1$), thereby staying well inside the perturbative regime mentioned in section 3.2. Much stronger radiation reaction effects could be expected when scaling the system to larger bunches. In the introduction, the magnitude of the effective radiation reaction force was estimated assuming a wavelength of 1 μm . Taking now, for instance, a CO_2 laser with a wavelength of 10 μm , ten times larger bunches still scatter light coherently. Since the coherent Thomson cross section scales as $\sigma_T \propto N^2 \propto R^6$, in that case an effective force $F_T = \sigma_T I/c$ of the order of kN rather than mN may be

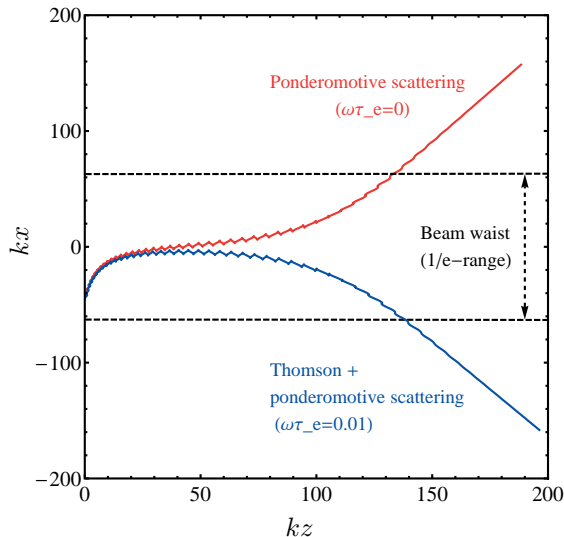


Figure 3.3: See Fig. (3.2), with the initial position changed to $\mathbf{x}_0 = (-7.1\lambda, 0)$.

expected, equivalent to accelerating fields $F_P/(Ne)$ approaching PV/m rather than TV/m. Thus, the radiation reaction force in this case completely dominates the bunch dynamics. In this radiation reaction dominated regime $\omega\tau_e \sim 1$, the averaged description Eqs. (3.5)-(3.10) is no longer valid, and analysis of the dynamics is restricted to the instantaneous equations of motion (3.1) or (3.11). However, in this regime the validity of these equations is at issue. Eq. (3.1) can be shown to be valid for a subwavelength but finite charged body when the mass equivalent of its electrostatic energy $U/c^2 \sim (Ne)^2/(\epsilon_0 R c^2)$ is less than its mechanical mass Nm_e [152]. From the definition of τ_e , this requirement is equivalent to $\omega\tau_e < kR$, in which case Eq. (3.11) is valid as well [153, 154]. But in the present case this requirement is not satisfied, as $\omega\tau_e \sim 1 \gg kR$ here. Thus the experiment in the radiation reaction dominated regime can provide valuable insights, as the departure from known equations can be controlled and studied.

We now give an example of acceleration using radiation reaction in the regime $\omega\tau_e \sim 1$, as it would result according to equation of motion (3.11). As before, the action of the radiation reaction force is restricted to the initial period following the creation of the electron bunch, while the bunch is still smaller than the wavelength. Therefore the large accelerating fields mentioned above are not effective as a driving acceleration mechanism. However, the initial radiation reaction dominated phase pre-accelerates and redirects the velocity of the bunch, which serves to stabilize subsequent ponderomotive acceleration. Consider the same laser pulse as used in the previous examples, but scaled ten times in all directions so that $\lambda = 10 \mu\text{m}$, $\tau_L = 2 \text{ ps}$ and

$w_0 = 10\lambda$. This CO₂ laser pulse contains 2.3 kJ of energy and has a peak dimensionless field strength $a_{\max} = 27$, which is presently available. The increased wavelength allows an electron bunch of initial size $R_0 = 160$ nm containing $N = 8.5 \cdot 10^8$ electrons, resulting as before in $kR_0 = 0.1$, but this time in a much bigger value $\omega\tau_e = 1$. The non-relativistic cluster model of [150] does not apply for such a large amount of charge. We assume a relativistic initial electron bunch velocity of $\beta_0 = 0.9$ instead, as is also indicated by Liseykina *et al.* [125]. Substituting $P_{\text{esc}} \equiv \beta_0/\sqrt{1-\beta_0^2}$ and $a_{\text{crit}} \equiv a_{\max}$ in Eq. (3.15), the resulting expansion rate is such that the bunch stays smaller than the wavelength for about one optical cycle, just as in the previous examples.

Fig. 3.4 shows the trajectory and momentum of this electron bunch in the laser pulse. The initial bunch position was set to $\mathbf{x}_0 = (\lambda, 0)$, the initial position of the laser pulse along the z -axis was chosen centered around x -axis so that the bunch started its movement at the pulse maximum, and the optical phase offset ϕ_0 was chosen such that the optical cycle was at its maximum at $t = 0$ and \mathbf{x}_0 . From the figure the effect of the initial period of radiation reaction is evident: the large radial velocity of the bunch is suppressed immediately preventing an early escape from the beam waist, after which the bunch is strongly accelerated in the direction of propagation of the laser pulse. The inset of the p_z -panel of Fig. 4 shows the long-term evolution of the momentum in this direction. The bunch is first accelerated by the leading edge of the laser pulse and then decelerated by the trailing edge, as is characteristic for laser-vacuum acceleration. The energy of the bunch is increased to $\gamma \approx 600$, corresponding to an energy of 0.3 GeV per electron. In the case without radiation reaction, the bunch is quickly expelled from the laser beam. Consequently, the energy gained is much less. The cusp-like features in the corresponding p_z - and p_x -plots of Fig. 3.4 agree with previous results [155, 156] in comparable cases of ponderomotive scattering.

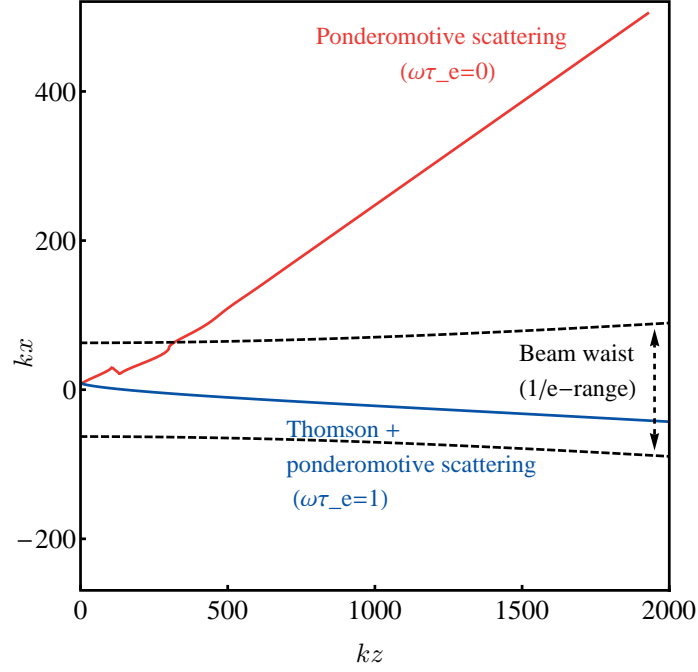


Figure 3.4: a) Trajectory of an electron bunch accelerated by a laser pulse with parameters $\lambda = 10 \mu\text{m}$, $I = 1 \cdot 10^{19} \text{ W/cm}^2$, $\tau_L = 2 \text{ ps}$, and $w_0 = 10\lambda$, calculated for the case including radiation reaction (Thomson + ponderomotive scattering, $\omega\tau_e = 1$) during the initial period $0 \leq T \leq 2\pi$ and for the case without radiation reaction (ponderomotive scattering, $\omega\tau_e = 0$). The trajectories have been calculated using Eq. (3.11) with $\mathbf{F}_L = q(\mathbf{E} + \mathbf{v} \times \mathbf{B})$, taking for \mathbf{E} and \mathbf{B} Eqs. (3.17)-(3.20). The initial position was $\mathbf{x}_0 = (\lambda, 0)$ and the initial velocity was $\beta_0 = 0.9\mathbf{e}_x$.

(Continued on the next page)

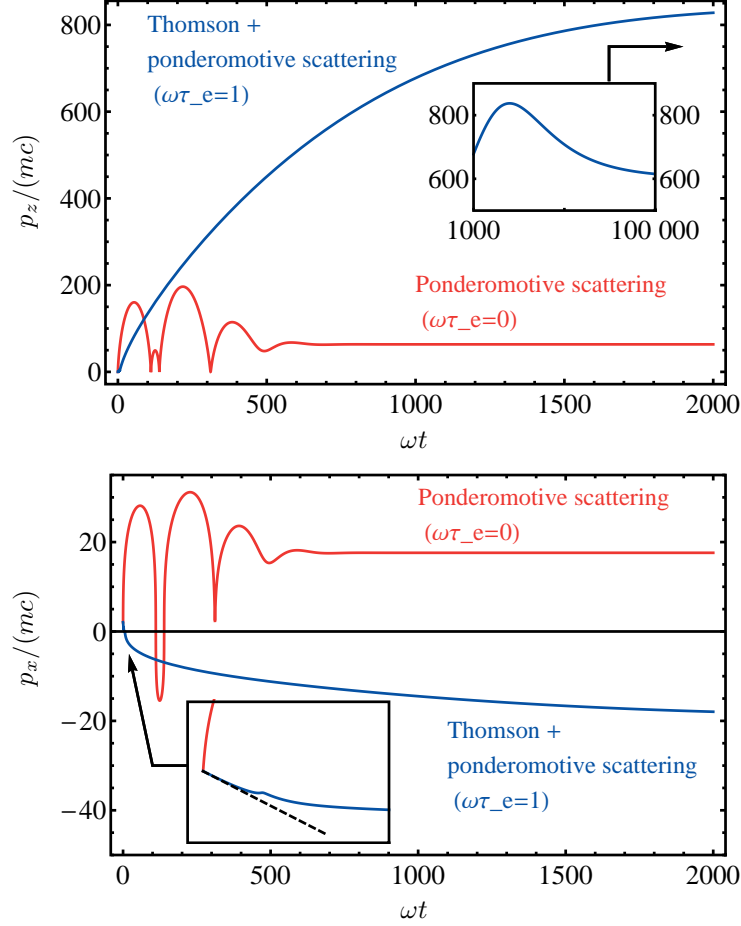


Figure 3.4: (Continued from the previous page)

b) Longitudinal momentum of the bunch as a function of time;
c) Transverse momentum of the bunch as a function of time, calculated for the case including radiation reaction (Thomson + ponderomotive scattering, $\omega\tau_e = 1$) during the initial period $0 \leq T \leq 2\pi$ and for the case without radiation reaction (ponderomotive scattering, $\omega\tau_e = 0$). The solid lines have been calculated using Eq. (3.11) with $\mathbf{F}_L = q(\mathbf{E} + \mathbf{v} \times \mathbf{B})$, taking for \mathbf{E} and \mathbf{B} Eqs. (3.17)-(3.20). The inset of the upper panel shows the long-term behavior of the longitudinal momentum for the case including radiation reaction. The inset of the lower panel is a zoom-in on the first optical period; the slope of the dashed line is according to Eq. (3.16). The initial position was $\mathbf{x}_0 = (\lambda, 0)$ and the initial velocity was $\beta_0 = 0.9\mathbf{e}_x$.

In the case including radiation reaction, it may seem strange that the bunch starts, at $t = 0$, with a downward radial acceleration while the laser electric field points upward at that moment. This, however, is a consequence of the large value of $\omega\tau_e$ as can be inferred from Eq. (3.11). Namely, at $t = 0$ the optical field at the bunch position is maximum, so that

$$qE_x = qcB_y = m_e c \omega a_{\max};$$

$$\frac{d\mathbf{F}_L}{dt} = q \frac{d\mathbf{v}}{dt} \times \mathbf{B},$$

while $p_z = 0$. Substituting the above in the x - and z -components of Eq. (3.11), writing $d\mathbf{v}/dt$ in terms of the momentum $\mathbf{p} = \gamma m \mathbf{v}$, and rearranging, one finds in dimensionless form the x -component

$$\left. \frac{dP_x}{dT} \right|_{t=0} = a_{\max} \frac{1 - \omega\tau_e a_{\max} \gamma_0^2 \beta_0}{1 + \gamma_0^2 (\omega\tau_e a_{\max})^2} \approx -\frac{\beta_0}{\omega\tau_e}, \quad (3.16)$$

where $\gamma_0 \equiv (1 - \beta_0^2)^{-1/2}$. On the right hand side it has been used that $\omega\tau_e a_{\max} \beta_0 \gg 1$ in the example of Fig. 3.4. In the inset of the p_x -panel of Fig. 3.4, the initial acceleration Eq. (3.16) is indicated by the sloped line.

Eq. (3.16) suggests that the initial velocity of the bunch can be redirected by means of a short period of radiation reaction choosing favorable parameters a_{\max} and $\omega\tau_e$, which may be exploited to efficiently accelerate the bunch into the direction of propagation of the laser. Whether this scheme, and the results of this section in general, are realistic depends on the way the validity of Eq. (3.11) extends into the present radiation reaction dominated regime. This may be studied by means of the proposed setup, which also may offer further opportunities to experimentally test radiation reaction theories.

3.6 Conclusion

The current developments in laser technology make it possible to obtain subwavelength electron bunches of very high charge density. With that, a qualitatively new regime is accessed in which coherently enhanced radiation reaction effects become significant. In this chapter, we have analyzed some of these effects in the context of laser-vacuum experiments. It has been shown that the radiation reaction force affects the bunch dynamics notably, even if the radiation reaction can still be treated as a small perturbation on the optical time scale. Considering larger bunches containing more charge, we demonstrated that the radiation reaction effects may even become strong enough to be exploited in effective bunch acceleration schemes, although this is also where the theory is still controversial and needs further development. It is clear

that the coherently enhanced radiation reaction of high-density electron bunches offers interesting new possibilities, both as a technological tool in the development of novel acceleration schemes, and as an experimentally accessible system to study the fundamental topic of radiation reaction.

Appendix 3.A Laser field representations

In this chapter, when evaluating the Lorentz force \mathbf{F}_L in Eq. (3.11), the following fields are used [144]:

$$\frac{qE_x}{m_e c \omega} = \frac{(kw_0)^2 a_{\max}}{4} \left(I_1 + \frac{I_2}{X} \right); \quad (3.17)$$

$$\frac{qE_z}{m_e c \omega} = \frac{(kw_0)^2 a_{\max}}{4} I_4; \quad (3.18)$$

$$\frac{qB_y}{m_e \omega} = \frac{(kw_0)^2 a_{\max}}{4} \left(I_1 - \frac{I_2}{X} + I_3 \right); \quad (3.19)$$

$$E_y = cB_x = cB_z = 0, \quad (3.20)$$

in which

$$\begin{aligned} I_1 &\equiv \int_0^1 \exp\left(-\frac{(kw_0)^2 b^2}{4}\right) \left(1 + \sqrt{1-b^2}\right) \sin \phi J_0(Xb) b db; \\ I_2 &\equiv \int_0^1 \exp\left(-\frac{(kw_0)^2 b^2}{4}\right) \frac{1}{\sqrt{1-b^2}} \sin \phi J_1(Xb) b^2 db; \\ I_3 &\equiv \int_0^1 \exp\left(-\frac{(kw_0)^2 b^2}{4}\right) \frac{1}{\sqrt{1-b^2}} \sin \phi J_0(Xb) b^3 db; \\ I_4 &\equiv \int_0^1 \exp\left(-\frac{(kw_0)^2 b^2}{4}\right) \left(1 + \frac{1}{\sqrt{1-b^2}}\right) \cos \phi J_1(Xb) b^2 db; \\ \phi &\equiv T - Z\sqrt{1-b^2} + \phi_0, \end{aligned}$$

and where ϕ_0 is the phase offset of the optical field. These expressions describe a Gaussian beam which propagates along the z -direction, is polarized in the x -direction, and is focused to a waist of size w_0 . The fields above are multiplied by an envelope function $\cos^2(\pi\eta/(2\omega\tau_L))$ to obtain a laser pulse of length τ_L instead of a full beam. To evaluate the field intensity a^2 in the averaged equations (3.5-3.10), the simpler paraxial approximation is used according to

$$a^2 = \left[a_{\max} \frac{w_0}{w} \exp\left(-\frac{w_0^2}{w^2} X^2\right) \cos^2\left(\frac{\pi\eta}{2\omega\tau_L}\right) \right]^2; \quad (3.21)$$

$$w \equiv w_0 \sqrt{1 + 4 \frac{Z^2}{(kw_0)^4}}.$$

Bibliography

- [111] T. Tajima and J. M. Dawson, “Laser electron accelerator,” *Phys. Rev. Lett.* **43**, 267–270 (1979).
- [112] S. P. D. Mangles, C. D. Murphy, Z. Najmudin, A. G. R. Thomas, J. L. Collier, A. E. Dangor, E. J. Divall, P. S. Foster, J. G. Gallacher, C. J. Hooker, D. A. Jaroszynski, A. J. Langley, W. B. Mori, P. A. Norreys, F. S. Tsung, R. Viskup, B. R. Walton, and K. Krushelnick, “Monoenergetic beams of relativistic electrons from intense laser-plasma interactions,” *Nature (London)* **431**, 535–538 (2004).
- [113] C. G. R. Geddes, Cs. Toth, J. van Tilborg, E. Esarey, C. B. Schroeder, D. Bruhwiler, C. Nieter, J. Cary, and W. P. Leemans, “High-quality electron beams from a laser wakefield accelerator using plasma-channel guiding,” *Nature (London)* **431**, 538–541 (2004).
- [114] J. Faure, Y. Glinec, A. Pukhov, S. Kiselev, S. Gordienko, E. Lefebvre, J.-P. Rousseau, F. Burgy, and V. Malka, “A laser-plasma accelerator producing monoenergetic electron beams,” *Nature (London)* **431**, 541–544 (2004).
- [115] A. Maksimchuk, S. Gu, K. Flippo, and D. Umstadter, “Forward ion acceleration in thin films driven by a high-intensity laser,” *Phys. Rev. Lett.* **84**, 4108–4111 (2000).
- [116] M. Borghesi, J. Fuchs, S. V. Bulanov, A. J. Mackinnon, and P. K. Patel, “Fast ion generation by high-intensity laser irradiation of solid targets and applications,” *Fusion Sci. Technol.* **49**, 412–439 (2006).
- [117] G. V. Stupakov and M. S. Zolotarev, “Ponderomotive laser acceleration and focusing in vacuum for generation of attosecond electron bunches,” *Phys. Rev. Lett.* **86**, 5274–5277 (2001).
- [118] H. F. Wang, L. P. Shi, B. Lukyanchuk, C. Sheppard, and C. T. Chong, “Creation of a needle of longitudinally polarized light in vacuum using binary optics,” *Nature Photonics* **2**, 501–505 (2008).
- [119] U. Saalman, Ch. Siedschlag, and J. M. Rost, “Mechanisms of cluster ionization in strong laser pulses,” *J. Phys. B* **39**, R39–R77 (2006).

- [120] V. P. Krainov and M. B. Smirnov, “Cluster beams in the superintense femtosecond laser pulse,” *Phys. Reports* **370**, 237–331 (2002).
- [121] Y. L. Shao, T. Ditmire, J. W. G. Tisch, E. Springate, J. P. Marangos, and M. H. R. Hutchinson, “Multi-keV electron generation in the interaction of intense laser pulses with Xe clusters,” *Phys. Rev. Lett.* **77**, 3343–3346 (1996).
- [122] E. Springate, S. A. Aseyev, S. Zamith, and M. J. J. Vrakking, “Electron kinetic energy measurements from laser irradiation of clusters,” *Phys. Rev. A* **68**, 053201 (2003).
- [123] T. Fennel, T. Döppner, J. Passig, C. Schaal, J. Tiggesbäumker, and K.-H. Meiwes-Broer, “Plasmon-enhanced electron acceleration in intense metal-cluster interactions,” *Phys. Rev. Lett.* **98**, 143401 (2007).
- [124] L. M. Chen, J. J. Park, K.-H. Hong, I. W. Choi, J. L. Kim, J. Zhang, and C. H. Nam, “Measurement of energetic electrons from atomic clusters irradiated by intense femtosecond laser pulses,” *Phys. Plasmas* **9**, 3595–3599 (2002).
- [125] T. V. Liseykina, S. Pirner, and D. Bauer, “Relativistic attosecond electron bunches from laser-illuminated droplets,” *Phys. Rev. Lett.* **104**, 095002 (2010).
- [126] Y. Fukuda, Y. Akahane, M. Aoyama, Y. Hayashi, T. Homma, N. Inoue, M. Kando, S. Kanazawa, H. Kiriya, S. Kondo, H. Kotaki, S. Masuda, M. Mori, A. Yamazaki, K. Yamakawa, E. Yu. Echkina, I. N. Inovenkov, J. Koga, and S. V. Bulanov, “Ultrarelativistic electron generation during the intense, ultrashort laser pulse interaction with clusters,” *Phys. Lett. A* **363**, 130–135 (2007).
- [127] J. Meyer-ter-Vehn and H.-C. Wu, “Coherent Thomson backscattering from laser-driven relativistic ultra-thin electron layers,” *Eur. Phys. J. D* **55**, 433–441 (2009).
- [128] H.-C. Wu and J. Meyer-ter-Vehn, “The reflectivity of relativistic ultra-thin electron layers,” *Eur. Phys. J. D* **55**, 443–449 (2009).
- [129] B. Qiao, M. Zepf, M. Borghesi, B. Dromey, and M. Geissler, “Coherent x-ray production via pulse reflection from laser-driven dense electron sheets,” *New J. Phys.* **11**, 103042 (2009).
- [130] V. I. Veksler, “The principle of coherent acceleration of charged particles,” *Sov. Atom. Energy* **2**, 525–528 (1957).
- [131] S. V. Bulanov, T. Z. Esirkepov, J. Koga, and T. Tajima, “Interaction of electromagnetic waves with plasma in the radiation-dominated regime,” *Plasma Phys. Reports* **30**, 196–213 (2004).
- [132] A. S. Il’in, V. V. Kulagin, and V. A. Cherepenin, “Acceleration of dense electron bunches at the front of a high-power electromagnetic wave,” *Plasma Phys. Reports* **27**, 1048–1056 (2001).

- [133] V. V. Kulagin, V. A. Cherepenin, and H. Suk, “Compression and acceleration of dense electron bunches by ultraintense laser pulses with sharp rising edge,” *Phys. Plasmas* **11**, 5239–5249 (2004).
- [134] W. K. H. Panofsky and M. Phillips, *Classical electricity and magnetism* (Addison-Wesley, Reading, 1962) 2nd ed.
- [135] F. Rohrlich, *Classical charged particles* (World Scientific, Singapore, 2007) 3rd ed.
- [136] H. A. Lorentz, *The theory of electrons* (Teubner, Leibzig, 1916).
- [137] M. Abraham, *Elektromagnetische Theorie der Strahlung* (Teubner, Leibzig, 1923).
- [138] P. A. M. Dirac, “Classical theory of radiating electrons,” *Proc. Royal Soc. London A* **167**, 148–169 (1938).
- [139] L. D. Landau and E. M. Lifshitz, *Classical theory of fields* (Pergamon, Oxford, 1975) 4th rev. ed.
- [140] C. Teitelboim, “Splitting of the Maxwell tensor: radiation reaction without advanced fields,” *Phys. Rev. D* **1**, 1572–1582 (1970).
- [141] J. A. Heras and R. F. O’Connell, “Generalization of the Schott energy in electrodynamic radiation theory,” *Am. J. Phys.* **74**, 150–153 (2006).
- [142] Y. I. Salamin and F. H. M. Faisal, “Harmonic generation by superintense light scattering from relativistic electrons,” *Phys. Rev. A* **54**, 4383–4395 (1996).
- [143] T. W. B. Kibble, “Mutual refraction of electrons and photons,” *Phys. Rev.* **150**, 1060–1069 (1966).
- [144] B. Quesnel and P. Mora, “Theory and simulation of the interaction of ultraintense laser pulses with electron in vacuum,” *Phys. Rev. E* **58**, 3719–3732 (1998).
- [145] J. D. Jackson, *Classical electrodynamics* (Wiley, New York, 1999) 3rd ed.
- [146] G. W. Ford and R. F. O’Connell, “Relativistic form of radiation reaction,” *Phys. Lett. A* **174**, 182–184 (1993).
- [147] G. W. Ford and R. F. O’Connell, “Radiation reaction in electrodynamics and the elimination of runaway solutions,” *Phys. Lett. A* **157**, 217–220 (1991).
- [148] H. Hora, M. Hoelss, W. Scheid, J.W. Wang, Y.K. Ho, F. Osman, and R. Castillo, “Principle of high accuracy for the nonlinear theory of the acceleration of electrons in a vacuum by lasers at relativistic intensities,” *Laser and Particle Beams* **18**, 135–144 (2000).

- [149] F. V. Hartemann, S. N. Fochs, G. P. Le Sage, N. C. Luhmann Jr., J. G. Woodworth, M. D. Perry, Y. J. Chen, and A. K. Kerman, “Nonlinear ponderomotive scattering of relativistic electrons by an intense field at focus,” *Phys. Rev. E* **51**, 4833–4843 (1995).
- [150] P. B. Parks, T. E. Cowan, R. B. Stephens, and E. M. Campbell, “Model of neutron-production rates from femtosecond-laser-cluster interactions,” *Phys. Rev. A* **63**, 063203 (2001).
- [151] M. V. Ammosov, “Influence of the Coulomb repulsion between electrons on their energy spectrum in the case of the nonlinear surface photoeffect,” *J. Opt. Soc. Am. B* **8**, 2260–2264 (1991).
- [152] R. Medina, “Radiation reaction of a classical quasi-rigid extended charge,” *J. Phys. A: Math. Gen.* **39**, 3801–3816 (2009).
- [153] F. Rohrlich, “The correct equation of motion of a classical point charge,” *Phys. Lett. A* **283**, 276–278 (2001).
- [154] F. Rohrlich, “Dynamics of a classical quasi-point charge,” *Phys. Lett. A* **303**, 307–310 (2002).
- [155] I. Y. Dodin and N. J. Fisch, “Relativistic electron acceleration in focused laser fields after above-threshold ionization,” *Phys. Rev. E* **68**, 056402 (2003).
- [156] A. L. Galkin, V. A. Egorov, M. P. Kalashnikov, V. V. Korobkin, M. Yu. Romanovsky, O. B. Shiryayev, and V. A. Trofimov, “Energy distribution of electrons expelled from relativistically intense laser beam,” *Contrib. Plasma Phys.* **49**, 544–549 (2009).

4

Polarization-dependent ponderomotive gradient force in a standing wave

Abstract - The ponderomotive force is derived for a relativistic charged particle entering an electromagnetic standing wave with a general three-dimensional field distribution and a nonrelativistic intensity, using a perturbation expansion method. It is shown that the well-known ponderomotive gradient force expression does not hold for this situation. The modified expression is still of simple gradient form, but contains additional polarization-dependent terms. These terms arise because the relativistic translational velocity induces a quiver motion in the direction of the magnetic force, which is the direction of large field gradients. Consistent perturbation expansion of the equation of motion leads to an effective doubling of this magnetic contribution. The derived ponderomotive force generalizes the polarization-dependent electron motion in a standing wave obtained earlier [A.E. Kaplan and A.L. Pokrovsky, Phys. Rev. Lett. **95**, 053601 (2005)]. Comparison with simulations in the case of a realistic, non-idealized, three-dimensional field configuration confirms the general validity of the analytical results.

Publication status - The work described in this chapter has been published by P. W. Smorenburg, J. H. M. Kanters, A. Lassise, G. J. H. Brussaard, L. P. J. Kamp, and O. J. Luiten in Phys. Rev. A **83**, 063810 (2011).

4.1 Introduction

The ponderomotive force is a time-averaged force experienced by a charged particle in an oscillating electromagnetic (EM) field that is spatially inhomogeneous. In the standard perturbative approach [157, 158], it is shown that a charged particle in an oscillating EM field attains an oscillatory quiver momentum superimposed on a slowly varying guiding center momentum $\bar{\mathbf{p}}$. The latter is subject to the classical ponderomotive force \mathbf{F}_p :

$$\frac{d\bar{\mathbf{p}}}{dt} = \mathbf{F}_p = -\frac{e^2}{2\epsilon_0 m c \omega^2} \nabla I(\mathbf{x}), \quad (4.1)$$

where m is the mass of the particle, e its charge, ϵ_0 the permittivity, ω the frequency of the EM field and $I(\mathbf{x})$ the position-dependent field intensity. The classical ponderomotive force is of gradient form, and always directed toward regions of low field intensity. The ponderomotive force is observed and exploited in a wide range of contexts. In laser-plasma physics, the ponderomotive force drives the formation of laser wakefields that are used for next generation electron accelerators [159–162]. Ion beams are produced by intense laser irradiation of thin foils, in which the ponderomotive force plays an essential role [163, 164]. Schemes have been proposed for ponderomotive laser-vacuum acceleration of electrons [165, 166]. In Paul traps, ions are confined by a ponderomotive potential [167]. In electron beam diagnostics, the length of electron bunches is measured by sequentially scattering different sections of the bunch using the ponderomotive force of a laser pulse [168, 169].

The field gradients that can be obtained in a single laser pulse are set by the laser pulse duration longitudinally and the focal spot transversely. For many applications of the ponderomotive force this means that, in order to obtain a sufficiently strong force, field intensities are required that are large enough to cause a relativistic quiver motion (which happens if the normalized amplitude of the vector potential, $a \equiv eA/mc = e\sqrt{2I/(\epsilon_0 c)}/(mc\omega) \gtrsim 1$, i.e. $I \gtrsim 2 \cdot 10^{18}$ W/cm² for a wavelength of 800 nm). Relativistic field intensities necessitate more complicated descriptions of the average EM force [170–172], or at least restricts the domain of validity of Eq. (4.1) [173, 174]. An intermediate situation occurs when an already relativistic particle enters an EM field with nonrelativistic intensity. A relativistic derivation [175] shows that this introduces an additional factor $\sqrt{1 + \bar{\mathbf{p}}^2/(mc)^2 + a^2/2}$ in the denominator of Eq. (4.1), resulting in an accurate description for practical situations [176].

An alternative to the application of a relativistic laser pulse is the use of a standing wave. In this configuration the nodes and antinodes are spaced on the scale of the wavelength, resulting in large field gradients. For example, a standing wave produced by two counterpropagating EM waves with wavelength $\lambda = 800$ nm and a very modest, nonrelativistic peak field intensity of 10^{15} W/cm², already causes ponderomotive

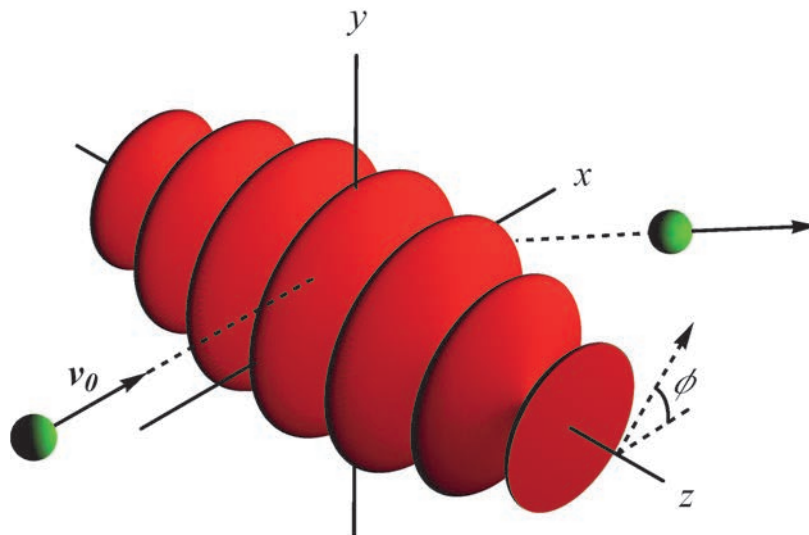


Figure 4.1: Charged particle with initial velocity v_0 , which is deflected by the ponderomotive force of a standing EM wave oriented with its nodal planes parallel to the (x, y) -plane. The dashed arrow indicates the polarization direction for the case considered in Section 4.3.1.

forces of the order of $F_p/e \sim 1$ GV/m. For this reason, a number of applications of the ponderomotive force have been proposed that take advantage of the large field gradients in a standing EM wave. Hebeisen et al. [177] suggested a table-top standing wave version of the bunch length measurement setup mentioned previously. Following an earlier idea [178], Balcou proposed a novel X-ray free electron laser based on the wiggling of electrons in the ponderomotive potential of a standing wave [179]. Faure et al. used a standing wave formed by colliding laser pulses to pre-accelerate electrons ponderomotively in a laser-wakefield setup [180], demonstrating that the production of monoenergetic electron beams can be made stable and reproducible in that way [181–183]. Baum and Zewail proposed to create attosecond electron pulse trains by bunching of an electron beam due to a co-moving ponderomotive beat potential between laser pulses of different frequencies [184].

In view of all these important technological applications, a thorough understanding of the ponderomotive force in a standing wave is essential. The scattering of charged particles by a standing EM wave was first described in a quantum-mechanical context by Kapitza and Dirac [185], and since then many papers have appeared on this

subject [186–190]. Nevertheless, there are only few classical electrodynamical studies on the standing wave ponderomotive force [191–194]. Most publications on the ponderomotive force have concentrated on propagating EM waves, establishing the validity of Eq. (4.1) in that context [157, 158, 175]. Eq. (4.1) is also applied to the standing wave configuration, implicitly assuming that it remains valid in that case as well. In 2005, however, Kaplan and Pokrovsky [195, 196] calculated the time-averaged equation of motion of an electron in a standing wave for a number of field polarizations, and their results showed that the ponderomotive force depends on the polarization. Most notably, the ponderomotive force can even change its direction toward high field regions for certain situations. Clearly, these results are in conflict with the polarization-independent Eq. (4.1) that is commonly used. Kaplan and Pokrovsky did not provide an alternative expression for the ponderomotive force, however.

We would now first like to show, on the basis of simple arguments, that it can be understood that the ponderomotive force in a standing wave is polarization-dependent. Consider Fig. 4.1, showing a particle with charge e and initial velocity \mathbf{v}_0 parallel to the x -axis, incident on a standing wave with electric field \mathbf{E} and magnetic field \mathbf{B} . The wave is oriented with its nodal planes parallel to the (x, y) -plane, so that the spatial variation of the field is much more rapid in the z -direction than in the transverse direction. This is the typical system considered in this chapter. When the particle enters the EM field, it will start to quiver in the polarization direction in response to the oscillating electric force $e\mathbf{E}$. This 'electric quiver', combined with the Lorentz force equation, leads to the well-known average force, Eq. (4.1), independent of the polarization direction. However, the incident particle will also quiver in response to the magnetic force $\approx e(\mathbf{v}_0 \times \mathbf{B})$. This 'magnetic quiver' can be comparable in magnitude to the electric quiver for relativistic particles. Because the magnetic quiver is in the z -direction, the particle samples a large field gradient, leading to an additional contribution to the ponderomotive force that is comparable to the electric one. And since the magnetic force and hence the amplitude of the magnetic quiver depend on the angle between \mathbf{v}_0 and \mathbf{B} , the magnetic contribution is dependent on the polarization direction.

In this chapter, the ponderomotive force is derived for a relativistic particle entering a nonrelativistic standing wave with a general three-dimensional field distribution. It is shown that indeed Eq. (4.1), or the relativistic equivalent, does not hold for this situation. This may have important implications for experiments and proposals based on the standing wave ponderomotive force. The main result of this chapter, Eq. (4.21), shows that the modified ponderomotive force is still of simple gradient form, but contains additional polarization-dependent terms. We thus generalize the results of Kaplan and Pokrovsky, which follow naturally from our ponderomotive force expression. This chapter is structured as follows. In Section 4.2, the polarization-dependent ponderomotive gradient force in a standing wave, Eq (4.21), is derived

using a perturbation expansion method. The origin of the additional polarization-dependent terms is discussed. Next, Eq. (4.21) is applied in Section 4.3 to calculate the averaged equation of motion of an electron in specific standing wave geometries, reproducing the results obtained by Kaplan and Pokrovsky. In Section 4.4, we validate our ponderomotive force expression by testing it against numerical simulations of electron trajectories in a realistic, non-idealized field configuration.

4.2 The polarization-dependent ponderomotive force

4.2.1 Assumptions

First consider the idealized case of two plane EM waves of equal frequency ω that counterpropagate along the z -axis and add to form a standing wave. In the Coulomb gauge, the vector potential \mathbf{A} of this ideal standing wave is then purely harmonic in time t and position z , i.e. $(\partial^2/\partial t^2 + \omega^2)\mathbf{A} = \mathbf{0}$ and $(\partial^2/\partial z^2 + k^2)\mathbf{A} = \mathbf{0}$, where $k = \omega/c$ with c the speed of light. Furthermore, the vector potential satisfies $A_z = 0$ and $\nabla_{\perp} A_i = \mathbf{0}$, where $i = x, y$.

In practical applications, however, an EM standing wave differs from this idealized situation in two ways. First, the standing wave has a finite transverse extent, leading to a small but nonzero transverse gradient $\nabla_{\perp} A_i$ and a small longitudinal component A_z . These two quantities are related by the gauge condition $\nabla \cdot \mathbf{A} = 0$, and scale analysis of the latter shows that, symbolically,

$$\frac{A_z}{A_{\perp}} \sim \frac{\nabla_{\perp}}{\partial/\partial z} \sim \epsilon. \quad (4.2)$$

Here, $\epsilon \ll 1$ is a small parameter measuring the magnitude of the field inhomogeneity, and will be used as the expansion parameter in the derivation that follows. For example, in Gaussian laser beams focused to a waist of size w_0 , this parameter is $\epsilon \sim (kw_0)^{-1}$.

Secondly, the standing wave has a finite lifetime, so that the vector potential is only quasi-monochromatic:

$$\frac{\partial^2 \mathbf{A}}{\partial(\omega t)^2} + \mathbf{A} = O(\delta A); \quad \frac{\partial^2 \mathbf{A}}{\partial(kz)^2} + \mathbf{A} = O(\delta A), \quad (4.3)$$

where $\delta \ll 1$ is another small parameter measuring the monochromaticity. For a standing wave produced by counterpropagating laser pulses of temporal length σ , for example, this parameter is $\delta \sim (\omega\sigma)^{-1}$.

In addition, in this chapter the EM field is assumed to be of nonrelativistic intensity, which means that

$$\frac{eA}{mc} \equiv a \ll 1. \quad (4.4)$$

For reasons of clarity, for the moment it is assumed that $a \sim \epsilon$. However, the derivation below can be generalized straightforwardly to other field strengths such as $a \sim \epsilon^2$ or $a \sim \epsilon^{1/2}$, leading to the same result. Appendix 4.B gives a short description of the generalized derivation.

4.2.2 Perturbation expansions

Before considering the dynamics of a charged particle in a standing wave in detail, let us first determine what time scales are involved. First, there is the time scale of the quiver motion, which is the optical time scale ω^{-1} . Second, there is the time scale on which the motion of the guiding center changes. Substitution of an ideal standing wave $\mathbf{A} = A_0 \mathbf{e}_x \cos kz \sin \omega t$ in Eq. (4.1) and integrating yields oscillatory motion in the z -direction, with a typical frequency $\Omega = eA_0\omega/(\sqrt{2}mc)$. Thus the guiding center motion in the z -direction changes on a second, longer time scale $(a\omega)^{-1} \sim (\epsilon\omega)^{-1}$. Finally, in a realistic standing wave, the nonzero transverse field gradient causes transverse ponderomotive forces, which in view of Eqs. (4.1) and (4.2) are weaker than the longitudinal ponderomotive forces by a factor ϵ . Therefore the transverse guiding center motion changes on a third, still longer time scale $(\epsilon^2\omega)^{-1}$.

Having established the three time scales of the problem, next consider the equations of motion of a charged particle in the standing wave [197]:

$$\frac{d}{d(\omega t)} \left(\frac{\mathbf{p}}{mc} + \frac{e\mathbf{A}}{mc} \right) = \frac{1}{\gamma} \left(\frac{\lambda \nabla e\mathbf{A}}{2\pi mc} \right) \cdot \frac{\mathbf{p}}{mc}; \quad (4.5)$$

$$\frac{d(k\mathbf{x})}{d(\omega t)} = \frac{1}{\gamma} \frac{\mathbf{p}}{mc}, \quad (4.6)$$

in which $\gamma = \sqrt{1 + p^2/(mc)^2}$ is the Lorentz factor, and the dyadic notation $\nabla \mathbf{A}$ has been used [198]. Eqs. (4.5)-(4.6) have been made dimensionless by dividing the usual equations by $mc\omega$ and c respectively. Below, these equations are solved by expressing the various quantities in perturbation expansions in terms of ϵ . Subsequently, terms of like order in ϵ will be collected and equated [199]. We use the symbol ' O_s ' to denote 'on the order of', i.e. $f = O_s(\epsilon^i)$ means $0 < \lim_{\epsilon \downarrow 0} f/\epsilon^i < \infty$, in distinction with $f = O(\epsilon^i)$ which is equivalent to $0 \leq \lim_{\epsilon \downarrow 0} f/\epsilon^i < \infty$. Superscripts in parentheses denote the order of the terms.

First, the momentum is expanded as

$$\mathbf{p} = \sum_{i=0}^{\infty} \mathbf{p}^{(i)}; \quad \mathbf{p}^{(i)} = O_s(\epsilon^i). \quad (4.7)$$

Note that $\mathbf{p}^{(0)}$ would be the momentum in the absence of the standing wave field, that is, the initial momentum, since $\mathbf{p} \rightarrow \mathbf{p}^{(0)}$ as $a \sim \epsilon \downarrow 0$. Next, each order $\mathbf{p}^{(i)}$ is decomposed into a slowly varying guiding center part $\bar{\mathbf{p}}^{(i)} = \langle \mathbf{p}^{(i)} \rangle$ and a rapidly varying quiver part $\tilde{\mathbf{p}}^{(i)} = \mathbf{p}^{(i)} - \langle \mathbf{p}^{(i)} \rangle$. Here, $\langle \cdot \rangle$ denotes time-averaging on the time scale ω^{-1} . Upon substitution of this decomposition in the left-hand side of Eq. (4.5), each term is differentiated with respect to ωt . This preserves the order of magnitude of the fast quantities $\tilde{\mathbf{p}}^{(i)}$, since these vary on the time scale ω^{-1} , i.e. $d\tilde{\mathbf{p}}^{(i)}/d(\omega t) = O_s(\epsilon^i)$. However, from the discussion above, the slow quantities $\bar{p}_z^{(i)}$ and $\bar{\mathbf{p}}_{\perp}^{(i)}$ vary over longer time scales, so that differentiation increases their order according to $d\bar{p}_z^{(i)}/d(\omega t) = O_s(\epsilon^{i+1})$ and $d\bar{\mathbf{p}}_{\perp}^{(i)}/d(\omega t) = O_s(\epsilon^{i+2})$ respectively. More formally, these order relations may be established using the multiple scale technique [199], considering p_z a function of the two variables ωt and $\epsilon \omega t$ and considering \mathbf{p}_{\perp} a function of the two variables ωt and $\epsilon^2 \omega t$. Multiple scale analysis has been applied in a relativistic derivation of the ponderomotive force in propagating EM radiation [172].

Next, the expansion (4.7) is substituted in the reciprocal Lorentz factor $1/\gamma$. Extracting the zeroth order part $\gamma^{(0)} = \sqrt{1 + (\mathbf{p}^{(0)})^2}/(mc)^2$, this gives

$$\begin{aligned} \frac{1}{\gamma} &= \frac{1}{\gamma^{(0)} \sqrt{1 + (mc\gamma^{(0)})^{-2} (2\mathbf{p}^{(0)} \cdot \mathbf{p}^{(1)} + O(\epsilon^2))}} \\ &= \frac{1}{\gamma^{(0)}} - \frac{\mathbf{p}^{(0)} \cdot \mathbf{p}^{(1)}}{(mc)^2 (\gamma^{(0)})^3} + O(\epsilon^2) \equiv \left(\frac{1}{\gamma}\right)^{(0)} + \left(\frac{1}{\gamma}\right)^{(1)} + O(\epsilon^2). \end{aligned} \quad (4.8)$$

The quantity $(1/\gamma)^{(1)}$ is the first-order time-dependent variation of the reciprocal Lorentz factor with respect to the constant value $(1/\gamma)^{(0)}$. As will be shown below, this variation leads to an additional contribution in the final ponderomotive force expression.

Finally, below it will be required to take the time average of expressions involving powers of \mathbf{A} or its derivatives. These time averages need to be taken along the trajectory of the particle; that is, in the average $\langle \mathbf{A}(\mathbf{x}(t), t) \rangle$, the vector potential is to be evaluated at $\mathbf{x} = \mathbf{x}(t)$. To bring out this position dependence explicitly, the position is also expanded in a perturbation expansion in terms of ϵ :

$$\mathbf{x} = \sum_{i=0}^{\infty} \mathbf{x}^{(i)}; \quad \frac{d\mathbf{x}^{(i)}}{dt} = O_s(\mathbf{p}^{(i)}) = O_s(\epsilon^i). \quad (4.9)$$

Again, each order $\mathbf{x}^{(i)}$ is decomposed into a slowly varying guiding center part $\bar{\mathbf{x}}^{(i)} = \langle \mathbf{x}^{(i)} \rangle$ and a rapidly varying quiver part $\tilde{\mathbf{x}}^{(i)} = \mathbf{x}^{(i)} - \langle \mathbf{x}^{(i)} \rangle$. Then the vector potential can be expanded in a Taylor series around $\mathbf{x} = \sum \bar{\mathbf{x}}^{(i)} \equiv \bar{\mathbf{x}}$,

$$\mathbf{A}(\mathbf{x}(t), t) = \bar{\mathbf{A}} + \tilde{z}^{(1)}(t) \frac{\partial \bar{\mathbf{A}}}{\partial z} + O(\epsilon^3). \quad (4.10)$$

Here and in the remainder of the chapter, an overbar on the vector potential denotes evaluation at the guiding center position, i.e. $\bar{\mathbf{A}} \equiv \mathbf{A}(\bar{\mathbf{x}}, t)$. In writing the series in Eq. (4.10), it has been anticipated that $\tilde{\mathbf{x}}^{(0)} = \mathbf{0}$, as will be shown below.

4.2.3 Order-by-order solution of equation of motion

Substitution of the expansions (4.7)-(4.10) in the equations of motion (4.5)-(4.6), and collecting terms of equal order in ϵ , results in two equations at each order of ϵ . These order equations are listed in Appendix 4.A. Order-by-order solution, balancing in each equation the averaged parts and the oscillating parts separately, yields the zeroth order quantities

$$\bar{\mathbf{p}}^{(0)} = \mathbf{p}_0; \quad (4.11)$$

$$\tilde{\mathbf{p}}^{(0)} = \mathbf{0}; \quad (4.12)$$

$$\frac{d\bar{\mathbf{x}}^{(0)}}{dt} = \frac{\mathbf{p}_0}{m\gamma^{(0)}}; \quad (4.13)$$

$$\tilde{\mathbf{x}}^{(0)} = \mathbf{0}, \quad (4.14)$$

in which \mathbf{p}_0 is the initial momentum. As expected, at zeroth order (that is, in the limit $a \sim \epsilon \downarrow 0$ where both the field strength and field inhomogeneity are zero) the motion is equal to what it would be if the EM field were absent. For the first order quantities, it is found that

$$\tilde{\mathbf{p}}_{\perp}^{(1)} = -e\mathbf{A}_{\perp}; \quad (4.15)$$

$$\frac{d\tilde{p}_z^{(1)}}{dt} = \frac{e}{m\gamma^{(0)}} \frac{\partial \bar{\mathbf{A}}_{\perp}}{\partial z} \cdot \mathbf{p}_{0\perp}; \quad (4.16)$$

$$\frac{d\tilde{z}^{(1)}}{dt} = \frac{1}{m\gamma^{(0)}} \left(\tilde{p}_z^{(1)} + p_{0z} \frac{e\mathbf{A}_{\perp} \cdot \mathbf{p}_{0\perp} - p_{0z}\tilde{p}_z^{(1)}}{(mc\gamma^{(0)})^2} \right); \quad (4.17)$$

$$\frac{d\bar{z}^{(1)}}{dt} = \frac{\tilde{p}_z^{(1)}}{m\gamma^{(0)}}. \quad (4.18)$$

Eq. (4.15) expresses the well-known result that, in an oscillating EM field, at lowest order the quiver momentum balances the vector potential, such that the canonical momentum $\mathbf{p} + e\mathbf{A}$ is conserved. Eq. (4.18) will be used in Section 4.3 for the description of the guiding center motion. Eqs. (4.16)-(4.17) describe the quiver motion in the direction normal to the plane of polarization of the standing wave, which is the direction of strong field gradient. This is the magnetic quiver motion described in the Introduction. Time differentiation of Eq. (4.17) and substitution of Eq. (4.16) yields

$$\frac{d^2\tilde{z}^{(1)}}{dt^2} = \frac{e}{(m\gamma^{(0)})^2} \left((1 - \beta_{0z}^2) \frac{\partial \bar{\mathbf{A}}_{\perp}}{\partial z} + \frac{\beta_{0z}}{c} \frac{d\mathbf{A}_{\perp}}{dt} \right) \cdot \mathbf{p}_{0\perp}, \quad (4.19)$$

where $\beta_0 = \mathbf{p}_0/(mc\gamma^{(0)})$ is the initial velocity divided by c . We now restrict to the situation that β_{0z} is sufficiently small so that the second term in parentheses in Eq. (4.19) is negligible, which is the case if $\beta_{0z} \ll 1$. Then, in addition, using Eq. (4.3) the full time derivative may be written $d^2/dt^2 = (\partial/\partial t + \mathbf{v} \cdot \nabla)^2 = -\omega^2 + O(\epsilon, \delta, \beta_{0z})$, so that double time integration yields

$$\tilde{z}^{(1)} = -\frac{e}{(m\gamma^{(0)})^2 \omega^2} \frac{\partial \bar{\mathbf{A}}_{\perp}}{\partial z} \cdot \mathbf{p}_{0\perp} [1 + O(\delta, \beta_{0z})]. \quad (4.20)$$

The bracketed factor expresses the error introduced by the integration. Eq. (4.20) clearly shows that the amplitude of the magnetic quiver motion is polarization-dependent: if $\mathbf{p}_{0\perp}$ is parallel to \mathbf{A}_{\perp} , this amplitude may be substantial, while for $\mathbf{p}_{0\perp}$ perpendicular to \mathbf{A}_{\perp} , it vanishes at first order. This reinstates the argument made in the Introduction: if $\mathbf{p}_{0\perp} \parallel \mathbf{A}_{\perp}$, the momentum is largely perpendicular to the magnetic field, resulting in a substantial magnetic force and quiver amplitude. Conversely, if $\mathbf{p}_{0\perp} \perp \mathbf{A}_{\perp}$, the momentum is largely parallel to the magnetic field, with vanishing magnetic force and quiver amplitude.

As a final step, we substitute Eqs. (4.11)-(4.15) and (4.20) in the right-hand sides of the remaining order equations (4.33)-(4.34), and take the time average of these equations. Then the left-hand sides reduce to the rate of change of the first order guiding center momentum, $d\bar{\mathbf{p}}^{(1)}/dt$. The right-hand sides reduce to a single gradient:

$$\frac{d\bar{\mathbf{p}}^{(1)}}{dt} \approx -\frac{e^2}{2m\gamma^{(0)}} \nabla \left\langle \bar{\mathbf{A}}_{\perp}^2 - (\beta_{0\perp} \cdot \bar{\mathbf{A}}_{\perp})^2 + \left(\frac{\partial (\beta_{0\perp} \cdot \bar{\mathbf{A}}_{\perp})}{\partial(kz)} \right)^2 \right\rangle. \quad (4.21)$$

This is the polarization-dependent ponderomotive force in a nonrelativistic standing wave for a particle with $\beta_{0z} \ll 1$; it is the main result of this chapter. The approximate sign expresses a relative error of the order of $\beta_{0z} + \delta$. In the limit $\beta_{0\perp} \rightarrow 0$, Eq. (4.21) reduces to the well-known polarization-independent ponderomotive force, Eq. (4.1), with the relativistic factor $\gamma^{(0)} \approx \sqrt{1 + \bar{\mathbf{p}}^2/(mc)^2 + a^2/2}$ included in the

denominator. For $\beta_{0\perp} \neq 0$, however, the two polarization-dependent terms of Eq. (4.21) become significant.

The term in Eq. (4.21) proportional to $(\partial(\beta_{0\perp} \cdot \bar{\mathbf{A}}_{\perp})/\partial kz)^2$ originates from including the magnetic quiver motion, Eq. (4.20), in the Taylor expansion of the vector potential, Eq. (4.10). It accounts for the fact that the z -position oscillates in phase with the temporal oscillation of the field. Therefore, when a field gradient in the z -direction is present, the particle systematically samples higher fields at selected phases of the electric quiver motion in the direction of \mathbf{A}_{\perp} , and lower fields at other phases. The induced nonzero average force is negligible in most applications of the ponderomotive force. But in a standing wave the derivative in $\partial^2/\partial(kz)^2$ is of order unity, so that this term is comparable to the other terms in Eq. (4.21).

The origin of the term in Eq. (4.21) proportional to $(\beta_{0\perp} \cdot \bar{\mathbf{A}}_{\perp})^2$ can be traced back to including the first order term $(1/\gamma)^{(1)}$ in the expansion of the Lorentz factor, Eq. (4.8), rather than approximating $\gamma \approx \gamma^{(0)}$ throughout.

4.2.4 Time-averaged Hamiltonian

The ponderomotive force on a charged particle in an electromagnetic field can also be derived using a Hamiltonian description, showing that this force is essentially the gradient of the time-averaged Hamiltonian of the particle [200]. Indeed, the right hand side of Eq. (4.21) can be written as such. To see this, note that combination of Eqs. (4.15)-(4.16) and (4.20) gives

$$\frac{d\bar{\mathbf{p}}^{(1)}}{dt} \approx -\nabla \left\langle \gamma_0 m c^2 + \frac{(\tilde{\mathbf{p}}^{(1)})^2}{2\gamma_0 m} - \frac{(\mathbf{p}_0 \cdot \tilde{\mathbf{p}}^{(1)})^2 c^2}{2(\gamma_0 m c)^3} \right\rangle, \quad (4.22)$$

where the term $\nabla(\gamma_0 m c^2) \equiv \mathbf{0}$ has been added for convenience. The quantity within angular brackets is just the average of the Hamiltonian $H = \sqrt{m^2 c^4 + p^2 c^2}$, in which the momentum p and the square root have been expanded up to second order in ϵ .

4.3 Wiggling motion in a standing wave

The last term of the z -component of Eq. (4.21) may be rewritten by performing the z -differentiations and using Eq. (4.3), after which Eq. (4.21) becomes

$$\frac{d\bar{p}_z^{(1)}}{dt} \approx -\frac{e^2}{2m\gamma^{(0)}} \frac{\partial}{\partial z} \left\langle \bar{\mathbf{A}}_{\perp}^2 - 2(\beta_{0\perp} \cdot \bar{\mathbf{A}}_{\perp})^2 \right\rangle. \quad (4.23)$$

We now evaluate Eq. (4.23) for the linearly and circularly polarized standing waves considered by Pokrovsky and Kaplan.

4.3.1 Linear polarization

Let the standing wave be produced by two counterpropagating plane waves of equal amplitude and frequency that are collinearly polarized in the direction $\mathbf{e}_p = \mathbf{e}_x \cos \phi + \mathbf{e}_y \sin \phi$, as is indicated in Fig. 4.1 by the dashed arrow. Then the vector potential is $\mathbf{A} = A_0 \mathbf{e}_p \cos kz \sin \omega t$. Suppose that a charged particle enters the standing wave parallel to the x -axis with initial velocity β_0 . Differentiating Eq. (4.18), and substituting Eq. (4.23), gives the equation of motion for the guiding center of the particle in the z -direction:

$$\frac{d^2 k\bar{z}}{d(\omega t)^2} - a_0^2 \frac{1 - 2\beta_0^2 \cos^2 \phi}{4(\gamma^{(0)})^2} \sin(2k\bar{z}) \approx 0, \quad (4.24)$$

in which $a_0 = eA_0/(mc)$. Eq. (4.24) shows that the guiding center makes pendulum-like oscillations in the z -direction (it wiggles in the ponderomotive potential), with equilibrium points at $k\bar{z} = n\pi/2$ and a small-amplitude frequency $\Omega = a_0 \omega \sqrt{|1 - 2\beta_0^2 \cos^2 \phi|}/(\sqrt{2}\gamma^{(0)})$.

First, consider polarization parallel to the initial velocity, that is, $\cos \phi = 1$. Then Eq. (4.24) reduces to Eq. (40) of Ref. [196] after rewriting $\beta_0 = p_0/(mc\gamma^{(0)})$. As was noted in Ref. [196], the most striking feature of this configuration is that the guiding center oscillations vanish for $\beta_0 = 1/\sqrt{2}$; in terms of the guiding center motion, the standing wave is invisible to the particle for this value of initial velocity. When β_0 is increased above $1/\sqrt{2}$, the stable and unstable equilibrium points of Eq. (4.24) reverse their positions, i.e. the ponderomotive force changes direction towards high field regions. This is the relativistic reversal described in Ref. [196].

For polarization perpendicular to the initial velocity of the particle, $\cos \phi = 0$. Then Eq. (4.24) becomes identical to Eq. (52) of Ref. [196]. For this polarization, the magnitude of the ponderomotive force and the wiggling frequency are independent of the initial velocity, and the relativistic reversal effect is absent.

4.3.2 Circular polarization

If the standing wave is produced by two counterpropagating plane waves that are circularly polarized with opposite helicities, the vector potential is equal to $\mathbf{A} = A_0 \cos kz (\mathbf{e}_x \cos \omega t + \mathbf{e}_y \sin \omega t)$. Thus the standing wave has equally spaced nodes and antinodes along the z -axis, while locally the field direction rotates around the z -axis with time. Again combining Eqs. (4.18) and (4.23) and substituting the vector potential now gives

$$\frac{d^2 k\bar{z}}{d(\omega t)^2} - \frac{a_0^2}{2(\gamma^{(0)})^4} \sin(2k\bar{z}) \approx 0, \quad (4.25)$$

which equals Eq. (56) of Ref. [196] taking into account that the field amplitude used there is $A_0/\sqrt{2}$. Thus, in this configuration the equilibrium points are the same as in the linearly polarized case described by Eq. (4.24) for $\cos\phi = 0$, although the magnitude of the ponderomotive force is a factor $(\gamma^{(0)})^2$ weaker.

For counterpropagating circularly polarized waves of equal helicity, the vector potential reads $A_0 \sin\omega t (\mathbf{e}_x \sin kz + \mathbf{e}_y \cos kz)$. In this case, the standing wave is polarized in a helix along the z -axis. Eqs. (4.18) and (4.23) yield

$$\frac{d^2 k\bar{z}}{d(\omega t)^2} + \frac{a_0^2 \beta_0^2}{2 (\gamma^{(0)})^2} \sin(2k\bar{z}) \approx 0, \quad (4.26)$$

which is the same as Eq. (62) of Ref. [196] after rewriting $\beta_0 = p_0/(mc\gamma^{(0)})$ and taking into account the different definition of the field amplitude. As was noted in Ref. [196], the field intensity is homogeneous along the z -axis, so that Eq. (4.1) predicts zero ponderomotive force. However, the modified ponderomotive force expression, Eq. (4.21), shows that this force is nonzero, so that Eq. (4.26) still yields wiggling motion of the guiding center.

In summary, all the equations of motion (4.24)-(4.26) can be derived from a single ponderomotive force expression, Eq. (4.21). We have therefore generalized the results of Kaplan and Pokrovsky, who started from the Lorentz force equation for each individual case. Moreover, Eq. (4.21) also gives the transverse component of ponderomotive force, which was not considered in Ref. [196].

4.4 Comparison with simulations

In this section, Eq. (4.21) is tested against numerical simulations of electron trajectories in a realistic, non-idealized standing wave field. We have used the GPT code which uses an embedded fifth order Runge-Kutta method with adaptive stepsize control [201]. For comparison with the simulations, Eq. (4.21) is needed in terms of the electric field rather than the vector potential. From Eq. (4.3), the potential is approximately harmonic in time, so that $\langle \bar{\mathbf{A}}_{\perp}^2 \rangle \approx \omega^{-2} \langle \bar{\mathbf{E}}_{\perp}^2 \rangle$. Therefore $\bar{\mathbf{A}}_{\perp}$ may be effectively replaced by $\bar{\mathbf{E}}_{\perp}/\omega$ in Eq. (4.21).

We consider again the configuration shown in Fig. 4.1, this time with two identical Gaussian laser beams in the fundamental mode that counterpropagate along the z -axis, have a central wavelength $\lambda = 800$ nm and a peak intensity $I_0 = 2.0 \cdot 10^{14}$ W/cm², and are focused in a common waist of size $w_0 = 12.5$ μ m at $z = 0$. For these parameters, $\epsilon \sim (kw_0)^{-1} = 0.01$ and $a = 0.01$ so that the theory of Section 4.2 is valid. The beams are assumed to be pulsed with a Gaussian pulse shape of length

$\sigma = 85$ fs, and timed such that the centers of the pulses coincide at $z = 0$ at time $t = 0$. This configuration yields a standing wave around the origin with length $\sim c\sigma$ and width $\sim w_0$, and with a lifetime $\sim \sigma$ around $t = 0$. Furthermore, we assume that the pulses are collinearly polarized in the direction $\mathbf{e}_p = \mathbf{e}_x \cos \phi + \mathbf{e}_y \sin \phi$, similar to the case considered in Section 4.3.1. In each of the following cases, the trajectory is calculated of an electron entering with initial velocity $\beta_0 = \beta_0 \mathbf{e}_x$ for $t \ll -\sigma$, and with the initial position chosen such that, at $t = 0$, the position of the electron would be $(x, y, z) = (0, w_0/2, \lambda/8)$ in absence of the laser fields. Then the electron meets the standing wave close to the origin, has interaction with it for some time $\sim \sigma$, and leaves the interaction region in a deflected direction. The initial position has been chosen such that the electron samples the highest available field gradients both in the z -direction and in the perpendicular direction, in order to maximize the ponderomotive effects.

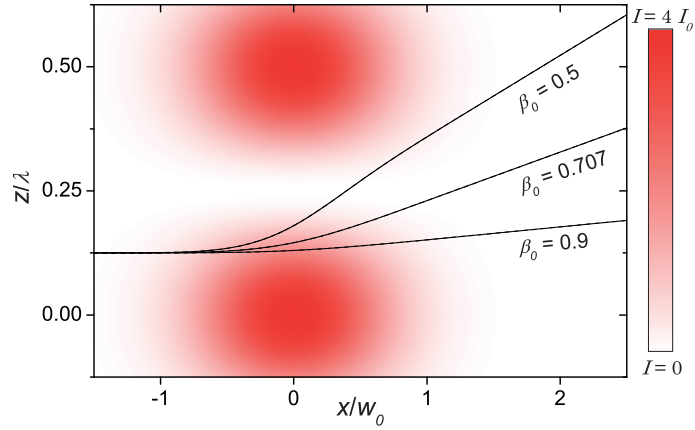


Figure 4.2: Trajectory of an electron incident on a standing wave that is polarized in the y -direction (out of plane), for three different initial velocities β_0 . The color map shows the field intensity of the standing wave in the (z, x) -plane at time $t = 0$. For each initial velocity, the plot actually includes three trajectories, calculated with the methods GPT, OLD, and NEW respectively; in each case all three lines overlap to within the linewidth.

In Figs. 4.2 and 4.3, the trajectory of the electron is shown as viewed from the negative y -axis, for several values of β_0 and for two different polarizations. Trajectories were calculated using three different methods:

- (GPT) numerical integration of the exact equations of motion using the GPT code (solid lines);
- (OLD) calculation according to the classical ponderomotive force, Eq. (4.1) (dashed lines);
- (NEW) calculation according to our polarization-dependent ponderomotive force, Eq. (4.21), with $\overline{\mathbf{A}}_{\perp}$ replaced by $\overline{\mathbf{E}}_{\perp}/\omega$ (dash-dotted lines).

Standard paraxial field expressions have been used [176]; these are listed in Appendix 4.C for reference.

Fig. 4.2 shows the configuration in which the polarization is perpendicular to the initial velocity. In this case the polarization-dependent terms of Eq. (4.21) vanish, and Eq. (4.21) reduces to the classical expression, Eq. (4.1). Indeed, for all three initial velocities the three descriptions yield identical trajectories to within the width of the lines, showing that the classical expression gives an excellent description of the averaged motion of the electron. The usual behavior can be seen in which the electron is deflected towards low-intensity regions.

In Fig. 4.3, however, the situation is very different. Here, the polarization is parallel to the initial velocity, so that the polarization-dependent terms of Eq. (4.21) become important. Because of this, in Fig. 4.3(a) the magnitude of the ponderomotive force is smaller than in the corresponding case of Fig. 4.2 ($\beta_0 = 0.5$), the ponderomotive force vanishes in Fig. 4.3(b), and it even changes direction towards the high-intensity region in Fig. 4.3(c). In all of these cases, the resulting trajectories are excellently predicted by Eq. (4.21). Fig. 4.3 demonstrates the relativistic reversal described in Ref. [196] and Section 4.3.1. Meanwhile, Eq. (4.1) is insensitive to the polarization direction, so that the trajectories (dashed lines) are incorrectly predicted to be identical to the corresponding cases in Fig. 4.2. The insets of Fig. 4.3 are close-ups of the solid lines, showing that these actually consist of the smooth, time-averaged trajectory predicted by Eq. (4.21) (dash-dotted line), and the GPT trajectory. The latter contains also the quiver motion, which has components in the x -direction (Eq. (4.15)) and the z -direction (Eq. (4.20)) and is therefore visible in the plane of drawing of Fig. 4.3. The frequency of this quiver motion is ω while the electron moves forward with a velocity $\beta_x \approx \beta_{0x}$, so that the spatial period of the quiver motion is $1/(\beta_{0x}\lambda)$. This has been made visible by scaling the x -axes of the insets. In Fig. 4.2, the quiver motion would not be visible in a close-up because it is perpendicular to the plane of drawing, since $\overline{\mathbf{A}}_{\perp} \cdot \mathbf{p}_{0\perp} = 0$ in Eq. (4.20) and the z -component of the quiver motion vanishes.

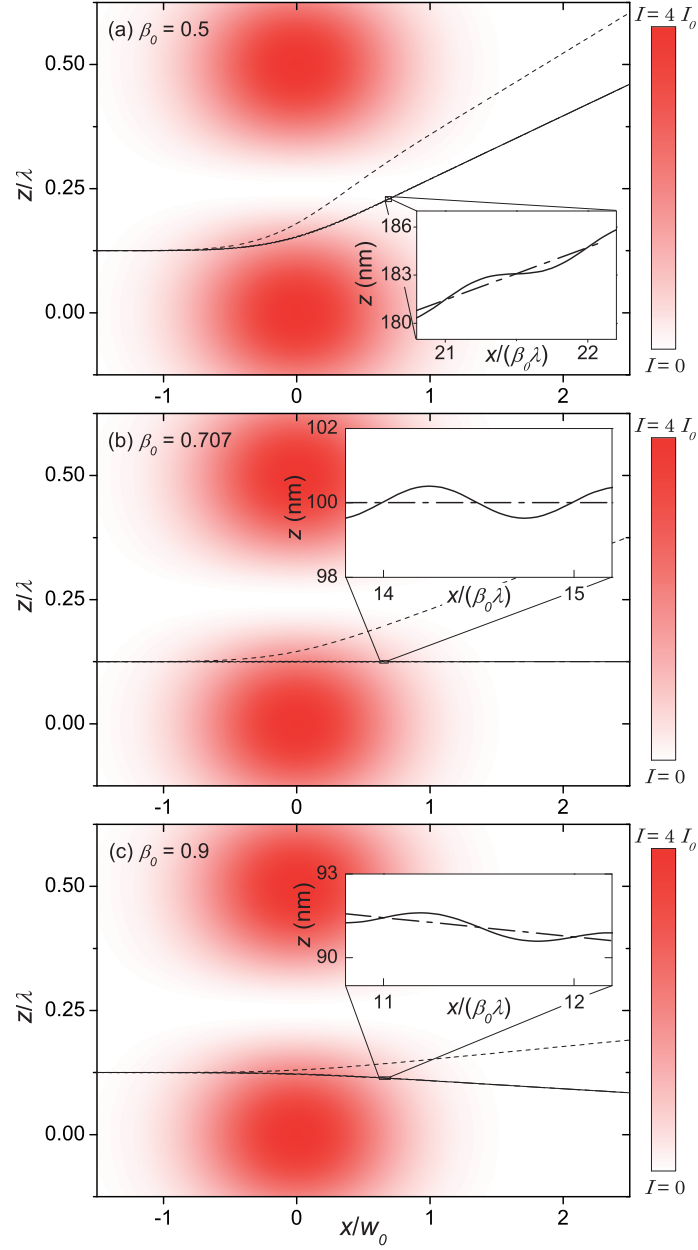


Figure 4.3: Trajectory of an electron incident on a standing wave that is polarized in the x -direction (left-right), for an initial velocity β_0 equal to (a) 0.5; (b) $0.707 \approx 1/\sqrt{2}$; (c) 0.9. The color map shows the field intensity of the standing wave in the (z, x) -plane at time $t = 0$. In each plot, the trajectory has been calculated with the methods GPT (solid line), OLD (dashed line) and NEW (dash-dotted line).

In order to show some ponderomotive effects in the perpendicular direction as well, in Fig. 4.4 a sideview is given of the trajectories of Fig. 4.3(a), as seen from the positive z -axis. Note from the vertical scale that in this direction the deflection of the electron is very small due to the very small field gradient. Nevertheless, again it is clear from the figure that Eq. (4.21) accurately predicts the electron trajectory, contrary to the classical expression. Thus Eq. (4.21) gives a precise description of the three-dimensional electron trajectory in a realistic, non-idealized field configuration. We have also repeated the simulations for combinations of ϵ and a other than $a \sim \epsilon$. Whenever both ϵ and a are less than about 0.1, consistent with the assumptions $a, \epsilon \ll 1$ made in Section 4.2, we find the same level of agreement with the GPT results.

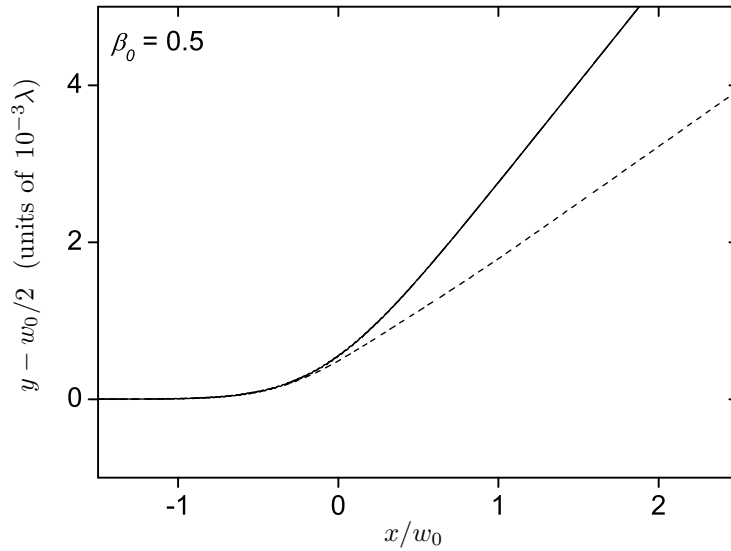


Figure 4.4: Sideview from the positive z -axis of the trajectories shown in Fig. 4.3(a). The trajectories has been calculated with the methods GPT (solid line), OLD (dashed line) and NEW (overlapping with GPT).

4.5 Conclusion

The classical polarization-independent ponderomotive force is commonly used to describe the time-averaged motion of charged particles in an inhomogeneous oscillating EM field. It is generally assumed that this is an accurate description, at least for nonrelativistic intensities. However, we have shown that this is not always true. If the field configuration possesses a direction in which the field changes on the scale of the wavelength, i.e. in a standing wave, and in addition the charged particle is relativistic, the ponderomotive force is modified. In particular, it becomes dependent on

the polarization of the field. Because of this, the ponderomotive force may even vanish, or change direction toward high field regions, as was found earlier [195]. We have derived the modified ponderomotive force expression for these configurations, which is of gradient form like the classical expression. Comparison with simulations in the case of a realistic, non-idealized, three-dimensional field configuration confirmed the general validity of the analytical results.

The modifications of the ponderomotive force derived here may have important implications for applications that involve the ponderomotive interaction of relativistic charged particles and standing EM waves. For example, in the electron bunch length measurement based on ponderomotive scattering of the electrons by a standing wave [177], the polarization of the wave is essential for an optimal design of the experimental setup. In the proposed X-ray free electron laser relying on the wiggling motion of electrons induced by the ponderomotive force in a standing wave [179], the frequency of wiggling and hence that of the stimulated radiation directly depend on the polarization. Experimental tests involving the controlled scattering of electrons by a standing wave have confirmed the classical ponderomotive force expression [186] and Kapitza-Dirac diffraction [187] using nonrelativistic electrons. It would be very interesting to extend these experiments to relativistic electrons to test the polarization-dependent ponderomotive force, Eq. (4.21), in the classical limit, and to study the polarization-dependence of Kapitza-Dirac diffraction.

Appendix 4.A Order equations

Substitution of the expansions (4.7)-(4.10) in the equations of motion (4.5)-(4.6), and collecting terms of equal order in ϵ , results in the following order equations. The components of the vector potential and the spatial derivatives have been treated as $e\mathbf{A}_\perp/(mc) = O_s(\epsilon)$, $eA_z/(mc) = O_s(\epsilon^2)$, $\lambda\nabla_\perp = O_s(\epsilon)$ and $\lambda\partial/\partial z = O_s(1)$ consistent with Eq. (4.2) and the assumption $a \sim \epsilon$. For reasons of clarity, the equations are displayed in dimensional form.

$O_s(1)$:

$$\frac{d\tilde{\mathbf{p}}^{(0)}}{dt} = \mathbf{0}; \quad (4.27)$$

$$\frac{d(\bar{\mathbf{x}} + \tilde{\mathbf{x}})^{(0)}}{dt} = \frac{(\bar{\mathbf{p}} + \tilde{\mathbf{p}})_\perp^{(0)}}{m\gamma^{(0)}}. \quad (4.28)$$

$O_s(\epsilon)$:

$$\frac{d\tilde{\mathbf{p}}_{\perp}^{(1)}}{dt} + e\frac{d\mathbf{A}_{\perp}}{dt} = \mathbf{0}; \quad (4.29)$$

$$\frac{d\left(\tilde{p}_z^{(0)} + \tilde{p}_z^{(1)}\right)}{dt} = \frac{e}{m\gamma^{(0)}} \frac{\partial \bar{\mathbf{A}}_{\perp}}{\partial z} \cdot (\bar{\mathbf{p}} + \tilde{\mathbf{p}})_{\perp}^{(0)}; \quad (4.30)$$

$$\frac{d(\bar{\mathbf{x}} + \tilde{\mathbf{x}})^{(1)}}{dt} = \frac{(\bar{\mathbf{p}} + \tilde{\mathbf{p}})^{(1)}}{m\gamma^{(0)}} - \frac{(\bar{\mathbf{p}} + \tilde{\mathbf{p}})^{(0)} \cdot (\bar{\mathbf{p}} + \tilde{\mathbf{p}})^{(1)}}{(mc\gamma^{(0)})^2} \frac{(\bar{\mathbf{p}} + \tilde{\mathbf{p}})^{(0)}}{m\gamma^{(0)}}. \quad (4.31)$$

$O_s(\epsilon^2)$:

$$\frac{d\left(\tilde{\mathbf{p}}_{\perp}^{(0)} + \tilde{\mathbf{p}}_{\perp}^{(2)}\right)}{dt} = \frac{e}{m\gamma^{(0)}} (\nabla_{\perp} \bar{\mathbf{A}}_{\perp}) \cdot (\bar{\mathbf{p}} + \tilde{\mathbf{p}})_{\perp}^{(0)}; \quad (4.32)$$

$$\begin{aligned} \frac{d\left(\tilde{p}_z^{(1)} + \tilde{p}_z^{(2)}\right)}{dt} + e\frac{dA_z}{dt} &= \frac{e}{m\gamma^{(0)}} \left[\tilde{z}^{(1)} \frac{\partial^2 \bar{\mathbf{A}}_{\perp}}{\partial z^2} \cdot (\bar{\mathbf{p}} + \tilde{\mathbf{p}})_{\perp}^{(0)} + \frac{\partial \bar{\mathbf{A}}_{\perp}}{\partial z} \cdot (\bar{\mathbf{p}} + \tilde{\mathbf{p}})_{\perp}^{(1)} \right. \\ &\quad \left. + \frac{\partial \bar{A}_z}{\partial z} (\bar{\mathbf{p}} + \tilde{\mathbf{p}})_z^{(0)} - \frac{(\bar{\mathbf{p}} + \tilde{\mathbf{p}})^{(0)} \cdot (\bar{\mathbf{p}} + \tilde{\mathbf{p}})^{(1)}}{(mc\gamma^{(0)})^2} \frac{\partial \bar{\mathbf{A}}_{\perp}}{\partial z} \cdot (\bar{\mathbf{p}} + \tilde{\mathbf{p}})_{\perp}^{(0)} \right]. \end{aligned} \quad (4.33)$$

$O_s(\epsilon^3)$:

$$\begin{aligned} \frac{d\left(\tilde{\mathbf{p}}_{\perp}^{(1)} + \tilde{\mathbf{p}}_{\perp}^{(3)}\right)}{dt} &= \frac{e}{m\gamma^{(0)}} \left[\tilde{z}^{(1)} \left(\nabla_{\perp} \frac{\partial \bar{\mathbf{A}}_{\perp}}{\partial z} \right) \cdot (\bar{\mathbf{p}} + \tilde{\mathbf{p}})_{\perp}^{(0)} + (\nabla_{\perp} \bar{\mathbf{A}}_{\perp}) \cdot (\bar{\mathbf{p}} + \tilde{\mathbf{p}})_{\perp}^{(1)} \right. \\ &\quad \left. + (\nabla_{\perp} \bar{A}_z) (\bar{\mathbf{p}} + \tilde{\mathbf{p}})_z^{(0)} - \frac{(\bar{\mathbf{p}} + \tilde{\mathbf{p}})^{(0)} \cdot (\bar{\mathbf{p}} + \tilde{\mathbf{p}})^{(1)}}{(mc\gamma^{(0)})^2} (\nabla_{\perp} \bar{\mathbf{A}}_{\perp}) \cdot (\bar{\mathbf{p}} + \tilde{\mathbf{p}})_{\perp}^{(0)} \right]. \end{aligned} \quad (4.34)$$

Appendix 4.B General field strength

The ponderomotive force, Eq. (4.21), has been derived under the assumption that $a \sim \epsilon$. Since this expression is the result of balancing terms of equal order in the equations of motion, one might expect that it would be affected by changing the order of magnitude of the vector potential to, for instance, $a \sim \epsilon^2$. This is not the case, however. We only give a sketch of the generalized derivation for arbitrary $a \ll 1$.

Repeating first the order expansion method for the case $a \sim \epsilon^n$, $n \geq 1$, it is not difficult to find the lowest order slowly varying term and the lowest order rapidly varying term of the expansions of \mathbf{p} and $1/\gamma$. Also, the first two terms of the expansion of \mathbf{A} follow straightforwardly. The right-hand side of the equation of motion (4.5) is then formed by factoring out the product of these three expansions. Taking the time average of the result, it is found that the lowest order terms that are nonzero on average are precisely those that form the ponderomotive force given by Eq. (4.21).

In terms of the corresponding set of order equations analogues to those in Appendix 4.A, the first $2n - 1$ orders of the momentum equations yield zero right-hand sides upon averaging, while the $2n$ -th and $(2n + 1)$ -th orders evaluate to respectively the z -component and perpendicular component of Eq. (4.21).

Also the opposite situation in which $1 \gg a \sim \epsilon^{1/n}$, $n \geq 1$, is possible. Since in this case factors of \mathbf{A} in the equations of motion lead to terms of fractional order in ϵ , it is appropriate to expand all quantities in power series in terms of $\epsilon^{1/n}$ rather than ϵ . This is effected by using the same power series expansions as before, with the understanding that $\mathbf{p}^{(i)} = O_s(\epsilon^{i/n})$ rather than $\mathbf{p}^{(i)} = O_s(\epsilon^i)$, for example. Except for this modification, the derivation of the ponderomotive force is analogous to that for the case $a \sim \epsilon^n$ considered above, and again Eq. (4.21) is found. Thus Eq. (4.21) is valid for arbitrary $a \ll 1$.

Appendix 4.C Fields used in numerical calculations

The solid lines in Figs. 4.2-4.4 have been calculated by numerical integration of the equations of motion

$$\frac{d\mathbf{p}}{dt} = e \left(\mathbf{E} + \frac{1}{\gamma} \mathbf{p} \times \mathbf{B} \right); \quad (4.35)$$

$$\frac{d\mathbf{x}}{dt} = \frac{\mathbf{p}}{m\gamma}, \quad (4.36)$$

using for \mathbf{E} and \mathbf{B} the following paraxial Gaussian beam fields [176]. For polarization in the x -direction ($\phi = 0$),

$$\mathbf{E} = \mathbf{E}_+ \exp\left(-\frac{(z+ct)^2}{4(c\sigma)^2}\right) + \mathbf{E}_- \exp\left(-\frac{(z-ct)^2}{4(c\sigma)^2}\right); \quad (4.37)$$

$$\mathbf{B} = \mathbf{B}_+ \exp\left(-\frac{(z+ct)^2}{4(c\sigma)^2}\right) + \mathbf{B}_- \exp\left(-\frac{(z-ct)^2}{4(c\sigma)^2}\right); \quad (4.38)$$

$$\mathbf{E}_\pm = E_0 \frac{w_0}{w} \left(\mathbf{e}_x \cos \psi_\pm \pm \frac{xw_0}{z_R w} \mathbf{e}_z \sin \chi_\pm \right); \quad (4.39)$$

$$\mathbf{B}_\pm = \frac{E_0 w_0}{c w} \left(\mp \mathbf{e}_y \cos \psi_\pm - \frac{yw_0}{z_R w} \mathbf{e}_z \sin \chi_\pm \right), \quad (4.40)$$

in which $E_0 = \sqrt{2I_0/(\epsilon_0 c)}$ is the peak electric field amplitude, $w = w_0 \sqrt{1 + z^2/z_R^2}$ is the beam waist, $z_R = kw_0^2/2$ is the Rayleigh length, and the Gouy phases are

$$\psi_{\pm} = \omega t \pm \left(kz - \arctan \frac{z}{z_R} + \frac{z}{z_R} \frac{x^2 + y^2}{w^2} \right); \quad (4.41)$$

$$\chi_{\pm} = \omega t \pm \left(kz - 2 \arctan \frac{z}{z_R} + \frac{z}{z_R} \frac{x^2 + y^2}{w^2} \right). \quad (4.42)$$

The dashed lines in Figs. 4.2-4.4 have been calculated according to Eq. (4.1) with $I(\mathbf{x}, t) = \epsilon_0 c \langle \overline{E_x^2} \rangle$ using Eq. (4.37) for $\overline{E_x}$. The dash-dotted lines have been calculated according to Eq. (4.21) with $\overline{\mathbf{A}}_{\perp}$ replaced by $\overline{E_x}/\omega$. For polarization in the y -direction ($\phi = \pi/2$), replace $x \rightarrow y$ and $y \rightarrow -x$ in the expressions above.

Bibliography

- [157] H. A. H. Boot and R. B. R. S. Harvie, "Charged particles in a non-uniform radio-frequency field," *Nature (London)* **180**, 1187 (1957).
- [158] A. V. Gaponov and M. A. Miller, "Potential wells for charged particles in a high-frequency electromagnetic field," *Sov. Phys. JETP* **7**, 168–169 (1958).
- [159] T. Tajima and J. M. Dawson, "Laser electron accelerator," *Phys. Rev. Lett.* **43**, 267–270 (1979).
- [160] S. P. D. Mangles, C. D. Murphy, Z. Najmudin, A. G. R. Thomas, J. L. Collier, A. E. Dangor, E. J. Divall, P. S. Foster, J. G. Gallacher, C. J. Hooker, D. A. Jaroszynski, A. J. Langley, W. B. Mori, P. A. Norreys, F. S. Tsung, R. Viskup, B. R. Walton, and K. Krushelnick, "Monoenergetic beams of relativistic electrons from intense laser-plasma interactions," *Nature (London)* **431**, 535–538 (2004).
- [161] C. G. R. Geddes, Cs. Toth, J. van Tilborg, E. Esarey, C. B. Schroeder, D. Bruhwiler, C. Nieter, J. Cary, and W. P. Leemans, "High-quality electron beams from a laser wakefield accelerator using plasma-channel guiding," *Nature (London)* **431**, 538–541 (2004).
- [162] J. Faure, Y. Glinec, A. Pukhov, S. Kiselev, S. Gordienko, E. Lefebvre, J.-P. Rousseau, F. Burgy, and V. Malka, "A laser-plasma accelerator producing monoenergetic electron beams," *Nature (London)* **431**, 541–544 (2004).
- [163] J. Denavit, "Absorbition of high-intensity subpicosecond lasers on solid density targets," *Phys. Rev. Lett.* **69**, 3052–3055 (1992).
- [164] J. Badziak, S. Glowacz, S. Jablonski, P. Parys, J. Wolowski, and H. Hora, "Laser-driven generation of high-current ion beams using skin-layer ponderomotive acceleration," *Laser and Particle Beams* **23**, 401–409 (2005).
- [165] E. Esarey, P. Sprangle, and J. Krall, "Laser acceleration of electrons in vacuum," *Phys. Rev. E* **52**, 5443–5453 (1995).

-
- [166] J. L. Chaloupka and D. D. Meyerhofer, "Observation of electron trapping in an intense laser beam," *Phys. Rev. Lett.* **83**, 4538–4541 (1999).
- [167] W. Paul, "Electromagnetic traps for charged and neutral particles," *Rev. Mod. Phys.* **62**, 531–540 (1990).
- [168] B. J. Siwick, A. A. Green, C. T. Hebeisen, and R. J. D. Miller, "Characterization of ultrashort electron pulses by electron-laser pulse cross correlation," *Opt. Lett.* **30**, 1057–1059 (2005).
- [169] C. T. Hebeisen, R. Ernstorfer, M. Harb, T. Dartigalongue, R. E. Jordan, and R. J. D. Miller, "Femtosecond electron pulse characterization using laser ponderomotive scattering," *Opt. Lett.* **31**, 3517–3519 (2006).
- [170] D. Bauer, P. Mulser, and W.H. Steeb, "Relativistic ponderomotive force, uphill acceleration, and transition to chaos," *Phys. Rev. Lett.* **75**, 4622–4625 (1995).
- [171] D. R. Bituk and M. V. Fedorov, "Relativistic ponderomotive forces," *J. Exp. Theor. Phys.* **89**, 640–646 (1999).
- [172] E. A. Startsev and C. J. McKinstrie, "Multiple scale derivation of the relativistic ponderomotive force," *Phys. Rev. E* **55**, 7527–7535 (1997).
- [173] I. Y. Dodin and N. J. Fisch, "Relativistic electron acceleration in focused laser fields after above-threshold ionization," *Phys. Rev. E* **68**, 056402 (2003).
- [174] S. P. Goreslavskii, N. B. Narozhny, O. V. Shcherbachev, and V. P. Yakovlev, "The dynamics and radiation of a relativistic electron in the field of an intense, focused laser pulse," *Laser Phys.* **3**, 418–430 (1993).
- [175] T. W. B. Kibble, "Mutual refraction of electrons and photons," *Phys. Rev.* **150**, 1060–1069 (1966).
- [176] B. Quesnel and P. Mora, "Theory and simulation of the interaction of ultraintense laser pulses with electron in vacuum," *Phys. Rev. E* **58**, 3719–3732 (1998).
- [177] C. T. Hebeisen, G. Sciaini, M. Harb, R. Ernstorfer, T. Dartilongue, S. G. Kruglik, and R. J. D. Miller, "Grating enhanced ponderomotive scattering for visualization and full characterization of femtosecond electron pulses," *Opt. Express* **16**, 3334–3341 (2008).
- [178] M. V. Fedorov, K. B. Oganesyan, and A. M. Prokhorov, "Free-electron laser based on the effect of channeling in an intense standing light-wave," *Appl. Phys. Lett.* **53**, 353–354 (1988).
- [179] P. Balcou, "Proposal for a Raman X-ray free electron laser," *Eur. Phys. J. D* **59**, 525–537 (2010).

- [180] J. Faure, C. Rechatin, A. Norlin, A. Lifschitz, Y. Glinec, and V. Malka, “Controlled injection and acceleration of electrons in plasma wakefields by colliding laser pulses,” *Nature (London)* **444**, 737–739 (2006).
- [181] E. Esarey, R. F. Hubbard, W. P. Leemans, A. Ting, and P. Sprangle, “Electron injection into plasma wake fields by colliding laser pulses,” *Phys. Rev. Lett.* **79**, 2682–2685 (1997).
- [182] H. Kotaki, S. Masuda, M. Kando, J. K. Koga, and K. Nakajima, “Head-on injection of a high quality electron beam by the interaction of two laser pulses,” *Phys. Plasmas* **11**, 3296–3302 (2004).
- [183] G. Fubiani, E. Esarey, C. B. Schroeder, and W. P. Leemans, “Beat wave injection into plasma waves using two interfering laser pulses,” *Phys. Rev. E* **70**, 016402 (2004).
- [184] P. Baum and A. H. Zewail, “Attosecond electron pulses for 4d diffraction and microscopy,” *Proc. Nat. Acad. Sci. USA* **104**, 18409–18414 (2007).
- [185] P. L. Kapitza and P. A. M. Dirac, “The reflection of electrons from standing light waves,” *Proc. Cambridge Philos. Soc.* **29**, 297–300 (1933).
- [186] P. H. Bucksbaum, D. W. Schumacher, and M. Bashkansky, “High-intensity Kapitza-Dirac effect,” *Phys. Rev. Lett.* **61**, 1182–1185 (1988).
- [187] D. L. Freimund, K. Aflatooni, and H. Batelaan, “Observation of the Kapitza-Dirac effect,” *Nature (London)* **413**, 142–143 (2001).
- [188] M. V. Fedorov, “Stimulated scattering of electrons by photons and adiabatic switching on hypothesis,” *Opt. Commun.* **12**, 205–209 (1974).
- [189] H. Batelaan, “Colloquium: Illuminating the Kapitza-Dirac effect with electron matter optics,” *Rev. Mod. Phys.* **79**, 929–941 (2007).
- [190] X. F. Li, J. T. Zhang, Z. Z. Xu, P. M. Fu, D. S. Guo, and R. R. Freeman, “Theory of the Kapitza-Dirac diffraction effect,” *Phys. Rev. Lett.* **92**, 233603 (2004).
- [191] A. Bahari and V. D. Taranukhin, “Ponderomotive forces in a bipolarized standing wave,” *Laser Phys.* **14**, 113–118 (2004).
- [192] S. C. Hartman and J. B. Rosenzweig, “Ponderomotive focusing in axisymmetrical rf linacs,” *Phys. Rev. E* **47**, 2031–2037 (1993).
- [193] W. Allan, “Plasma energization by the ponderomotive force of magnetospheric standing Alfvén waves,” *J. Geophys. Res. Space Phys.* **98**, 11383–11390 (1993).

- [194] I. Y. Dodin and N. J. Fisch, “Nonadiabatic tunneling in ponderomotive barriers,” *Phys. Rev. E* **74**, 056404 (2006).
- [195] A. E. Kaplan and A. L. Pokrovsky, “Fully relativistic theory of the ponderomotive force in an ultraintense standing wave,” *Phys. Rev. Lett.* **95**, 053601 (2005).
- [196] A. L. Pokrovsky and A. E. Kaplan, “Relativistic reversal of the ponderomotive force in a standing laser wave,” *Phys. Rev. A* **72**, 043401 (2005).
- [197] D. J. Griffiths, *Introduction to electrodynamics* (Prentice Hall, Upper Saddle River, 1989) 2nd ed., p. 320.
- [198] P. M. Morse and H. Feshbach, *Methods of theoretical physics* (McGraw-Hill, New York, 1953) vol. 1, p. 65.
- [199] A. H. Nayfeh, *Perturbation methods* (Wiley, New York, 1973).
- [200] P. Mulser, “Resonance absorption and ponderomotive action,” in *Handbook of plasma physics*, Vol. 3, edited by M. N. Rosenbluth, R. Z. Sagdeev, A. Rubenchik, and S. Witkowski (North-Holland, Amsterdam, 1991) p. 456.
- [201] M. J. de Loos and S. B. van der Geer, “General Particle Tracer: a new 3D code for accelerator and beam line design,” in *Proc. EPAC’96, Sitges, 1996*, Vol. 2, edited by S. Myers, A. Pacheco, R. Pascual, Ch. Petit-Jean-Genaz, and J. Poole (Institute of Physics, Bristol, 1996) pp. 1241–1243, <http://www.pulsar.nl/gpt>.

5

Heating mechanisms in radio frequency driven ultracold plasmas

Abstract - Several mechanisms by which an external electromagnetic field influences the temperature of a plasma are studied analytically and specialized to the system of an ultracold plasma (UCP) driven by a uniform radio frequency (RF) field. Heating through collisional absorption is reviewed and applied to UCPs. Furthermore, it is shown that the RF field modifies the three body recombination process by ionizing electrons from intermediate high-lying Rydberg states and upshifting the continuum threshold, resulting in a suppression of three body recombination. Heating through collisionless absorption associated with the finite plasma size is calculated in detail, revealing a temperature threshold below which collisionless absorption is ineffective.

Publication status - The work described in this chapter has been published by P. W. Smorenburg, L. P. J. Kamp, and O. J. Luiten in Phys. Rev. A **85**, 063413 (2012).

5.1 Introduction

Conventional plasmas are formed when atoms are ionized by strong electric fields or collisions with other particles. Due to the large excess energy inherent in such ionization processes, the resulting electron temperature is typically comparable to the ionization potential, which is on the order of an electronvolt, equivalent to some 10^4 K. In marked contrast, ultracold neutral plasmas (UCPs), created by photo-ionization of a cloud of laser-cooled atoms [202], have an electron temperature close to 1 K. UCPs typically consist of some 10^8 singly-ionized atoms localized in a millimeter-sized cloud of Gaussian density profile, with a correspondingly low particle density [203]. The combination of low temperature and low density makes UCPs unique plasma systems. They can be close to the strongly-coupled regime where the Coulomb interaction energy between the particles exceeds the thermal energy, as is quantified by the coupling parameter

$$\Gamma = \frac{e^2}{4\pi\epsilon_0 r_w k_B T} \quad (5.1)$$

exceeding unity, where e is the electron charge, ϵ_0 the vacuum permittivity, k_B Boltzmann's constant, T the plasma temperature, and $r_w = [3/(4\pi n)]^{1/3}$ the Wigner-Seitz radius with n the number density. Due to their high coupling parameter, UCPs behave in many respects similar to strongly-coupled plasmas near solid state density, such as laser-ionized atomic clusters [204] or thin films [205], inertial confinement fusion targets [206] and astrophysical plasmas [207]. The dynamics of solid state density plasmas, however, takes place at the time scale of the inverse plasma frequency, which lies in the attosecond to femtosecond regime. This seriously complicates diagnostics. In contrast, UCPs evolve on the time scale of picoseconds to microseconds. This enables excellent time-resolved diagnostic techniques, including charged particle detection [208], absorption imaging [209] and fluorescence monitoring [210]. In addition, the careful preparation and ionization of atomic clouds allows accurate control over the initial temperature, density profile, and ionization state. UCPs may therefore serve as versatile and experimentally accessible model systems for high-density plasmas that are difficult to diagnose.

An important class of experiments on solid state density plasmas involves plasmas created by laser irradiation of atomic clusters in a gas jet. Characteristic of these experiments is that the laser pulse length is comparable to the lifetime of the plasma. Therefore the studied system typically consists of a cluster plasma that is not only near to strongly-coupled, but is also strongly driven by a radiation field. This leads to complicated dynamics that is difficult to unravel [204]. Research on laser-cluster interaction would therefore benefit from UCP experiments in which this interaction is mimicked. Since atomic clusters are typically smaller than the laser wavelength, the

appropriate model system is an UCP driven by a strong radio-frequency (RF) field. Interpretation of observations in such experiments on RF driven UCPs, however, requires a detailed understanding of the mechanisms by which the RF field and the UCP interact. In this chapter, we consider how the RF field influences the plasma temperature, both directly through RF energy absorption mechanisms and indirectly through modification of the three body recombination process, the latter being a main heat source in UCPs.

In current UCP experiments, RF fields are used in a diagnostic way to probe plasma modes. Plasma resonance can be detected as an increased yield of electrons leaving the UCP [211]. Combined with knowledge of the mode properties [212], this can be used to determine the plasma density and expansion as a function of time. Using the same technique, the presence of acoustic or Tonks-Dattner modes in an UCP has been observed in addition to the fundamental mode [213]. In these experiments, the collective response of the plasma electrons to the RF field has been studied in quite some detail. However, the RF amplitude is kept low to avoid disturbances other than plasma resonances, and little attention is paid to other interaction mechanisms. Nevertheless, as we will describe in this chapter, the RF field influences the plasma also via incoherent processes. In their Tonks-Dattner modes experiment, Fletcher et al. [213] indeed observe the onset of field-induced effects at large probing amplitudes. Although lower RF amplitudes justify the use of standard plasma quantities, such as the Spitzer collision frequency applied in the interpretation of the fundamental plasma resonance measurements [212], or the Debye length mentioned in support of the analysis of the Tonks-Dattner modes [213], one should be aware of the possible high-amplitude modifications of such quantities induced by the RF field. Finally, the expansion of an UCP is driven by the thermal pressure of the electrons. It is therefore important to understand the various ways in which the RF field contributes to the heat budget of the plasma.

In this chapter, we take the electric field strength E_0 in the plasma as a given quantity, and consider what influence this field has on several microscopic processes. For underdense plasmas, E_0 is approximately equal to the externally applied RF field. For denser plasmas, E_0 may be significantly enhanced by the polarization field generated by the plasma itself. This is particularly relevant under conditions of resonance with plasma modes, in which case the absorption of RF energy by the UCP is dominated by the strong dependence of E_0 on the driving frequency [214]. The determination of the frequency response of the UCP, and hence the polarization fields, is actively being studied [212–215], but is outside the scope of this thesis. Nevertheless, our results may be directly applied once E_0 is known.

This chapter is organized as follows. We consider two mechanisms by which the UCP can directly absorb energy from the RF field: collisional absorption and collisionless absorption due to the finite size of the plasma. The first of these has been studied extensively already in other contexts [216–226]. In Section 5.2, we therefore only cite the main results from literature and discuss their relevance for RF driven UCPs. In Section 5.3, we study the process of three body recombination in the presence of an RF field, and show that the recombination rate can be strongly suppressed by the field. Next, in Section 5.4, we consider the collisionless absorption mechanism mentioned above, which has been mainly studied in the context of solid-state density plasmas [227–234]. We show that the approximations usually adopted are not appropriate for UCPs. We provide an improved description by specializing a derivation of the collisionless absorption rate due to Zaretsky et al. [231] to the case of UCPs. We conclude and summarize in Section 5.5.

5.2 Collisional absorption

5.2.1 Collision frequency

At low to moderate RF field strengths, the energy absorption of a plasma is dominated by collisional absorption, or inverse Bremsstrahlung [235]. The physical cause of the absorption is that individual electrons, oscillating due to the RF field, deflect in the Coulomb fields of the approximately stationary ions, resulting in a net energy gain. The average effect of the Coulomb fields can be described phenomenologically as an effective frictional force $\mathbf{F} = -m\nu_{ei}\mathbf{v}$ in the equation of motion of the electron, and the energy absorption rate per electron by the power $P_{ei} = -\langle \mathbf{F} \cdot \mathbf{v} \rangle$. Here, m is the electron mass, ν_{ei} is the effective electron-ion collision frequency, and \mathbf{v} is the electron velocity. Expressing the velocity in terms of the driving electric field gives [216]

$$P_{ei} = 2\nu_{ei}U_p, \quad (5.2)$$

where $U_p = (eE_0)^2/(4m\omega^2)$ is the quiver energy, or ponderomotive potential, in the RF field with amplitude E_0 and frequency ω . Here and in the remainder, we assume a linearly polarized RF field, and absorb any field enhancement due to plasma resonance in the magnitude E_0 . Importantly, Eq. (5.2) defines the collision frequency as merely a scaled absorption rate, rather than predicting the absorption from a predetermined collision frequency. Consequently, ν_{ei} is not necessarily equal to the Spitzer collision frequency [236]

$$\nu_S = \sqrt{\frac{2}{3\pi}}\omega_p\Gamma^{3/2}\ln\Lambda, \quad (5.3)$$

which is commonly used for plasmas without RF fields. Nevertheless, the collision frequency Eq. (5.3) is sometimes used for driven plasmas as well, and also in the

context of RF absorption by UCPs [212, 237]. In Eq. (5.3), singly ionized atoms are assumed, ω_p is the plasma frequency, and $\ln \Lambda$ is the Coulomb logarithm that will be discussed below.

Underlying any calculation of the collisional absorption rate is some model for the scattering of an electron by the Coulomb field of an ion, which generally depends on the electron velocity. Because two velocity scales are involved, namely the thermal velocity $v_{\text{th}} = \sqrt{k_B T_e / m}$ and the quiver velocity magnitude $v_{\text{osc}} = eE_0 / (m\omega)$, the collision frequency depends on the ratio $v_{\text{osc}} / v_{\text{th}}$. Here, T_e is the electron temperature of the plasma. The effective collision frequency has been calculated first by classical kinetic theory using the Landau collision integral [216, 217]. The result can be written as [222]

$$\nu_{\text{ei}} = \nu_S \cdot {}_2F_2\left(\frac{3}{2}, \frac{3}{2}; 2, \frac{5}{2}; -\frac{v_{\text{osc}}^2}{2v_{\text{th}}^2}\right), \quad (5.4)$$

where ${}_2F_2$ denotes the generalized hypergeometric function [238] that has the limiting forms

$${}_2F_2(\dots) \approx \begin{cases} 1 & v_{\text{osc}} \ll v_{\text{th}} \\ 6\sqrt{\frac{2}{\pi}} \left(\frac{v_{\text{th}}}{v_{\text{osc}}}\right)^3 \left[\ln\left(\frac{v_{\text{osc}}}{2v_{\text{th}}}\right) + 1.0\right] & v_{\text{osc}} \gg v_{\text{th}}. \end{cases} \quad (5.5)$$

More advanced and alternative calculations largely confirm these results [218–223].

The collision frequency of Eq. (5.4) is plotted in Fig. 5.1 as a function of the velocity ratio. In RF experiments with UCPs, this ratio can vary over the full range $v_{\text{osc}} \ll v_{\text{th}}$ to $v_{\text{osc}} \gg v_{\text{th}}$ [211]. The decrease of the collision frequency for increasing v_{osc} can be understood from the well-known fact that the Rutherford scattering cross section for an electron by an ion is inversely proportional to the fourth power of the relative velocity, so that driving the plasma stronger makes the electrons less susceptible to deflections and hence to energy gain. Note that the Spitzer frequency Eq. (5.3) with Eq. (5.1) substituted is proportional to v_{th}^{-3} , while the second line of Eq. (5.5) contains the factor $(v_{\text{th}}/v_{\text{osc}})^3$. Effectively, therefore, and apart from a logarithmic factor, the content of Eq. (5.4) is that the thermal velocity is replaced by the quiver velocity in the collision frequency when $v_{\text{osc}} \gg v_{\text{th}}$. In fact, this effect is such that the collision absorption rate P_{ei} given by Eq. (5.2) decreases with field strength as E_0^{-1} rather than increases, which is a well-known phenomenon in laser-plasma physics [235]. This behavior is not only relevant when large RF field strengths are applied, but also when UCPs are driven resonantly. This is because the electric field is strongly enhanced at densities for which the plasma frequency equals the RF frequency. In particular, the amplitude of the electron oscillations is then limited by the dominant damping mechanism, which in view of Fig. 5.1 may no longer be

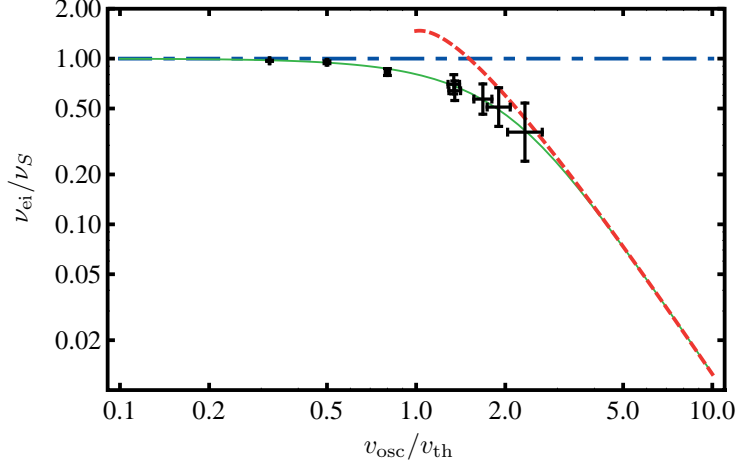


Figure 5.1: Effective electron-ion collision frequency for collisional absorption scaled to the Spitzer collision frequency, as a function of the ratio of quiver velocity to thermal velocity. Solid green line: theoretical collision frequency Eq. (5.4); dash-dotted blue line: weak field limit $v_{\text{osc}} \ll v_{\text{th}}$ given by Eq. (5.5); dashed red line: strong field limit $v_{\text{osc}} \gg v_{\text{th}}$ given by Eq. (5.5); black error bars: collision frequency according to numerical simulations.

collisional absorption. For sufficiently small ν_{ei} , excitation of plasma waves can become important [239], although this is outside the scope of this thesis. In Section 5.4 another competing damping mechanism is presented.

We have performed numerical simulations in order to verify that the theoretical result Eq. (5.4) indeed continues to hold in the rather exotic case of UCPs. In the simulations, an UCP was modeled by 4000 electrons and 4000 singly-charged ions, randomly placed within a spherical region. Subsequently, the trajectories of all particles under the influence of both a homogeneous oscillating external electric field and the instantaneous interparticle Coulomb forces were calculated using the GPT particle tracking code [240]. This was done for various values of the external electric field amplitude E_0 ; more details can be found in Refs. [241]. For each run, the total (kinetic plus potential) energy U_{tot} present in the system was evaluated as a function of time. Apart from the collective oscillations associated with the forcing by the external field, which can be removed using Fourier techniques [241], U_{tot} increased monotonically in each case. This could be attributed to collisional absorption. By Eq. (5.2), the observed rate of increase in U_{tot} yields a numerical evaluation of the collision frequency equal to $\nu_{\text{ei}} = (2NU_p)^{-1}dU_{\text{tot}}/dt$, where N is the number of electrons participating in the heating process. These numerical results are shown in Fig. 5.1 in black. The quantities v_{th} and ν_S required for scaling were taken according to the temperature corresponding with U_{tot} . For N , the number of electrons present within a sphere concentric with the plasma and having twice the initial plasma radius was

taken, thereby discarding escaped electrons that could not have interacted with the plasma ions. The error bars in Fig. 5.1 represent the uncertainty in the temperature due to the variation in U_{tot} during the simulated time interval, which increases with E_0 and hence with v_{osc} . In the figure, the agreement between the numerical and theoretical results is excellent. This confirms that Eq. (5.4), which has been derived in the context of more conventional plasmas, continues to be valid in case of ultracold, finite-sized case of UCPs.

5.2.2 Coulomb logarithm

A second important consequence of the RF field is that the Coulomb logarithm $\ln \Lambda$ in Eq. (5.3) is modified. This is particularly relevant for UCPs because the traditional expression $\ln \Lambda = \ln(\Gamma^{-2/3})$ loses its validity in case of strong coupling $\Gamma \gtrsim 1$. The Coulomb logarithm arises from cutting off the Coulomb collision integral at both large and small impact parameters in elementary calculations of the scattering cross section of an electron by an ion [242]. However, the physical arguments used to choose these cut-offs are traditionally based on thermal electron velocities only, and the cut-offs will change when in addition the quiver velocity is taken into account. This can be confirmed by explicit calculation [220], yielding $\ln \Lambda \approx \ln(b_{max}/b_{min})$, with

$$b_{max} = \frac{v_{eff}}{\max(\omega, \omega_p)}; \quad (5.6)$$

$$b_{min} = \frac{e^2}{4\pi\epsilon_0 m v_{eff}^2}; \quad (5.7)$$

$$v_{eff} \equiv \sqrt{v_{th}^2 + v_{osc}^2}. \quad (5.8)$$

Here the classical limit $v_{eff} < e^2/(2\epsilon_0\hbar)$ has been assumed, where $2\pi\hbar$ is Planck's constant. Eqs. (5.6)-(5.8) show that also in the Coulomb logarithm, as before, the quiver velocity effectively takes over the role of the thermal velocity in the limit $v_{osc} \gg v_{th}$. This suggests more generally that kinetic processes in UCPs that depend on the electron temperature may be strongly modified by the presence of an RF field. In the next section, we further validate this notion by showing that the three body recombination rate in an UCP can be strongly suppressed by an RF field.

5.3 Three-body recombination

In the process of three body recombination (TBR), an electron recombines with an ion, while the excess potential energy is carried away by a second electron. In UCPs, TBR is the dominant recombination channel [203] due to the strong scaling of the TBR rate R with temperature, which is $R \propto T_e^{-9/2}$ according to conventional theory [243, 244]. However, the unphysical divergent behavior of the rate as $T_e \rightarrow 0$ indicates that this scaling must break down at sufficiently low temperatures. Modifi-

cations of the rate associated with the nonideality of strongly coupled plasmas have been demonstrated analytically [245–248] and with molecular dynamics simulations [249, 250]. Also quantum effects associated with the wave character of the electrons can play a role at sufficiently low temperatures, if the electronic De Broglie wavelength becomes noticeable on the spatial scale of the TBR process [251]. On the other hand, in current experiments UCPs remain mainly outside the strongly coupled regime [252], so that numerical models of the expansion dynamics of UCPs that are based on the conventional TBR rate are able to accurately describe experimental results [253]. We will show now that, in addition to any possible strong coupling effects, the presence of an RF field suppresses the TBR rate to a temperature scaling of $R \propto T_e^{-1}$, which is much milder than the conventional $R \propto T_e^{-9/2}$ dependency. We do not consider the mentioned quantum effects, which are presumably small since the quiver motion of the electrons ensures a small De Broglie wavelength.

We determine the TBR rate along the lines of an elementary analytical derivation by Hinnov and Hirschberg [243], adapted to the situation in which $v_{\text{osc}} \gg v_{\text{th}}$. The TBR rate found by Hinnov and Hirschberg has been confirmed by extensive Monte Carlo simulations [244] to within a factor of order unity, showing that their model captures the essential physics despite its simplicity. To exhibit the RF field effects clearly, we therefore choose to use this simple analytical model rather than performing a detailed numerical study, although the latter will be important to test the results derived here. Let us first briefly review the conventional case where the RF field is absent. Quantum mechanically, a TBR event may be described as an electron making a cascade of transitions between adjacent energy levels of an atom until it reaches the deeply bound states. Under conditions applicable to UCPs, these transitions are mainly effected by collisions with other, free electrons. The process is illustrated in the left panel of Fig. 5.2. Considering an electron at any particular energy level $U_i < 0$, there is both a finite probability that the next collision will result in an upward transition, and a finite probability that a downward transition results. It can be shown [243] that the upward transition probability increases with respect to the downward transition probability as U_i grows closer to the continuum, and that upward transitions dominate for levels less than an energy $\sim k_B T_e$ below the continuum. Any electron ending up in the energy band $-k_B T_e < U_i < 0$, shown in gray in Fig. 5.2, is therefore likely to re-ionize, while electrons below this band are likely to fully recombine. Hence, as far as TBR is concerned, one may qualify the levels $-k_B T_e < U_i < 0$ as effectively unbound, and approximate the amount of eventually recombining electrons with those electrons that skip this band altogether by making a direct collisional transition from the continuum to anywhere below the bottleneck level $-k_B T_e$. The validity of this approximation has been confirmed by simulations [244]. Summing the probabilities of such transitions over all possible initial and final energies of the recombining electron and over all possible energies of the free electron, one finds indeed the usual TBR rate proportional $T_e^{-9/2}$ [243].

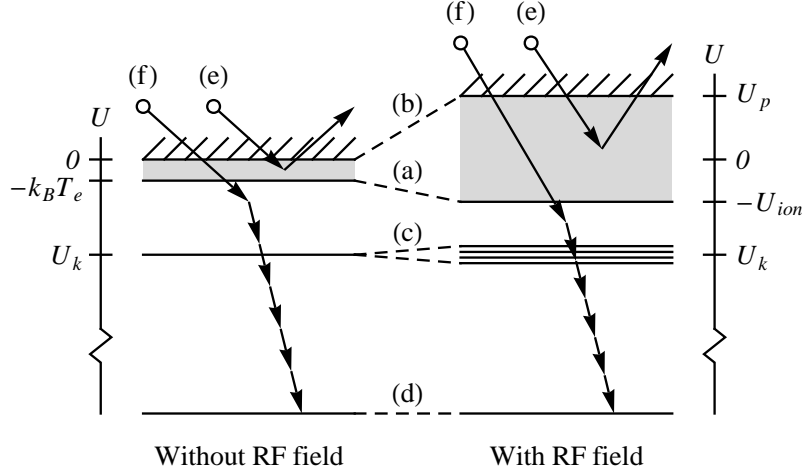


Figure 5.2: Energy diagram of three body recombination with and without RF field. The gray bands show energies from which re-ionization is likely. An arbitrary high energy level $U_k < 0$ has been drawn; on the sides the energy scale has been indicated. The bottleneck level is moved by the RF field (a). The RF field induces a Stark shift of the continuum threshold (b), Stark splitting of highly excited levels (c); and much smaller shifts of deeply bound states (d). (e): electron that re-ionizes after a collisional transition from the continuum to above the bottleneck level; (f): electron that recombines by making a cascade to deeply bound states after a collisional transition below the bottleneck level.

When an RF field is present, two essential modifications must be made to this picture, as illustrated by the right panel of Fig. 5.2. First, the RF field interferes with the collisional cascade towards deeply bound levels, because it can ionize electrons from highly excited levels. It is well-known that the character of a field ionization process depends upon the applied field strength and frequency in relation to the binding energy of the electron; accordingly different regimes such as multiphoton- and tunneling ionization may be identified. We consider microwave or lower frequencies and kV/m field strengths, in which case field ionization from highly excited levels is well-described by classical over-the-barrier ionization in a quasistatic electric field [254]. This has also been verified experimentally [255–257]. Accordingly, the combined potential $U = -e/(4\pi\epsilon_0 r) - E_0 z$ of the ion and the external field has a saddle point along the z -axis of height $\sqrt{e^3 E_0 / (\pi\epsilon_0)} \equiv -U_{ion}$, and any electrons with energies $U_i > -U_{ion}$ will rapidly escape from the ion by going over this saddle point. Such a static description is valid because, in the case at hand, the applied frequency ω is much smaller than the classical Kepler frequency ω_i of the energy levels U_i close to $-U_{ion}$. Also the inverse process, in which free electrons enter the vicinity of the ion in the presence of a low-frequency field and which is the low-frequency equivalent of

stimulated radiative recombination, has been observed [258, 259]. The lowering of the Coulomb barrier to $-U_{ion}$ due to the external field thus defines a range of energies $U > -U_{ion}$ that are effectively unbound. Regarding the three body recombination process, any electron ending up in this energy range is more likely to ionize than to proceed with a downward collisional cascade. Thus, analogous to the field-free case, only free electrons that make a direct collisional transition to states below the bottleneck level $-U_{ion}$ will contribute to the TBR rate, but now the bottleneck level is set by the field and no longer by the plasma property $-k_B T_e$.

A second influence of the RF field is the fact that the energy of both free and bound electrons will change due to the field. For free electrons, the energy increment is just the quiver energy $U_p = mv_{osc}^2/4$. As a result the continuum threshold shifts up by U_p as well (see Fig. 5.2), which is a well-known effect in multiphoton ionization experiments [260]. This upshift is important for the TBR process since free electrons will now have to loose an additional energy U_p in order to recombine with an ion. Combined with the adapted bottleneck, the minimum energy loss to effect a TBR event has thus increased from $k_B T_e$ in the field-free case to $U_p + U_{ion}$ in the case with field, as is illustrated in Fig. 5.2 by the gray bands. This suppresses the TBR rate significantly. Finally, the energy change of the bound levels due to the RF field is the AC Stark shift. However, the energy levels that are available for TBR are the levels below $-U_{ion}$, for which the shift is approximately equal to the DC Stark shift because $\omega_i \gg \omega$. For states just below $-U_{ion}$, the electric field exceeds the Inglis-Teller limit, which means that the Stark splitting of the manifolds with principal quantum number k is large enough to fill the energy space with states more or less homogeneously [254]. An additional observed effect due to this strong Stark mixing in an AC field is that electrons may ionize from below $-U_{ion}$ via subsequent upward Landau-Zener transitions [254]. We neglect this effect because it is a much slower process than direct over-the-barrier-ionization [261]. Resonant atomic transitions that might be induced by the RF field are not included either, although they may have an effect on the collisional cascade.

We now recalculate the TBR rate in the presence of an RF field, taking account of the field modifications described above. By the method of detailed balance, under the hypothetical condition of thermal equilibrium the rate of collisional transitions from the continuum $U > U_p$ to the bound energy level $U_i < U_{ion}$ is equal to the rate of the inverse process, which are ionizing transitions from the bound level to the continuum caused by electron impact. From the well-known [243] cross section $S_i(U)$ for a collisional energy transfer of at least $|U_i| + U_p$ from a moving electron with energy U to a stationary electron, the rate of collisional ionization from level U_i per unit plasma volume is

$$R_i = \int_{|U_i|+U_p}^{\infty} n_i n_e v S_i(U) f(U) dU. \quad (5.9)$$

Here, $f(U)$ is the energy distribution function of free electrons, v is the electron velocity corresponding to energy U , and n_i is the density of electrons in level U_i . The rate of TBR via level i , which is the inverse process, is obtained by substituting for n_i the equilibrium value from the Saha equation [242], because the two rates must be equal at equilibrium. Let us first consider the case where $U_p \ll U_{ion}$, that is, for relatively high frequencies or low fields, and denote the corresponding TBR rate by R_0 . In this case $U \gg U_p$ in the whole integration domain of Eq. (5.9), so that $f(U)$ may be approximated by an ordinary Boltzmann distribution without the need to correct it for the quiver motion. Evaluating the integral in Eq. (5.9), substituting the Saha value for n_i , and summing over all energy levels below $-U_{ion}$, gives the total TBR rate

$$R_0 = \sum_i R_i \approx \frac{e^4 \hbar^3 n_e^3}{4g\epsilon_0^2 m^2 (k_B T_e)^3} \int_{-\infty}^{-U_{ion}} F\left(\frac{U}{k_B T_e}\right) D(U) dU, \quad (5.10)$$

where $F(x) \equiv \exp(-x) \text{Ei}(x) - 1/x$ with Ei the exponential integral [262] and g is the degeneracy of the ionic ground state. The sum over states has been approximated by an integral over the bound energy, resulting in the density of states $D(U)$ as a factor. Approximating the atomic potential with that of hydrogen, $D(U) \approx 1/2 \text{Ry}^{3/2} |U|^{-5/2}$, where $\text{Ry} = 13.6 \text{ eV}$ is the Rydberg energy. For kV/m field strengths, $|U|/(k_B T_e) \gg 1$ over the whole integration domain of Eq. (5.10), so that the function F can be approximated by its asymptotic value $F \approx (k_B T_e/U)^2$. Then the remaining integral contains the field effects, but is independent of the temperature. This means that the temperature scaling of the TBR rate that is derived here is insensitive to errors due to our approximate description of the energy U_{ion} and the Stark shift structure, although the prefactor may change somewhat in a more detailed calculation. Integration of Eq. (5.10) gives

$$R_0 \approx \frac{\pi^2}{7g} \sqrt{\frac{2}{m}} \left(\frac{e^2}{4\pi\epsilon_0}\right)^5 \frac{n_e^3}{U_{ion}^{7/2} k_B T_e} \approx 2.6 \cdot 10^{-27} \frac{n_e^3 [\text{cm}^{-9}]}{U_{ion}^{7/2} k_B T_e [\text{eV}^{9/2}]} \text{cm}^{-3} \text{s}^{-1}, \quad (5.11)$$

assuming $g = 2$. Within a factor of order unity, this three body recombination rate is equal to the accepted result for the case without RF field [244], except that $7/2$ powers of $k_B T_e$ have been replaced by the energy U_{ion} characterizing the applied field. This reduces the strongly divergent behavior $R \propto T_e^{-9/2}$ to the much milder dependency $R \propto T_e^{-1}$. Thus three body recombination may be significantly suppressed by application of an RF field. A similar field-induced suppression of the TBR rate has been considered before [247], although in that work the so-called plasma microfield was accounted for rather than an externally applied field. The calculated TBR rate for singly charged ions was $1.4 \cdot 10^{-31} \Gamma_Z n_p^7 n_e^3 / (k_B T_e)$ in the units of Eq. (5.11), with

$\Gamma_Z \approx 2$ and n_p the principal quantum number at the bottleneck level defined in Ref. [247]. Using our bottleneck level instead by substituting $n_p = \sqrt{\text{Ry}/U_{ion}}$ precisely gives Eq. (5.11), including the correct numerical factor, showing that both results agree.

Eq. (5.11) is valid for $U_p \ll U_{ion}$ only. However, the calculation is easily generalized to arbitrary U_p by including the quiver motion of the free electrons in the calculation. The details are given in Appendix 5.B; the result is

$$R = R_0 G \left(\frac{U_p}{U_{ion}} \right), \quad (5.12)$$

where R_0 is the rate given by Eq. (5.11) and G is a correction factor. The latter is given by Eq. (5.34) and is approximately equal to

$$G(x) \approx \left[1 + (\beta x)^{1/\alpha} \right]^{-5\alpha/2}, \quad (5.13)$$

with $\alpha = 1.137$ and $\beta = (2/7)^{2/5}$.

5.4 Collisionless absorption

5.4.1 Absorption models

Even without the presence of electron-ion collisions, individual electrons in a plasma can absorb energy from an applied electric field. For bulk plasmas, this collisionless absorption effect is the well-known Landau damping [236], in which electrons can gain net energy from a high-frequency propagating electric wave, despite the fact that the high-frequency electric force tends to cancel out on the average. This is possible when the thermal velocity of the electron is close to the velocity of the wave, so that the electric field is approximately static in the electron frame of reference. Essential for this mechanism is a resonance between thermal motion and applied field. In plasmas of finite size, such as an UCP, the thermal motion of electrons is necessarily confined by the plasma boundaries, so the assumption of rectilinear motion implicit in the Landau damping mechanism of bulk plasmas is no longer appropriate. Rather, the electrons perform quasi-periodic motion in the electrostatic potential of the plasma, as is detailed below. Furthermore, the electric field in the plasma is homogeneous rather than a propagating wave when the applied wavelength is much larger than the plasma size, such as in the case of an RF field applied to an UCP. Nevertheless, electrons may on the average gain energy, and this is again due to a resonance between the thermal motion and the applied field. This is why the collisionless absorption of finite plasmas has been called Landau damping as well [228, 263], although the char-

acter of the correlation is quite different. In this section, we calculate the RF energy absorption of an UCP by this mechanism. To avoid confusion, it should be noted that the resonance between thermal motion and RF field that is meant here has nothing to do with the more familiar plasma resonance. The electrons in the plasma have an individual thermal motion superposed on a collective quiver motion; the resonance meant here concerns the first of these, while plasma resonance relates to the latter.

First, we mention a number of other approaches to collisionless absorption and argue why these are less appropriate for UCPs in RF fields. In the above description of collisionless absorption, the applied field plays the role of a perturbation on the thermal motion of the electrons. One may change perspective and look at the quiver motion of the electrons as being the primary motion, perturbed by a thermal one. Because the details of the thermal motion are determined by the details of the plasma potential, this can be interpreted as an oscillating electron having interaction with the plasma potential itself. This view is particularly appropriate when the potential can be approximated by an infinitely deep well, so that the 'interaction with the potential' simply becomes 'collisions with the plasma boundary'. Then the collision frequency of electrons with the plasma boundary is on average

$$\nu_p \sim \frac{v}{\sigma} \quad (\text{hard wall model}), \quad (5.14)$$

where σ is the plasma size, and v is the characteristic velocity of the electrons that is taken to be the thermal velocity [231], a combination of thermal and quiver velocity [230] or Fermi velocity [228] depending on the model used. On average the electrons gain an energy $2U_p$ per hard wall collision, in analogy with Eq. (5.2). The result (5.14) also follows as a special case from the more general Landau damping approach when specialized to a hard wall potential [231]. While a flat potential with hard walls, and hence the resulting absorption rate $2vU_p/\sigma$, may be a good approximation for large metallic clusters [228, 230], it is not for UCPs. In the process of creation of an UCP from an atomic cloud, part of the electrons escape from the plasma immediately after photoionization of the cloud. This continues until the accumulated charge imbalance self-limits further loss of electrons. The resulting spherically symmetric Coulomb potential of the UCP with a typical Gaussian density distribution is [203]

$$U(r) = U_0 \left[1 - \frac{\sqrt{\pi}\sigma}{2r} \operatorname{erf} \left(\frac{r}{\sigma} \right) \right], \quad (5.15)$$

where $\operatorname{erf}(r/\sigma)$ denotes the error function [262], and r is the distance to the cloud center. The depth of the potential saturates to $U_0 \sim k_B T_e$ by nature of the charging process. Clearly, the hard wall potential is not a very good approximation in this case and a more detailed calculation of the energy absorption is necessary to account for the smoothness of the potential.

Another absorption mechanism that is considered important for large metal clusters is the Brunel effect [229], in which electrons at the plasma boundary are pulled out of the plasma by the applied electric field and then driven back into the plasma as the field reverses direction. When the plasma is sufficiently overdense, the interaction effectively stops once the electron has moved deeper into the plasma than the skin depth, resulting in net energy gain because the electron cannot be brought back to rest by the evanescent field. The resulting absorption rate, divided by $2U_p$ for comparison, gives again the hard wall collision frequency Eq. (5.14), with v the high-frequency velocity. In an UCP, however, the Brunel mechanism is not in effect either, since typically the skin depth, which is comparable to c/ω_p with ω_p the plasma frequency, is much larger than the plasma size.

Finally, when the applied field is so strong that the oscillation amplitude of individual electrons is comparable to or larger than the plasma size, one can hardly speak of the applied field as a perturbation, and other descriptions of the electron motion such as nonlinear oscillators [232–234] or scattering off the plasma potential [264] are more appropriate. Here we do not consider such strong field effects.

5.4.2 RF absorption by electrons in a general potential

We now proceed to calculate the collisionless RF energy absorption by an UCP, taking account of the smooth plasma potential shape shown in Eq. (5.15) rather than resorting to a hard wall approximation. We make use of the calculational method developed by Zaretsky et al. [231]. When forcing an UCP with an RF signal, the electric field in the plasma consists of the external RF field, the polarization field caused by any excited plasma modes, and the field corresponding to the plasma potential Eq. (5.15). The combination of the first two fields may be considered a fast harmonic perturbation on the latter field. Although UCPs behave entirely classically [203], a quantum mechanical description of this situation proves best suited to calculate the RF energy absorption. Accordingly, the electrons occupy bound states in the plasma potential, and can change states by absorption or emission of an RF photon. The quantum mechanical calculation of the absorption is given in detail in Ref. [231]. A spatially homogeneous RF field is assumed, which rules out strong local field enhancements such as those generated by plasma resonances. Therefore the following calculation is restricted to underdense plasmas. In summary, perturbation theory is applied, in which the transition probability of electrons between any pair of states is given by Fermi's Golden rule [265]. The number of RF photons absorbed by the plasma equals the difference between the number of electron transitions to a higher state and those to a lower state, and the absorbed RF energy is this amount multiplied by the photon energy. Exploiting, in addition, the fact that the system dimension σ is much larger than the typical De Broglie wavelength of the electrons, one can adopt the quasi-classical or Bohr-Sommerfeld theory to approximate quantum mechanical quantities

by their classical analogues [265]. Although results for a general three-dimensional potential are available [231], we will use the one-dimensional analogs because then the mathematics is much more transparent. This does not represent a major error since the energy transfer from the RF field to the plasma proceeds via electrons that move partially resonant with the applied field. This means that only one component of the electron trajectories, namely the one that is parallel to the applied field, contributes to the RF absorption, so that the problem is essentially one-dimensional. Explicit calculation of the RF absorption in both the full three-dimensional and corresponding one-dimensional hard wall potential [231] confirms that the latter captures the general behavior.

Expressing as before the absorbed RF power P_p due to collisionless absorption in terms of an effective frequency ν_p , it is found that [231]

$$P_p = 2\nu_p U_p; \quad (5.16)$$

$$\nu_p = \frac{\pi m \omega^3}{Z k_B T_e} \sum_{s=0}^{\infty} \left[\frac{|X(\epsilon)|^2}{|d\Omega/d\epsilon|} \exp\left(-\frac{\epsilon}{k_B T_e}\right) \right]_{\epsilon=\epsilon_s}. \quad (5.17)$$

Here, $\Omega(\epsilon)$ is the oscillation frequency of the classical trajectory $x(\epsilon, t)$ of a particle with energy ϵ in the unperturbed potential,

$$X(\epsilon) = \frac{\Omega(\epsilon)}{2\pi} \int_0^{2\pi/\Omega(\epsilon)} x(\epsilon, t) \exp(i\omega t) dt \quad (5.18)$$

is the Fourier component of the classical trajectory at the frequency of the perturbation,

$$Z = \int \exp\left(-\frac{\epsilon}{k_B T_e}\right) \frac{d\epsilon}{\Omega(\epsilon)} \quad (5.19)$$

is the partition function of the electron distribution over the energy states, which is assumed a Boltzmann distribution here, and the sum in Eq. (5.17) is over energies that are roots of the equation

$$(2s + 1) \Omega(\epsilon_s) = \omega. \quad (5.20)$$

Without attempting to explain all details underlying Eqs. (5.17-5.20) here, it is noted [231] that the only contributions to the absorbed energy come from those electrons whose trajectory is in resonance with the applied field according to Eq. (5.20). This is the correlation between thermal motion and applied field also characteristic for bulk Landau damping. Furthermore, the contributions in Eq. (5.17) are proportional to $|X|^2$, the spectral content of the trajectory at the applied frequency. However, the dominant frequencies in the spectrum of the trajectory will be on the order of the

oscillation frequency $\Omega(\epsilon)$. In a potential such as Eq. (5.15) with r replaced by x , this frequency will be comparable to that of a harmonic oscillator potential with the same curvature at $x = 0$, that is, to $\Omega \sim \sqrt{2U_0/(3m\sigma^2)} \equiv \omega_0$. Therefore, it is expected that the RF energy absorption strongly depends on the ratio ω/ω_0 . In addition, the ratio of particle energy ϵ and thermal energy $k_B T_e$ appears in Eq. (5.17), the former being limited to values smaller than the potential depth U_0 , so there will be some weak secondary dependency on the ratio $U_0/(k_B T_e)$ as well. These properties are indeed found below.

In the classical UCP system the energy level spacing is much smaller than $k_B T_e$, therefore the sum in Eq. (5.17) may be approximated by integration. A subsequent change of integration variable from s to ϵ_s introduces an extra factor $(d\epsilon_s/ds)^{-1}$, which is the density of resonant states. This factor is obtained by differentiating Eq. (5.20) with respect to s , yielding $|d\Omega/d\epsilon|_{\epsilon=\epsilon_s} \cdot d\epsilon_s/ds = 2\Omega^2/\omega$. Accordingly, Eq. (5.17) becomes

$$\nu_p \approx \frac{\pi m \omega^4}{2Z k_B T_e} \int \left| \frac{X(\epsilon)}{\Omega(\epsilon)} \right|^2 \exp\left(-\frac{\epsilon}{k_B T_e}\right) d\epsilon, \quad (5.21)$$

where the subscript s has been dropped.

5.4.3 RF absorption in a model plasma potential

Eq. (5.21) allows explicit calculation of the absorbed RF power, if the classical trajectories in the potential are known analytically. However, for the particular potential Eq. (5.15), closed expressions for the trajectories are not available. In order to still make quantitative estimates for the energy absorption, instead of Eq. (5.15) we use a model potential with the same general shape for which the trajectories are known analytically:

$$U(x) = \frac{m\omega_1^2 x^2}{2} \left(1 - \frac{x^2}{a^2}\right), \quad (5.22)$$

where a is a positive constant with units of length. Eq. (5.22) is the potential of a Duffing oscillator commonly used to describe the motion of a mass on a cubic softening spring. Although this potential differs from the actual UCP potential Eq. (5.15), we note that from a physical point of view the most important characteristics of the UCP potential are the temperature, which sets the potential depth U_0 , and the charge density, which sets the curvature $m\omega_0^2$ at the bottom of the potential. Therefore we should obtain a reasonable estimate for the energy absorption by choosing the model potential accordingly, setting the curvature $m\omega_1^2$ equal to $m\omega_0^2$ and the potential depth $m\omega_1^2 a^2/8 \equiv U_1$ equal to U_0 . Important as well is that the infinitely differentiable UCP potential is modeled by an equally smooth one, and that both potentials approach their edge with vanishing slope. In Fig. 5.3 the two potentials are compared.

A particle is bound by the potential Eq. (5.22) only if its energy ϵ is less than U_1 . For such a bound particle the classical trajectory, starting at time $t = 0$ at position $x = 0$, can be shown to be given by the periodic function [266]

$$x(\epsilon, t) = a\sqrt{\frac{u}{2v}} \operatorname{sn}\left(\sqrt{\frac{v}{2}}\omega_1 t, \frac{u}{v^2}\right), \quad (5.23)$$

where $\operatorname{sn}(y, m^2)$ is the Jacobi elliptic function with argument y and modulus m , and $u = \epsilon/U_1$ is the particle energy in units of the potential depth, and $v = 1 + \sqrt{1 - u}$. The frequency Ω with which the particle oscillates back and forth in the potential is given by [266]

$$\Omega(\epsilon) = \frac{\pi\sqrt{v}}{2\sqrt{2}K(u/v^2)}\omega_1, \quad (5.24)$$

where $K(m^2)$ is the complete elliptic integral of the first kind with modulus m . In the limit of vanishing particle energy $\epsilon \rightarrow 0$, the trajectory (5.23) approaches harmonic motion with frequency ω_1 , while the motion becomes anharmonic with the frequency monotonically decreasing to zero as the energy grows to U_1 .

In Appendix 5.A the absorbed power is calculated by using Eqs. (5.23) and (5.24) in Eq. (5.21). The exact result Eq. (5.30) for the effective collision frequency is

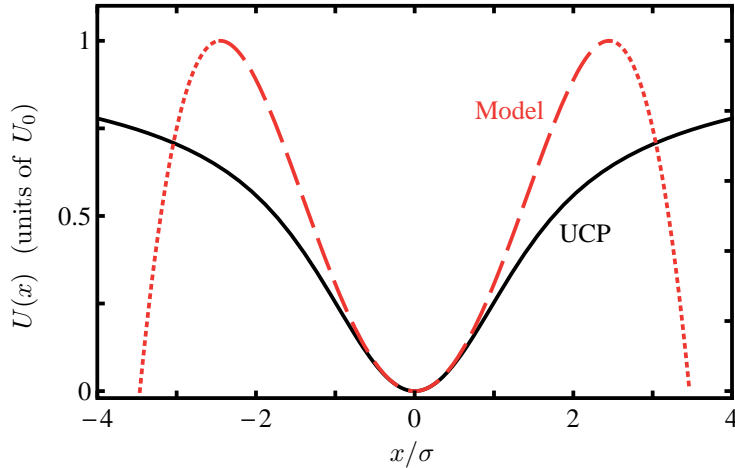


Figure 5.3: Model potential (red dashed line, Eq. (5.22)) compared to the actual UCP potential (black solid line, Eq. (5.15)). The parameters have been set to $\omega_1 = \omega_0$ and a such that $U_1 = U_0$. The dotted parts of the model potential are not used.

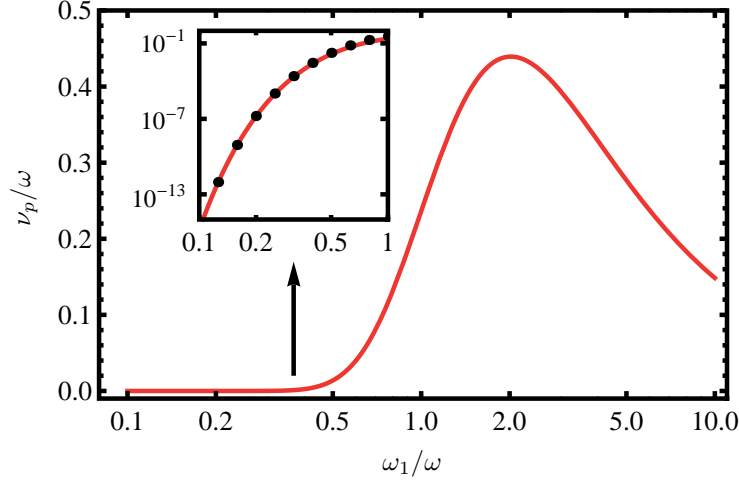


Figure 5.4: Effective collision frequency ν_p for RF absorption due to the finite plasma size, as a function of the ratio of the frequency characterizing the potential ω_1 to the RF frequency ω . A potential depth equal to $k_B T_e$ has been assumed. The inset shows the behavior for $\omega_1/\omega < 1$ on a logarithmic scale, comparing the exact result Eq. (5.30) (solid curve) to the approximate result Eq. (5.25) (dots).

plotted in Fig. 5.4 as a function of ω_1/ω , assuming a potential depth equal to $k_B T_e$. Also plotted is the asymptotic approximation, valid for $\omega_1/\omega \ll 1$,

$$\left(\frac{\nu_p}{\omega}\right)_{\text{Model}} = C(Y) \left(\frac{\omega}{\omega_1}\right)^2 \exp\left(-\sqrt{2\pi} \frac{\omega}{\omega_1}\right), \quad (5.25)$$

which fits the exact result very well. In a typical UCP, $\sigma \sim 1$ mm and $T_e \sim 1$ K [203], while in a typical RF experiment $\omega/(2\pi) > 1$ MHz [211], so that usually the asymptotic regime of Eq. (5.25) is in effect. The prefactor $C(Y)$ is given by Eq. (5.31) and depends on the ratio $Y = U_1/k_B T_e$. As argued previously, the choice of model potential parameters that best represents the actual UCP potential is $\omega_1 = \omega_0$ and $U_1 = U_0 \sim k_B T_e$, giving $Y \sim 1$. The corresponding prefactor in Eq. (5.25) lies in the range $C = 20 - 35$ for $Y = 0.5 - 2.0$.

From Fig. 5.4 and Eq. (5.25), it is clear that the collisionless RF absorption by an UCP strongly depends on ω_1/ω , that is, on the ratio of the frequency at which the thermal motion of the UCP electrons takes place to the RF frequency. This strong dependency was anticipated above from the fact that the collision frequency Eq. (5.17) is proportional to the spectral content of the trajectory at the RF frequency: when ω_1 and ω do not differ too much, the RF forcing and the electron motion take place on more or less the same time scale, so that the electron motion contains an appreciable

Fourier component at the RF frequency, resulting in resonant and efficient energy transfer. Since all oscillation frequencies given by Eq. (5.24) are in fact less than ω_1 , the average oscillation frequency will be less than ω_1 as well, so that in Fig. 5.4 the peak in the energy transfer occurs at a somewhat higher value than $\omega_1/\omega = 1$, corresponding to a somewhat slower forcing.

An important feature of Fig. 5.4 and Eq. (5.25) is the threshold-like behavior of ν_p : for $\omega_1 \gtrsim \omega$ the absorption is significant, while for $\omega_1/\omega \rightarrow 0$ it decreases exponentially. The inset shows that this decrease is very rapid, so that collisionless absorption is completely negligible if $\omega_1 \ll \omega$. This condition can be written as $1 \gg \omega_1/\omega \sim \omega_0/\omega \equiv \sqrt{2U_0/(3m\sigma^2\omega^2)} \sim v_{\text{th}}/(\sigma\omega)$. Physically, this corresponds to the situation in which a low temperature yields by assumption a shallow potential with slow electrons, so that almost no electrons traverse the plasma within one RF oscillation. Combined with the lack of steep features in the smooth potential, this means that there is almost no electron motion available at the RF frequency that is susceptible to resonant absorption. One may thus define a critical temperature

$$k_B T_p = m\omega^2\sigma^2 \quad (5.26)$$

that separates a temperature regime $T_e \gtrsim T_p$ in which collisionless absorption is significant and a regime $T_e \ll T_p$ where it is negligibly small. Note that this behavior is not at all described by the hard wall approximation Eq. (5.14). The reason for this is that an electron bouncing between hard plasma boundaries abruptly changes its velocity at every wall collision, giving rise to high-frequency components essentially regardless of the velocity. Therefore Eq. (5.14) predicts significant collisionless absorption at any temperature, but is valid only for steep plasma potentials.

5.4.4 Validity for the actual UCP potential

As we just described, the collisionless absorption rate in the model plasma potential exponentially decreases with the ratio $v_{\text{th}}/(\sigma\omega)$. Since the physical arguments leading to Eq. (5.26) are valid for any general smooth plasma potential, also in actual UCPs the collisionless absorption rate will quickly decrease once the electron temperature is below the critical temperature T_p . However, one may still ask whether the decay constant of this decrease (i.e. the factor $\sqrt{2}\pi$ in Eq. (5.25)) is also representative for actual UCPs, or depends on the potential shape. Lacking analytical expressions for the trajectories $x(t)$ in the UCP potential, this cannot be verified by explicit calculation. Nevertheless, the decay constant can be calculated by quantifying the asymptotic behavior of the Fourier coefficients of the trajectories, using the so-called Darboux's Principle [267]. This however requires considering the analytical continuation of $x(t)$ to the complex t -plane. The details are rather technical and are relegated to Appendix 5.C. The main result is that the quantity $|X(\epsilon)|^2$ in Eq. (5.21) for the UCP potential

contains an extra factor of approximately $\exp(2\omega/\omega_0)$ as compared to the case of the model potential, independent of the particle energy ϵ and for sufficiently large ω/ω_0 . Including this extra factor in the result Eq. (5.25), the asymptotic rate of decrease of the collision frequency is approximately equal to

$$\left(\frac{\nu_p}{\omega}\right)_{\text{UCP}} \propto \exp\left[-\left(\sqrt{2}\pi - 2\right)\frac{\omega}{\omega_0}\right]. \quad (5.27)$$

Although the decay constant $\sqrt{2}\pi - 2$ is smaller than that of Eq. (5.25) and Fig. 5.4, it is still of the same order of magnitude. Also in the UCP case, therefore, the collisionless absorption is negligible for $\omega_0 \ll \omega$, or equivalently for temperatures below T_p given by Eq. (5.26).

5.5 Discussion and conclusions

In this chapter, we considered three mechanisms by which an RF field influences the temperature of an UCP. First, RF energy is absorbed through the well-known process of collisional absorption, in which electrons gain energy during Coulomb collisions with ions. Second, the RF field modifies the TBR rate by ionizing electrons from intermediate high-lying Rydberg states. Third, resonance between the motion of electrons in the plasma potential and the RF field may give rise to collisionless energy absorption. For all of these processes, naive extrapolations from well-known formulas are inadequate for UCPs or strong RF fields. For example, the electron-ion collision frequency Eq. (5.4) is much smaller than the Spitzer frequency for strong RF fields, suppressing the collisional absorption rate. As we indicated, this is because the quiver velocity effectively takes over the role of the thermal velocity, or equivalently, because the temperature is replaced by the ponderomotive potential in the collision frequency. Likewise, the TBR rate in strong RF fields is much smaller than expected from the commonly used $T_e^{-9/2}$ -scaling, partly because the conventional TBR bottleneck level characterizing the plasma is replaced by the energy U_{ion} characterizing the RF field. Figure 5.5 schematically shows the various heating regimes in terms of the RF field amplitude and frequency; the strong-field effects apply to the area above the slanted line. As discussed in the previous section, collisionless absorption is only relevant at sufficiently high temperatures or low frequencies, as is represented by the area to the left of the vertical line in Fig. 5.5.

We conclude this chapter by giving two numerical examples. The RF experiment of Fletcher et al. [213] was well within the weak-field regime (*a, b*) of Fig. 5.5 according to the reported experimental values. Using these values in Eqs. (5.2-5.8), (5.16) and (5.25) gives absorption rates per electron of $P_{ei}/k_B = 3 \text{ K}/\mu\text{s}$ and $P_p/k_B = 0.002 \text{ K}/\mu\text{s}$ at the highest frequency and amplitude reported in Ref. [213]. Considering the electron temperature of 100 K and the typical plasma expansion time

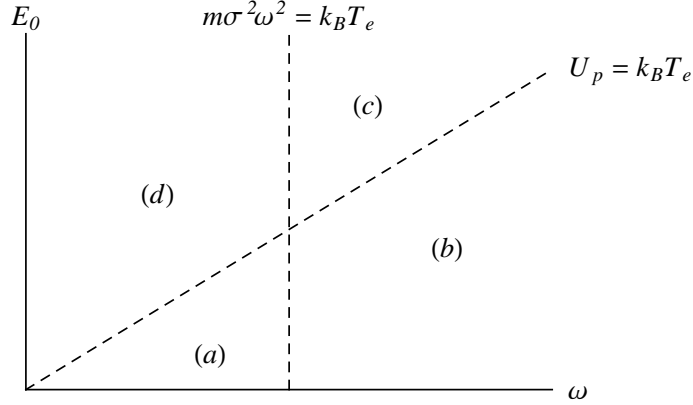


Figure 5.5: Heating regimes for RF-driven UCPs in terms of the applied frequency ω and field strength E_0 . (a,b): Collisional absorption rate according to Spitzer collision frequency and TBR rate according to $T_e^{-9/2}$ -scaling; (c,d): Collisional absorption rate according to collision frequency Eq. (5.4) and TBR rate according to Eq. (5.11). (a,d): Collisionless absorption relevant; (b,c): Collisionless absorption negligible.

of microseconds, these low absorption rates will not influence the plasma temperature and expansion much. For somewhat larger RF amplitudes, however, the collisional absorption starts to become significant on the time scale of the plasma expansion, which may be related to the high-field effects observed in the experiment.

As an example in the regime (c) of Fig. (5.5), consider an applied field with an amplitude of 0.1 MV/m at a frequency of 28 GHz, which is currently available [268]. We deliberately choose this relatively high frequency because otherwise the oscillation amplitude of the plasma electrons would exceed the plasma size at such a large field strength, which situation is outside the scope of this thesis. Choosing further $\sigma = 1$ mm, $T_e = 1$ K and $n = 10^8$ cm $^{-3}$, Eqs. (5.2-5.8), (5.12),(5.16) and (5.25) give $P_{ei}/k_B = 4 \cdot 10^2$ K/ μ s and $R/n_e = 3 \cdot 10^{-7}$ μ s $^{-1}$, while the collisionless absorption rate is vanishingly small. Thus collisional absorption is expected to heat the plasma to the 100 K scale during the expansion time of the plasma, while the chance that an individual electron recombines is very small. Now compare these numbers to the corresponding results obtained from standard expressions. Using the Spitzer collision frequency instead of Eq. (5.4) would give $P_{ei}/k_B = 4 \cdot 10^5$ K/ μ s, which would predict immediate heating of the UCP to conventional eV plasma temperatures. According to the usual $T_e^{-9/2}$ -scaling (Eq. (5.11) with U_{ion} replaced by $k_B T_e$), the TBR rate per electron would be $R/n_e = 50$ μ s $^{-1}$. Assuming an energy release of $\sim k_B T_e$ per recombination, this would result in a heating rate per electron on the order of 10 2 K/ μ s due to TBR alone, although of course this rate would be quickly quenched as

the electron temperature rises. Based on the hard wall approximation Eq. (5.14) with $v = v_{\text{th}}$, the collisionless absorption rate would be $P_p/k_B = 1 \cdot 10^3 \text{ K}/\mu\text{s}$ rather than exponentially small. From these numbers it is clear that it is essential to properly take into account strong field effects on the one hand, and the smooth UCP plasma potential on the other hand. For the application of a very strong microwave field to an UCP, it changes the predicted effect from destroying the plasma immediately to only heating it up moderately.

In summary, we have analytically studied well-known plasma heating mechanisms and specialized them to the system of an UCP driven by a uniform, and possibly strong, RF field. Benchmarking our results against molecular dynamics simulations will yield valuable additional insights, and will also identify any additional RF effects that were addressed here. Among these are, for example, plasma cloud deformations expected when the electron oscillation amplitude becomes comparable to the plasma size, relativistic effects, plasma waves and other instabilities. RF experiments aimed at the detection of plasma resonances rely on adequate modeling of the UCP expansion dynamics, which will benefit from detailed knowledge of RF heating mechanisms such as those discussed in this chapter. Furthermore, in virtue of comparable coupling parameters, RF-driven UCPs may be seen as millimetre-sized scale models of laser-driven solid state density plasmas. Understanding the ways in which ultracold plasmas interact with RF fields is therefore also relevant for such high-density systems.

Appendix 5.A Effective collision frequency

The Fourier series of the trajectory (5.23) equals [266]

$$x(\epsilon, t) = 2a \frac{\Omega}{\omega_1} \sum_{n=0}^{\infty} \frac{\sin[(2n+1)\Omega t]}{\sinh\left[(2n+1) \frac{\pi K(1-u/v^2)}{2K(u/v^2)}\right]}. \quad (5.28)$$

Substituting Eq. (5.20) in Eq. (5.18), and comparing with (5.28), it follows that

$$\left| \frac{X(\epsilon)}{\Omega(\epsilon)} \right| = \frac{a}{\omega_1} \operatorname{csch} \left[\frac{\omega}{\omega_1} \sqrt{\frac{2}{v}} K(1-u/v^2) \right]. \quad (5.29)$$

Using this quantity in Eq. (5.21), and changing the integration variable to $u = \epsilon/U_1$, results in

$$\frac{\nu_{\text{pot}}}{\omega} = \pi^2 \sqrt{2} \frac{\omega^3}{\omega_1^3} Y \frac{\int_0^1 \operatorname{csch}^2 \left[\frac{\omega}{\omega_1} \sqrt{\frac{2}{v}} K(1-u/v^2) \right] \exp(-Yu) du}{\int_0^1 v^{-1/2} K(u/v^2) \exp(-Yu) du}, \quad (5.30)$$

where $Y = U_1/k_B T_e$. The integrations are over energies smaller than the potential depth, corresponding to bound electrons, since transitions to the continuum do not give rise to energy increase of the ensemble that is left behind. When ω_1/ω is much smaller than unity, to a good approximation $\operatorname{csch} Z \approx 2 \exp(-Z)$ in the numerator of Eq. (5.30). Furthermore, the argument Z of the csch -function is smallest at $u = 1$, so that the region around the upper integration limit will give the dominant contribution to the integral in Eq. (5.30), and Z may be approximated by its Taylor series around $u = 1$. This gives $\operatorname{csch} Z \approx 2 \exp[-(\pi/\sqrt{2})(\omega/\omega_1)(1 + 3\delta/16)]$, where $\delta = 1 - u$. Similarly, in the integral in the denominator of Eq. (5.30), the elliptic function diverges at $u = 1$, so that again the region around the upper integration limit will give the dominant contribution, and the elliptic function may be approximated by its asymptotic value [262]. This gives $v^{-1/2} K(u/v^2) \approx -\ln(\delta/64)/4$. With these approximations, the integrals in Eq. (5.30) can be solved analytically, yielding Eq. (5.25), with

$$C(Y) = \frac{256\pi}{3} \frac{Y^2}{\operatorname{Ein} Y + 6 \ln 2 (\exp Y - 1)}. \quad (5.31)$$

Here, Ein denotes the modified exponential integral [262, 269].

Appendix 5.B TBR rate for arbitrary ratio U_p/U_{ion}

The energy distribution function of the free electrons in the presence of an RF field may be approximated by the shifted Boltzmann distribution

$$f(U) = \frac{2\sqrt{U-U_p}}{\sqrt{\pi}(k_B T_e)^{3/2}} \exp\left(-\frac{U-U_p}{k_B T_e}\right) \Theta(U-U_p),$$

where Θ denotes the Heaviside step function and the shift U_p accounts for the quiver energy of the electrons. Substituting in Eq. (5.9) this distribution function, the cross section $S_i(U)$ given in Ref. [243], and the rms velocity $v = \sqrt{2U/m}$ corresponding to energy U , and changing the integration variable to the thermal energy $U_{th} = U - U_p$, gives

$$R_i = Q \int_{|U_i|}^{\infty} \left(\frac{1}{|U_i| + U_p} - \frac{1}{U_{th} + U_p} \right) \sqrt{\frac{U_{th}}{U_{th} + U_p}} \exp\left(-\frac{U_{th}}{k_B T_e}\right) dU_{th}, \quad (5.32)$$

with $Q \equiv n_i n_e m e^4 / [2\epsilon_0^2 (2\pi m k_B T_e)^{3/2}]$. For field strengths > 1 kV/m and typical UCP temperatures, $|U_i| > U_{ion} \gg k_B T_e$, so that the exponent in Eq. (5.32) falls off rapidly compared to the rate of variation of the pre-exponential factor; furthermore the integrand is only significant close to the lower integration limit. The pre-exponential factor may therefore be approximated by the first term of its Taylor-expansion around $U_{th} = |U_i|$. Performing the integration with this approximation,

substituting for n_i the equilibrium value from the Saha equation [242], and summing as before the result over all energy levels below $-U_{ion}$ by means of the rule $R = \sum R_i \approx \int R_i D(U_i) dU_i$ with $D(U_i)$ the density of states, gives the total TBR rate

$$R \approx \frac{\pi^2}{7g} \sqrt{\frac{2}{m}} \left(\frac{e^2}{4\pi\epsilon_0} \right)^5 \frac{n_e^3}{U_{ion}^{7/2} k_B T_e} G\left(\frac{U_p}{U_{ion}}\right); \quad (5.33)$$

$$G(x) \equiv \frac{7}{2x^3} \left(\frac{15 + 20x + 3x^2}{3(x+1)^{3/2}} - \frac{5 \operatorname{arcsinh} \sqrt{x}}{\sqrt{x}} \right). \quad (5.34)$$

The relative error in the approximation for the function $G(x)$ given in Eq. (5.13) is less than 6% for any value of x .

Appendix 5.C Decay rate of ν_p for UCPs

We use the following theorem [267]:

The coefficients of the Fourier series $\sum a_n \sin(n\Omega t)$ of a $2\pi/\Omega$ -periodic function $y(t)$, which is infinitely many times differentiable, decay asymptotically as $a_n \propto \exp(-\Omega\tau n)$. The constant τ equals $\min |\operatorname{Im} t_j|$, where t_j denote the singularities of the function $y(t)$ in the complex t -plane.

Writing $\omega = (\omega/\Omega) \cdot \Omega$ in Eq. (5.18) shows that X is essentially the ω/Ω -th Fourier coefficient of the function $x(\epsilon, t)$, so that according to the theorem the integrand in the collision frequency Eq. (5.21) is proportional to

$$|X|^2 \propto \exp(-2\omega\tau); \quad \tau = \min |\operatorname{Im} t_j| \quad (5.35)$$

for large ω . This expression is easily checked for the model potential: the elliptic function in the trajectories Eq. (5.23) has singularities along the lines $\operatorname{Im} t = \pm \omega_1^{-1} \sqrt{2/v} K(1 - u/v^2) \equiv \pm \tau$ in the complex t -plane [266]. Substitution in Eq. (5.35) yields the behavior of $|X|^2$ for large ω , which coincides precisely with what is found in Appendix 5.A, Eq. (5.29) by explicit calculation.

Applying Eq. (5.35) to the actual UCP potential requires explicit expressions for the trajectories $x(\epsilon, t)$, however these are not known. Instead, the inverse function $t(\epsilon, x)$ may be obtained by integration of the equation of motion $m d^2 x / dt^2 = -dU(x)/dx$, yielding

$$t(\epsilon, x) = \sqrt{\frac{m}{2}} \int_0^x \frac{dz}{\sqrt{\epsilon - U(z)}}. \quad (5.36)$$

Here, the initial conditions $x = 0$ and $dx/dt = \sqrt{2\epsilon/m}$ at $t = 0$ have been assumed,

and $U(z)$ denotes the UCP potential Eq. (5.15) with $r = z$. Equation (5.35) requires knowledge of the singularities t_j of the functions $x(\epsilon, t)$, which may be categorized as either poles, logarithmic branch points or algebraic branch points. (More pathological singularities such as $\exp(1/z)$ at $z = 0$ are not considered here.) An algebraic branch point in $x(\epsilon, t)$ corresponds to a critical point in the inverse function $t(\epsilon, x)$, at which $dt/dx = 0$. Differentiating Eq. (5.36) with respect to x , it follows that $U(z)$ must diverge at such a point if the derivative dt/dx is to vanish. But the UCP potential Eq. (5.15) is an entire function, so that this does not occur for any finite complex z , hence $x(\epsilon, t)$ does not have any algebraic branch points.

Considering next poles and logarithmic branch points in $x(\epsilon, t)$, at such points the position diverges while the complex time has some finite value. In terms of the inverse function Eq. (5.36) then, there exist contours C_j in the complex x -plane from the origin to infinity such that $t(\epsilon, x) \rightarrow t_j$ with $|t_j| < \infty$ as $x \rightarrow \infty$ along C_j . In view of Eq. (5.35) we are interested in the contour that yields the time t_j with the smallest imaginary part. A complication in finding this contour is the presence of the square root in Eq. (5.36), because of which the integrand has branch cuts in the complex z -plane. Adopting the standard choice of letting the branch cuts coincide with the points at which the argument of the root is real and negative, these cuts start at the zeros of the function $\epsilon - U(z)$ and extend to $\pm i\infty$ without crossing. Fig. 5.6 shows the resulting branch cut structure for the case $\epsilon = U_0/2$; the integrand in the lower half-plane is the complex conjugate of that in the upper half-plane. Also drawn are two possible contours from the origin to infinity. Now, the potential $U(z)$ in Eq. (5.36) contains the error function $\text{erf}(z/\sigma)$, which has the property [262] that its value is close to unity for $|z/\sigma| \gtrsim 1$ in the shaded sectors in Fig. 5.6, while its amplitude grows superexponentially as $z \rightarrow \infty$ in the non-shaded sectors. Therefore the integrand in Eq. (5.36) will be essentially constant along parts of contours that cross the shaded sector, such as C_2 , so that a large contribution to the integral is accumulated along these parts. Hence we may expect that the contour yielding the smallest possible value of t_j is the contour that avoids the shaded sectors altogether, that is, the contour C_1 along the imaginary axis. With this conjecture, we calculate τ in Eq. (5.35) by integrating Eq. (5.36) along C_1 for several values of the particle energy ϵ . The result is shown in Fig. 5.7, together with the analogous result for the model potential. As is clear from the figure, for any particle energy τ for the UCP potential is approximately one unit ω_0^{-1} less than that for the model potential. Hence, asymptotically for large ω , the quantity $|X|^2$ in Eq. (5.21) will contain an extra factor $\exp(2\omega/\omega_0)$ as compared to the case of the model potential, independent of ϵ . The resulting rate of decrease of the collision frequency is given in Eq. (5.27).

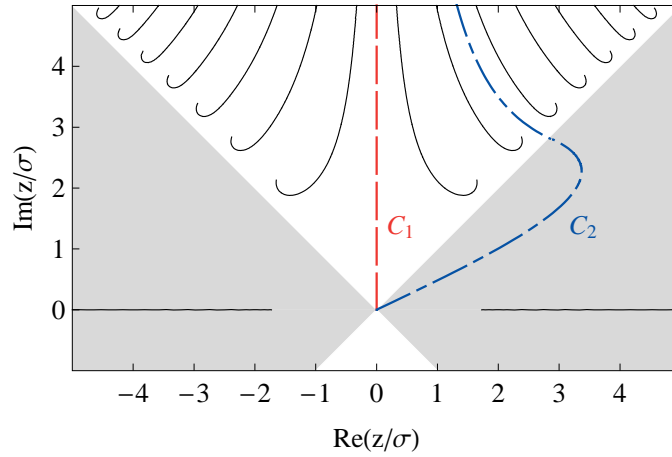


Figure 5.6: Branch cuts (black solid lines) of the integrand of Eq. (5.36) in the complex z -plane, using $u = 1$. In the shaded sectors $|\arg z| < \pi/4$ and $|\pi - \arg z| < \pi/4$, the error function behaves as $\text{erf}(z/\sigma) \rightarrow 1$ as $|z/\sigma| \rightarrow \infty$. Two possible contours from the origin to infinity are shown.

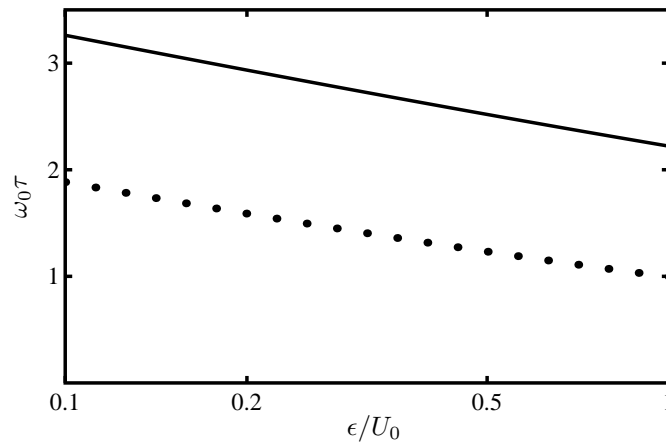


Figure 5.7: Decay constant τ in Eq. (5.25) as a function of particle energy. Solid line: analytical result for the model potential Eq. (5.15) assuming $\omega_1 = \omega_0$ and $U_1 = U_0$; dots: numerical result for the UCP potential (5.22).

Bibliography

- [202] T. C. Killian, S. Kulin, S. D. Bergeson, L. A. Orozco, C. Orzel, and S. L. Rolston, "Creation of an ultracold neutral plasma," *Phys. Rev. Lett.* **83**, 4776–4779 (1999).
- [203] T. C. Killian, T. Pattard, T. Pohl, and J. M. Rost, "Ultracold neutral plasmas," *Phys. Reports* **449**, 77–130 (2007).
- [204] Th. Fennel, K.H. Meiwes-Broer, J. Tiggesbäumker, P.G. Reinhard, P. M. Dinh, and E. Suraud, "Laser-driven nonlinear cluster dynamics," *Rev. Mod. Phys.* **82**, 1793–1842 (2010).
- [205] S. P. Hatchett, C. G. Brown, T. E. Cowan, E. A. Henry, J. S. Johnson, M. H. Key, J. A. Koch, A. B. Langdon, B. F. Lasinski, R. W. Lee, A. J. Mackinnon, D. M. Pennington, M. D. Perry, T. W. Phillips, M. Roth, T. C. Sangster, M. S. Singh, R. A. Snavely, M. A. Stoyer, S. C. Wilks, and K. Yasuike, "Electron, photon, and ion beams from the relativistic interaction of Petawatt laser pulses with solid targets," *Phys. Plasmas* **7**, 2076–2082 (2000).
- [206] S. X. Hu, B. Militzer, V. N. Goncharov, and S. Skupsky, "Strong coupling and degeneracy effects in inertial confinement fusion implosions," *Phys. Rev. Lett.* **104**, 235003 (2010).
- [207] G. Chabrier, F. Douchin, and A. Y. Potekhin, "Dense astrophysical plasmas," *J. Phys.: Condensed Matter* **14**, 9133–9139 (2002).
- [208] W. H. Li, M. W. Noel, M. P. Robinson, P. J. Tanner, T. F. Gallagher, D. Comparat, B. L. Tolra, N. Vanhaecke, T. Vogt, N. Zahzam, P. Pilet, and D. A. Tate, "Evolution dynamics of a dense frozen Rydberg gas to plasma," *Phys. Rev. A* **70**, 042713 (2004).
- [209] C. E. Simien, Y. C. Chen, P. Gupta, S. Laha, Y. N. Martinez, P. G. Mickelson, S. B. Nagel, and T. C. Killian, "Using absorption imaging to study ion dynamics in an ultracold neutral plasma," *Phys. Rev. Lett.* **92**, 143001 (2004).
- [210] E. A. Cummings, J. E. Daily, D. S. Durfee, and S. D. Bergeson, "Fluorescence measurements of expanding strongly coupled neutral plasmas," *Phys. Rev. Lett.* **95**, 235001 (2005).
- [211] S. Kulin, T. C. Killian, S. D. Bergeson, and S. L. Rolston, "Plasma oscillations and expansion of an ultracold neutral plasma," *Phys. Rev. Lett.* **85**, 318–321 (2000).
- [212] S. D. Bergeson and R. L. Spencer, "Neutral-plasma oscillations at zero temperature," *Phys. Rev. E* **67**, 026414 (2003).

- [213] R. S. Fletcher, X. L. Zhang, and S. L. Rolston, “Observation of collective modes of ultracold plasmas,” *Phys. Rev. Lett.* **96**, 105003 (2006).
- [214] K. A. Twedt and S. L. Rolston, “Electronic detection of collective modes of an ultracold plasma,” *Phys. Rev. Lett.* **108**, 065003 (2012).
- [215] A. Lyubonko, T. Pohl, and J. M. Rost, “Collective energy absorption of ultracold plasmas through electronic edge-modes,” *New J. Phys.* **14**, 053039 (2012).
- [216] V. P. Silin, “Nonlinear high-frequency plasma conductivity,” *Sov. Phys. JETP* **20**, 1510 (1965).
- [217] P. J. Catto and T. Speciale, “Strong field inverse Bremsstrahlung via a Lorentz model,” *Phys. Fluids* **20**, 167–168 (1977).
- [218] J. Dawson and C. Oberman, “High-frequency conductivity and the emission and absorption coefficients of a fully ionized plasma,” *Phys. Fluids* **5**, 517–524 (1962).
- [219] C. D. Decker, W. B. Mori, J. M. Dawson, and T. Katsouleas, “Nonlinear collisional absorption in laser-driven plasmas,” *Phys. Plasmas* **1**, 4043–4049 (1994).
- [220] P. Mulser, F. Cornolti, E. Bésuelle, and R. Schneider, “Time-dependent electron-ion collision frequency at arbitrary laser intensity-temperature ratio,” *Phys. Rev. E* **63**, 016406 (2000).
- [221] R. K. Osborn, “Nonlinear Bremsstrahlung,” *Phys. Rev. A* **5**, 1660–1662 (1972).
- [222] H. Brysk, “Multiphoton inverse Bremsstrahlung,” *J. Phys. A: Math. Gen.* **8**, 1260–1264 (1975).
- [223] T. Bornath, M. Schlanges, P. Hilse, and D. Kremp, “Nonlinear collisional absorption in dense laser plasmas,” *Phys. Rev. E* **64**, 026414 (2001).
- [224] H. J. Kull and L. Plagne, “Quantum-mechanical dielectric model of the electron-ion collision frequency in strong laser fields,” *Phys. Plasmas* **8**, 5244–5256 (2001).
- [225] G. J. Pert, “Inverse Bremsstrahlung in strong radiation fields at low temperatures,” *Phys. Rev. E* **51**, 4778–4789 (1995).
- [226] Y. Shima and H. Yatom, “Inverse Bremsstrahlung energy-absorption rate,” *Phys. Rev. A* **12**, 2106–2117 (1975).
- [227] J. Blocki, Y. Boneh, J. R. Nix, J. Randrup, M. Robel, A. J. Sierk, and W. J. Swiatecki, “One-body dissipation and super-viscosity of nuclei,” *Ann. Phys. (NY)* **113**, 330–386 (1978).
- [228] C. Yannouleas and R. A. Broglia, “Landau damping and wall dissipation in large metal clusters,” *Ann. Phys. (NY)* **217**, 105–141 (1992).

- [229] F. Brunel, “Not-so-resonant, resonant absorption,” *Phys. Rev. Lett.* **59**, 52–55 (1987).
- [230] F. Megi, M. Belkacem, M. A. Bouchene, E. Suraud, and G. Zwicknagel, “On the importance of damping phenomena in clusters irradiated by intense laser fields,” *J. Phys. B: At. Mol. Opt. Phys.* **36**, 273–282 (2003).
- [231] D. F. Zaretsky, Ph. A. Korneev, and S. V. Popruzhenko, “Collisionless absorption of intense laser radiation in nanoplasma,” *Quantum Elec.* **37**, 565–574 (2007).
- [232] I. Y. Kostyukov, “Stochastic heating and stochastic outer ionization of an atomic cluster in a laser field,” *J. Exp. Theor. Phys.* **100**, 903–910 (2005).
- [233] P. Mulser, M. Kanapathipillai, and D. H. H. Hoffmann, “Two very efficient nonlinear laser absorption mechanisms in clusters,” *Phys. Rev. Lett.* **95**, 103401 (2005).
- [234] M. Kundu and D. Bauer, “Nonlinear resonance absorption in the laser-cluster interaction,” *Phys. Rev. Lett.* **96**, 123401 (2006).
- [235] P. Mulser and D. Bauer, *High power laser-matter interaction* (Springer, Berlin, 2010).
- [236] L. Spitzer, Jr., *Physics of fully ionized gases* (Interscience, New York, 1962) 2nd rev. ed.
- [237] L. Ronghua and H. Shensheng, “The radio-frequency absorption in ultracold neutral plasma,” *Phys. Lett. A* **373**, 1663–1666 (2009).
- [238] L. C. Andrews, *Special functions for engineers and applied mathematicians* (Macmillan, New York, 1985).
- [239] F. W. Crawford and K. J. Harker, “Energy absorption in cold inhomogeneous plasmas: the Herlofson paradox,” *J. Plasma Phys.* **8**, 261–286 (1972).
- [240] M. J. de Loos and S. B. van der Geer, “General Particle Tracer: a new 3D code for accelerator and beam line design,” in *Proc. Fifth Eur. Part. Acc. Conf.*, Vol. 2, edited by S. Myers, A. Pacheco, R. Pascual, Ch. Petit-Jean-Genaz, and J. Poole (Sitges, Spain, 1996) pp. 1241–1243, <http://www.pulsar.nl/gpt>.
- [241] M. Sebregts, *Numerical simulations of heating mechanisms in ultracold plasmas*, Bachelor thesis No. CQT 2012-05, Eindhoven University of Technology (2012); K. W. C. A. van der Straten, Master thesis, Eindhoven University of Technology (expected 2013).
- [242] M. Mitchner, *Partially ionized gases* (Wiley-Interscience, New York, 1973).

- [243] E. Hinnov and J. G. Hirschberg, “Electron-ion recombination in dense plasmas,” *Phys. Rev.* **125**, 795–801 (1962).
- [244] P. Mansbach and J. Keck, “Monte Carlo trajectory calculations of atomic excitation and ionization by thermal electrons,” *Phys. Rev.* **181**, 275–289 (1969).
- [245] M. Schlanges and Th. Bornath, “Ionization and recombination coefficients for a dense nonideal hydrogen plasma: effects of screening and degeneracy,” *Physica A* **192**, 262–279 (1993).
- [246] Th. Bornath, Th. Ohde, and M. Schlanges, “Reaction rates for dense nonideal alkali plasmas,” *Physica A* **211**, 344–358 (1994).
- [247] Y. Hahn, “Plasma density effects on the three-body recombination rate coefficients,” *Phys. Lett. A* **231**, 82–88 (1997).
- [248] Y. Hahn, “Relaxation of cold plasmas and threshold lowering effect,” *Phys. Rev. E* **64**, 046409 (2001).
- [249] G. Bannasch and T. Pohl, “Rydberg-atom formation in strongly correlated ultracold plasmas,” *Phys. Rev. A* **84**, 052710 (2011).
- [250] T. Pohl, D. Vrinceanu, and H. R. Sadeghpour, “Rydberg atom formation in ultracold plasmas: small energy transfer with large consequences,” *Phys. Rev. Lett.* **100**, 223201 (2008).
- [251] S. X. Hu, “Three-body recombination of atomic ions with slow electrons,” *Phys. Rev. Lett.* **98**, 133201 (2007).
- [252] F. Robicheaux and J. D. Hanson, “Simulation of the expansion of an ultracold plasma,” *Phys. Rev. Lett.* **88**, 055002 (2002).
- [253] P. Gupta, S. Laha, C. E. Simien, H. Gao, J. Castro, T. C. Killian, and T. Pohl, “Electron-temperature evolution in expanding ultracold plasmas,” *Phys. Rev. Lett.* **99**, 075005 (2007).
- [254] G. M. Lankhuijzen and L. D. Noordam, “Rydberg ionization: from field to photon,” *Adv. At. Mol. Opt. Phys.* **38**, 121–153 (1997).
- [255] T. F. Gallagher, “Above-threshold ionization in low-frequency limit,” *Phys. Rev. Lett.* **61**, 2304–2307 (1988).
- [256] T. F. Gallagher and T. J. Scholz, “Above-threshold ionization at 8 GHz,” *Phys. Lett. A* **40**, 2762–2765 (1989).
- [257] D. A. Tate, D. G. Papaioannou, and T. F. Gallagher, “Phase-sensitive above-threshold ionization of Rydberg atoms at 8 GHz,” *Phys. Lett. A* **42**, 5703–5708 (1990).

- [258] E. S. Shuman, R. R. Jones, and T. F. Gallagher, “Multiphoton assisted recombination,” *Phys. Rev. Lett.* **101**, 263001 (2008).
- [259] K. R. Overstreet, R. R. Jones, and T. F. Gallagher, “Phase-dependent electron recombination in a microwave field,” *Phys. Rev. Lett.* **106**, 033002 (2011).
- [260] P. H. Bucksbaum, R. R. Freeman, M. Bashkansky, and T. J. McIlrath, “Role of the ponderomotive potential in above-threshold ionization,” *J. Opt. Soc. Am. B* **4**, 760–764 (1987).
- [261] R. B. Watkins, R. B. Vrijen, W. M. Griffith, M. Gatzke, and T. F. Gallagher, “Microwave ionization of sodium with subnanosecond 8-GHz pulses,” *Phys. Rev. A* **56**, 4976–4984 (1997).
- [262] M. Abramowitz and I. A. Stegun, *Handbook of mathematical functions* (Dover, New York, 1972) 9th printing.
- [263] D. F. Zaretsky, Ph. A. Korneev, S. V. Popruzhenko, and W. Becker, “Landau damping in thin films irradiated by a strong laser field,” *J. Phys. B: At. Mol. Opt. Phys.* **37**, 4817–4830 (2004).
- [264] I. Yu. Kostyukov, “Inverse-Bremsstrahlung absorption of an intense laser field in cluster plasma,” *JETP Letters* **73**, 393–397 (2001).
- [265] L. D. Landau and E. M. Lifshitz, *Quantum mechanics* (Pergamon, Oxford, 1965) 2nd rev. ed.
- [266] D. F. Lawden, *Elliptic functions and applications* (Springer-Verlag, New York, 1989).
- [267] J. P. Boyd, *Chebyshev and Fourier spectral methods* (Dover, Mineola, 2001) 2nd rev. ed.
- [268] T. Kariya, R. Minami, T. Imai, M. Ota, Y. Endo, S. Kubo, T. Shimosuma, H. Takahashi, Y. Yoshimura, S. Ito, T. Mutoh, K. Sakamoto, and Y. Mitsunaka, “Development of 28 GHz and 77 GHz, mega-watt gyrotrons for fusion devices,” *J. Infrared Milli. Terahz. Waves* **32**, 295–310 (2011).
- [269] S. A. Schelkunoff, “Proposed symbols for the modified cosine and exponential integral,” *Quart. Appl. Math.* **2**, 90 (1944).

6

Ponderomotive manipulation of cold subwavelength plasmas

Abstract - Ponderomotive forces (PFs) induced in cold subwavelength plasmas by an externally applied electromagnetic wave are studied analytically. To this end, the plasma is modeled as a sphere with a radially varying permittivity, and the internal electric fields are calculated by solving the macroscopic Maxwell equations using an expansion in Debye potentials. It is found that the PF is directed opposite to the plasma density gradient, similarly to large-scale plasmas. In case of a uniform density profile, a residual spherically symmetric compressive PF is found, suggesting possibilities for contactless ponderomotive manipulation of homogeneous subwavelength objects. The presence of a surface PF on discontinuous plasma boundaries is derived. This force is essential for a microscopic description of the radiation-plasma interaction consistent with momentum conservation. It is shown that the PF integrated over the plasma volume is equivalent to the radiation pressure exerted on the plasma by the incident wave. The concept of radiative acceleration of subwavelength plasmas, proposed earlier, is applied to ultracold plasmas. It is estimated that these plasmas may be accelerated to keV ion energies, resulting in a neutralized beam with a brightness comparable to that of current high-performance ion sources.

Publication status - The work described in this chapter has been published by P. W. Smorenburg, L. P. J. Kamp, and O. J. Luiten in Phys. Rev. E **87**, 023101 (2013).

6.1 Introduction

Finite-sized plasmas driven by electromagnetic radiation are the subject of active studies in various research fields. Ultracold plasmas [270], which are created by photoionization of a cloud of laser-cooled atoms, are an exotic example of such finite-sized plasmas. They have an electron temperature as low as $T_e \sim 10$ K, an electron density in the range of $n_e \sim 10^{15} - 10^{16} \text{ m}^{-3}$, and consist of singly-ionized atoms. Ultracold plasmas are routinely probed with RF and microwave fields, enabling the observation of phenomena such as plasma oscillations [271, 272], Tonks-Dattner resonances [273], and modes associated with nonneutral plasmas [274, 275]. These observations in turn yield valuable fundamental insights into the plasma dynamics in the ultracold regime. Laser-irradiated nanoplasmas [276, 277] constitute another class of finite-sized plasmas driven by electromagnetic radiation. Laser-driven atomic clusters are utilized as novel sources of intense pulses of electrons [278, 279], ions [280], and extreme ultraviolet [281, 282] and x-ray [283] radiation. Directional proton beams can be produced by laser-irradiation of dense sub-micrometer-sized plasmas created from water droplets [284]. Because the plasma frequency $\omega_p \propto \sqrt{n_e}$ in nanoplasmas is a factor $\sim 10^5$ higher than in ultracold plasmas, nanoplasmas are usually subjected to optical rather than RF and microwave radiation. It is interesting that, despite the vastly different parameter regimes, ultracold plasmas and nanoplasmas have in common that the plasma size is smaller than the typically applied wavelength $\lambda \sim 2\pi c/\omega_p$.

As long as the fields driving a finite-sized plasma are not so large that the excursions of the oscillating plasma electrons become comparable to the plasma size, escape of electrons and the resulting subsequent Coulomb expansion of the plasma are relatively unimportant [285]. In this so-called ambipolar or quasi-neutral regime (usually at electric field strengths below 1 MV/m for microwave radiation or at laser intensities $I \lesssim 10^{20} \text{ W/m}^2$ for optical frequencies), the plasma dynamics can be described hydrodynamically. In the one-fluid plasma model [286], the plasma dynamics is governed by two force density contributions. The first of these is the well-known hydrodynamic force density $-\nabla p$, with $p = n_e k_B T_e$ the plasma pressure and k_B Boltzmann's constant, which is present regardless of whether or not an external field is applied. The other is the ponderomotive force density,

$$\mathbf{f} = -n_e \nabla \frac{e^2 E^2}{4m_e \omega^2} \equiv -n_e \nabla \phi_p, \quad (6.1)$$

induced by the external field. Here, e is the elementary charge, E the electric field strength, m_e the electron mass, ω the applied frequency, and ϕ_p is the so-called ponderomotive potential. The force Eq. (6.1) was originally derived for single electrons in an inhomogeneous ac field [287, 288], and later extended to plasma media on the basis of the plasma fluid equations [289, 290].

Eq. (6.1) is a time-averaged force density nonlinear in the field strength, and is therefore distinctly different from instantaneous linear forces that dominate in driven finite-sized plasmas under conditions of plasma resonance. The latter situation has been studied in earlier work [271–275], emphasizing the resonant absorption of energy and a considerable emission of electrons from the plasma. In contrast, the focus of this paper is on underdense plasmas where such resonant effects are absent, and the nonlinear force Eq. (6.1) becomes significant.

The relative importance of the hydrodynamic and ponderomotive forces, as is expressed in the ratio $\eta \equiv |-\nabla p|/|\mathbf{f}| \sim k_B T_e / \phi_p$, differs in nanoplasmas and ultracold plasmas in the quasi-neutral regime. Nanoplasmas have a temperature of at least ~ 1 keV, so that $\eta \gtrsim 1$ in the quasi-neutral regime, and hydrodynamic forces play an important role. Nevertheless, it has been recognized that ponderomotive forces can significantly modify the plasma dynamics even at relatively low intensities of $I \sim 10^{19}$ W/m² [291]. This reflects the complicated macroscopic behavior of dense finite plasmas, in which the hydrodynamic and electromagnetic effects are intertwined and difficult to study separately. In contrast, hydrodynamic forces are very small in ultracold plasmas. For $\omega/2\pi = 1$ GHz and $T_e = 10$ K, the force ratio $\eta < 10^{-2}$ already for field strengths $E > 10$ kV/m. In moderately to strongly driven ultracold plasmas, therefore, hydrodynamic forces are negligible compared to ponderomotive forces, contrary to the case of laser-excited nanoplasmas. This makes ultracold plasmas unique systems that can exhibit ponderomotive effects that are obscured in high-density plasmas.

In this chapter, we study the ponderomotive forces induced in a finite-sized plasma by an applied electromagnetic wave, which are particularly important in the dynamics of ultracold plasmas, but are relevant to finite-sized plasmas in general. We concentrate on the typical circumstance that the plasma is smaller than the applied wavelength. The plasma is modeled as a sphere with a radially varying permittivity, and the electric field distribution is calculated by solving the macroscopic Maxwell equations in terms of an expansion in Debye potentials. This approach is commonly used to study the far field scattering properties of finite objects [292–299], with little attention for the electromagnetic fields inside the object. An exception is a recent calculation of resonance absorption in dense atomic clusters based on the internal fields [300]. Here, we apply the technique to describe the opto-mechanical forces induced by the applied wave in the plasma itself. In view of the compressibility of the plasma, these forces form an essential part of the interaction dynamics. The following properties are found. First, the ponderomotive force in the plasma bulk is directed outwards for natural profiles $dn_e/dr < 0$ and inwards for ‘inverted’ profiles $dn_e/dr > 0$, where r is the radial coordinate. Although this is similar to well-studied large-scale plasmas [289], there are also differences due to the subwavelength character of the system.

Moreover, we find a spherically symmetric compressive ponderomotive force even in case of a completely uniform density. The latter suggests possibilities for contactless ponderomotive manipulation of subwavelength objects, which is not limited to plasmas but extends to other media with a well-defined uniform density. Second, we show that sharp plasma boundaries give rise to a ponderomotive surface force in addition to the volume force corresponding to Eq. (6.1). This surface force proves to be an essential ingredient in a correct local description of the interaction of electromagnetic waves with subwavelength objects that is consistent with momentum conservation. Third, we consider the total ponderomotive force integrated over the plasma volume and show that it is equivalent to the radiation pressure exerted on the plasma by the incident wave. In the past, it has been proposed to accelerate subwavelength plasmas with this radiation pressure [301, 302]. Here, we assess the feasibility of this scheme for ultracold plasmas. We estimate that these plasmas may be accelerated to keV ion energies thanks to their extremely low temperature and correspondingly weak tendency to expand.

This chapter is organized as follows. In order to properly describe the effects mentioned above, the electromagnetic fields and ponderomotive forces in the plasma are first formulated analytically in general terms in sections 6.2 and 6.3 respectively. These sections therefore have a mathematical character. Explicit results for the derived ponderomotive forces are summarized in section 6.3.2, Eqs. (6.24)-(6.26). These results are subsequently applied to concrete examples of plasmas in sections 6.4 to 6.6. In section 6.4, a plasma with uniform density is considered, the compressive ponderomotive force is found, and the role of the ponderomotive surface force in the radiation pressure on the plasma is elucidated. Section 6.5 concerns numerically calculated ponderomotive forces in inhomogeneous plasmas, exhibiting distinct bulk and surface contributions. In section 6.6, radiative acceleration of ultracold plasmas is discussed. Section 6.7 concludes this chapter.

6.2 Fields

6.2.1 Expansion in Debye potentials

We consider a collisionless, unmagnetized, cold, spherical plasma with radius b , in interaction with an incident linearly polarized plane wave with electric field $\mathbf{E}_{ext} = E_0 \mathbf{e}_x \exp(ikz - i\omega t)$ and magnetic field $c\mathbf{B}_{ext} = E_0 \mathbf{e}_y \exp(ikz - i\omega t)$. In this section, we discuss the electromagnetic field distribution in such a plasma. This field is in general different from the externally applied field due to the presence of oscillating plasma electrons, which act as field sources themselves. However, it is well-known [303] that the oscillating electrons plus the neutralizing ion background can be represented by a harmonically varying dipole density or polarization \mathbf{P} . Accordingly, the plasma can be treated as a lossless dielectric medium with relative permittivity $\epsilon = 1 - \omega_p^2/\omega^2$, where

$\omega_p(r) = \sqrt{n_e e^2 / (m_e \epsilon_0)}$ is the local plasma frequency associated with the electron density $n_e(r)$ at radius r , and ϵ_0 is the vacuum permittivity. The electromagnetic fields in the plasma thus satisfy the homogeneous macroscopic Maxwell equations [304]. Solution of these equations is analogous to the classical Mie scattering problem [305], generalized to an object with a radially varying permittivity $\epsilon = \epsilon(r)$. This generalization has been worked out previously [292, 293, 295, 297]; we reproduce the results here. The fields in the region $r < b$ inside the plasma can be decomposed [304] into an electric (transverse magnetic) part $(\mathbf{E}, \mathbf{B})^e$ with $B_r^e = 0$ and a magnetic (transverse electric) part $(\mathbf{E}, \mathbf{B})^m$ with $E_r^m = 0$. These fields can be written in terms of two scalar Debye potentials $\Pi^{e,m}(\mathbf{r})$ as [306]

$$\begin{aligned}
 \mathbf{E}^m &= E_0 \mathbf{r} \times \nabla \Pi^m; & i\omega \mathbf{B}^m &= \nabla \times \mathbf{E}^m; \\
 -c\mathbf{B}^e &= E_0 \mathbf{r} \times \nabla \Pi^e; & -i\omega \mathbf{D}^e &= \nabla \times \mathbf{H}^e,
 \end{aligned} \tag{6.2}$$

where $\mathbf{D}^e = \epsilon_0 \epsilon \mathbf{E}^e$ and $\mathbf{H}^e = \mathbf{B}^e / \mu_0$ with μ_0 the vacuum permeability, and factors $\exp(-i\omega t)$ have been suppressed. In spherical coordinates (r, θ, φ) , the potentials evaluate to $\Pi^{e,m} = \sum_{n=1}^{\infty} \Pi_n^{e,m}$ with

$$\Pi_n^{e,m} = i^n \frac{2n+1}{n(n+1)} f_n^{e,m}(r) P_n^1(\cos \theta) \Phi^{e,m}(\varphi), \tag{6.3}$$

in which $\Phi^e = \cos \varphi$, $\Phi^m = \sin \varphi$, and P_n^1 denotes the associated Legendre function [307]. The radial functions $f_n^{e,m}$ satisfy the differential equations

$$\mathcal{L}_n^{e,m} [r f_n^{e,m}] = 0; \tag{6.4}$$

$$\mathcal{L}_n^{e,m} \equiv \frac{d^2}{dr^2} + \frac{d(\ln \delta^{e,m})}{dr} \frac{d}{dr} + k^2 \epsilon - \frac{n(n+1)}{r^2}, \tag{6.5}$$

with $\delta^e = \epsilon^{-1}$ and $\delta^m = 1$, and the boundary conditions

$$f_n^{e,m} \text{ regular at } r = 0; \tag{6.6}$$

$$f_n^{e,m}(b) = \left[j_n + a_n^{e,m} h_n^{(1)} \right]_{r=b}; \tag{6.7}$$

$$\delta^{e,m} \frac{(r f_n^{e,m})}{dr} \Big|_{r=b} = \frac{d}{dr} \left[r j_n + a_n^{e,m} r h_n^{(1)} \right]_{r=b}. \tag{6.8}$$

The quantities $a_n^{e,m}$ in Eqs. (6.7)-(6.8) are constants, and j_n and $h_n^{(1)}$ denote the spherical Bessel and Hankel functions of the first kind [307] with argument kr , respectively. Eqs. (6.7)-(6.8) ensure proper matching of the internal and external fields at the plasma boundary. In Eqs. (6.2)-(6.3), each partial potential $\Pi_n^{e,m}$ with the corresponding electric field $\mathbf{E}_n^{e,m}$ induces a particular oscillation mode of the electrons in the plasma [305], which has a current distribution $\mathbf{J}_n^{e,m} \propto \mathbf{E}_n^{e,m}$. The radiation emitted from the plasma by the current $\mathbf{J}_n^{e,m}$ has the form of n th-order electric (e) or magnetic (m) multipole radiation, with an amplitude proportional to $a_n^{e,m}$.

6.2.2 Quasistatic limit

In sections 6.4 and 6.5, we will calculate ponderomotive forces for concrete examples of subwavelength plasmas, based on the fields formulated in section 6.2.1. However, for $kb \ll 1$ the electric field inside the plasma can be approximated [305] by the quasistatic field $\mathbf{E}_{qs} \exp(-i\omega t)$, where \mathbf{E}_{qs} is the self-consistent field that would result in the plasma if the applied field \mathbf{E}_{ext} were replaced by the static field $E_0 \mathbf{e}_x$. Here, we therefore briefly describe this quasistatic field as well, so that the corresponding ponderomotive forces can be compared to the forces based on the full-wave electric field of section 6.2.1. We find that both approaches often agree very well, as expected, which makes the quasistatic description a useful way to quickly gain an impression of the fields and forces in a subwavelength plasma. However, we will also show that certain important physical effects are completely missing from the quasistatic description. One should therefore always be careful when using this approximation, as the full-wave approach is imperative to reveal all aspects of the interaction of the plasma with the applied wave.

The field \mathbf{E}_{qs} satisfies the static Maxwell equations $\nabla \cdot (\epsilon \mathbf{E}_{qs}) = 0$ and $\nabla \times \mathbf{E}_{qs} = \mathbf{0}$. Substituting in these equations

$$\mathbf{E}_{qs} = -E_0 \nabla \phi \quad (6.9)$$

results in a partial differential equation for ϕ that can be separated in spherical coordinates by writing $\phi = \psi(r)Y(\theta, \varphi)$. Solutions for the angular part are the spherical harmonics, of which only the particular harmonic $Y = \sin \theta \cos \varphi$ suits the symmetry of the problem. Accordingly,

$$\phi = \psi(r) \sin \theta \cos \varphi, \quad (6.10)$$

where the radial function $\psi(r)$ is determined by the differential equation

$$\left[\frac{d^2}{dr^2} + \left(\frac{2}{r} + \frac{1}{\epsilon} \frac{d\epsilon}{dr} \right) \frac{d}{dr} - \frac{2}{r^2} \right] \psi = 0. \quad (6.11)$$

The accompanying boundary conditions are that ψ be regular at $r = 0$, that both ψ and $\epsilon d\psi/dr$ be continuous at $r = b$, and that $-E_0 \nabla \phi \rightarrow E_0 \mathbf{e}_x$ as $r \rightarrow \infty$. These conditions evaluate to

$$\psi(0) \text{ regular at } r = 0; \quad (6.12)$$

$$\left(\epsilon \frac{d\psi}{dr} + \frac{2\psi}{r} \right)_{r=b} = -3. \quad (6.13)$$

The quasistatic solution (6.9)-(6.13) also follows directly from the more general results of the previous section by taking the appropriate limits; see Appendix 6.A.

6.2.3 Real and imaginary parts of $f_n^{e,m}$

Although the quasistatic field Eqs. (6.9)-(6.13) is generally a good approximation when $kb \ll 1$, it lacks certain features that are essential to describe a number of physical effects. As we will show later, the latter include the presence of a nonzero radiation pressure on the plasma and a compressive ponderomotive force in case of a uniform density profile. The description of these effects requires the use of the full-wave solution of Section 6.2.1. In particular, the boundary conditions Eq. (6.7)-(6.8), and hence the functions $f_n^{e,m}$, are in general complex-valued. The presence of the nonzero imaginary parts of $f_n^{e,m}$ leads to phase shifts in the corresponding fields contributions, and these phase shifts give rise to the mentioned physical effects. To describe these effects adequately in the next sections, we derive here a new representation for the functions $f_n^{e,m}$ in which the real and imaginary parts are conveniently separated. Eliminating the constants $a_n^{e,m}$ from Eqs. (6.7)-(6.8) gives, at $r = b$,

$$\delta^{e,m} \frac{d(r f_n^{e,m})}{dr} - \frac{d(r h_n^{(1)})}{dr} \frac{f_n^{e,m}}{h_n^{(1)}} = r h_n^{(1)} \frac{d(j_n/h_n^{(1)})}{dr}. \quad (6.14)$$

Replacing the Bessel functions in Eq. (6.14) by their limiting value for small argument [307], it is apparent that the imaginary part of $f_n^{e,m}$ is very small. This suggests to define auxiliary functions $g_n^{e,m}$ that, like $f_n^{e,m}$, are regular solutions of the differential equation

$$\mathcal{L}_n^{e,m} [r g_n^{e,m}] = 0, \quad (6.15)$$

but instead with a real-valued boundary condition that at $r = b$

$$\left[\delta^{e,m} \frac{d}{dr} - \left(\frac{1}{b} + \frac{d}{dr} \ln |h_n^{(1)}| \right) \right] r g_n^{e,m} = - \frac{y_n}{kb |h_n^{(1)}|^2}. \quad (6.16)$$

Here, y_n denotes the spherical Bessel function of the second kind [307] with argument kr . Eq. (6.16) has been obtained by replacing $f_n^{e,m} \rightarrow g_n^{e,m}$ in Eq. (6.14) and taking the real part of the equation assuming real $g_n^{e,m}$. By construction, solution of Eqs. (6.15)-(6.16) yields real-valued functions $g_n^{e,m}$ that approximate the real part of $f_n^{e,m}$ for small kb . The imaginary part of $f_n^{e,m}$ can be extracted from $g_n^{e,m}$ as follows. Since $f_n^{e,m}$ and $g_n^{e,m}$ satisfy the same differential equations but different boundary conditions,

$$f_n^{e,m} = \gamma_n^{e,m} g_n^{e,m}, \quad (6.17)$$

where $\gamma_n^{e,m}$ are constants. To determine these constants, we substitute Eq. (6.17) in Eq. (6.14), simplify the result by using Eq. (6.16), and solve for $\gamma_n^{e,m}$. This gives

$$\gamma_n^{e,m} = 1 + \frac{(j_n - g_n^{e,m})(g_n^{e,m} + iy_n)}{y_n^2 + (g_n^{e,m})^2} \Big|_{r=b} \quad (6.18)$$

$$= 1 + i \frac{j_n - g_n^{e,m}}{y_n} \Big|_{r=b} + O[(kb)^{4n+2}]. \quad (6.19)$$

Eqs. (6.17)-(6.19) give the real and imaginary parts of $f_n^{e,m}$ separately.

6.3 Forces

6.3.1 Ponderomotive volume and surface forces

Gradients in the electric field formulated in section 6.2 give rise to a ponderomotive volume force density according to Eq. (6.1). In addition to this well-known volume force, there can also exist a ponderomotive surface force density or pressure π_p acting on the boundary of the plasma. The presence of a surface force is easily established from Eq. (6.1). Suppose that at $r = b$ the plasma density changes discontinuously from a finite value to zero, such that the permittivity discontinuously increases to unity. Then, because of the boundary conditions that both the perpendicular component of $\epsilon \mathbf{E}$ and the tangential component of \mathbf{E} be continuous at $r = b$, the squared magnitude E^2 in Eq. (6.1) must be discontinuous and ∇E^2 must behave like a delta function. This singular feature represents an infinitely large volume force density present in a shell with infinitesimally small volume, that is, a surface force density. To evaluate this surface force density, we consider the total, integrated ponderomotive force \mathbf{F} acting on the plasma. The integration volume V is chosen to be a sphere with radius $b^+ \equiv \lim_{\Delta \downarrow 0}(b + \Delta)$ concentric with the plasma. Then, V is split in two contributions as

$$\mathbf{F} = \int \mathbf{f} dV^- + \iint_{b^-}^{b^+} \mathbf{f} r^2 dr d\Omega, \quad (6.20)$$

where $b^- \equiv \lim_{\Delta \downarrow 0}(b - \Delta)$, the volume V^- is a sphere with radius b^- , and $\int d\Omega$ denotes integration over the angular coordinates. In this way, the singularity in the ponderomotive force density is contained in the second integral of Eq. (6.20), so that this term will give the surface contribution to \mathbf{F} , while the first integral represents the ordinary ponderomotive volume forces. Furthermore, \mathbf{f} may be written as the time-average of the divergence of a tensor [290]:

$$\mathbf{f} = \left\langle \nabla \cdot \left(\epsilon_0 \epsilon \mathbf{E} \mathbf{E} + \frac{1}{\mu_0} \mathbf{B} \mathbf{B} - U \mathbf{I} \right) \right\rangle \equiv \langle \nabla \cdot \mathbf{T} \rangle, \quad (6.21)$$

where \mathbf{I} is the identity tensor, $U = (\epsilon_0 E^2 + \mu_0^{-1} B^2)/2$, and μ_0 is the vacuum permeability, and angular brackets denote time-averaging. Using Eq. (6.21) and Gauss' theorem for tensors [308], the second integral of Eq. (6.20) may be rewritten as

$$\iint_{b^-}^{b^+} \mathbf{f} r^2 dr d\Omega = \left\langle \int d\Omega^+ \cdot \mathbf{T} - \int d\Omega^- \cdot \mathbf{T} \right\rangle, \quad (6.22)$$

where Ω^\pm are spherical surfaces at $r = b^\pm$ with outward normal. Writing out the tensors in Eq. (6.22), and using the boundary conditions for the fields to express all field components in terms of those at $r = b^-$, gives

$$\mathbf{F} = \int \mathbf{f} dV^- - \int \pi_p d\Omega^-, \quad (6.23)$$

in which $\pi_p = -\epsilon_0 (\epsilon - 1)^2 E_r^2 / 4$. The quantity π_p represents an additional ponderomotive pressure that acts on the surface of a plasma with an abrupt plasma boundary. This pressure is always negative, corresponding to a surface force density in the outward direction. A surface force similar to Eq. (6.23) has been obtained earlier for the special case of a plane wave refracted by a plane plasma boundary [309].

To some extent, the surface force density found here may appear to be an artifact of the ponderomotive force expression Eq. (6.1). After all, in the plasma context this expression has originally been derived from a perturbation expansion of the equation of motion of single electrons [287, 288], and in that sense seems to be an approximate quantity. However, the force Eq. (6.1) follows identically [290] from the tensor in Eq. (6.21), which in turn follows strictly from the thermodynamics of continuous media [310]. Moreover, we have checked that integration of the arguably more fundamental averaged Lorentz force density $\langle \rho \mathbf{E} + \mathbf{J} \times \mathbf{B} \rangle$ gives the same result Eq. (6.23). Furthermore, momentum conservation requires that the total force Eq. (6.23) on the plasma balances the rate of momentum loss from the radiation field. As we will show in the next section, this is only the case in presence of the surface force density. Therefore, Eq. (6.23) is the best that can be done within a continuum model of the plasma medium.

6.3.2 Evaluation of the forces

In order to facilitate practical application of the derived analytical results, we summarize the previous sections by listing explicit expressions for the various forces used in the remainder of the chapter. Substituting the electric field Eqs. (6.2)-(6.3) in Eq. (6.1), and performing all differentiations, gives the following spherical components of the ponderomotive force density:

$$f_j = \chi \epsilon_0 k E_0^2 \sum_{n=1}^{\infty} \sum_{m=1}^{\infty} \left\{ \text{Re} (i^{m-n} \gamma_n^{m*} \gamma_m^m) R_{nm}^{j1} S_{nm}^{j1} \right. \\ \left. + \text{Re} (i^{m-n} \gamma_n^{e*} \gamma_m^e) [R_{nm}^{j2} S_{nm}^{j2} + R_{nm}^{j3} S_{nm}^{j3}] - \text{Im} (i^{m-n} \gamma_n^{e*} \gamma_m^m) R_{nm}^{j4} S_{nm}^{j4} \right\}, \quad (6.24)$$

where $j = r, \theta, \varphi$ and $\chi \equiv \epsilon - 1 = -\omega_p^2/\omega^2$. The functions $R = R(r)$ and $S = S(\theta, \varphi)$ are listed in Appendix 6.B. Note that the magnitude of the various contributions to the force essentially depend on the phase of the factors $\gamma_n^{e,m}$, which makes the formulation of section 6.2.3 particularly convenient for force calculations. Evaluation of the total ponderomotive force Eq. (6.23) requires integration of Eq. (6.24) over the plasma volume. The angular integrations can be performed analytically, and most terms in Eq. (6.24) integrate to zero. The cartesian x - and y -components of \mathbf{F} vanish completely in the integration over φ . In the remaining z component, only terms with particular combinations of n and m survive the integration over θ , which is shown in Appendix 6.B. The resulting total volume force is

$$\int \mathbf{f} dV^- = -\frac{\pi\epsilon_0 E_0^2}{k^2} \mathbf{e}_z \times \sum_{n=1}^{\infty} \left[\text{Im}(\gamma_n^{m*} \gamma_{n+1}^m) Y_n^1 + \text{Im}(\gamma_n^{e*} \gamma_{n+1}^e) (Y_n^2 + Y_n^3) + \text{Im}(\gamma_n^{e*} \gamma_n^m) Y_n^4 \right], \quad (6.25)$$

where the quantities $Y_n^{1,2,3,4}$ are one-dimensional integrals over $r = 0$ to b^- involving the functions $g_n^{e,m}$; these integrals are given in Eqs. (6.58)-(6.61). From Eq. (6.25) it is apparent that only modes in the combinations $(\mathbf{E}_n^e, \mathbf{E}_{n+1}^e)$, $(\mathbf{E}_n^m, \mathbf{E}_{n+1}^m)$, and $(\mathbf{E}_n^e, \mathbf{E}_n^m)$ give nonzero contributions to the total ponderomotive volume force. That is, these are the combinations that give rise to a force density with a preferred direction. The surface force in Eq. (6.23) involves only the electric (transverse magnetic) modes \mathbf{E}_n^e since these are the only ones having a nonzero radial electric field component E_r . Analogous to the volume force above, in the angular integrations of Eq. (6.23) all terms in E_r^2 vanish except for products $E_{n,r}^{e*} E_{n+1,r}^e$, resulting in

$$\int \pi_p d\Omega^- = \left[\frac{\pi\epsilon_0 E_0^2}{k^2} \mathbf{e}_z \frac{(\epsilon - 1)^2}{\epsilon^2} \sum_{n=1}^{\infty} n(n+1)(n+2) \text{Im}(\gamma_n^{e*} \gamma_{n+1}^e) g_n^e g_{n+1}^e \right]_{r=b^-}. \quad (6.26)$$

6.4 Homogeneous plasma

In the previous two sections, the fields and force densities induced by an electromagnetic wave in a spherical plasma with arbitrary $\epsilon(r)$ were formulated. In the remainder of this chapter, we apply the results to a number of practical density profiles. Here, we start with plasmas with uniform density, which is one of the few density profiles for which analytical expressions for the fields are available. This will enable us to validate the results of the previous sections. In addition, the limit of small radius allows for simple analytical expressions for both the ponderomotive force density and the total force. This yields some interesting new insights in the way radiation interacts with subwavelength objects.

6.4.1 Fields

We first verify the field expressions of section 6.2. For a uniform plasma density giving a constant relative permittivity ϵ_1 , Eq. (6.4) reduces to the spherical Bessel differential equation, and the expressions of section 6.2.1 reduce to the well-known Mie results [305]. For the quasistatic case $kb \ll 1$ of section 6.2.2, Eq. (6.11) reduces to the Euler differential equation, and it is found that $\psi = -3r/(\epsilon_1 + 2)$. This gives $\mathbf{E}_{qs} = 3E_0\mathbf{e}_x/(\epsilon_1 + 2)$, which is the well-known constant electric field in a homogeneous material sphere placed in a uniform static field [304], or the Mie solution in the Rayleigh limit $kb \rightarrow 0$ [305].

Using the functions $g_n^{e,m}$ of section 6.2.3 to evaluate the fields yields

$$g_n^{e,m} = A_n^{e,m} j_n(\sqrt{\epsilon_1}kr), \quad (6.27)$$

where the constants $A_n^{e,m}$ are obtained from the boundary condition Eq. (6.16). Explicit expressions are given in Appendix 6.C. It is also shown there that the functions $f_n^{e,m} = \gamma_n^{e,m} g_n^{e,m}$, from which the potentials Eq. (6.3) are generated, are equal to

$$f_n^e = \sqrt{\epsilon_1} d_n j_n(\sqrt{\epsilon_1}kr); \quad f_n^m = c_n j_n(\sqrt{\epsilon_1}kr), \quad (6.28)$$

where c_n and d_n are the coefficients of the internal field of the Mie solution in the customary formulation [305]. Comparison of the field definitions Eqs. (6.2)-(6.3) with those of the Mie solution [305] indeed confirms Eq. (6.28). All results of section 6.2 thus correctly reduce to the Mie solution in the special case of uniform permittivity.

6.4.2 Ponderomotive compression

For a homogeneous plasma, the ponderomotive force density Eq. (6.24) is readily evaluated by substituting Eq. (6.27), using the results Eqs. (6.62)-(6.63) for $A_n^{e,m}$ and $\gamma_n^{e,m}$. For the general case, this gives a series of elaborate expressions in terms of Bessel functions. A more manageable result is obtained in the small radius limit $kb \ll 1$, where the first few terms of the power series expansions Eqs. (6.66)-(6.73) for $A_n^{e,m}$ and $\gamma_n^{e,m}$ suffice. Using the latter in Eq. (6.24) gives, after considerable but straightforward algebra, the following lowest-order cartesian components of the ponderomotive force density:

$$\begin{aligned} \mathbf{f} &= -\frac{\chi_1^2 \epsilon_0 k^2 E_0^2 (ux\mathbf{e}_x + vy\mathbf{e}_y + wz\mathbf{e}_z)}{10(\epsilon_1 + 2)^2 (2\epsilon_1 + 3)^2 (3\epsilon_1 + 4)} + \dots; \\ u &= 458 + 807\epsilon_1 + 432\epsilon_1^2 + 43\epsilon_1^3 - 15\epsilon_1^4; \\ v &= 3(2\epsilon_1 + 3)^2 (18 + 13\epsilon_1); \\ w &= 416 + 794\epsilon_1 + 469\epsilon_1^2 + 61\epsilon_1^3 - 15\epsilon_1^4, \end{aligned} \quad (6.29)$$

where $\chi_1 = \epsilon_1 - 1$ and the dots represent terms of order $O(b^3, r^3)$. Interestingly, Eq. (6.29) shows that a ponderomotive force density is present in the plasma which scales linearly with position in all three (x, y, z) -directions. Figure 6.1 shows the corresponding three 'spring constants' $df_x/dx, df_y/dy, df_z/dz$ as function of ϵ_1 . Remarkably, the magnitude of the force density is almost equal in all directions irrespective of ϵ_1 . This is despite the fact that the exciting electromagnetic wave is not at all spherically symmetric, but propagates in the z -direction and is polarized in the x -direction. Moreover, the sign of each force component is opposite to that of the corresponding coordinate. Eq. (6.29) thus represents an almost isotropic, compressive ponderomotive force. In Fig. 6.1, the force correctly vanishes for $\epsilon_1 \uparrow 1$, that is, in the limit of an infinitely rarified plasma. We deliberately displayed only underdense plasmas to avoid the complication of plasma resonances. The latter necessitate a more detailed model of the permittivity including damping, which is outside the scope of this thesis. However, since no assumptions about the particular form of ϵ_1 have been made in deriving Eq. (6.29), this expression is valid as well for more detailed descriptions of the plasma medium.

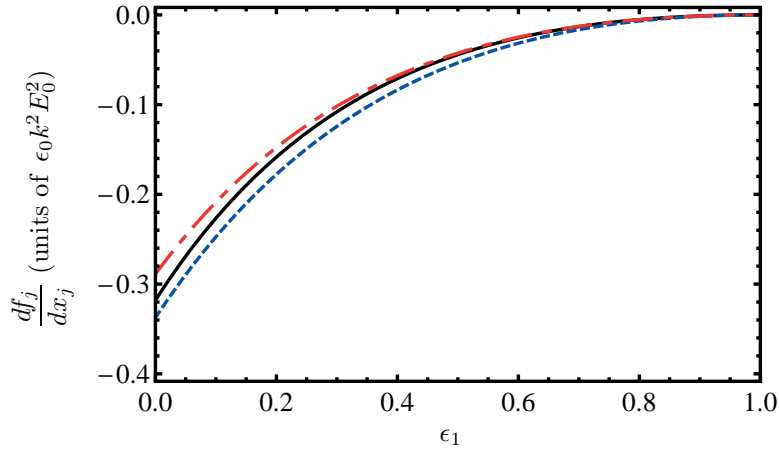


Figure 6.1: Cartesian x - (black solid), y - (blue dashed) and z - (red dash-dotted) components of the ponderomotive force Eq. (6.29), divided by the corresponding coordinate, as a function of the permittivity of the plasma.

Note that any compression is completely absent in the quasistatic description, which predicts a perfectly constant electric field in the plasma and hence a vanishing ponderomotive force. The full-wave description of section 6.2.1 is therefore essential to obtain Eq. (6.29). We also remark that Eq. (6.29) has some analogy with the magnetic pinch force familiar from stationary currents, which is due to the self-generated magnetic field. In the case of our small driven plasma, a representative magnitude of the current densities present in the plasma is that of the electric dipole mode, which is

$\mathbf{J}_1^e \approx -3i\epsilon_0\chi_1\omega E_0\mathbf{e}_x/(\epsilon_1 + 2)$. According to the Biot-Savart law [304], a hypothetical spherical medium carrying a stationary current density \mathbf{J}_1^e would generate a magnetic field equal to $\mu_0\mathbf{J}_1^e \times \mathbf{r}/3$. The resulting Lorentz force density would be directed toward the x -axis and would have a magnitude of $-3\epsilon_0\chi_1^2k^2E_0^2\sqrt{y^2 + z^2}/(\epsilon_1 + 2)^2$. The similarity with Eq. (6.17) is evident, both regarding the magnitude and the proportionality with position. The driven plasma we consider, of course, is more complex than this crude model because the currents are both time-varying and have more structure than \mathbf{J}_1^e . In addition, electric forces play an equally important role. For these reasons, the ponderomotive force turns out to be Eq. (6.29) rather than the force just described, that is, the force is approximately radially compressive rather than pinching toward a single axis.

Ponderomotive compression by means of the force Eq. (6.29) seems interesting for technological applications such as confinement of spherical subwavelength plasmas. However, Eq. (6.29) is in fact the lowest-order correction to the ponderomotive force due to the quasistatic field, which coincidentally vanishes for the special case of a homogeneous plasma. For other than uniform density profiles, the ponderomotive force is dominated by the inhomogeneous quasistatic field, as we will show in the next section. Therefore the applicability of Eq. (6.29) to practical plasmas is limited. On the other hand, Eq. (6.29) is very relevant in scattering experiments where other media with a well-defined constant density, such as water droplets, are subjected to electromagnetic radiation [311–313]. In addition, delicate physical processes that require contact-free observation of levitated droplets, such as surface vibrations [314], ice nucleation [315], and crystallization of salts [316], may be manipulated ponderomotively by application of an electromagnetic wave.

6.4.3 Total ponderomotive force

We next consider the total force on the plasma caused by the interaction with the incident wave. In scattering theory, the total force due to an incident wave is usually not formulated in terms of force densities, but rather is derived by calculating the rate at which momentum is carried away by the scattered radiation in the far field. This rate is identified with the total force on the body on account of momentum conservation [317]. In terms of the scattering coefficients $a_n^{e,m}$ in Eqs. (6.7)-(6.8), the force reads [292, 306]

$$\begin{aligned}
 \mathbf{F} &= \frac{2\pi I}{k^2 c} \mathbf{e}_z \\
 &\times \operatorname{Re} \sum_{n=1}^{\infty} \left[(2n+1)(a_n^e + a_n^m) - \frac{2n(n+2)}{n+1} (a_n^{e*} a_{n+1}^e + a_n^{m*} a_{n+1}^m) - \frac{2(2n+1)}{n(n+1)} a_n^{e*} a_n^m \right].
 \end{aligned} \tag{6.30}$$

In case of a small dielectric spherical scatterer with uniform permittivity ϵ_1 and radius $b \ll k^{-1}$, Eq. (6.30) gives the following expansion [292, 306]:

$$\mathbf{F} = \frac{8\pi k^4 b^6}{3} \frac{\chi_1^2}{(\epsilon_1 + 2)^2} \frac{I}{c} \mathbf{e}_z \left(1 - \frac{120 + 34\epsilon_1 - 29\epsilon_1^2 + \epsilon_1^3}{(\epsilon_1 + 2)(2\epsilon_1 + 3)} (kb)^2 + \dots \right). \quad (6.31)$$

Although certainly correct, this derivation of Eq. (6.31) does not give any information about the distribution of the force over the scatterer. This is contrary to calculating \mathbf{F} by integrating force densities such as in Eq. (6.23), where one starts from the force distribution itself. In particular, it becomes clear that only part of the force is acting on the bulk, the remainder presenting itself in the form of a surface force. To our knowledge, such a direct analytical evaluation of the force on a scattering sphere from the local fields has never been given, although the force Eq. (6.31) has been reproduced for special cases by numerically integrating the Maxwell stress tensor over the surface of the sphere [318], and by adding numerically calculated forces on a grid of dipoles representing the sphere [319]. Nevertheless, the force integration Eq. (6.23) also correctly leads to Eq. (6.31). Namely, substituting Eq. (6.27) together with the results (6.66)-(6.73) in the force expressions Eqs. (6.25)-(6.26), it is found that

$$\int \mathbf{f} dV^- = \frac{8\pi k^4 b^6}{3} \frac{\chi_1^2}{(\epsilon_1 + 2)^2} \frac{I}{c} \mathbf{e}_z \left(\frac{\epsilon_1 + 4}{2\epsilon_1 + 3} - \frac{Q_1 (kb)^2}{210(\epsilon_1 + 2)(2\epsilon_1 + 3)^2} + \dots \right); \quad (6.32)$$

$$-\int \pi_p d\Omega^- = \frac{8\pi k^4 b^6}{3} \frac{\chi_1^2}{(\epsilon_1 + 2)^2} \frac{I}{c} \mathbf{e}_z \left(\frac{\chi_1}{2\epsilon_1 + 3} - \frac{\chi_1 Q_2 (kb)^2}{70(\epsilon_1 + 2)(2\epsilon_1 + 3)^2} + \dots \right), \quad (6.33)$$

with

$$Q_1 \equiv 6720 + 3342\epsilon_1 - 1055\epsilon_1^2 - 215\epsilon_1^3 + 28\epsilon_1^4;$$

$$Q_2 \equiv 560 + 78\epsilon_1 - 185\epsilon_1^2.$$

Adding Eqs. (6.32)-(6.33) reproduces the total ponderomotive force Eq. (6.31) that was derived from momentum conservation. This confirms the validity of Eq. (6.23).

In Eqs. (6.32)-(6.33), the first terms in the large braces are dominant for small kb . Interestingly, the volume and surface contributions to the total force act in opposite directions, since χ_1 is negative for plasmas. Furthermore, the division of the total ponderomotive force into the volume and surface contributions is dependent on ϵ_1 , which is shown in Fig. 6.2. As before, the forces correctly vanish in the limit $\epsilon_1 \uparrow 1$ of an infinitely rarified plasma. The ratio of the magnitude of the surface contribution to that of the volume contribution grows as ϵ_1 drops, increasing to as much as 1/4 for $\epsilon_1 = 0$. This shows the ponderomotive surface force derived in section 6.3.1 is not merely a small correction to the conventional volume ponderomotive force, but rather is an essential ingredient in a correct local description of the radiation pressure on subwavelength objects.

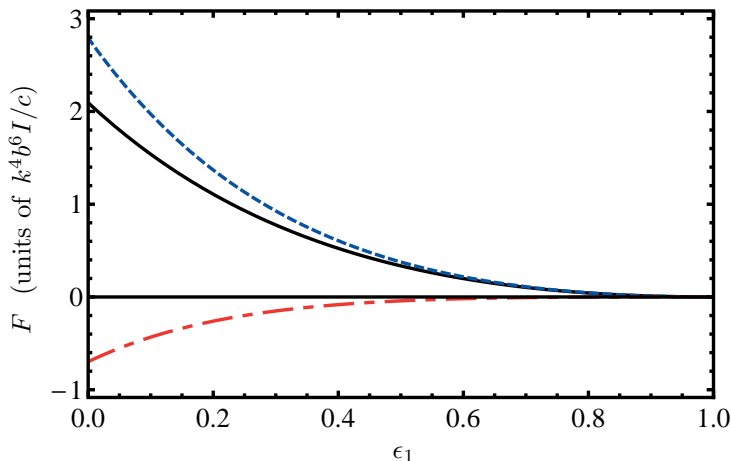


Figure 6.2: Division of total ponderomotive force Eq. (6.23) (black solid) into the volume contribution Eq. (6.32) (blue dashed) and surface contribution Eq. (6.33) (red dash-dotted) as a function of the permittivity of the plasma, for sufficiently small kb .

Finally, we note that we have only considered the limit $kb \ll 1$ here. It would be interesting to show analytically the equality of Eq. (6.23) with the general expression Eq. (6.30) for arbitrary kb . It is encouraging that the products of scattering coefficients in the second line of Eq. (6.30) represent the same combinations of modes that contribute to the integrated ponderomotive volume force Eq. (6.25). On the other hand, the single coefficients in the first line of Eq. (6.30) do not have an analogue in Eq. (6.25), which suggests that it is probably necessary to use certain special properties as well as recurrence relations for the Mie coefficients [320].

6.5 Inhomogeneous plasmas

The homogeneous plasma considered above allowed us to validate the analytical results of sections 6.2 and 6.3. In this section, we proceed to plasmas with radially varying density profiles. Lacking analytical solutions to the differential equations (6.15) that determine the fields, the results will be necessarily numerical. Experimentally, nanoplasmas that are field-ionized by laser pulses usually exhibit a natural density profile in which $dn_e/dr < 0$ everywhere. In contrast, ultracold plasmas may be created with any desired density profile by photo-ionizing an atomic cloud using imaging techniques [321]. In particular, 'inverted' profiles in which $dn_e/dr > 0$ in some range of r are possible. Such an inverted profile also results naturally when using sufficiently dense atomic clouds, that in their central region are optically thick for the excitation laser involved in the ionization scheme.

6.5.1 Ponderomotive force distribution

We have calculated the distribution of the ponderomotive force density for several density profiles by numerically solving the boundary value problem Eqs. (6.15)-(6.16) for the first few modes, and subsequently evaluating Eq. (6.24) truncated at $n \leq 3, m \leq 3$. We have concentrated on subwavelength plasmas with $kb \sim 0.1$, so that the truncated series proved to be sufficient to approximate the exact force density accurately. A shooting method was used to solve Eqs. (6.15)-(6.16), in which the numerical stability was improved by switching variables from $g_n^{e,m}$ to $x_n^{e,m} = g_n^{e,m}/(kr)^n$, and avoiding the singular point at $r = 0$ by imposing the condition $dx_n^{e,m}/dr = 0$ at a finite radius $r = r_0 \ll b$. Decreasing r_0 to $0.01b$ yielded sufficiently converged results.

In order to test our numerical code, we have calculated the force density in a homogeneous plasma with a smoothed edge according to the density profile $n_e(r) = \{1 - \tanh[\alpha(r/b - 9/10)]\} n_0/2 \equiv n_1(r)$, where α is a dimensionless parameter. Choosing $kb = 1/9$, this profile represents a plasma with density n_0 , which at radius $1/(10k)$ drops smoothly to zero within a small distance of about $4/(\alpha k)$. In Fig. 6.3(a), this profile is shown as the red dash-dotted line, with the corresponding vertical axis on the right of the figure. Since the calculational domain extends to $r = b$, the force density is thus evaluated up to radii outside the plasma, rather than up to an arbitrary point somewhere in the edge region $r \approx 1/(10k)$. The benefit of this approach over using the simpler discontinuous profile $n_e(r) = n_0\Theta(r - b)$ is that it is possible to study the volume force density in the edge region, which must tend to the surface force density in Eq. (6.23) as $\alpha \rightarrow \infty$. In the calculations, the plasma density n_0 was chosen such that $\epsilon_1 \equiv 1 - n_0 e^2/(\epsilon_0 m_e \omega^2) = 0.19$. In Fig. 6.3, the radial component of the volume force density Eq. (6.24) along the positive x -axis is shown by the black solid line, for $\alpha = 200$. We have deliberately chosen to present the x -direction, which is the polarization axis of the incident wave, because in this direction there is a strong radial electric field component E_r . Hence the surface force density defined in Eq. (6.23) is clearly exhibited, in contrast to some other directions such as the y -axis in which the surface force vanishes. It was derived in section 6.4.2 that, in the bulk of the plasma, the ponderomotive force density should be compressive and proportional to r , and given by Eq. (6.29). The latter result is indicated in Fig. 6.3(a) by the blue dots. The numerical data closely follow the analytical result, which validates our numerical code. The black dashed line in Fig. 6.3(a) show the force density according to the quasistatic electric field, which is determined by Eq. (6.9)-(6.13). As expected, the linear ponderomotive force is absent from the quasistatic description because the latter predicts a uniform electric field in the plasma bulk.

In Fig. 6.3(a) near the plasma edge at $kr = 1/(10k)$, the ponderomotive force density exhibits a steep positive peak. Fig. 6.3(b) is a close-up of the edge region, showing that this peak is positioned just on the inner side of the plasma edge. Note

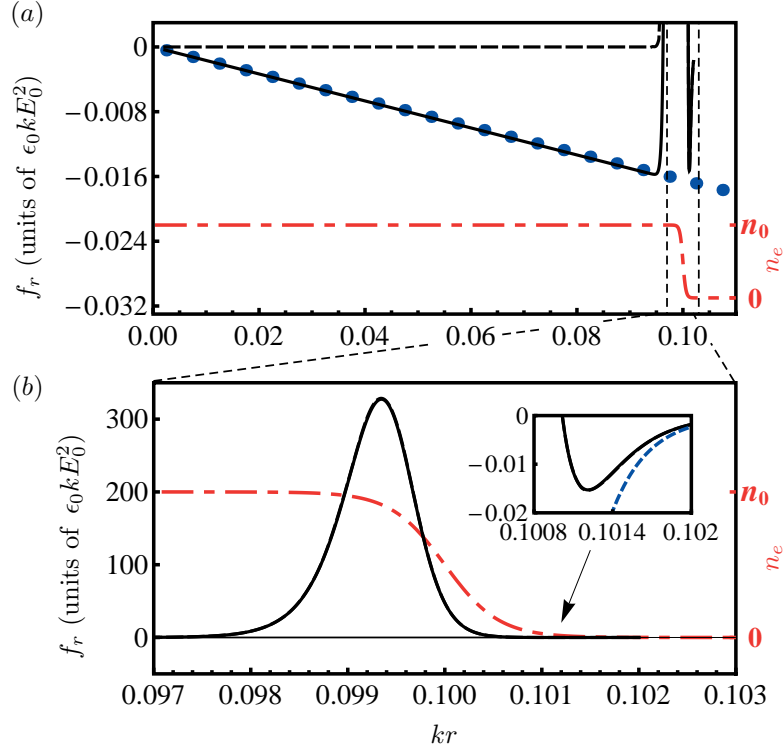


Figure 6.3: Radial component of the ponderomotive force density along the line $y = z = 0$, for a homogeneous plasma with smoothed edge. (a) Force density in the plasma bulk according to numerical evaluation of Eq. (6.24) assuming the full field (black solid), numerical evaluation of Eq. (6.1) assuming the quasistatic approximation (black dashed), and the analytical result Eq. (6.29) (blue dots). For orientation, the plasma density (red dot-dashed line) is shown together with the results. (b) Close-up of the edge region indicated by the vertical dashed lines in the upper panel. The dashed and solid curves overlap. The inset is a close-up of the horizontal axis, showing also the force Eq. (6.1) assuming the field of an equivalent electric dipole (blue dashed).

that the quasistatic field is also sufficient to correctly describe this feature, since the solid and dashed curves overlap perfectly. We found that for increasing values of α , the peak becomes ever higher and narrower, but the energy density defined by the surface area below the peak $u_0 = \int f_r dr$ stays approximately constant. This suggests that the peak will tend to the surface force density in Eq. (6.23) as $\alpha \rightarrow \infty$. The surface area u_1 represented by the latter is obtained by writing the surface force density $\pi_p \mathbf{e}_r$ at position $(x, y, z) = (b, 0, 0)$ as the volume force density $\mathbf{f}_p \equiv \pi_p \delta(r - b) \mathbf{e}_r$. Integrating $f_{p,r}$, and using the quasistatic approximation $E_r \approx 3E_0/(\epsilon_1 + 2)$, gives for the present case

$$u_1 = \int_{b^-}^{b^+} f_{p,r} dr = \frac{9\epsilon_0\chi_1^2 E_0^2}{4(\epsilon_1 + 2)^2} = 0.308\epsilon_0 E_0^2. \quad (6.34)$$

Numerical integration of a spline interpolation of the peak in Fig. 6.3(b) gives $u_0 = 0.307\epsilon_0 E_0^2$, in excellent agreement with Eq. (6.34). This confirms that the peaked volume force is the analogue of the surface force present in the limit of a discontinuous plasma boundary. The outward ponderomotive force in the plasma edge region is reminiscent of a similar force that is found in case of a one-dimensional stratified plasma layer irradiated by a plane wave [289]. However, the latter force is usually obtained by resorting to the WKB approximation to find the electric field, which is valid only when the plasma scale length is much larger than the wavelength. This is clearly not applicable for the subwavelength plasmas considered here. Furthermore, in the one-dimensional large scale length case, the force is proportional to $-\nabla n_e$ [289]. This is not found in our case either, as evidenced by the fact that the peak in Fig. 6.3(b) does not coincide with the inflection point of the density at $kr = 0.1$.

In Fig. 6.3(b), at the right side of the peak the force has a small overshoot to negative values, which is shown in the inset. The overshoot is visible as well in Fig. 6.3(a). The overshoot is caused by the inhomogeneous electric field outside the plasma, which is approximately that of an oscillating electric dipole [304]. Since the plasma density has not yet completely vanished around $kr = 0.1014$, the electric field gradient present there leads to a small but finite negative ponderomotive force density. The blue dashed line in the inset of Fig. 6.3(b) shows the force density Eq. (6.1) assuming the mentioned dipole field. The numerical result indeed approaches this line.

Figure 6.4 shows the ponderomotive force density for the plasma profiles $n_e(r) = \{3 \pm [1 - 200(kr)^2]\} n_1(r)/4$, where $n_1(r)$ was defined above, again evaluated along the positive x -axis. The profile with a plus (minus) sign represents a plasma with a quadratic bulge (dip) of the density in the central region, but with the same smoothed edge as in Fig. 6.3. The most important difference with respect to the flat profile discussed above is that the force density in the bulk is significantly larger than the linearly varying force density shown in Fig. 6.3(a). This is because already in the quasistatic approximation, the electric field for the profiles of Fig. 6.4 is inhomogeneous, whereas in the plasma of Fig. 6.3 it is constant. Therefore, the ponderomotive force depicted in Fig. 6.3 consists of merely small corrections to the vanishing contribution of the quasistatic field, whereas in Fig. 6.4(a) and 6.4(c) the force is completely dominated by the gradient of the quasistatic field itself. This is confirmed by the fact that the quasistatic and exact results in Fig. 6.4 overlap perfectly.

Interestingly, the direction of the ponderomotive force in Figs. 6.4(a) and 6.4(c) depends on the type of plasma profile: for natural profiles with $dn_e/dr < 0$, the force is directed outward; for inverted profiles with $dn_e/dr > 0$, it points inward. This

suggests that it is possible, at least in the plasma bulk, to tailor the force distribution by choosing a suitable initial density profile. For instance, it may be possible to devise a plasma in which ponderomotive forces balance hydrodynamic forces locally, which would mean that the plasma is stabilized rather than disturbed by application of an electromagnetic wave. However, the freedom to manipulate the ponderomotive force density is much more restricted in the edge region. Regardless of the type of density profile, at the plasma boundary the steep gradient in the plasma density invariably leads to the strongly peaked and outward ponderomotive force density found before, as is illustrated by Figs. 6.4(b) and 6.4(d). Obviously, this outward force is unfavorable for the stability of the plasma as it will tend to push electrons outwards.

6.5.2 Total ponderomotive force

We have calculated the total ponderomotive force acting on the plasmas considered in the previous section, by numerically evaluating the volume force integration Eq. (6.25) truncated at $n \leq 3$. The resulting forces are shown in Fig. 6.5 as a function of the permittivity ϵ_1 . Crosses represent the data according to Eq. (6.25). As a check, the forces have been calculated alternatively in terms of the scattered radiation, by numerically evaluating the scattering coefficients with Eq. (6.7), and substituting these coefficients in Eq. (6.30). The resulting forces are shown in Fig. 6.5 as open squares. Evidently, both methods agree very well, confirming the validity of Eq. (6.25) for arbitrary density profiles.

For a given value of ϵ_1 , the total force on the plasma with a quadratic dip (D) is systematically smaller than that on the homogeneous plasma (H) with the same radius, and the force on the plasma with a quadratic bulge (B) is still smaller. This is easily explained in terms of the radiation scattered from the incident wave by the three plasmas. At the chosen plasma size $kb = 1/9$, the electrons in the plasma move more or less coherently, so that the scattered radiation is predominantly electric dipole radiation with the radiated power proportional to the number N of electrons squared. By conservation of momentum, the momentum lost from the incident wave and therefore the resulting total force on the plasma are proportional to N^2 as well. For the three plasmas considered in Fig. 6.5, equal ϵ_1 implies equal densities n_0 , resulting in squared numbers of electrons in the ratios $N_H^2 : N_D^2 : N_B^2 = 1 : 0.64 : 0.49$. These ratios roughly fit the relative heights of the curves in Fig. 6.5. However, the coherent model just given is not precise, first because both higher order multipole moments and directional asymmetry in the scattered radiation have been neglected, and second because profile dependent resonant behavior for ϵ_1 near 0 has been disregarded. Nevertheless, we have numerically confirmed that the relative amplitudes of the total force on the three considered plasmas indeed tend to $N_H^2 : N_D^2 : N_B^2$ in the limits $kb \rightarrow 0$ and $\epsilon_1 \rightarrow 1$ where the coherent model becomes exact.

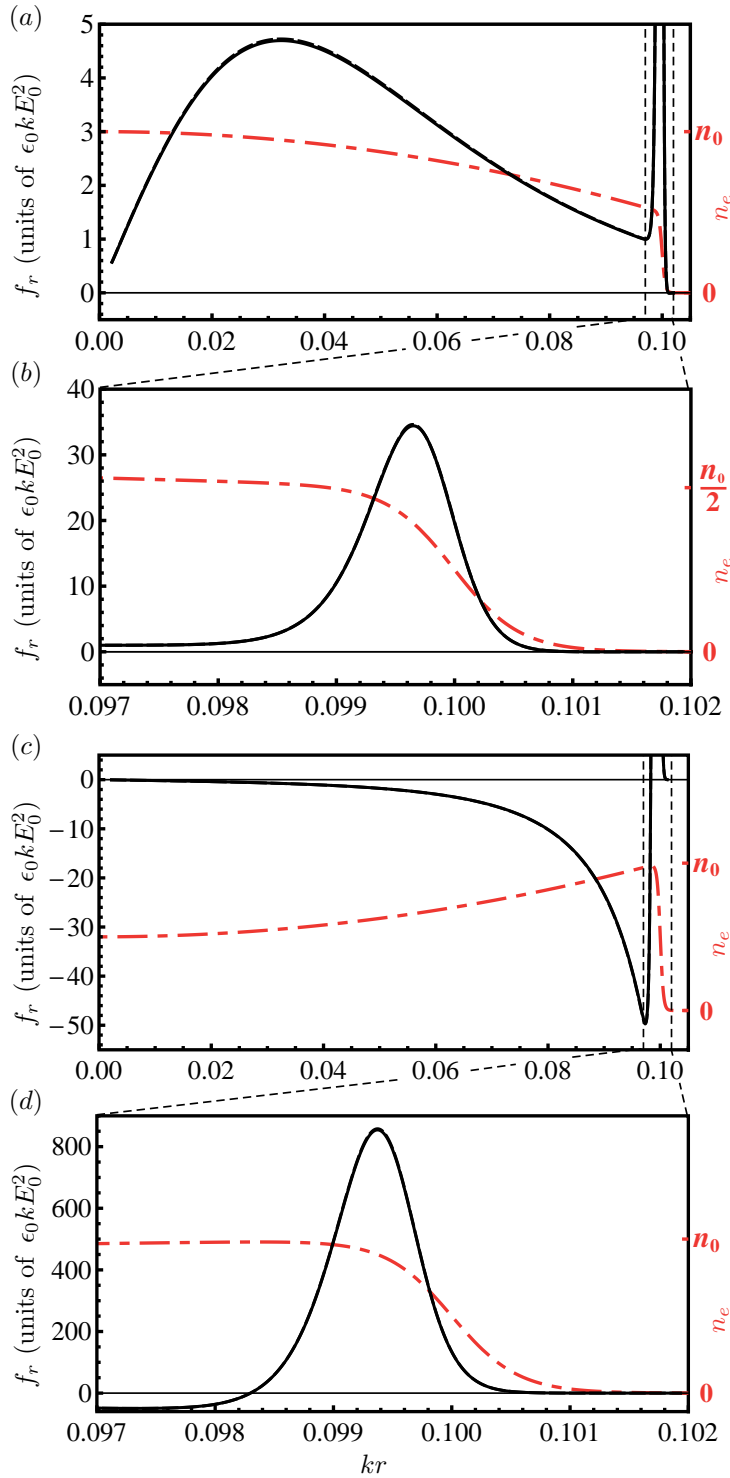


Figure 6.4: Radial component of the ponderomotive force density along the line $y = z = 0$, for density profiles with a smoothed edge and a quadratic bulge (a),(b) and dip (c),(d). For further details, see Fig. 6.3.

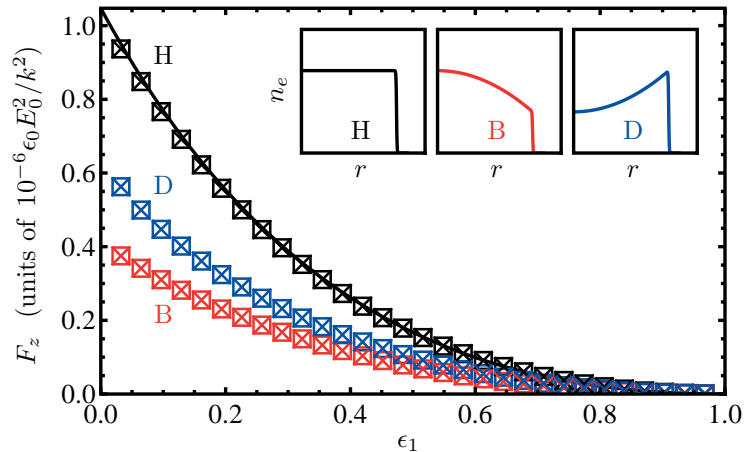


Figure 6.5: Total ponderomotive force as a function of the permittivity at the density n_0 , according to scattering theory (numerical evaluation of Eq. (6.30), open squares), integration of the volume force Eq. (6.25) (crosses), and Eq. (6.30) using the well-known Mie-coefficients (black solid line). Results are shown for a uniform profile (black, 'H') and profiles with a quadratic bulge (red, 'B') and dip (blue, 'D'); these profiles were defined in section 6.5.1 and have been sketched in the insets.

6.6 Acceleration of ultracold plasmas

In the previous sections, we have carefully examined both the distribution of ponderomotive force in an electromagnetically driven subwavelength plasma, and the total resultant force derived from it by volume integration. In summary, it was found that in the plasma bulk the ponderomotive force is directed radially inwards for inverted density profiles, that a strongly localized outward force dominates near the very edge of the plasma, and that the total force on the plasma is approximately proportional to N^2 . We are now in the position to assess the feasibility of practical acceleration of subwavelength plasmas based on the total ponderomotive force. This concept was put forward in the past by Veksler [301] and reviewed by Motz and Watson [302]. The original formulation [301] of the acceleration mechanism was that subwavelength plasmas should scatter incident radiation at an energy rate of N^2 times the single electron value $\sigma_T I$, where $\sigma_T = e^4 / (6\pi\epsilon_0^2 m_e^2 c^4)$ is the Thomson cross section. By conservation of momentum, this leads to a rate of momentum transfer to (or accelerating force on) the plasma of $N^2 \sigma_T I / c$. Indeed, the total force Eq. (6.30) derived from the scattered radiation reduces to this force in the appropriate limits [302]. What we have shown in this chapter is that this force is equivalent to the integrated ponderomotive force in the plasma.

Acceleration experiments in the 1960s based on the above scheme have produced ions with keV energies [322, 323]. However, static magnetic fields were necessary to confine the plasma in the transverse direction, and the exact acceleration mechanism was not very well understood [302]. Moreover, the very large energy spread of the ions showed that the plasma was not accelerated as a compact bunch but rather completely dispersed over the length of the accelerator. These experiments were therefore discontinued in favor of more promising acceleration schemes. The reason why the radiative method can at the present time be more viable is the current availability of ultracold plasmas. Because the electron temperature of these plasmas is extremely low (~ 10 K), hydrodynamic forces are very small, so that any violent plasma expansion is absent. Moreover, as mentioned before, the density distribution of ultracold plasmas can easily be tailored to an inverted profile, either by means of imaging techniques or by using optically thick atomic clouds. As we have shown, the bulk ponderomotive force is compressive for inverted profiles, which could further reduce the plasma expansion.

Let us consider the velocities attainable by radiative acceleration. For this purpose, it is important to realize that in practice the plasma is not a rigid object, but will in general expand, so that not only b , but also the density and hence ϵ will vary with time. The number of particles N , on the other hand, remains approximately fixed. The accelerating total force will therefore depend on b both directly through the coherence properties of the plasma and indirectly through its dependence on $\epsilon(b)$. Figure 6.6 shows this dependency for three different N , assuming a driving frequency of $\omega/2\pi = 1.3$ GHz (standard L-band microwaves) and a uniform density profile for which $\epsilon(b) = \epsilon_1 = 1 - 3N/(4\pi\epsilon_0 m_e \omega^2 b^3)$. Immediately apparent is the plateau in the force at $F_z/N^2 = \sigma_T I/c$, indicated by the horizontal dashed line, which corresponds to the force proposed by Vesksler [301]. At the high kb side, the force decreases rapidly once $kb \gtrsim 1$ because the plasma electrons do no longer scatter incident radiation coherently at such larger plasma sizes. As this effect is a geometrical one, it is not dependent on the number of particles. At the low kb side, each curve in Fig. 6.6 strongly increases around the plasma radius b_m at which the Mie resonance $\epsilon_1 = -2$ occurs. This is where the driving frequency matches the eigenfrequency of oscillations of the whole electron cloud of the plasma in the field of the ion cloud [277]. Since ϵ_1 depends on N , the radius b_m is different for the three cases in Fig. 6.6, indicated by the vertical dashed lines. We have also calculated the total force for the other density profiles considered in this chapter. This gives practically the same results on the scales of Fig. 6.6, although minor differences are found close to b_m due to different resonance properties, and for $kb \gtrsim 1$ due to different coherence properties. However, the plateau in the force is exactly the same, in accordance with the observation in section 6.5.2 that $F_z \propto N^2$ for all profiles if ϵ_1 is close to unity, that is, away from the Mie resonance.

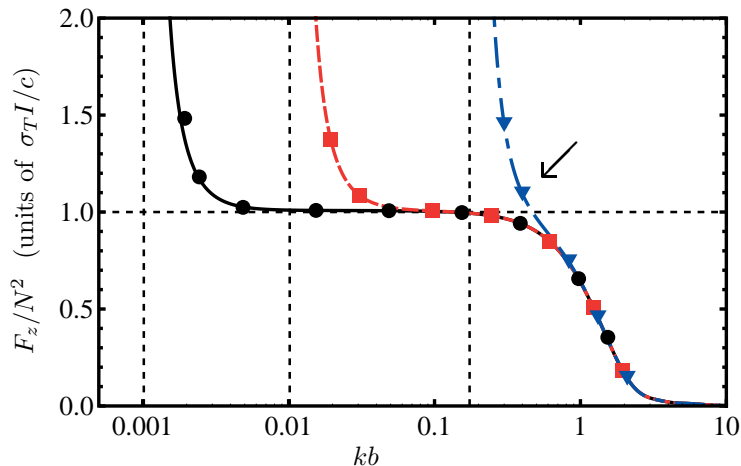


Figure 6.6: Total ponderomotive force as a function of plasma radius, when the particle number is fixed at $N = 10^4$ (black solid line and dots), $N = 10^7$ (red dashed line and squares), and $N = 5 \times 10^{10}$ (blue dash-dotted line and triangles) according to Eq. (6.30) using the well-known Mie-coefficients (lines) and integration of the volume force Eq. (6.25) (symbols). A uniform profile and a driving frequency of $\omega/2\pi = 1.3$ GHz have been assumed. The horizontal dashed line represents the force according to coherently enhanced Thomson scattering; the vertical dashed lines indicate the radius at which Mie resonance occurs. The datapoint indicated by the arrow is discussed in the main text.

Now, for acceleration purposes the plasma size should presumably be in the ‘plateau range’ of Fig. 6.6, in order to both have a significant acceleration and at the same time avoid plasma resonances. Experimentally, the latter invariably lead to significant electron loss and heating in both nanoplasma [277] and ultracold plasma [271, 274] experiments, and should therefore be avoided despite the greatly enhanced accelerating force. Secondly, the number of particles N should be chosen as large as possible to maximize F_z . However, for too large N the plateau range disappears as the resonance radius b_m grows larger than k^{-1} . The dash-dotted curve in Fig. 6.6 represents about the largest N that allows for a plasma that is both coherent and non-resonant at the chosen driving frequency of 1.3 GHz. Incidentally, the corresponding value $N = 5 \times 10^{10}$ is also one of the largest numbers of atoms that have actually been magneto-optically cooled and trapped [324]. In that experiment, the atomic cloud consisted of sodium. Let us estimate what energies may be attained when this particular cloud is ionized and accelerated by 1.3 GHz microwave radiation. A suitable plasma radius, indicated in Fig. 6.6 by the data point with an arrow, would be 1.5 cm (even larger atomic clouds with sizes up to a few centimeters have been successfully produced [325]). Existing L-band klystrons [326] can produce microwave pulses with length $\tau = 1.5$ ms at a power exceeding 10 MW. At this power and with diffraction-limited focusing, the intensity is about $I = 35$ kW/cm². The resulting

electron oscillation amplitude is still much smaller than the plasma radius, so that the plasma should still behave as a dielectric as has been assumed in this chapter. Assuming that kb remains smaller than unity throughout the microwave pulse, the momentum transferred to the plasma is $p = \tau N^2 \sigma_T I / c$. The corresponding kinetic energy per ion is $U = (p/N)^2 / (2m_i) = 2.7$ keV, where $m_i = 3.8 \times 10^{-26}$ kg is the atomic mass of sodium. Thus the energies reachable by radiative acceleration are quite substantial.

Although keV energies are nowhere near those attained in conventional accelerators, it should be emphasized that an accelerated ultracold plasma is still an object with very special properties. First of all, it is an accelerated neutral beam, whereas other acceleration methods involve charged beams. An exception to some extent is acceleration of partially neutralized ion beams from laser-irradiated foils [327]. However, in the latter method beam properties such as the energy spread are still poor ($\sim 10\%$). An accelerated ultracold plasma, on the other hand, may have remarkable beam quality. For ions at nonrelativistic energies, such as in the field of focused ion beams [328], beam quality is usually expressed [329] in terms of the reduced brightness $B_r = eI_{\text{peak}} / (2\pi^2 \xi^2 m_i c^2)$, where I_{peak} is the peak ion current and $\xi = b\sqrt{k_B T_i / (m_i c^2)} / 2$ is the transverse thermal emittance with T_i the ion temperature. Present state-of-the-art ion beams, produced using liquid-metal ion sources [328], have a brightness up to $B_r = 10^6$ A/m²srV at a current in the picoampere to nanoampere range. In case of our ultracold plasma, the temperature of the ion component usually equilibrates to a few Kelvin [270], resulting in an emittance of $\xi < 1$ nm. The peak ion current is $I_{\text{peak}} = \pi b^2 e n_e v = 0.06$ A, where $v = p / (Nm_i)$ is the velocity of the plasma, yielding a brightness of $B_r > 10^5$ A/m²srV. The brightness of the ions of an accelerated ultracold plasma may thus be comparable to that of existing high-performance ion sources, but at a much higher current, and with the important difference that an ultracold plasma is a neutralized beam. This combination of properties puts an accelerated ultracold plasma in a yet unexplored parameter regime, which may well enable new applications. In particular, a neutral beam does not suffer the space charge problems usually associated with high brightness charged particle beams. In ion milling applications [328], a neutral beam would alleviate problems due to charging of insulating samples.

The above estimates being encouraging, it is important to realize that they are based on the assumption that the plasma stays coherent throughout the ms microwave pulse, that is, that $kb \lesssim 1$. However, one may expect that the low but finite electron temperature of the plasma leads to some plasma expansion due to the hydrodynamic pressure gradient $\nabla n_e k_B T_e$. On the other hand, for inverted plasma density profiles in which $dn_e/dr > 0$, this gradient can be directed inwards, leading to compression rather than expansion. Moreover, as mentioned before, the ponderomotive force is directed inwards as well for inverted profiles, giving an additional compressive action.

To fully assess the time-dependence of the plasma size, therefore, one should study the evolution of the density profile under influence of the self-consistent hydrodynamic and ponderomotive forces. Such an analysis is outside the scope of this thesis. We do note that the characteristic hydrodynamic expansion rate of usual undriven, Gaussian ultracold plasmas is $db/dt \sim \sqrt{k_B T_e/m_i}$ [270]. If the plasma considered above would expand at this rate with $T_e = 10$ K, it would still take some 0.4 ms before the plasma grows larger than $kb = 1$. The interaction time τ assumed above is of the same order of magnitude and therefore seems reasonable.

Another assumption made above is that the plasma does not appreciably heat up due to the microwave interaction. In absence of plasma resonances, the most important heating mechanism [330] is inverse Bremsstrahlung due to electron-ion collisions. In the strong-field regime $e^2 E_0^2 / (4m_e \omega^2) \gg k_B T_e$ under consideration here, the electron-ion collision rate is $\nu_{ei} \sim n_e e m_e \omega^3 / (\pi^2 \epsilon_0^2 E_0^3)$ [331], and the resulting heating rate per electron is $P_{ei} = \nu_{ei} e^2 E_0^2 / (2m_e \omega^2)$. In the example above, $\nu_{ei} \sim 3 \text{ s}^{-1}$ only, giving $P_{ei} = 10^{-19}$ W. This corresponds to a temperature increase of only $P_{ei}/k_B = 8$ K/ms. The plasma should therefore indeed remain ultracold during the acceleration process.

Finally, we should mention the strongly peaked outward ponderomotive near the edge of the plasma, which is of course disadvantageous for the stability of the plasma. Initially, the electrons in the edge region will probably be expelled from the plasma by this force. However, very soon, after a sufficient number N_1 of electrons has escaped, the resulting charging of the plasma will prevent any further electron loss. This happens as soon as the Coulomb potential $U_C = N_1 e^2 / (4\pi \epsilon_0 b)$ of the plasma is larger than the kinetic energy U_1 that can be supplied to an electron by the ponderomotive force peak. The latter equals $U_1 = u_1/n_e$, where u_1 is given by Eq. (6.34) for a homogeneous plasma. For the plasma considered in this section, the condition $U_C = U_1$ gives $N_1/N = 0.3\%$ only. Electron loss due to the ponderomotive force peak at the plasma edge should therefore remain relatively unimportant. Particle tracking simulations are necessary to further elucidate the behavior of electrons near the very plasma edge.

6.7 Conclusions

In this chapter, we have studied the ponderomotive forces induced in a subwavelength plasma by an externally applied electromagnetic wave. We found that the ponderomotive force in the plasma bulk is directed outwards for natural profiles $dn_e/dr < 0$ and inwards for 'inverted' profiles $dn_e/dr > 0$. For a completely homogeneous plasma, a spherically symmetric compressive ponderomotive force remains, suggesting possibilities for contactless ponderomotive manipulation of homogeneous subwavelength

objects. Furthermore, we showed that the force in the plasma bulk is accompanied by a strongly peaked outward ponderomotive force near sharp plasma edges. In the limit that the plasma boundary tends to a discontinuous step in the density, this force peak tends to a ponderomotive surface force, which in turn makes an essential contribution to the total radiation pressure on the plasma. Finally, we have discussed the feasibility of radiative acceleration of ultracold plasmas. Based on existing technologies and conservative estimates, we estimated that these plasmas may be accelerated to keV ion energies, resulting in a neutralized beam with a brightness comparable to current high-performance ion sources.

Subsequent fluid simulations should address the plasma dynamics and the self-consistent evolution of the density profile. Furthermore, in this chapter we have adopted a continuum model of the plasma medium, which of course must break down at some point. We expect granularity effects to become first apparent near the plasma boundary, where the Debye length becomes comparable to the scale length of the plasma. Adequate modeling of the behavior of particles near the very plasma edge should therefore be based on particle tracking simulations invoking the full-wave expansion Eq. (6.2)-(6.3) of the fields. Extension of our results to plasma sizes comparable to or larger than the wavelength will be very interesting as well. It is clear that ponderomotive forces play an important role in electromagnetically driven finite-sized plasmas in general, and in ultracold plasmas in particular. A thorough understanding of these forces will enable opportunities for active ponderomotive plasma manipulation, including the compression and acceleration of ultracold neutral plasmas.

Appendix 6.A Quasistatic limit from general field expressions

We first estimate which potential Eq. (6.3) becomes dominant in the quasistatic limit. As mentioned in 6.2.3, $f_n^{e,m} \sim (kb)^n$ if $kb \ll 1$. Consequently, the lowest-order modes $\Pi_1^{e,m}$ are dominant, the high-order modes being progressively smaller. Furthermore, assuming in Eq. (6.2) that symbolically $\nabla \sim b^{-1}$, it follows that $|\mathbf{E}_n^e| \gg |\mathbf{E}_n^m|$. Hence, the dominant contribution to the electric field is the electric dipole mode, which is equal to

$$\mathbf{E} \approx \mathbf{E}_1^e \approx E_0 \nabla \left(\frac{3}{2k\epsilon} \frac{d(rf_1^e)}{dr} \sin \theta \cos \varphi \right). \quad (6.35)$$

Here, the identity

$$\frac{1}{k\epsilon} \nabla \times (\mathbf{r} \times \nabla \Pi^e) = -\frac{1}{k} \nabla \left(\frac{1}{\epsilon} \frac{\partial(r\Pi^e)}{\partial r} \right) - k\mathbf{r}\Pi^e \quad (6.36)$$

has been used. Comparison of Eqs. (6.9) and (6.35) shows that the function $\xi = -(3/2k\epsilon)d(rf_1^e)/dr$ must reduce to ψ in the quasistatic limit, the latter being defined

by the boundary value problem (6.11)-(6.13). This can be shown by noting that in Eq. (6.4) the propagation term $k^2\epsilon$ is much smaller than the other terms in the quasistatic limit. Neglecting the propagation term, taking $n = 1$, and multiplying Eq. (6.4) by $d/dr + 2/r$, yields

$$0 = \left[\frac{d^2}{dr^2} + \left(\frac{2}{r} + \frac{1}{\epsilon} \frac{d\epsilon}{dr} \right) \frac{d}{dr} - \frac{2}{r^2} \right] \xi. \quad (6.37)$$

Similarly, multiplying Eq. (6.14) by $-3/kb$ and taking $n = 1$, approximating the Bessel functions by their limiting value for small argument, and rewriting $f_1^e(b)$ using Eq. (6.4), gives

$$-3 = \left(\epsilon \frac{d\xi}{dr} + \frac{2\xi}{r} \right)_{r=b}. \quad (6.38)$$

From Eqs. (6.11), (6.13), (6.37) and (6.38), ψ and ξ satisfy the same differential equation and the same boundary conditions, which shows that $\xi \approx \psi$ when $kb \ll 1$. Hence the general solution for the electric field given in the section 6.2.1 approaches the quasistatic field given in section 6.2.2.

Appendix 6.B Explicit expressions for ponderomotive forces

In the ponderomotive volume force density Eq. (6.24),

$$R_{nm}^{r1} = \frac{d(rR_{nm}^{\theta1})}{dr} = \frac{2 - \delta_{nm}}{k} \left(g_n^m \frac{dg_m^m}{dr} + g_m^m \frac{dg_n^m}{dr} \right); \quad (6.39)$$

$$R_{nm}^{r2} = \frac{d(rR_{nm}^{\theta2})}{dr} = n(n+1)m(m+1) \frac{2 - \delta_{nm}}{(kr)^3 \epsilon^2} \times \left[g_n^e \frac{d(rg_m^e)}{dr} + g_m^e \frac{d(rg_n^e)}{dr} - 2 \left(2 + \frac{r}{\epsilon} \frac{d\epsilon}{dr} \right) g_n^e g_m^e \right]; \quad (6.40)$$

$$R_{nm}^{r3} = \frac{d(rR_{nm}^{\theta3})}{dr} = \frac{2 - \delta_{nm}}{(kr)^3 \epsilon^2} \left\{ [n(n+1) - \epsilon(kr)^2] g_n^e \frac{d(rg_m^e)}{dr} + [m(m+1) - \epsilon(kr)^2] g_m^e \frac{d(rg_n^e)}{dr} - 2 \frac{d(rg_n^e)}{dr} \frac{d(rg_m^e)}{dr} \right\}; \quad (6.41)$$

$$R_{nm}^{r4} = \frac{d(rR_{nm}^{\theta4})}{dr} = \frac{2}{(kr)^2 \epsilon} \left\{ \frac{d(rg_n^e)}{dr} \frac{d(rg_m^m)}{dr} - 2g_m^m \frac{d(rg_n^e)}{dr} + [n(n+1) - \epsilon(kr)^2] g_n^e g_m^m \right\}; \quad (6.42)$$

$$R_{nm}^{\theta1} = R_{n,m}^{\varphi1} = \frac{2 - \delta_{nm}}{kr} g_n^m g_m^m; \quad (6.43)$$

$$R_{nm}^{\theta2} = R_{n,m}^{\varphi1} = n(n+1)m(m+1) \frac{2 - \delta_{nm}}{(kr)^3 \epsilon^2} g_n^e g_m^e; \quad (6.44)$$

$$R_{nm}^{\theta 3} = R_{n,m}^{\varphi 1} = \frac{2 - \delta_{nm}}{(kr)^3 \epsilon^2} \frac{d(rg_n^e)}{dr} \frac{d(rg_m^e)}{dr}; \quad (6.45)$$

$$R_{nm}^{\theta 4} = R_{n,m}^{\varphi 1} = \frac{2}{(kr)^2 \epsilon} g_m^m \frac{d(rg_n^e)}{dr}; \quad (6.46)$$

$$S_{nm}^{r1} = \frac{(2n+1)(2m+1)}{n(n+1)m(m+1)} \left(\frac{P_n^1 P_m^1}{\sin^2 \theta} \cos^2 \varphi + \frac{dP_n^1}{d\theta} \frac{dP_m^1}{d\theta} \sin^2 \varphi \right); \quad (6.47)$$

$$S_{nm}^{r2} = \frac{(2n+1)(2m+1)}{n(n+1)m(m+1)} P_n^1 P_m^1 \cos^2 \varphi; \quad (6.48)$$

$$S_{nm}^{r3} = \frac{(2n+1)(2m+1)}{n(n+1)m(m+1)} \left(\frac{dP_n^1}{d\theta} \frac{dP_m^1}{d\theta} \cos^2 \varphi + \frac{P_n^1 P_m^1}{\sin^2 \theta} \sin^2 \varphi \right); \quad (6.49)$$

$$S_{nm}^{r4} = \frac{(2n+1)(2m+1)}{n(n+1)m(m+1)} \left(\frac{dP_n^1}{d\theta} \frac{P_m^1}{\sin \theta} \cos^2 \varphi + \frac{P_n^1}{\sin \theta} \frac{dP_m^1}{d\theta} \sin^2 \varphi \right); \quad (6.50)$$

$$S_{nm}^{\theta j} = \frac{\partial S_{nm}^{rj}}{\partial \theta}; \quad (6.51)$$

$$S_{nm}^{\varphi j} = \frac{1}{\sin \theta} \frac{\partial S_{nm}^{rj}}{\partial \varphi}, \quad (6.52)$$

where δ_{nm} is the Kronecker delta, and $j = 1 \dots 4$. In Eqs. (6.41)-(6.42), the differential equation (6.15) has been applied to rewrite second derivatives.

The z component f_z of Eq. (6.24) consists of terms that are proportional to $X_{nm}^j = R_{nm}^{rj} S_{nm}^{rj} \cos \theta - R_{nm}^{\theta j} S_{nm}^{\theta j} \sin \theta$, with $j = 1 \dots 4$. In the volume integration of f_z in Eq. (6.23), integrating by parts the second term of X_{nm}^j with respect to θ , and using the functional relations in Eqs. (6.39)-(6.42) and (6.51), transforms the angular integrations to

$$\int X_{nm}^j d\Omega = \frac{d(r^3 R_{nm}^{\theta j})}{dr} \int S_{nm}^{rj} \cos \theta d\Omega. \quad (6.53)$$

The remaining four integrals $j = 1 \dots 4$ on the right side of Eq. (6.53) are equal to [332]

$$\int S_{nm}^{r1} \cos \theta d\Omega = \begin{cases} \frac{2\pi q^2 (q+1)(q+2)^2}{(2q+1)(2q+3)} & m = n \pm 1; \\ 0 & m \neq n \pm 1; \end{cases} \quad (6.54)$$

$$\int S_{nm}^{r2} \cos \theta d\Omega = \begin{cases} \frac{2\pi q (q+1)(q+2)}{(2q+1)(2q+3)} & m = n \pm 1; \\ 0 & m \neq n \pm 1; \end{cases} \quad (6.55)$$

$$\int S_{nm}^{r3} \cos \theta d\Omega = \int S_{n,m}^{r1} \cos \theta d\Omega; \quad (6.56)$$

$$\int S_{nm}^{r4} \cos \theta d\Omega = \begin{cases} \frac{2\pi n(n+1)}{2n+1} & m = n; \\ 0 & m \neq n, \end{cases} \quad (6.57)$$

with $q = \min(n, m)$. The resulting total volume force is given in Eq. (6.25), in which

$$Y_n^1 = \frac{n(n+2)}{n+1} \int_0^{b^-} \chi \frac{d}{dr} \left[(kr)^2 g_n^m g_{n+1}^m \right] dr; \quad (6.58)$$

$$Y_n^2 = n(n+1)(n+2) \int_0^{b^-} \chi \frac{d}{dr} \left[\frac{g_n^e g_{n+1}^e}{\epsilon^2} \right] dr; \quad (6.59)$$

$$Y_n^3 = \frac{n(n+2)}{n+1} \int_0^{b^-} \chi \frac{d}{dr} \left[\frac{1}{\epsilon^2} \frac{d(rg_n^e)}{dr} \frac{d(rg_{n+1}^e)}{dr} \right] dr; \quad (6.60)$$

$$Y_n^4 = \frac{2n+1}{n(n+1)} \int_0^{b^-} \chi \frac{d}{dr} \left[\frac{kr g_n^m}{\epsilon} \frac{d(rg_n^e)}{dr} \right] dr. \quad (6.61)$$

Appendix 6.C Radial functions for homogeneous sphere

Solving Eqs. (6.15)-(6.16) for a homogeneous sphere with permittivity ϵ_1 gives $g_n^{e,m} = A_n^{e,m} j_n(\sqrt{\epsilon_1} kr)$, with

$$A_n^{e,m} = \frac{y_n}{kb |h_n^{(1)}|^2 G_n^{e,m}}; \quad (6.62)$$

$$G_n^{e,m} \equiv \delta^{e,m} (n \tilde{j}_n - \sqrt{\epsilon_1} kb \tilde{j}_{n-1}) + \left(1 + b \frac{d}{dr} \ln |h_n^{(1)}| \right) \tilde{j}_n,$$

where \tilde{j}_n denotes the spherical Bessel function with argument $\sqrt{\epsilon_1} kb$ and $j_n, y_n, h_n^{(1)}$ are spherical Bessel functions with argument kb . Substituting $g_n^{e,m}$ in Eq. (6.18) and expanding braces yields

$$\gamma_n^{e,m} = \frac{kb |h_n^{(1)}|^2 h_n^{(2)} G_n^{e,m}}{y_n \left[\tilde{j}_n - ikb |h_n^{(1)}|^2 G_n^{e,m} \right]}, \quad (6.63)$$

with $h_n^{(2)}$ the n th-order spherical Hankel function of the second kind [307] and argument kb . Multiplying in Eq. (6.63) the term \tilde{j}_n by the identity $1 = (j_{n+1} y_n - j_n y_{n+1}) (kb)^2$, and simplifying the denominator, gives

$$A_n^e \gamma_n^e = \frac{i(kb)^{-2}}{\sqrt{\epsilon_1} h_n^{(1)} \tilde{J}_{n+1} - h_{n+1}^{(1)} \tilde{J}_n}; \quad (6.64)$$

$$A_n^m \gamma_n^m = \frac{i(kb)^{-2}}{\frac{h_n^{(1)} \tilde{J}_{n+1}}{\sqrt{\epsilon_1}} - h_{n+1}^{(1)} \tilde{J}_n + \frac{(n+1)\chi_1}{\epsilon_1 kb} h_n^{(1)} \tilde{J}_n}. \quad (6.65)$$

Eqs. (6.64)-(6.65) are equal to c_n and $\sqrt{\epsilon_1} d_n$ respectively, where c_n and d_n are the internal Mie coefficients [305]. Taylor expansions about $kb = 0$ of Eqs. (6.62)-(6.63) are

$$A_1^e = \frac{3\sqrt{\epsilon_1}}{\epsilon_1 + 2} \left(1 + \frac{\chi_1(\epsilon_1 + 10)}{10(\epsilon_1 + 2)} (kb)^2 + \dots \right); \quad (6.66)$$

$$A_2^e = \frac{5}{3(2\epsilon_1 + 3)} \left(1 + \frac{\chi_1(2\epsilon_1 + 7)}{14(2\epsilon_1 + 3)} (kb)^2 + \dots \right); \quad (6.67)$$

$$A_3^e = \frac{7\epsilon_1^{-1/2}}{(3\epsilon_1 + 4)} \left(1 + \frac{\chi_1(5\epsilon_1 + 12)}{30(3\epsilon_1 + 4)} (kb)^2 + \dots \right); \quad (6.68)$$

$$A_1^m = \frac{1}{\sqrt{\epsilon_1}} \left(1 + \frac{\chi_1}{6} (kb)^2 + \dots \right); \quad (6.69)$$

$$A_2^m = \frac{1}{\epsilon_1} \left(1 + \frac{\chi_1}{10} (kb)^2 + \dots \right); \quad (6.70)$$

$$\gamma_1^e = 1 + \frac{2i\chi_1(kb)^3}{3(\epsilon_1 + 2)} \left(1 + \frac{3(\epsilon_1 - 2)}{5(\epsilon_1 + 2)} (kb)^2 + \dots \right); \quad (6.71)$$

$$\gamma_2^e = 1 + \frac{i\chi_1(kb)^5}{15(2\epsilon_1 + 3)} + \dots; \quad (6.72)$$

$$\gamma_1^m = 1 + \frac{i\chi_1(kb)^5}{45} + \dots. \quad (6.73)$$

The imaginary part of other $\gamma_n^{e,m}$ are of order $O[(kb)^7]$.

Bibliography

- [270] T. C. Killian, T. Pattard, T. Pohl, and J. M. Rost, “Ultracold neutral plasmas,” *Phys. Reports* **449**, 77–130 (2007).
- [271] S. Kulin, T. C. Killian, S. D. Bergeson, and S. L. Rolston, “Plasma oscillations and expansion of an ultracold neutral plasma,” *Phys. Rev. Lett.* **85**, 318–321 (2000).
- [272] S. D. Bergeson and R. L. Spencer, “Neutral-plasma oscillations at zero temperature,” *Phys. Rev. E* **67**, 026414 (2003).
- [273] R. S. Fletcher, X. L. Zhang, and S. L. Rolston, “Observation of collective modes of ultracold plasmas,” *Phys. Rev. Lett.* **96**, 105003 (2006).

- [274] K. A. Twedt and S. L. Rolston, “Electronic detection of collective modes of an ultracold plasma,” *Phys. Rev. Lett.* **108**, 065003 (2012).
- [275] A. Lyubonko, T. Pohl, and J. M. Rost, “Collective energy absorption of ultracold plasmas through electronic edge-modes,” *New J. Phys.* **14**, 053039 (2012).
- [276] V. P. Krainov and M. B. Smirnov, “Cluster beams in the super-intense femtosecond plaser pulse,” *Phys. Rep.* **370**, 237–331 (2002).
- [277] Th. Fennel, K.-H. Meiwes-Broer, J. Tiggesbäumker, P.-G. Reinhard, P. M. Dinh, and E. Suraud, “Laser-driven nonlinear cluster dynamics,” *Rev. Mod. Phys.* **82**, 1783–1842 (2010).
- [278] L. M. Chen, J. J. Park, K.-H. Hong, J. L. Kim, J. Zhang, and C. H. Nam, “Emission of a hot electron jet from intense femtosecond-laser-cluster interactions,” *Phys. Rev. E* **66**, 025402(R) (2002).
- [279] Y. Fukuda, Y. Akahane, M. Aoyama, Y. Hayashi, T. Homma, N. Inoue, M. Kando, S. Kanazawa, H. Kiriya, S. Kondo, H. Kotaki, S. Masuda, M. Mori, A. Yamazaki, K. Yamakawa, E. Yu. Echkina, I. N. Inovenkov, J. Koga, and S. V. Bulanov, “Ultrarelativistic electron generation during intense, ultrashort laser pulse interaction with clusters,” *Phys. Lett. A* **363**, 130–135 (2007).
- [280] Y. Fukuda, A. Ya. Faenov, M. Tampo, T. A. Pikuz, T. Nakamura, M. Kando, Y. Hayashi, A. Yogo, H. Sakaki, T. Kameshima, A. S. Pirozhkov, K. Ogura, M. Mori, T. Zh. Esirkepov, J. Koga, A. S. Boldarev, V. A. Gasilov, A. I. Magunov, T. Yamauchi, R. Kodama, P. R. Bolton, Y. Kato, T. Tajima, H. Daido, and S. V. Bulanov, “Energy increase in multi-MeV ion acceleration in the interaction of a short pulse laser with a cluster-gas target,” *Phys. Rev. Lett.* **103**, 165002 (2009).
- [281] M. Mori, T. Shiraishi, E. Takahashi, H. Suzuki, L. B. Sharma, E. Miura, and K. Kondo, “Extreme ultraviolet emission from Xe clusters excited by high-intensity lasers,” *J. Appl. Phys.* **90**, 3595–3601 (2001).
- [282] S. Ter-Avetisyan, U. Vogt, H. Stiel, M. Schnürer, I. Will, and P. V. Nickles, “Efficient extreme ultraviolet emission from xenon-cluster jet targets at high repetition rate laser illumination,” *J. Appl. Phys.* **94**, 5489–5496 (2003).
- [283] L. M. Chen, F. Liu, W. M. Wang, M. Kando, J. Y. Mao, L. Zhang, J. L. Ma, Y. T. Li, S. V. Bulanov, T. Tajima, Y. Kato, Z. M. Sheng, Z. Y. Wei, and J. Zhang, “Intense high-contrast femtosecond K-shell x-ray source from laser-driven Ar clusters,” *Phys. Rev. Lett.* **104**, 215004 (2010).
- [284] S. Ter-Avetisyan, B. Ramakrishna, R. Prasad, M. Borghesi, P. V. Nickles, S. Steinke, M. Schnürer, K. I. Popov, L. Ramunno, N. V. Zmitrenko, and

- V. Yu. Bychenkov, "Generation of a quasi-monoenergetic proton beam from laser-irradiated sub-micron droplets," *Phys. Plasmas* **19**, 073112 (2012).
- [285] Y. Kishimoto, T. Masaki, and T. Tajima, "High energy ions and nuclear fusion in laser-cluster interaction," *Phys. Plasmas* **9**, 589–601 (2002).
- [286] P. Mulser and D. Bauer, *High power laser-matter interaction* (Springer, Berlin, 2010).
- [287] H. A. H. Boot and R. B. R. S. Harvie, "Charged particles in a non-uniform radio-frequency field," *Nature* **180**, 1187 (1957).
- [288] A. V. Gaponov and M. A. Miller, "Potential wells for charged particles in a high-frequency electromagnetic field," *Sov. Phys. JETP-USSR* **7**, 168–169 (1958).
- [289] H. Hora, "Nonlinear confining and deconfining forces associated with the interaction of laser radiation with plasma," *Phys. Fluids* **12**, 182–191 (1969).
- [290] J. W. Shearer and J. L. Eddleman, "Laser light forces and self-focusing in fully ionized plasmas," *Phys. Fluids* **16**, 1753–1761 (1973).
- [291] H. M. Milchberg, S. J. McNaught, and E. Parra, "Plasma hydrodynamics of the intense laser-cluster interaction," *Phys. Rev. E* **64**, 056402 (2001).
- [292] M. Kerker, *The scattering of light and other electromagnetic radiation* (Academic Press, New York, 1969).
- [293] C. T. Tai, "The electromagnetic theory of the spherical Luneberg lens," *Appl. Sci. Res. B* **7**, 113–130 (1958).
- [294] C. T. Tai, "Maxwell fish-eye treated by Maxwell equations," *Nature* **182**, 1600–1601 (1958).
- [295] P. J. Wyatt, "Scattering of electromagnetic plane wave from inhomogeneous spherically symmetric objects," *Phys. Rev.* **127**, 1837–1843 (1962).
- [296] P. E. Bisbing, "Electromagnetic scattering by an exponentially inhomogeneous plasma sphere," *IEEE Trans. Antennas Propag.* **14**, 219–224 (1966).
- [297] L. Sun and K. W. Yu, "Broadband electromagnetic transparency by graded metamaterials: scattering cancellation scheme," *J. Opt. Soc. Am. B* **28**, 994–1001 (2011).
- [298] T. X. Hoang, X. Chen, and C. J. R. Sheppard, "Interpretation of the scattering mechanism for particles in a focused beam," *Phys. Rev. A* **86**, 033817 (2012).
- [299] S. Orlov, U. Peschel, T. Bauer, and P. Banzer, "Analytical expansion of highly focused vector beams into vector spherical harmonics and its application to Mie scattering," *Phys. Rev. A* **85**, 063825 (2012).

- [300] A. R. Holkundkar and N. K. Gupta, “Effect of radial density profile on resonance absorption in laser-cluster interaction,” *Contrib. Plasma Phys.* **49**, 403–412 (2009).
- [301] V. I. Veksler, “The principle of coherent acceleration of charged particles,” *Atomic Energy* **2**, 525–528 (1957).
- [302] H. Motz and C. J. H. Watson, “The radio-frequency confinement and acceleration of plasmas,” in *Advances in electronics and electron physics*, Vol. 23, edited by L. Marton (Academic Press, New York, 1967) pp. 153–302.
- [303] V. L. Ginzburg, *The propagation of electromagnetic waves in plasmas* (Pergamon, Oxford, 1964).
- [304] W. K. H. Panofsky and M. Phillips, *Classical electricity and magnetism* (Dover, Mineola, 2005) 2nd ed.
- [305] C. F. Bohren and D. R. Huffman, *Absorption and scattering of light by small particles* (Wiley, New York, 1983).
- [306] The potentials in Eq. (6.2) were developed for homogeneous spheres by P. Debye, “Der Lichtdruck auf Kugeln von beliebigem Material,” *Ann. Physik* **30**, 57–136 (1909) and generalized to radially inhomogeneous objects by a number of authors (see p. 232 of Ref. [292]).
- [307] M. Abramowitz and I. A. Stegun, *Handbook of mathematical functions* (Dover, New York, 1965).
- [308] P. M. Morse and H. Feshbach, *Methods of theoretical physics* (McGraw-Hill, New York, 1953).
- [309] R. Klíma and Petržílka, “On some radiation pressure effects produced by wave packets in plasmas,” *J. Phys. A* **8**, 829–837 (1975).
- [310] L. D. Landau, E. M. Lifshitz, and L. P. Pitaevskii, *Electrodynamics of continuous media* (Elsevier, Amsterdam, 2007) 2nd rev. ed.
- [311] D. Duft and T. Leisner, “The index of refraction of supercooled solutions determined by the analysis of optical rainbow scattering from levitated droplets,” *Int. J. Mass Spectrosc.* **233**, 61–65 (2004).
- [312] A. D. Ward, M. Zhang, and O. Hunt, “Broadband Mie scattering from optically levitated aerosol droplets using a white LED,” *Opt. Express* **16**, 16390–16403 (2008).
- [313] T. R. Lettieri, W. D. Jenkins, and D. A. Swyt, “Sizing of individual optically levitated evaporating droplets by measurement of resonances in the polarization-ratio,” *Appl. Opt.* **20**, 2799–2805 (1981).

- [314] R. J. A. Hill and L. Eaves, “Vibrations of a diamagnetically levitated water droplet,” *Phys. Rev. E* **81**, 056312 (2010).
- [315] P. Stockel, I. M. Weidinger, H. Baumgartel, and T. Leisner, “Rates of homogeneous ice nucleation in levitated H₂O and D₂O droplets,” *J. Phys. Chem. A* **109**, 2540–2546 (2005).
- [316] S. E. Wolf, J. Leiterer, M. Kappl, F. Emmerling, and W. Tremel, “Early homogeneous amorphous precursor stages of calcium carbonate and subsequent crystal growth in levitated droplets,” *J. Am. Chem. Soc.* **130**, 12342–12347 (2008).
- [317] For recent examples of such calculations, see A. Ya. Bekshaev, O. V. Angelsky, S. G. Hanson, and C. Yu. Zenkova, “Scattering of inhomogeneous circularly polarized optical field and mechanical manifestation of the internal energy flows,” *Phys. Rev. A* **86**, 023847 (2012); R. Gómez-Medina, L. S. Froufe-Pérez, M. Yépez, F. Scheffold, M. Nieto-Vesperinas, and J. J. Sáenz, “Negative scattering asymmetry parameter for dipolar particles: Unusual reduction of the transport mean free part and radiation pressure,” *Phys. Rev. A* **85**, 035802 (2012).
- [318] A. Drobnik and K. Lukaszewski, “Direct calculations of radiation pressure for spherical particles,” *J. Opt. Soc. Am. A* **7**, 943–945 (1990).
- [319] A. G. Hoekstra, M. Frijlink, L. B. F. M. Waters, and P. M. A. Sloot, “Radiation forces in the discrete-dipole approximation,” *J. Opt. Soc. Am. A* **18**, 1944–1953 (2001).
- [320] C. F. Bohren, “Recurrence relations for the Mie coefficients,” *J. Opt. Soc. Am. A* **4**, 612–613 (1987).
- [321] A. J. McCulloch, D. V. Sheludko, S. D. Saliba, S. C. Bell, M. Junker, K. A. Nugent, and R. E. Scholten, “Arbitrarily shaped high-coherence electron bunches from cold atoms,” *Nature Phys.* **7**, 785–788 (2011).
- [322] V. I. Veksler, I. R. Gekker, É. Ya. Gol’ts, G. A. Delone, B. P. Kononov, O. V. Kudrevatova, G. S. Luk’yanchikov, M. S. Rabinovich, M. M. Savchonko, K. A. Sarksyian, K. F. Sergeichev, V. A. Silin, and L. É. Tsopp, “Interaction of plasmoids with an electromagnetic wave,” *Atomic Energy* **18**, 12–16 (1965).
- [323] B. P. Kononov, K. A. Sarksyian, V. A. Silin, and L. É. Tsopp, “Acceleration of plasma by an H₁₁-type electromagnetic wave in a circular waveguide,” *Sov. Phys. Tech. Phys.* **10**, 36–39 (1965).
- [324] W. Ketterle, K. B. Davis, M. A. Joffe, A. Martin, and D. E. Pritchard, “High densities of cold atoms in a dark spontaneous-force optical trap,” *Phys. Rev. Lett.* **70**, 2253–2256 (1993).

- [325] J. Schoser, *Erzeugung eines Bose-Einstein-Kondensats in einer stark anisotropen Magnetfalle*, Ph.D. thesis, Physikalisches Institut der Universität Stuttgart (2003).
- [326] Y. H. Chin, “Design and performance of L-band and S-band multi beam klystrons,” in *Proc. XXIV Lin. Acc. Conf.* (Victoria, Canada, 2008) pp. 369–373.
- [327] A. Henig, S. Steinke, M. Schnürer, T. Sokollik, R. Hörlein, D. Kiefer, D. Jung, J. Schreiber, B. M. Hegelich, X. Q. Yan, J. Meyerter Vehn, T. Tajima, P. V. Nickles, W. Sandner, and D. Habs, “Radiation-pressure acceleration of ion beams driven by circularly polarized laser pulses,” *Phys. Rev.* **103**, 245003 (2009).
- [328] J. Orloff, M. Utlaut, and L. Swanson, *High resolution focused ion beams: FIB and its applications* (Kluwer Academic, New York, 2003).
- [329] O. J. Luiten, B. J. Claessens, S. B. van der Geer, M. P. Reijnders, G. Taban, and E. J. D. Vredenburg, “Ultracold electron sources,” *Int. J. Mod. Phys.* **22**, 3882–3897 (2007).
- [330] P. W. Smorenburg, L. P. J. Kamp, and O. J. Luiten, “Heating mechanisms in radio-frequency-driven ultracold plasmas,” *Phys. Rev. A* **85**, 063413 (2012).
- [331] V. P. Silin, “Nonlinear high-frequency plasma conductivity,” *Sov. Phys. JETP* **20**, 1510 (1965).
- [332] Eq. (6.55) is obtained by writing $(2m + 1)P_m^1 = mP_{m+1}^1 + (m + 1)P_{m-1}^1$ and using the orthogonality relations of the Legendre functions [307]; Eqs. (6.54) and (6.57) are well-known from scattering theory in calculation of the asymmetry parameter [305].

7

Direct generation of terahertz surface plasmon polaritons on a wire using electron bunches

Abstract - We propose to generate terahertz Surface Plasmon Polaritons (SPPs) on a metal wire by launching electron bunches onto a tapered end of the wire. To show the potential of this method we solve Maxwell's equations for the appropriate boundary conditions. The metal wire tip is modeled by a perfectly conducting semi-infinite cone. It is shown that the SPPs can be recovered from the idealized fields by well-known perturbation techniques. The emitted radiation is strongly concentrated into a narrow solid angle near the cone boundary for cones with a small opening angle. We calculate that, using currently available technology, sub-picosecond SPPs with peak electric fields of the order of MV/cm on a 1 mm diameter wire can be obtained.

Publication status - The work described in this chapter has been published by P. W. Smorenburg, W. P. E. M. op 't Root, and O. J. Luiten in Phys. Rev. B **78**, 115415 (2008).

7.1 Introduction

Terahertz Surface Plasmon Polaritons (THz SPPs) on a metal wire recently received a lot of attention [333–342]. It has been shown that these SPPs can efficiently be focused below the diffraction limit by periodically corrugating the wire [339, 340], or tapering the wire into a tip [341]. This leads to electromagnetic THz pulses that are both very strong and highly localized, making it possible to study materials at THz frequencies with sub-wavelength spatial resolutions [343, 344]. Applications include near-field optical microscopy [345, 346], imaging of semiconductor structures [347, 348] or biological tissues [349, 350], single particle sensing [351, 352] and THz spectroscopy [353, 354]. Another benefit of the wire geometry is that it acts as an efficient waveguide for THz SPPs. Recently it has been shown that THz SPPs can propagate along a wire over long distances with low attenuation and dispersion [333–337]. This enables endoscopic delivery of THz radiation to samples in applications where line-of-sight access is not available [333]. Several other structures have been proposed as waveguides for THz SPPs, including coaxial lines [355], metal tubes [356] and non-metallic guides [357, 358]. However, the feasibility of these guides is limited by either high attenuation or high dispersion. An exception is the parallel-plate waveguide [359], but in this case the large cross-sectional area may be a problem for many THz applications.

Despite the promising properties of THz SPPs guided by a metal wire, it has proven difficult to efficiently generate SPPs of appreciable amplitude. In contrast, over the last years several sources have become available that generate intense *free-space* THz radiation pulses, with broad bandwidth and peak electric fields that approach the MV/cm regime. Technologies of the latter include accelerator-based sources generating coherent radiation [360–362] and table-top systems producing radiation by optical rectification of femtosecond laser pulses [363]. However, up to now efficient coupling of these free-space THz pulses into the guided mode on a wire has been difficult. Currently, THz SPPs are generated by scattering the linearly polarized free-space waves into a radially polarized wave, which is then coupled onto the wire [333]. However, due to the poor spatial overlap between the free-space radiation waveform and the SPP waveform, the coupling efficiency is very low (typically less than 1% [364]). Hence the attainable SPP electric field strength is limited to the kV/cm range by current methods. A proposed method to overcome this low coupling efficiency is to create radially polarized THz radiation using a radially symmetric photoconductive antenna [364].

In this chapter, we propose a novel method to generate THz SPPs on a wire *directly*, that is, without the creation of free-space THz radiation as an intermediate step. Similar to the method proposed in Ref. [364], in our method the guided mode on the wire is excited by a radially polarized field, thereby avoiding the poor coupling efficiency described above. We propose to generate THz SPPs by launching electron

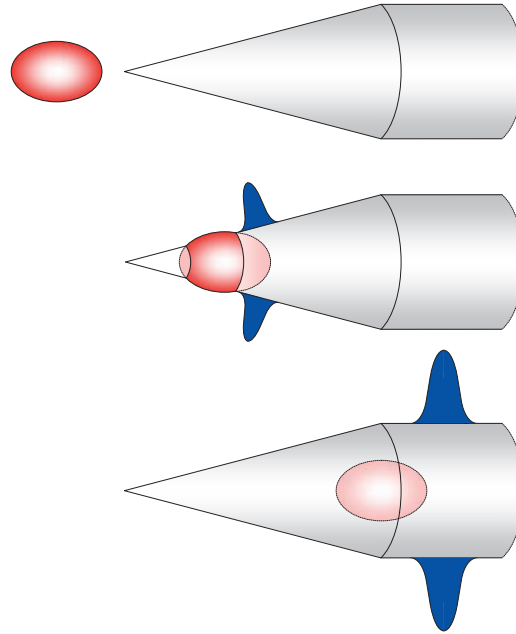


Figure 7.1: Principle of THz SPP (blue pulse) generation on a wire by launching electron bunches (red) onto a conical tip.

bunches onto a metal wire which is tapered into a conical tip, as is illustrated in Fig. 7.1. When passing the conical vacuum-metal boundary, the bunch will generate a radially polarized coherent transition radiation (CTR) field, of which THz SPPs along the boundary are part. These excited SPPs will propagate onto the wire subsequently. We calculate that, with currently available electron bunches, sub-picosecond SPPs with peak electric fields of the order of MV/cm could be created on a 1 mm diameter metal wire.

Transition radiation is generated when an electron passes a vacuum-metal boundary [365–367], and the radiation is radially polarized due to the radial polarization of the Coulomb field of the electron [368]. The radiated energy from a single electron is very small. However, when N electrons pass the boundary and radiate coherently, they produce N^2 as much energy as a single electron. In the latter case, the radiated energy can be considerable. Because the radiation profile and spectrum depend on the bunch form, CTR is a well-known diagnostic tool to characterize the spatial distribution of electron bunches [369–373]. Note that in this chapter we use the term ‘coherence’ as it is commonly used in classical electromagnetism, that is, referring to the constructive interference of the electromagnetic field contributions from dif-

ferent parts of the source. Such coherent field addition takes place if the electrons are compressed into a bunch of dimensions less than the wavelength, which means that bunches of size $\sim 300 \mu\text{m}$ radiate coherently at frequencies up to about 1 THz. Recently, such generation of intense free-space THz radiation by CTR emitted at a planar interface has been demonstrated, using linac [374] or laser-wakefield [375] accelerated bunches and resulting in electric fields of the order of MV/cm after focusing of the radiation.

We propose to generate THz SPPs directly by launching electron bunches onto a tapered wire tip, instead of coupling free-space CTR emitted at a planar interface onto a metal wire. This has a two benefits; first, electrons are capable of exciting SPPs directly, in contrast to photons where an additional coupling medium is necessary to match the wave vectors of the photons and SPPs. Second, for sharp tips the electrons pass the vacuum-metal boundary at grazing incidence, which enhances the transition radiation due to an increased radiation formation length [376].

It is well known that the radiated power of transition radiation is proportional to $\log \gamma$ [365], where $\gamma = (1 - \beta^2)^{-1/2}$ is the relativistic factor of the electron bunch. Therefore, in principle there is no need to accelerate the bunch to high energies; typically $\gamma = 5-10$, i.e. an electron energy of 2-5 MeV, is sufficient for transition radiation methods. Furthermore, it has been shown previously that mildly relativistic bunches of the required size can be made using a table-top setup [377-380]. Thus, a technological benefit of our method is that it can be applied using an overall table-top system.

In this chapter we calculate analytically what THz SPP electric fields can be obtained by launching electron bunches onto a tapered metal tip. Hence a considerable part of this chapter will be devoted to an analytical calculation of the transition radiation that is produced by the bunch impinging on the conical tip in Fig. 7.1. This calculation amounts to finding a solution of Maxwell's equations for the electric field. This field should be consistent with the presence of the electron bunch and should satisfy appropriate boundary conditions at the metal surface. However, fully solving Maxwell's equations for a conical geometry is notoriously difficult. The problem is greatly simplified by assuming that the metal is an ideal conductor, so that the electric field is perpendicular to the metal surface outside the tip and is zero inside the tip. In making this assumption, however, one inherently neglects the possibility of the existence of SPPs. Nevertheless, for good conductors, the SPPs can be recovered from the idealized field by well-known perturbation techniques. This is the approach followed in this chapter. Furthermore, since we are only interested in the SPPs that result at distances from the tip that are large compared to the wavelength, we have applied far field approximations, which greatly simplify the calculations.

The remainder of this chapter is organized as follows. In section 7.2, it is shown how the SPP field may be obtained from the idealized field. Having this connection established, we proceed to calculate the transition radiation field of a point charge impinging on an ideally conducting conical tip in section 7.3. In section 7.4 the results of this calculation are presented for a number of concrete cases for the opening angle of the tip. It will be shown that for sharp tips the transition radiation strongly concentrates into a narrow bundle grazing the tip surface, leading to very intense SPP fields. In section 7.5 it is shown that the calculated field expressions exactly agree with closed analytical expressions obtained by different methods for the limiting cases of a tip with a very large opening angle (that is, a planar surface) and that of a tip with a very small opening angle (that is, a semi-infinite line). The results for the single point charge are then extended to the case of electron bunches in section 7.6. This allows calculation of the SPP field that can be readily obtained in practical applications, which is shown in section 7.7. The final section summarizes the conclusions of this chapter.

Nearly all quantities in this chapter are expressed in Fourier transformed form according to $X \equiv X(\omega) \equiv (2\pi)^{-1/2} \int_{-\infty}^{\infty} X(t)e^{i\omega t} dt$. Time-domain quantities will be denoted explicitly like $X(t)$.

7.2 SPPs as perturbation of radiation field at ideal conductor

Considered throughout the chapter is a semi-infinite metal cone with an opening angle of 2δ placed along the negative z -axis of a spherical coordinate system, and a charge q moving along the positive z -axis towards the cone tip, as shown in Fig. 7.2. Suppose that, using the idealization that the metal is a perfect conductor, the magnetic field can be calculated analytically for every point P outside the cone. In the case of a good, but not perfect conductor this idealized field can be extended into the conductor by approximate methods. This is common practice in resonant cavity and waveguide design and yields the well-known skin field [381]

$$\mathbf{E}_{\text{skin}} \approx (1 - i) \sqrt{\frac{\omega}{2\mu\sigma}} e^{(1-i)\frac{\xi}{\Delta}} (\mathbf{n} \times \mathbf{B}_{\parallel}), \quad (7.1)$$

with

$$\Delta = \sqrt{\frac{2}{\mu\omega\sigma}} \quad (7.2)$$

the skin depth. Here, \mathbf{B}_{\parallel} is the idealized magnetic field at the surface (which is parallel to the surface). Further, \mathbf{n} denotes the outward normal vector at the metal surface and ξ a coordinate along this vector, μ the permeability and σ the conductivity of the metal. As is typical for good conductors, the skin field decreases exponentially

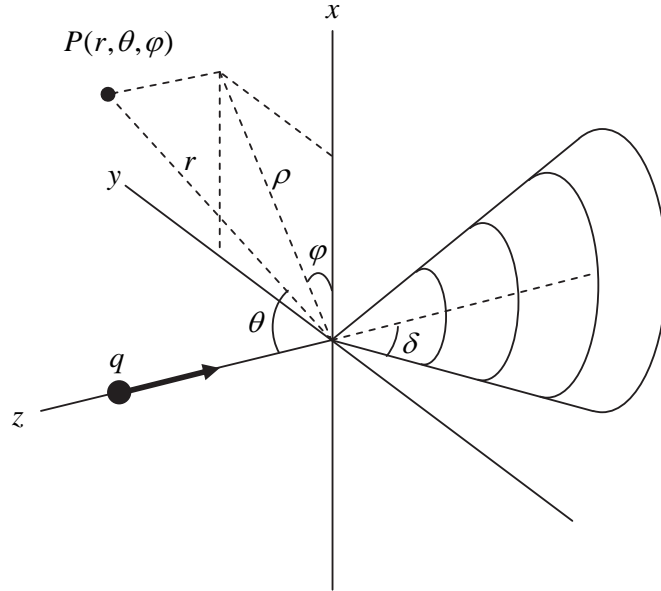


Figure 7.2: Definition of coordinates.

with the depth $-\xi$ into the metal. In the following sections, the idealized fields are calculated, from which the skin field (7.1) can be determined for every point on the cone surface. This skin field and the accompanying magnetic field can be seen as electromagnetic disturbances in the metal skin with a forced distribution $\mathbf{B}_{\parallel}(r, \pi - \delta, \phi)$. They will propagate independently as SPPs along the cone surface and onto a wire only if their waveform matches that of the SPPs, that is, if the field (7.1) is matched with freely propagating surface waves. To see whether this is true, the electric SPP field \mathbf{E}_{SPP} on a non-ideal cone has to be calculated and compared to the skin field (7.1).

The field \mathbf{E}_{SPP} is a solution of the homogeneous Helmholtz equation

$$(\nabla^2 + k^2)\mathbf{E}_{\text{SPP}} = \mathbf{0}, \quad (7.3)$$

with boundary conditions appropriate to the conical geometry of Fig. 7.2. Unfortunately, no closed-form solutions exist for this. However, the eikonal or WKB-approximation may be used to approximate \mathbf{E}_{SPP} for small opening angle cones [341]. This is shown in Appendix 7.A. Applying the Drude model [382] for the permittivity of the metallic cone, the result is that

$$\mathbf{E}_{\text{SPP}} \approx (1-i)\sqrt{\frac{\omega}{2\mu\sigma}} \exp\left[(1-i)\frac{\rho - |z|\tan\delta}{\Delta}\right] B_0 e^{ik_z z} \mathbf{e}_z \quad (7.4)$$

is an approximate solution of Eq. (7.3), provided that

$$k|z| \gg 1; \quad (7.5)$$

$$\frac{|z|\tan\delta}{\Delta} \gg 1; \quad (7.6)$$

$$\left|\frac{d}{da} \frac{1}{k_z(a)}\right| \tan\delta \ll 1. \quad (7.7)$$

In Eq. (7.7), $k_z(a)$ denotes the propagation constant of SPPs along a cylinder with radius a , which is discussed in Appendix 7.A. Comparison of Eqs. (7.1) and (7.4) shows that the skin field obtained from a calculation of the idealized field outside the cone is of the same form as the field of freely propagating SPPs, identifying the amplitude B_0 with $|\mathbf{B}_{\parallel}|$. Of course, this is only true if the idealized field is polarized in the ϕ -direction, but this is exactly the property of transition radiation that we exploit using the cone geometry.

Therefore, we can conclude that the amplitude of the transition radiation field at the cone surface, calculated under the assumption of an ideally conducting cone, can be identified with the amplitude of the excited SPPs, as long as conditions (7.5)-(7.7) apply. Thus we proceed by calculating the idealized field in the next sections, returning to the SPP field in the final section of this chapter.

7.3 Radiation field calculation

7.3.1 Dyadic Green's function

To calculate the electric radiation field generated by the moving point charge in Fig. 7.2, we use a dyadic Green's function method. Dyadic Green's functions are an important tool in electromagnetic theory [383, 384] and are often used to calculate how incoming electromagnetic radiation is scattered by some given body [385]. In contrast, the incoming field considered here is that of a moving physical charge; in particular, the field propagates in the negative z -direction with a speed less than that of light. Considering the idealized situation of a perfectly conducting cone embedded in vacuum, the total electric field outside the cone satisfies the inhomogeneous Helmholtz equation

$$(\nabla^2 + k^2)\mathbf{E} = \epsilon_0^{-1}\nabla\rho - i\omega\mu_0\mathbf{J} \quad \text{for} \quad 0 \leq \theta < \pi - \delta, \quad (7.8)$$

where ρ is the charge density, \mathbf{J} the current density and ϵ_0 and μ_0 the permittivity and permeability of vacuum. At the cone, the field is subject to the boundary condition

$$\mathbf{n} \times \mathbf{E} = \mathbf{0} \quad \text{at} \quad \theta = \pi - \delta. \quad (7.9)$$

Furthermore, we are interested in the far field part of the electric field, that is, in that component which represents electromagnetic radiation. This component \mathbf{E}_T is the transverse part [381] of the vector field \mathbf{E} such that

$$\nabla \cdot \mathbf{E}_T = 0. \quad (7.10)$$

As is known, while applying a Green's function method one first calculates the field response at some position \mathbf{r} due to a unit point source at another position \mathbf{r}_0 , and then integrates the result over the full source distribution to obtain the full field. More exactly, the method is as follows [383]. Suppose that a dyadic (i.e. nine-component) function \mathfrak{G} of two coordinate vectors \mathbf{r} and \mathbf{r}_0 can be found, such that

$$(\nabla^2 + k^2) \mathfrak{G}(\mathbf{r}, \mathbf{r}_0) = \mathfrak{I} \delta^3(\mathbf{r} - \mathbf{r}_0) \quad \text{for} \quad 0 \leq \theta < \pi - \delta, \quad (7.11)$$

where \mathfrak{I} is the identity dyadic or idemfactor and δ^3 is the three-dimensional Dirac delta function. Suppose further that, at the cone, \mathfrak{G} satisfies the boundary condition

$$\mathbf{n} \times \mathfrak{G} = \mathfrak{D} \quad \text{at} \quad \theta = \pi - \delta, \quad (7.12)$$

with \mathfrak{D} the zero dyadic. Then it can be shown that the transverse part of the electric field that satisfies Eqs. (7.8)-(7.9) is given by

$$\mathbf{E}_T(\mathbf{r}) = -i\omega\mu_0 \iiint_{V_0} \mathfrak{G}_T(\mathbf{r}, \mathbf{r}_0) \cdot \mathbf{J}(\mathbf{r}_0) dV_0, \quad (7.13)$$

where V_0 is the entire space outside the cone. Here, the dyadic \mathfrak{G}_T is the transverse part of \mathfrak{G} [383], i.e. the part of \mathfrak{G} for which

$$\nabla \cdot \mathfrak{G}_T = \mathbf{0}. \quad (7.14)$$

Eq. (7.13) can be derived by manipulation of Eqs. (7.8)-(7.12) and depends on the vanishing of several surface integrals; this is shown in Appendix 7.B. Note in particular the well-known result that the far field only depends on the current density and not on the charge density.

With Eq. (7.13), the problem of finding the radiation field generated by the point charge in Fig. 7.2 is reduced to evaluation of the dyadic Green's function \mathfrak{G}_T and current density \mathbf{J} and a three-dimensional integration. The time-domain and Fourier transformed current densities of a point charge that moves along the z -axis in the negative direction with velocity βc , and passes the origin at time $t = 0$, are given in Cartesian coordinates by

$$\mathbf{J}(t) = -q\beta c \delta(x)\delta(y)\delta(z + \beta ct) \mathbf{e}_z, \quad t < 0; \quad (7.15)$$

$$\mathbf{J}(\omega) = -(2\pi)^{-1/2} q \delta(x)\delta(y) \exp\left(-i\frac{k}{\beta}z\right) \mathbf{e}_z, \quad z > 0. \quad (7.16)$$

Thus, in the Fourier domain the current takes the form of a line distribution along the positive z -axis. The dyadic Green's function \mathfrak{G} of course depends on the geometry of the volume V_0 , that is, on the angle δ . Several representations for \mathfrak{G} are known, one of which takes the form of an expansion in terms of dyadic products of the eigenfunctions of the vectorial Helmholtz equation [383, 384]. This expansion is shown in full in Appendix 7.C. Taking the transverse part \mathfrak{G}_T of this representation as specified by Eqs. (7.13) and (7.14), and keeping only terms that yield a nonzero contribution to the integral in Eq. (7.13), reduces the Green's function to a simpler form. This is shown in Appendix 7.C; the result is

$$\mathfrak{G}_T = -ik \sum_{\sigma} \frac{\alpha_{\sigma}^2}{\sigma(\sigma+1)} \begin{cases} \mathbf{N}_{\sigma}^{(1)}(\mathbf{r})\mathbf{N}_{\sigma}^{(3)}(\mathbf{r}_0) & r < r_0 \\ \mathbf{N}_{\sigma}^{(1)}(\mathbf{r}_0)\mathbf{N}_{\sigma}^{(3)}(\mathbf{r}) & r > r_0 \end{cases}, \quad (7.17)$$

where the eigenvalues $\{\sigma\}$ are the solutions of Eq. (7.84), α_{σ} and \mathbf{N}_{σ} are given by Eqs. (7.79) and (7.83) respectively, and subscripts $m = 0$ have been omitted.

7.3.2 Field quantities in the far zone

Substitution of the current (7.16) and the Green's function (7.17) in Eq. (7.13) yields an expression for the transverse electric field generated by the moving point charge. As is shown in Appendix 7.D, in the far zone $kr \rightarrow \infty$ this expression reduces to

$$\mathbf{E}_T \approx \frac{\mu_0 \omega q}{\sqrt{2\pi}} \frac{e^{ikr}}{kr} \sum_{\sigma} \alpha_{\sigma}^2 e^{-i\sigma \frac{\pi}{2}} I_{\sigma}(\beta) P_{\sigma}^1(\cos \theta) \mathbf{e}_{\theta}, \quad (7.18)$$

with

$$I_{\sigma}(\beta) \equiv \frac{\sqrt{\pi} \Gamma(\sigma)}{2\Gamma(\sigma + \frac{3}{2})} e^{-i\sigma \frac{\pi}{2}} \left(\frac{\beta}{2}\right)^{\sigma} {}_2F_1\left(\frac{\sigma}{2}, \frac{\sigma+1}{2}; \sigma + \frac{3}{2}; \beta^2\right). \quad (7.19)$$

Here, Γ denotes the Gamma function and ${}_2F_1$ is the hypergeometric function. The curl of the electric field yields the magnetic field in the far zone:

$$\mathbf{B} = \frac{1}{i\omega} \nabla \times \mathbf{E}_T \approx \frac{\mu k q}{\sqrt{2\pi}} \sum_{\sigma} \alpha_{\sigma}^2 e^{-i\sigma \frac{\pi}{2}} I_{\sigma}(\beta) P_{\sigma}^1(\cos \theta) \frac{e^{ikr}}{kr} \mathbf{e}_{\phi}. \quad (7.20)$$

The (time-integrated) energy flow per unit of surface area per unit of frequency is given by the spectral Poynting vector [368]

$$\mathbf{S}(\omega) = \frac{2}{\mu} \operatorname{Re}[\mathbf{E}_T(\omega) \times \mathbf{B}^*(\omega)], \quad (7.21)$$

here defined such that $\mathbf{a} \cdot \int_0^\infty \mathbf{S}(\omega) d\omega$ gives the energy flow per unit of area in the direction of a unit vector \mathbf{a} . The spectral brightness, defined as the energy flow W per unit of frequency ω per unit of solid angle Ω , is

$$\frac{\partial^2 W}{\partial \omega \partial \Omega} = r^2 \mathbf{e}_r \cdot \mathbf{S}(\omega), \quad (7.22)$$

which yields

$$\frac{\partial^2 W}{\partial \omega \partial \Omega} = \frac{q^2}{4\pi\epsilon_0 c} \left| \sum_{\sigma} 2\alpha_{\sigma}^2 e^{-i\sigma\frac{\pi}{2}} I_{\sigma}(\beta) P_{\sigma}^1(\cos\theta) \right|^2. \quad (7.23)$$

This is the transition radiation generated by the moving point charge in Fig. 7.2 as it passes from vacuum into the perfectly conducting cone at the cone tip, resolved into the spectral components ω and the observation angle θ . Note that the brightness does not depend on the frequency, which is characteristic for transition radiation from a point charge [365]. Of course, for a physical metal, the permittivity is frequency dependent, so that the brightness quickly decreases as the frequency approaches the metal's plasma frequency. Therefore the total radiated energy $\iint \frac{\partial^2 W}{\partial \omega \partial \Omega} d\omega d\Omega$ remains finite. However, here we are interested in THz frequencies, which are well below typical plasma frequencies.

Finally, to obtain the radiated energy per unit of frequency, or spectral intensity, the spectral brightness is integrated over the angular coordinates. This gives

$$\frac{\partial W}{\partial \omega} = \frac{q^2}{\pi\epsilon_0 c} \sum_{\sigma} \left(\frac{\alpha_{\sigma 0}^4}{\alpha_{\sigma 1}^2} |I_{\sigma}|^2 + 2 \operatorname{Re} \sum_{\tau > \sigma} \alpha_{\tau 0}^2 \alpha_{\sigma 0}^2 e^{-i(\tau-\sigma)\frac{\pi}{2}} I_{\tau} I_{\sigma}^* p_{\tau, \sigma} \right), \quad (7.24)$$

with $\alpha_{\sigma 0}$ and $\alpha_{\sigma 1}$ given by Eq. (7.79), and [386]

$$p_{\tau, \sigma} = \frac{2\pi \sin \delta}{\tau(\tau+1) - \sigma(\sigma+1)} \times [P_{\tau}^1(-\cos \delta) P_{\sigma}^2(-\cos \delta) - P_{\sigma}^1(-\cos \delta) P_{\tau}^2(-\cos \delta)], \quad (7.25)$$

and where the asterisk denotes complex conjugation.

7.3.3 Spectral brightness in the narrow-angle cone limit

To validate the results of the previous section with alternative analytic methods later on, the behavior of the spectral brightness in the narrow-angle cone limit will be discussed. In order to obtain this behavior, we study the form of the dyadic Green's function (7.17) in this limit. The Green's function depends on the cone opening

angle δ via the set of eigenvalues $\{\sigma\}$, which are the solutions of Eq. (7.84). Its angular dependency is described by the Legendre functions in Eq. (7.83), and from the previous section it is apparent that only the component

$$\mathbf{e}_{z_0} \cdot \mathfrak{G}_T \cdot \mathbf{e}_\theta = -ik \sum_{\sigma} \alpha_{\sigma}^2 \left(\mathbf{e}_{z_0} \cdot \mathbf{N}_{\sigma}^{(1)}(\mathbf{r}_0) \right) \left(\mathbf{e}_\theta \cdot \mathbf{N}_{\sigma}^{(3)}(\mathbf{r}) \right) \quad (7.26)$$

of the Green's function contributes to the spectral intensity (7.23). In Ref. [387] a similar series is studied and the following results are obtained.

As $\delta \rightarrow 0$, (the cone approaches a half-line), the eigenvalues approach the integers from above, such that

$$\sigma_n = n + n_0; \quad n_0 \rightarrow \frac{1}{2 \ln \frac{2}{\delta}} \quad (7.27)$$

as $\delta \rightarrow 0$, with $n \in \mathbb{N}$. The terms $\mathbf{e}_\theta \cdot \mathbf{N}_{\sigma}^{(3)}(\mathbf{r})$ in Eq. (7.26) contain non-integer degree, first order Legendre functions. These grow very rapidly near the cone boundary if $\delta \ll 1$, because then the argument $\cos \theta$ approaches the singularity $\lim_{x \rightarrow -1} P_{\sigma}^1(x) = \infty$. The functions may be approximated by

$$P_{n+n_0}^1(\cos \theta) \approx P_n^1(\cos \theta) + (-1)^{n+1} \frac{2n_0}{\sin \theta} \quad \text{for } n_0 \ll 1. \quad (7.28)$$

On the other hand, the terms $\mathbf{e}_{z_0} \cdot \mathbf{N}_{\sigma}^{(1)}(\mathbf{r}_0)$ in Eq. (7.26) contain zeroth order Legendre functions which are evaluated at $\theta_0 = 0$. This is because the source current (7.16) is confined to the z -axis where $\mathbf{e}_{z_0} = \mathbf{e}_{r_0}$. Hence

$$P_{n+n_0}(\cos \theta_0) = P_n(\cos \theta_0) \equiv 1 \quad (7.29)$$

irrespective of n_0 . Finally, the scale factors α_{σ} are approximately equal to

$$\alpha_{n+n_0}^2 \approx \alpha_n^2 = \frac{2n+1}{4\pi}. \quad (7.30)$$

Note that Eq. (7.28) splits the non-integer degree Legendre functions in a regular term $P_n^1(\cos \theta)$ and an additional term $(-1)^{n+1} 2n_0 / \sin \theta$. The latter strongly grows near the cone boundary, where $\pi - \theta \ll 1$, but is small otherwise due to the smallness of n_0 . The extent of the angular regime in which the second term is dominant may be characterized by the angle at which this term becomes larger than the regular term. For each $n \geq 1$, this angle is larger than

$$\theta_c = \pi - \sqrt{\frac{1}{\ln \frac{2}{\delta}}}. \quad (7.31)$$

In Eq. (7.28), the regular term vanishes altogether for $n = 0$ since $P_0^1(x) \equiv 0$, but also in this case Eq. (7.31) is a convenient measure for the angular extent of the second term since the latter grows larger than unity at this angle.

Substituting Eqs. (7.27)-(7.30) in the series (7.26), it is found that the Green's function component resembles

$$\mathbf{e}_{z_0} \cdot \mathfrak{G}_T \cdot \mathbf{e}_\theta \approx -ik \sum_{n=1}^{\infty} \alpha_n^2 \left(\mathbf{e}_{z_0} \cdot \mathbf{N}_n^{(1)}(\mathbf{r}_0) \right) \left(\mathbf{e}_\theta \cdot \mathbf{N}_n^{(3)}(\mathbf{r}) \right) \quad (7.32)$$

in the regime $0 \leq \theta < \theta_c$, while it grows as

$$\mathbf{e}_{z_0} \cdot \mathfrak{G}_T \cdot \mathbf{e}_\theta \propto \frac{1}{\pi - \theta} \quad (7.33)$$

in the regime $\theta_c < \theta < \pi - \delta$, that is, close to the cone boundary. Now, Eq. (7.32) may be recognized as the appropriate component of the dyadic Green's function for free space [383]. Therefore, for a narrow-angle cone and in the regime $0 < \theta < \theta_c$, the transition radiation profile (7.23) resembles the radiation that the point charge in Fig. 7.2 (which travels along half the z -axis and disappears in the origin) would produce *without* the presence of the cone. On the other hand, in the regime $\theta_c < \theta < \pi - \delta$ the electric field is proportional to $(\pi - \theta)^{-1}$ by Eqs. (7.33) and (7.13), so that the spectral brightness grows as

$$\frac{\partial^2 W}{\partial \omega \partial \Omega} \propto \frac{1}{(\pi - \theta)^2} \quad \text{for} \quad \theta_c < \theta < \pi - \delta \quad (7.34)$$

near the cone boundary. In the very limit that $\delta \rightarrow 0$, Eq. (7.31) yields that $\theta_c \rightarrow \pi$. Thus, in this limit, the transition radiation is composed of two contributions: (i) the radiation pattern produced by a point charge moving in free space along half the z -axis, and (ii) an infinitesimally thin, infinitely high radiation peak along the negative z -axis. The latter may be seen as the contribution of a surface wave propagating along the infinitesimally thin cone, which will be shown in section 7.5 using an alternative method. First, however, the results (7.23)-(7.24) for the spectral brightness and intensity will be presented in the next section.

7.4 Numerical results

In Fig. 7.3 the spectral brightness (7.23) has been plotted for several values of the cone opening angle. For the charge velocity a relativistic factor of $\gamma \equiv (1 - \beta^2)^{-1/2} = 5$ has been taken. The series has been truncated after 30 terms in each case. The same truncation has been used in the remaining figures of this chapter.

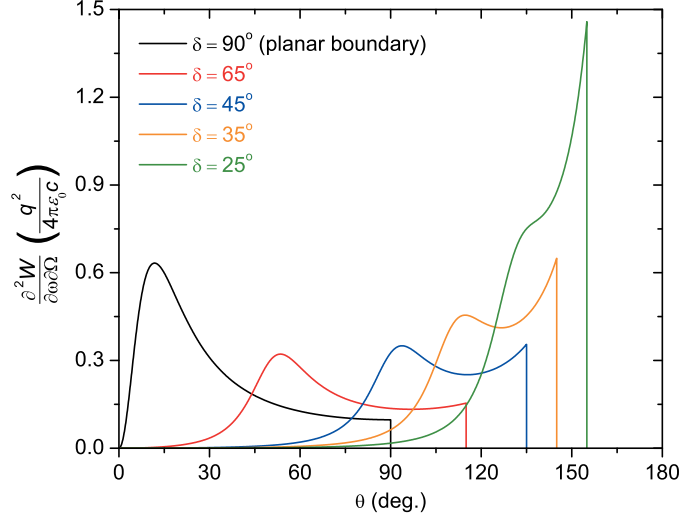


Figure 7.3: Angular spectral brightness profile for several cone opening angles, generated by a point charge moving with $\gamma = 5$. The vertical lines represent the cut-off of the fields at the cone boundary $\theta = \pi - \delta$. The series of Eq. (7.23) has been truncated after 30 terms in the numerical evaluation.

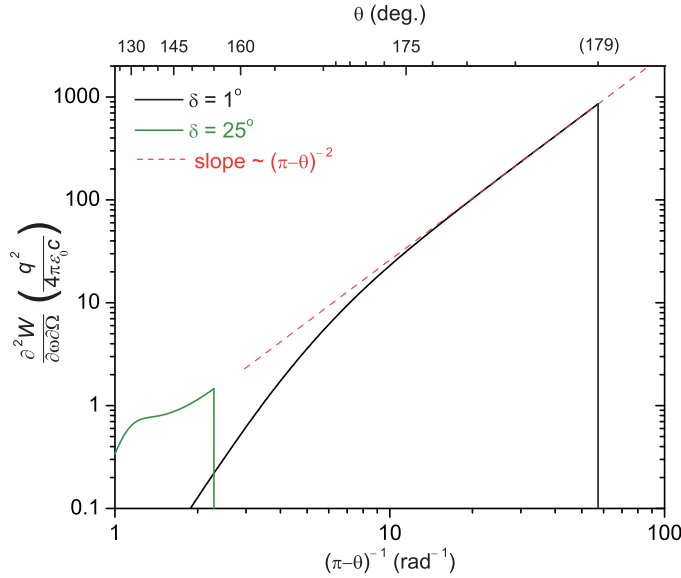


Figure 7.4: Angular spectral brightness profile near the cone boundary for a narrow-angle cone ($\delta = 1^\circ$). As a reference, the spectral brightness for a 25° cone has been plotted in both Fig. 7.3 and this figure. See also the comments below Fig. 7.3.

Apparent from Fig. 7.3 is that (i) The brightness profile contains a 'specular' peak near $\theta = \pi - 2\delta$, which moves towards the cone boundary as the opening angle decreases; (ii) as the opening angle decreases, the brightness profile develops a 'surface' peak at the cone boundary; (iii) this surface peak rapidly grows with decreasing opening angle and dominates the specular peak when $\delta < 25^\circ$.

The first radiation peak mentioned above is called 'specular' since it is analogous to the specular reflection that would be observed at $\theta = \pi - 2\delta$ if free electromagnetic radiation would be axially incident on the cone instead of a point charge. In the present case, however, the incident Coulomb field propagates in the negative z -direction with a speed less than that of light. Therefore a Fourier decomposition of the field differs somewhat from a superposition of free e.m. waves with the wave number $k = \omega/c$, causing the deviation of the specular peak from the angle $\pi - 2\delta$. Indeed, the specular peak tends to this angle when high values of γ are chosen.

The development of the surface peak with decreasing opening angle clearly shows the result of section 7.3.3 that the spectral brightness becomes peaked near the cone boundary in the narrow-angle cone limit. To study the surface peak in this limit, the spectral brightness has been plotted on a doubly logarithmic scale in Fig. 7.4 for a half opening angle of $\delta = 1^\circ$. Note from the scales that the peak height has increased very rapidly as compared to the $\delta = 25^\circ$ case. Also, the peak is very narrow with a FWHM of about 0.5° . The peak shows the asymptotic narrow-angle cone behavior given by Eq. (7.34), which is indicated in Fig. 7.4 by the red dashed line. The estimate (7.31) for the left bound of the regime that is dominated by the surface peak gives $\theta_c = 2.7$ for $\delta = 1^\circ$. Indeed, around this value of θ the surface peak shown in Fig. 7.4 rapidly grows larger than unity and starts to dominate the brightness profile. The $\propto (\pi - \theta)^{-2}$ -behavior sets in at somewhat larger angles since Eq. (7.31) is a lower estimate.

As has been discussed in section 7.2, to estimate the amplitude of SPPs the transition radiation field will excite, the quantity of interest is the magnetic field at the cone boundary. Thus, in the light of THz SPP generation by transition radiation, another very important advantage of the cone geometry is evident: the excited SPPs can be increased by orders of magnitude by tapering the tip into a very narrow cone. This is illustrated once more in Fig. 7.5, in which the spectral brightness evaluated at the cone boundary has been plotted as a function of half opening angle. The spectral brightness increases four orders of magnitude over the range $\delta = 90^\circ \rightarrow \delta = 1^\circ$, corresponding to an increase of two orders of magnitude in the magnetic field and SPP amplitude.

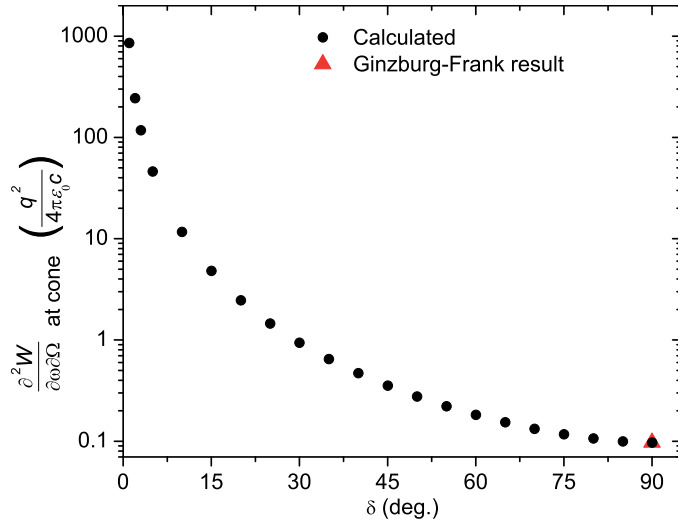


Figure 7.5: Spectral brightness at the cone boundary as a function of half cone opening angle, generated by a point charge moving with $\gamma = 5$. The Ginzburg-Frank result Eq. (7.35) for a planar boundary has been plotted as well.

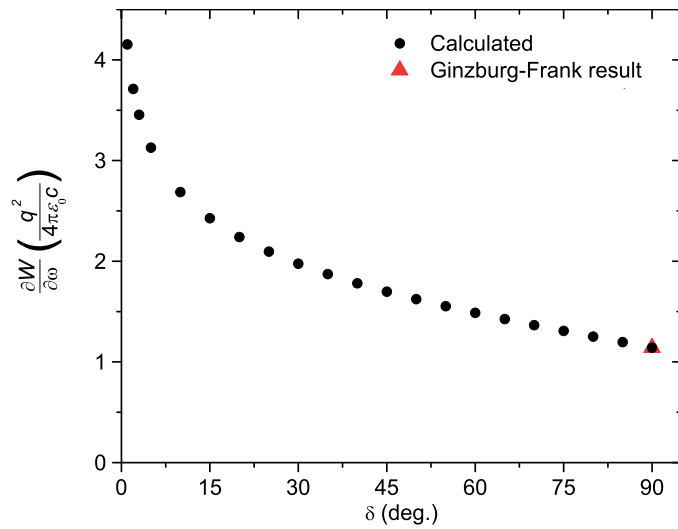


Figure 7.6: Spectral intensity as a function of half cone opening angle, generated by a point charge moving with $\gamma = 5$. The Ginzburg-Frank result for a planar boundary, given by Eq. (7.35) integrated over the angular coordinates, has been plotted as well.

Of interest as well is the spectral intensity (7.24). This quantity has been plotted in Fig. 7.6 as a function of half opening angle. The intensity increases only a factor of four over the range $\delta = 90^\circ \rightarrow \delta = 1^\circ$, in contrast to the rapid growth of the brightness near the cone boundary. Thus, the primary effect of a small opening angle is not so much that more radiation energy is generated, but rather that the radiation strongly concentrates into a narrow solid angle grazing the cone boundary.

7.5 Validation

In order to validate the results obtained in the previous sections, we compare the result (7.23) for the spectral brightness with results obtained by alternative methods, in both the limit of a large cone opening angle (planar boundary or $\delta = 90^\circ$) and the limit of a narrow cone opening angle (semi-infinite line or $\delta \rightarrow 0$).

7.5.1 Planar boundary limit

The transition radiation field generated by a point charge that is normally incident on a planar boundary between different media has been calculated in closed exact form by Ginzburg and Frank [365]. In the special case that one of the media is a perfect conductor and the other is vacuum, their result for the spectral brightness reduces to

$$\frac{\partial^2 W}{\partial \omega \partial \Omega} = \frac{q^2}{4\pi\epsilon_0 c} \left(\frac{\beta \sin \theta}{\pi(1 - \beta^2 \cos^2 \theta)} \right)^2. \quad (7.35)$$

A plot of this expression as a function of θ proves identical to the black graph in Fig. 7.3 for the planar boundary. Likewise, the Ginzburg-Frank results that are shown as well in Figs. 7.5 and 7.6 are equal to the corresponding values calculated with our theory. Thus, the result (7.23) for the spectral brightness is in exact agreement with the closed form result (7.35) of Ginzburg and Frank. This equivalence can also be obtained analytically as we will show now. For a planar boundary $\delta = \pi/2$, the eigenvalues σ defined by Eq. (7.84) reduce to the odd positive integers. This makes it possible to use the integral representation of the integer order spherical Bessel function [388],

$$j_{2n+1}(kz_0) = (-1)^n \int_0^{\pi/2} \sin(kz_0 \cos s) P_{2n+1}(\cos s) \sin s ds, \quad (7.36)$$

in the definition Eq. (7.93) of the quantities $I_{2n+1}(\beta)$. This gives

$$I_{2n+1}(\beta) = (-1)^n \int_0^{\pi/2} H(s) P_{2n+1}(\cos s) \sin s ds, \quad (7.37)$$

with

$$H(s) \equiv \int_0^\infty \frac{\sin(kz_0 \cos s) e^{-i\frac{k}{\beta}z_0}}{z_0} dz_0. \quad (7.38)$$

Substitution of Eqs. (7.37)-(7.38) in the electric field Eq. (7.18) yields

$$\mathbf{E}_T \approx \frac{\mu_0 \omega q}{(2\pi)^{3/2}} \frac{e^{ikr}}{ikr} \mathbf{e}_\theta \frac{d}{d\theta} \sum_{n=0}^{\infty} c_{2n+1} \tilde{P}_{2n+1}(\cos \theta); \quad (7.39)$$

$$c_{2n+1} \equiv \int_0^{\pi/2} H(s) \tilde{P}_{2n+1}(\cos s) \sin s ds. \quad (7.40)$$

Here, $\tilde{P}_{2n+1}(\cos \theta) \equiv \sqrt{2\pi} \alpha_{2n+1} P_{2n+1}(\cos \theta)$ denote Legendre polynomials normalized such that $\int_0^{\pi/2} [\tilde{P}_{2n+1}(\cos \theta)]^2 \sin \theta d\theta = 1$; furthermore the property $P_{2n+1}^1(\cos \theta) = (d/d\theta)P_{2n+1}(\cos \theta)$ was used. The sum in Eq. (7.39) can be recognized as an expansion of the function $H(\theta)$ in terms of the orthonormal functions \tilde{P}_{2n+1} on the domain $\theta \in (0, \pi/2)$ with weighting function $\sin \theta$. Replacing this sum accordingly by Eq. (7.38) with $s \rightarrow \theta$, and performing successively the differentiation $d/d\theta$ and the integration with respect to z_0 , gives

$$\mathbf{E}_T = \frac{\mu_0 \omega q}{(2\pi)^{3/2}} \frac{e^{ikr}}{kr} \frac{\beta \sin \theta}{1 - \beta^2 \cos^2 \theta}. \quad (7.41)$$

The spectral brightness corresponding to this electric field equals Eq. (7.35). The brightness Eq. (7.23) for general cone angles δ thus correctly reduces to the Ginzburg-Frank result in the planar boundary limit $\delta \rightarrow \pi/2$.

7.5.2 Semi-infinite line limit

One approximate method to obtain the scattered electromagnetic field, which results if some known field is incident on a conducting object, is the Physical Theory of Diffraction (PTD) method. The method is commonly used in antenna theory [389]. The primary approximation in the method is to suppose that the surface current density \mathbf{K} on the conductor surface satisfies the boundary condition

$$\mu_0 \mathbf{K} = 2\mathbf{n} \times \mathbf{B}_{\text{in}} \text{ rather than } \mu_0 \mathbf{K} = \mathbf{n} \times \mathbf{B}_{\text{tot}} \quad (7.42)$$

where \mathbf{B}_{in} is the (unperturbed) incident magnetic field and \mathbf{B}_{tot} the total (incident plus scattered) magnetic field. Thus, the magnetic field contribution at the surface induced by the surface current is assumed to be equal to the incident field. From the resulting approximate surface current distribution, the scattered electromagnetic fields may be calculated by evaluation of the standard electromagnetic vector potential.

The PTD method has been subjected to some criticisms [389]. The most important objection in the case of a cone as a scatterer is that the curvature of the surface is infinite at the tip, which in general makes Eq. (7.42) a poor approximation. However, the method has been successfully applied to accurately calculate the radar cross section of a narrow-angle, semi-infinite cone [385, 390, 391]. Moreover, rigorous expansions of the surface current density exist that are in good agreement with the PTD approximation near the cone tip [392]. Therefore, we proceed by applying the PTD method to the transition radiation problem, and the results will show to be in perfect agreement with the results obtained in section 7.3.3.

In the present case, the incident field \mathbf{B}_{in} is that generated by the moving point charge, extended into the region $z < 0$. The current distribution \mathbf{J} of this charge is given by Eq. (7.16). Now, the current \mathbf{J} generates \mathbf{B}_{in} , and this field in turn generates the current \mathbf{K} according to Eq. (7.42). Because of the symmetry that both currents \mathbf{J} and \mathbf{K} are confined to the z -axis, it follows from Eq. (7.42) that simply

$$\mathbf{K} = 2\mathbf{J} \quad \text{for} \quad z < 0, \quad (7.43)$$

which is the current of a uniformly moving point charge $2q$. Now, the *total* electric far field is the radiation field produced by \mathbf{K} at $z < 0$ and \mathbf{J} at $z > 0$ *combined*. From this combination we may remove a common charge q moving along the complete z -axis, since the latter will not radiate at all. Thus, the effective radiation source reduces to a point charge q moving along the negative z -axis and surrounded by free space. This confirms the first contribution predicted at the end of section 7.3.3.

To obtain the fields in some more detail, we consider the current distribution $I(z)$ of the effective source, which is

$$I(z) = -(2\pi)^{-1/2} q e^{-i\frac{k}{\beta}z} \quad \text{for} \quad z < 0. \quad (7.44)$$

Note that $I(z)$ has the units of a Fourier transformed current. One may proceed by calculation of the vector potential generated by this current distribution, which involves transformation to the k -domain and contour integration techniques [393]. However, the electromagnetic fields can be obtained directly in a more elegant way, by recognizing Eq. (7.44) as the current distribution of a linear traveling wave antenna of the slow type [394] with one of the endpoints placed at infinity. Traveling wave antennas carry a linearly phased current, as given by the factor $e^{-i\frac{k}{\beta}z}$, while 'slow' refers to the fact that the propagation velocity βc is less than that of light in vacuum. Recently, a similar antenna model has been successfully used to describe the radiation from a metal tip coupled to THz pulses generated with a photoconductive switch [395]. An important property of traveling wave antennas is that they generate two distinct electromagnetic field contributions, namely (i) they carry a radially

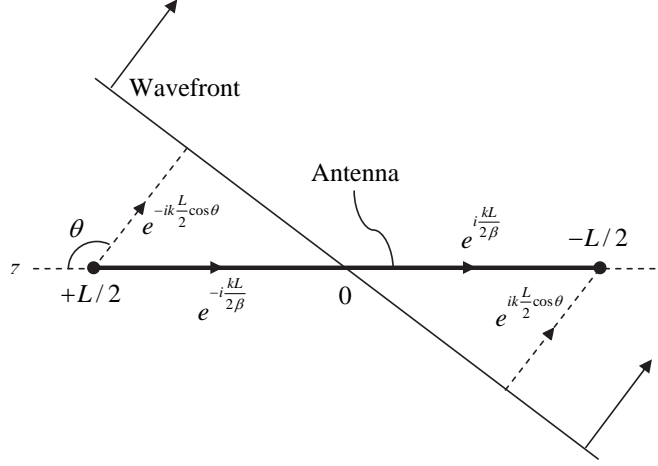


Figure 7.7: Linear slow wave antenna with the endpoints at $z = \pm L/2$, radiating in the direction θ . Both endpoints radiate spherical waves, which acquire mutual phase differences at the shown wavefront due to different optical path lengths. The direction of wave propagation along the different paths has been indicated by arrowheads, together with the associated phase factor introduced in the field expression (7.45).

evanescent electromagnetic field along their length, that is, a surface wave; and (ii) they radiate from their endpoints only. Regarding the current (7.44) as a limiting case of a slow wave antenna, the first of these contributions carries energy into an infinitesimally small solid angle around $\theta = \pi$. This contributes an additional peak to the spectral brightness profile at $\theta = \pi$ that is infinitesimally thin and infinitely high. This confirms the second property predicted at the end of section 7.3.3.

Summarizing, by qualitative arguments the Green's function method of section 7.3 agrees with the PTD method and antenna theory used above. As an additional and a more quantitative check, we now calculate the spectral brightness using the antenna model. Fig. 7.7 shows a linear slow wave antenna with a current distribution $I(z) = I_0 e^{-i\frac{k}{\beta}z}$ and with the endpoints at $z = \pm L/2$, radiating in the direction θ . The electric radiation field of this antenna in the far zone is given by [394]

$$\mathbf{E}_T = -I_0 \frac{\mu_0 c}{4\pi} \frac{e^{ikr}}{r} \frac{\beta \sin \theta}{1 + \beta \cos \theta} \left(e^{ik\frac{L}{2}(\cos \theta + \beta^{-1})} - e^{-ik\frac{L}{2}(\cos \theta + \beta^{-1})} \right). \quad (7.45)$$

Now, the traveling wave $e^{-i\frac{k}{\beta}z}$ along the antenna gives a harmonic excitation of the endpoint in $z = \pm L/2$ with a phase of $e^{\mp i\frac{kL}{2\beta}}$ with respect to the origin, so that it will radiate spherical waves with this phase. The waves from both endpoints subsequently add in the far field with an additional phase $e^{\mp i\frac{kL}{2} \cos \theta}$ due to the path difference in-

duced by the orientation of the antenna with respect to the direction of propagation. The different phase factors in the two field contributions are indicated in Fig. 7.7. Observe in Eq. (7.45) that the phase factors in large braces correspond exactly to those just described, so that factor in front of the braces may be interpreted as the radiation generated by a single endpoint. This is also noted in Ref. [393] for the case of a strip carrying a traveling wave. From the symmetry of the problem and the fact that the first line of Eq. (7.45) changes sign under the substitution $(\beta, \theta) \rightarrow (-\beta, \pi - \theta)$, the endpoints have equal radiation patterns but with opposite sign, hence the minus sign in the second line.

Returning to the semi-infinite antenna represented by the current (7.44), only the radiation from the endpoint at $z = 0$ contributes to the far field at observation angles $\theta \neq \pi$, since the other endpoint is placed at an infinite distance. From Eq. (7.45) with $I_0 \equiv -(2\pi)^{-1/2}q$, the electric field in the far zone is

$$\mathbf{E}_T = \frac{\mu_0 q c}{2(2\pi)^{\frac{3}{2}}} \frac{e^{ikr}}{r} \frac{\beta \sin \theta}{1 + \beta \cos \theta}. \quad (7.46)$$

Applying Eqs. (7.20)-(7.22) to this field yields the spectral brightness

$$\frac{\partial^2 W}{\partial \omega \partial \Omega} = \frac{q^2}{4\pi \epsilon_0 c} \left(\frac{\beta \sin \theta}{2\pi(1 + \beta \cos \theta)} \right)^2. \quad (7.47)$$

Now, Eq. (7.45) gives the free-space radiation field and does not include the surface wave traveling along the antenna. Therefore, in order to make a proper comparison of Eq. (7.47) with the result Eq. (7.23) obtained by the Green's function method, we have to consider the latter in the limit $\delta \rightarrow 0$ and take the free-space radiation part only. In terms of the regular regime $0 < \theta < \theta_c$ and the regime $\theta_c < \theta < \pi$ where the brightness is peaked considered in section 7.3.3, this is equivalent to letting θ_c approach π as $\delta \rightarrow 0$ and remove the resulting radiation peak along the z -axis. This is easily effected by enforcing $n_0 \equiv 0$ in Eq. (7.28), that is, by using in the expansion (7.23) integer degree Legendre functions. The resulting adapted series has been plotted in Fig. 7.8. Indeed, the remaining spectral brightness thus obtained is exactly the same as that given by Eq. (7.47).

In summary, the Green's function result for the spectral brightness is in exact agreement with both the Ginzburg-Frank result for the planar boundary limit and the PTD method for the narrow-angle cone limit. Therefore we are confident that the results obtained for the intermediate opening angles are reliable.

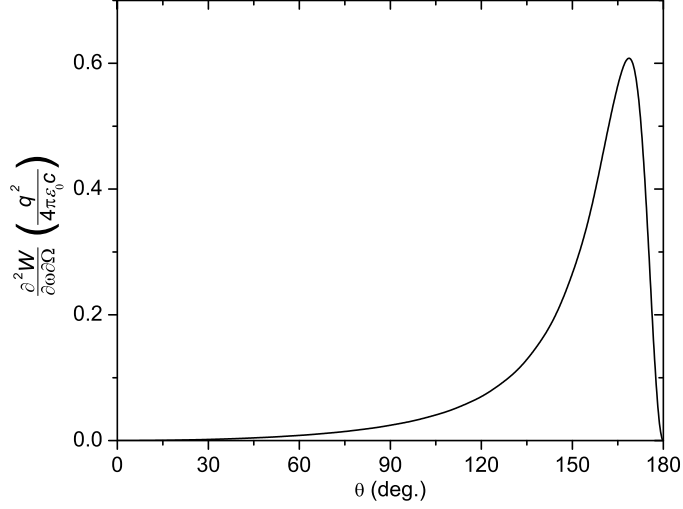


Figure 7.8: Angular spectral brightness profile in the limit that $\delta \rightarrow 0$. The limit has been taken by choosing the integers for the set of eigenvalues $\{\sigma\}$ in the series of Eq. (7.23). A point charge moving with $\gamma = 5$ has been assumed and the series has been truncated after 30 terms in the numerical evaluation.

7.6 Extension to electron bunches

In the introduction of this chapter we proposed to excite very strong SPPs using bunched electrons rather than a single point charge. To study the effect of such an extended source charge, we now replace the point charge in Fig. 7.2 by a general charge distribution that moves as a whole towards the cone tip without deforming, that is, by an electron bunch. Since different parts of the bunch will generate transition radiation at different times, the extent of the bunch in both the longitudinal and transverse direction will determine the magnitude of the radiation field by coherence effects. Below, the effects of the longitudinal and transverse extent of the bunch will be calculated separately. In the next section, the results will be combined to estimate the radiation field and SPP intensities generated by an electron bunch that can be readily obtained with present technology.

7.6.1 Bunches of finite length

The point charge of Fig. 7.2 passes the cone boundary at the origin at time $t = 0$. If instead a point charge is considered that passes the origin at some other time $t_1 \neq 0$, Eqs. (7.16) and (7.18) for the current distribution and electric field respectively are multiplied by a phase factor $e^{i\frac{c}{\beta}z_1}$, where $z_1 = \beta ct_1$ is the position of the charge on the z -axis at $t = 0$. Therefore, composing at $t = 0$ a line charge distribution $\lambda(z)$ on the z -axis from individual point charges and adding their electric fields yields

$$\mathbf{E}_T = \frac{1}{q} \left(\int_{-\infty}^{\infty} \lambda(z_1) e^{i\frac{k}{\beta} z_1} dz_1 \right) \mathbf{E}_{T0} \equiv F_L \mathbf{E}_{T0}. \quad (7.48)$$

Here, \mathbf{E}_T is the electric transition radiation field generated by the line distribution, q is the total charge of the distribution and \mathbf{E}_{T0} is the field that would be produced by a point charge of magnitude q . The quantity F_L appears frequently in radiation problems and is called the (longitudinal) form factor [396]. From Eqs. (7.20)-(7.22), the spectral brightness produced by the charge distribution is

$$\frac{\partial^2 W}{\partial \omega \partial \Omega} = |F_L|^2 \frac{\partial^2 W_0}{\partial \omega \partial \Omega}, \quad (7.49)$$

where $\partial^2 W_0 / \partial \omega \partial \Omega$ is the spectral brightness produced by a point charge of magnitude q . Evidently, the form factor decreases rapidly as $|kz_1/\beta|$ grows larger than unity in the integral of Eq. (7.48), corresponding to incoherent contributions to the radiation field from the different parts of the charge distribution. If, on the other hand, the distribution is not much longer than a single wavelength of interest, the radiation contributions add coherently, leading to very strong electric fields.

7.6.2 Bunches of finite transverse extent

To study the effect of the transverse extent of the charge distribution impinging on the cone tip, we consider an infinitesimally thin and homogeneously filled disk of charge with radius a and total charge q , with its center at the z -axis. The Fourier transformed current density of this disk is

$$\mathbf{J}(\omega) = -(2\pi)^{-1/2} \frac{q}{\pi a^2} e^{-i\frac{k}{\beta} z} \Theta(a - \rho) \mathbf{e}_z, \quad (7.50)$$

where Θ denotes the Heaviside step function. Substitution of this expression and the dyadic Green's function (7.17) in Eq. (7.13) yields an expression for the transverse electric field generated by the charged disk. Similar to the electric field generated by a point charge considered in Appendix 7.D, in the far zone $kr \rightarrow \infty$ this expression reduces to

$$\mathbf{E}_T(\mathbf{r}) \approx \frac{\mu_0 \omega q}{\sqrt{2\pi}} \frac{e^{ikr}}{kr} \sum_{\sigma} \frac{\alpha_{\sigma}^2 e^{-i\sigma \frac{\pi}{2}}}{\sigma(\sigma+1)} Q_{\sigma}(\beta, ka) P_{\sigma}^1(\cos \theta) \mathbf{e}_{\theta}; \quad (7.51)$$

where now

$$Q_{\sigma}(\beta, ka) \equiv \frac{k}{\pi a^2} \iiint_{V_0} e^{-i\frac{k}{\beta} z_0} \mathbf{e}_z \cdot \mathbf{N}_{\sigma}^{(1)}(\mathbf{r}_0) dV_0. \quad (7.52)$$

Because of the step function in Eq. (7.50), the integration volume V_0 in Q_{σ} is confined to a semi-infinite cylinder with a conical cut-out, as is shown in Fig. 7.9. In Appendix 7.E, the quantity Q_{σ} is analyzed further. It is shown that Eq. (7.52) can be

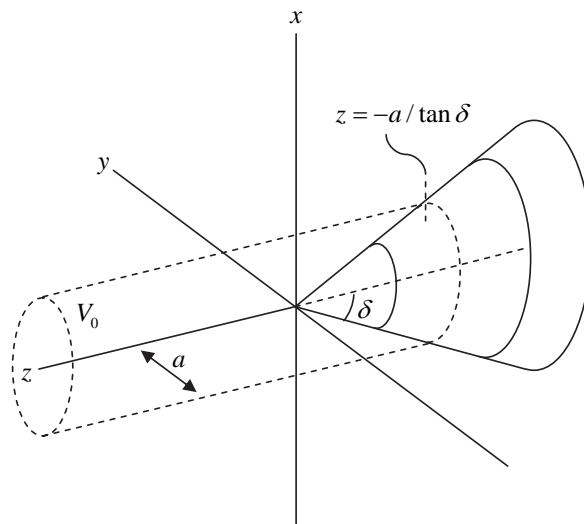


Figure 7.9: Integration volume V_0 to be used in Eq. (7.52).

reduced to a one-dimensional integral using the properties of the functions \mathbf{N}_σ . The expression thus obtained is checked by taking the limit $ka \rightarrow 0$, which yields the correct equivalent expression for a point charge. Finally, the remaining integration path is deformed in the complex s -plane in order to substitute exponential behavior for oscillatory behavior of the integrand along the path, which enables efficient numerical evaluation of Eq. (7.52). For any choice of the cone opening angle and the dimensionless disk size ka , Eq. (7.51) now permits numerical evaluation of the electric far field. As usual, Eqs. (7.20)-(7.22) translate the electric field to the spectral brightness.

As an example, Fig. 7.10 shows the spectral brightness profile thus obtained for a $\delta = 45^\circ$ cone and several values of ka . As the disk grows larger than about $a = k^{-1} = \lambda/(2\pi)$, radiation from different parts of the disk start to become incoherent, decreasing the spectral brightness magnitude. The surface peak decreases more rapidly with ka than the specular peak, which can be observed for other opening angles as well.

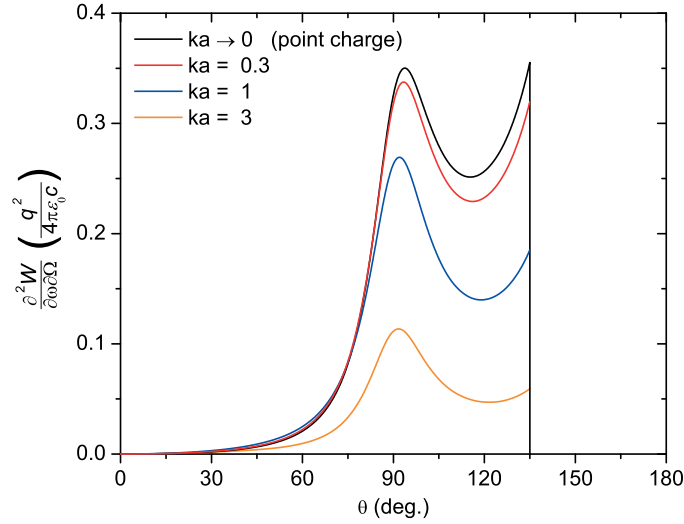


Figure 7.10: Angular spectral brightness profile for a $\delta = 45^\circ$ cone and several disk sizes ka . The same conditions as in Fig. 7.3 have been used. The black curve ($ka \rightarrow 0$) has been obtained using the point charge result Eq. (7.23).

To study the effect of the disk size on the spectral brightness in more detail, the spectral brightness at the cone boundary and the spectral intensity have been plotted as a function of ka in Figs. 7.11 and 7.12 respectively for several values of the opening angle. In the case of a planar boundary, extending a point charge to a disk has little effect on the considered quantity in both figures, until the disk radius grows larger than about $ka = 1$ after which the curves quickly decrease. One effect of choosing a smaller opening angle is that the coherence starts to break down at smaller disk radii, which is a disadvantage of the use of small opening angle cones. However, this effect is more than compensated by the greatly increased spectral brightness shown in Fig. 7.5. Moreover, for $ka > \sim 1$, small opening angle cones yield more coherent radiation compared to a planar boundary. This can be a significant advantage when it is technologically difficult to reduce the transverse bunch size.

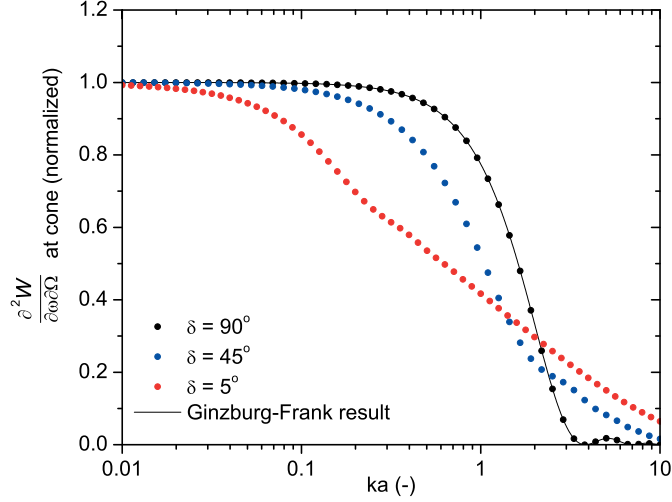


Figure 7.11: Spectral brightness at the cone boundary as a function of dimensionless disk size ka . It has been assumed that $\gamma = 5$. The curves have been normalized to their corresponding point charge result shown in Fig. 7.5. The solid line represents the analytical result for a planar boundary adjusted by the disk form factor (Eq. (7.55)).

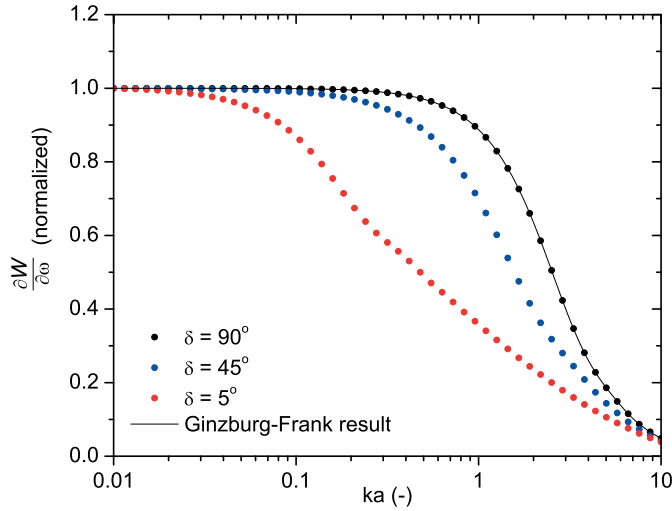


Figure 7.12: Spectral intensity as a function of dimensionless disk size ka . It has been assumed that $\gamma = 5$. The curves have been normalized to their corresponding point charge result shown in Fig. 7.6. The solid line represents the analytical result for a planar boundary, adjusted by the disk form factor (Eq. (7.56)).

As before, the results for the planar boundary $\delta = 90^\circ$ can be checked with the Ginzburg-Frank result Eq. (7.35). Analogous to the effect of a longitudinal extent of the charge distribution shown by Eq. (7.49), in the case of the disk the spectral brightness should be multiplied by a transverse form factor $|F_T|^2$, with [396]

$$F_T = \frac{1}{q} \int_0^{2\pi} \int_0^\infty \sigma(\rho, \phi) e^{ik_r \rho \cos \phi} \rho d\rho d\phi, \quad (7.53)$$

where $\sigma(\rho, \phi)$ is the surface charge distribution of the disk and $k_r = k \sin \theta$ is the radial component of the wave vector of the radiation under consideration. For the disk considered here, Eq. (7.53) yields

$$F_T = \frac{2J_1(ka \sin \theta)}{ka \sin \theta}, \quad (7.54)$$

where J is the cylindrical Bessel function. Thus, Ginzburg-Frank theory predicts a spectral brightness at the cone boundary $\theta = \pi/2$ proportional to

$$\frac{\partial^2 W}{\partial \omega \partial \Omega} \propto \left(\frac{J_1(ka)}{ka} \right)^2, \quad (7.55)$$

while the spectral intensity is proportional to

$$\frac{\partial W}{\partial \omega} \propto \int_0^{\pi/2} \left(\frac{J_1(ka \sin \theta)}{ka(1 - \beta^2 \cos^2 \theta)} \right)^2 \sin \theta d\theta. \quad (7.56)$$

In Figs. 7.11 and 7.12 these results have been plotted as well, and they are in excellent agreement with the numerical results.

7.6.3 Three-dimensional bunches

Combining the above results for the longitudinal and transverse extent of the source charge distribution to obtain the transition radiation from three-dimensional electron bunches is straightforward. Consider a bunch with a cylindrically symmetric charge density distribution $\tau(\rho, z)$ at time $t = 0$. Of course, the bunch may be thought of as composed of transverse slices of infinitesimal thickness dz and charge

$$dq(z) = dz \times 2\pi \int_0^\infty \tau(\rho, z) \rho d\rho \equiv \lambda_{\text{eff}}(z) dz, \quad (7.57)$$

and for each one of them the electric far field can be calculated by the method of section 7.6.2. Note that any charge distribution of the slice other than homogeneous will introduce additional factors in the integrand of Eq. (7.52), requiring additional numerical effort. The resulting field of the slice will always be less than that of a point

charge of equal magnitude dq due to the extent of the charge within the slice. To obtain the electric field produced by the complete bunch, the fields of the individual slices must be added. While doing so, the phase differences due to the longitudinal positions of the individual slices within the bunch have to be accounted for as was done in Eq. (7.48). Combining Eqs. (7.51) and (7.57) and including a longitudinal phase factor yields the electric far field of the bunch:

$$\mathbf{E}_T(\mathbf{r}) \approx \frac{\mu_0 \omega q}{\sqrt{2\pi}} \frac{e^{ikr}}{kr} \mathbf{e}_\theta \sum_\sigma \frac{\alpha_\sigma^2 e^{-i\sigma \frac{\pi}{2}}}{\sigma(\sigma+1)} P_\sigma^1(\cos \theta) \int_{-\infty}^{\infty} Q_\sigma(z_1) \frac{\lambda_{\text{eff}}(z_1)}{q} e^{i\frac{k}{\beta} z_1} dz_1. \quad (7.58)$$

Here, q is the charge of the whole bunch, and $Q_\sigma(z_1)$ is an integral similar to Eq. (7.52) that accounts for the transverse extent of charge within the slice at $z = z_1$ in the bunch. In the case that each transverse cross section is a homogeneously charged, hard-edged disk as in the previous section, $Q_\sigma(z_1) \equiv Q_\sigma(\beta, ka(z_1))$ is given exactly by Eq. (7.52), where $a(z_1)$ is the radius of the slice at $z = z_1$. If in addition each slice is equal, the bunch has the somewhat artificial form of a hard-edged, homogeneously charged cylinder with radius a and some length $2b$. In this case Q_σ becomes independent of z_1 , so that Eq. (7.58) reduces to Eq. (7.51) multiplied by an effective longitudinal form factor $F_{L,\text{eff}}$. The latter is given by Eq. (7.48) with $\lambda = \lambda_{\text{eff}}$ and equals

$$F_{L,\text{eff}} = \text{sinc} \left(\frac{kb}{\beta} \right). \quad (7.59)$$

7.7 Obtainable SPPs in the time domain

We now return to the experimental setup of Fig. 7.1 we propose to generate SPPs on a wire. In sections 7.3 through 7.6 we modeled the metal tip of the wire by a semi-infinite, perfectly conducting cone and showed how the radiation field generated by charge impinging on it can be calculated. Now, we will choose realistic electron bunches and apply the theory to them. As a realistic setup we choose a copper wire with radius $R = 0.5$ mm tapered into a $\delta = 5^\circ$ tip, which is sharp enough to benefit from the strong increase in the field amplitude shown in Fig. 7.5, but which is still easy to manufacture. For THz frequencies, it is easily verified that conditions (7.5) and (7.6) hold at the position where the conical tip smoothly evolves into the cylindrical wire (i.e. at $r = R/\sin \delta$, or $|z| = R/\tan \delta$ in Eqs. (7.5) and (7.6)). Analysis of the longitudinal wave vector $k_z(a)$ as a function of local radius $a = |z| \tan \delta$ shows that also condition (7.7) holds at this position [335]. So if in the setup of Fig. 7.1 the tip smoothly evolves into the wire, we can estimate the field strength of the generated SPPs propagating along the wire by evaluating our theory at radial position $r = R/\sin \delta$.

For the bunch form we choose homogeneously charged, hard-edged ellipsoids. Theoretically, such 'waterbag' bunches are the ideal particle distributions for controlled, high-brightness charged particle acceleration. Because of their linear internal fields they do not suffer from brightness degradation caused by space-charge forces [397, 398]. A practical recipe has been developed which results in almost ideal ellipsoidal bunches [377–380] using a table-top setup. The bunches are characterized by their charge q , their transverse half axis a and their longitudinal half axis $b = \beta cT/2$. We consider three bunches:

1. A 'conventional' bunch with $q = 100$ pC, $T = 500$ fs and $a = 200$ μm that we can presently make in the lab;
2. A 'short' bunch with $q = 100$ pC, $T = 100$ fs and $a = 140$ μm . Detailed numerical simulations have shown that such a bunch may readily be obtained by longitudinal compression of bunch 1 using a two-cell booster compressor [379];
3. A 'short and slim' bunch with $q = 100$ pC, $T = 100$ fs and $a = 50$ μm that is obtained by additional compression of bunch 2 in the transverse direction, which may be achieved in the near future.

For the three bunches above, we have calculated the electric field as a function of frequency, generated at the cone boundary a distance $r = R/\sin\delta$ from the cone tip. For this purpose the bunches were approximated by 100 cylindrical slices, so that the integrals in Eq. (7.58) were approximated by summations over the slices. To validate the numerical results, we compared the calculated spectra $E_{T\theta}(\omega)$ with those generated by cylindrical bunches with the same parameters q , a and b . The latter electric fields are given by the product of Eqs. (7.51) and (7.59). These fields may be seen as 'worst case' approximations for those generated by the ellipsoidal bunches, since the average distance between the charges within a cylindrical bunch is larger than that within the corresponding ellipsoidal bunch, leading to less coherent radiation. The calculated squared field amplitudes are shown in Fig. 7.13. The spectra have been normalized to the field E_0 generated at the same position $r = R/\sin\delta$ by a point charge of equal magnitude $q = 100$ pC, given by

$$E_0^2 \equiv \frac{\sin^2\delta}{2\epsilon_0 c R^2} \left. \frac{\partial^2 W}{\partial\omega\partial\Omega} \right|_{\theta=\pi-\delta}, \quad (7.60)$$

with $\partial^2 W/\partial\omega\partial\Omega$ given by Eq. (7.23). As expected, the field generated by an ellipsoidal bunch is greater than that of the corresponding cylindrical bunch for all frequencies. This difference is only slight, however, which means that the maximum transverse and longitudinal cross sections of the bunch are decisive for the coherence. The spectra are coherent up to the THz regime, which reflects the fact that the bunch dimensions have been brought down to the order of the 1 THz wavelength $2\pi k^{-1} \approx 300$ $\mu\text{m} \approx c \cdot 1$ ps by current technology.

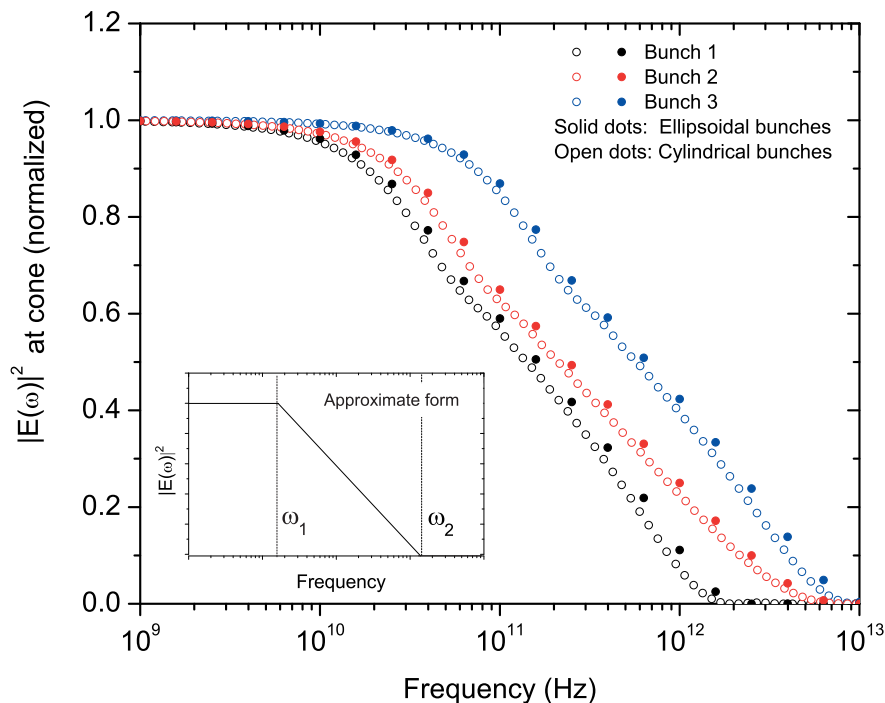


Figure 7.13: Squared electric field amplitude at the cone boundary, generated by the three bunches considered in section 7.7 (dots) and that of corresponding cylindrical bunches with the same charge and dimensions (solid lines). A relativistic factor of $\gamma = 5$ and a cone opening angle of $\delta = 5^\circ$ have been assumed. The curves have been normalized to the field amplitude generated by a point charge of equal magnitude as the bunches. The inset shows the approximate form of the curves used in section 7.7 to make time-domain estimations.

In order to find the pulse form of the SPPs that will be measured in practice in the setup of Fig. 7.1, the inverse Fourier transforms of the electric fields of Fig. 7.13 have to be calculated. A rigorous treatment of this is beyond the scope of this thesis. However, the field spectra raise the question whether the time domain pulse is governed by the THz regime, that is, whether the spectra do indeed represent sub-picosecond SPPs. In order to verify this, we approximate the inverse Fourier transform of the field spectra of Fig. 7.13. For this purpose the spectra are approximated by straight line segments, as is indicated in the inset of the figure. In Appendix 7.F the inverse Fourier transform of these approximate spectra is calculated. This yields an estimate of the peak electric field $E(t)_{\max}$ of the SPP pulse at the wire surface, and the pulse duration τ , which is defined as

$$\tau \equiv \frac{1}{E(t)_{\max}} \int_{-\infty}^{\infty} E(t) dt. \quad (7.61)$$

Table 7.1 shows the estimated peak electric field and duration of the SPP pulse as defined above, generated by the three considered bunches. As can be seen, the SPP pulse is governed by the high-frequency part of the field spectra, since $\tau < 1$ ps. From the table, the potential of the method we propose to generate THz SPPs is clear. First, by using currently available electron bunches, it is possible to excite sub-picosecond pulses, that is, SPPs with THz bandwidth can be generated on a wire. Second, these SPPs carry peak electric fields in the order of MV/cm. Such fields are several orders of magnitude higher than any SPP field that can currently be obtained by coupling free-space THz radiation onto a wire.

Table 7.1: Time-domain estimates of the peak SPP electric field $E(t)_{\max}$ (Eq. (7.108)) and pulse duration τ (Eq. (7.61)), using the parameters ω_1 and ω_2 in the field model (7.105).

Bunch	ω_1 (THz)	ω_2 (THz)	$E(t)_{\max}$ (MV/cm)	τ (ps)
1	$1.1 \cdot 10^{-2}$	2.0	0.35	0.64
2	$1.3 \cdot 10^{-2}$	5.0	0.82	0.27
3	$4.7 \cdot 10^{-2}$	8.2	1.4	0.16

7.8 Experimental verification

At the Eindhoven University of Technology, the generation of THz SPPs on a wire using electron bunches has been demonstrated experimentally [399]. To this end, electron bunches were created and accelerated to 3.1 MeV using an RF-photogun [400], after which they were fired at the tapered tip of an aluminum wire with a radius of 0.75 mm. The half opening angle of the tip was $\delta = 4^\circ$. A ZnTe crystal was mounted on top of the wire 8 cm from the tip in order to measure the electric field by time-resolved electro-optical detection [401]. The bunch possessed a charge of $q = 160$ pC, an rms transverse size of $a = 0.2$ mm, and an estimated length of $T = 5.4$ ps. At the position of the ZnTe crystal, pulsed electric fields were measured with a peak strength of $E(t)_{\max} \approx 0.005$ MV/cm and a pulse length of $\tau \approx 6$ ps. It was confirmed that the detected pulses indeed represented surface waves by verifying that the field had the expected radial dependence, and moreover that the pulses followed the wire along a bend introduced further downstream. More details can be found in Ref. [399].

The electron bunches in this experiment were of the same transverse size as bunch 1 of the previous section, but were a factor of ten longer and contained some more charge. In order to compare the measured results with those of section 7.7, we note

that 1) for a fixed bunch length and width, the generated electric field $E(t)_{\max}$ should be proportional to the bunch charge; 2) for a fixed transverse size, the pulse length τ should be proportional to the bunch length; and 3) it may be observed from Table 7.1 that the product $E(t)_{\max}\tau = 0.22$ psMV/cm in all three cases, that is, apparently this product is nearly independent of the bunch shape. Based on these rules and the data of bunch 1, we should therefore expect the measured pulse length to be $\tau = 10 \times 0.64 = 6.4$ ps, the mentioned product to be $E(t)_{\max}\tau = 1.6 \times 0.22 = 0.35$ psMV/cm, and hence the electric field to be $E(t)_{\max} = 0.35/6.4 = 0.05$ MV/cm. The measured pulse length agrees very well with these estimates. The measured electric field, however, is an order of magnitude weaker than expected. Nevertheless, it should be stressed that the observed pulses are still orders of magnitude more intense than those observed so far in other experiments [333, 364]. This is apparent from the fact that the detection of terahertz surface waves normally requires signal integration over many repetitions [333, 364], while in the current experiment a single shot is sufficient.

The discrepancy between the expected and observed electric field may be caused by imperfect alignment of the bunch trajectory with the wire axis, which was difficult to monitor in the experiment. Another possible cause for the discrepancy was identified as well [399]. Namely, the relativistic electrons impinging on the metal tip will be subjected to multiple scattering by the aluminum atoms; in addition they will excite secondary electrons. This causes a substantial amount of electrons to scatter out of the metal before all kinetic energy of the incident bunch has been dissipated. This picture is confirmed by a measured small *removal* of electrons from the wire upon impact of the electron bunch, rather than an increase. The scattered electrons emerging from the metal generate their own transition radiation that is detrimental for the main pulse propagating along the wire. However, assessing the significance of this mechanism quantitatively would require detailed modeling of the multiple scattering process. This is outside the scope of this thesis.

7.9 Conclusion

In conclusion, we propose a method to excite THz SPPs on a wire by launching electron bunches onto a conically tapered end of the wire. We have calculated analytically the radiation field generated by these bunches assuming a perfectly conducting semi-infinite cone. We have linked the results to the electric field strength and duration of the SPPs that are excited and propagate along the wire in a realistic setup. We have shown that, using currently available electron bunches, it is possible to generate sub-picosecond SPP pulses with peak electric fields of the order of MV/cm on a 1 mm diameter wire. Focusing of such Terahertz Surface Plasmon Polaritons may yield electromagnetic THz fields that are both very strong and highly localized, enabling non-linear THz experiments with sub-wavelength spatial resolution.

Appendix 7.A SPP field in conical geometry

Using the eikonal method to approximate the SPP electric field in a conical geometry [341], it is recognized that a thin slice of the cone at $z = z_0 < 0$ resembles part of a cylinder with radius $a = |z_0| \tan \delta$, so that locally the SPP fields resemble the fields of a surface wave propagating along such a cylinder. Hence, the SPP electric field in the conical geometry is approximated by

$$\mathbf{E}_{\text{SPP}}(\mathbf{r}) = \mathbf{E}_{\text{cyl}}(\mathbf{r}) \exp[i\psi(z)], \quad (7.62)$$

where $\psi(z)$ is a phase function to be determined, and $\mathbf{E}_{\text{cyl}}(\mathbf{r})$ is the field of a surface wave along a cylinder with radius a . The latter is given in cylindrical coordinates (ρ, ϕ, z) by [402]

$$\begin{pmatrix} E_{\text{cyl},\rho} \\ E_{\text{cyl},\phi} \\ E_{\text{cyl},z} \end{pmatrix} = \begin{pmatrix} k_z I_1(\kappa\rho) \\ 0 \\ i\kappa I_0(\kappa\rho) \end{pmatrix} \frac{c}{\epsilon_r k} \frac{B_0(z_0)}{I_1(\kappa a(z_0))}, \quad (7.63)$$

in which I_m denotes the m th-order modified Bessel function of the first kind, ϵ_r is the relative permittivity of the cylinder material, $k = \omega/c$ the vacuum wavenumber and B_0 is an amplitude with units of magnetic field. Like a , the latter may depend on the choice of z_0 as is indicated in Eq. (7.63). The parameters k_z and κ are the propagation constant in the z -direction and the radial attenuation factor respectively, and are related as

$$\sqrt{k_m^2 - k_z^2} = i\sqrt{|k_m^2 - k_z^2|} \equiv i\kappa \quad (7.64)$$

with $k_m = \sqrt{\epsilon_r}k$ the wavenumber in the cylinder material. For each radius a , the constant k_z can be determined solving a transcendental dispersion relation [402] that depends on ω and ϵ_r . For metals, applying the Drude model for the permittivity [382], one can calculate that

$$k_z \approx k \quad \text{and} \quad \kappa \approx \frac{1-i}{k\Delta} \quad (7.65)$$

at THz frequencies. Substituting these approximations into Eq. (7.63) gives

$$\mathbf{E}_{\text{cyl}} \approx (1-i)\sqrt{\frac{\omega}{2\mu\sigma}} \exp\left[(1-i)\frac{\rho - a(z_0)}{\Delta}\right] B_0(z_0) \mathbf{e}_z \quad (7.66)$$

for $a(z_0) \gg \Delta$. In the cone geometry, the SPP field will decrease as r^{-1} as it diverges from the cone tip, so that a form $B_0 \propto (z_0)^{-1}$ may be assumed for the field amplitude. Using this form and Eq. (7.65), substitution of Eqs. (7.62) and (7.66) in Eq. (7.3) and differentiation shows that Eq. (7.4) is an approximate solution of Eq. (7.3), provided that Eqs. (7.5)-(7.7) hold.

Appendix 7.B Derivation of Eq. (7.13)

Any vector field can be written as the sum of the gradient of some scalar field and the curl of some vector field [381], which are called the longitudinal and transverse part of the vector field respectively. Applying the Helmholtz operator $(\nabla^2 + k^2)$ on a vector field does not change its longitudinal or transverse property. Similarly, the dyadic Green's function in Eq. (7.11) may be split into longitudinal and transverse components $\mathfrak{G}_{\text{long}}$ and \mathfrak{G}_T , such that

$$\nabla \times \mathfrak{G}_{\text{long}} = \nabla_0 \times \mathfrak{G}_{\text{long}} = \mathfrak{D}; \quad (7.67)$$

$$\nabla \cdot \mathfrak{G}_T = \nabla_0 \cdot \mathfrak{G}_T = \mathbf{0}, \quad (7.68)$$

with \mathfrak{D} the zero dyadic. It can be shown that application of the Helmholtz operator on these dyadics gives [383]

$$\begin{aligned} (\nabla^2 + k^2)\mathfrak{G}_{\text{long}} &= \mathfrak{L}(\mathbf{r}, \mathbf{r}_0); \\ (\nabla^2 + k^2)\mathfrak{G}_T &= \mathfrak{T}(\mathbf{r}, \mathbf{r}_0), \end{aligned} \quad (7.69)$$

where the dyadics on the right hand side have the properties

$$\begin{aligned} \iiint \mathfrak{L} \cdot \mathbf{X}(\mathbf{r}_0) d^3 \mathbf{r}_0 &= \mathbf{X}_{\text{long}}(\mathbf{r}); \\ \iiint \mathfrak{T} \cdot \mathbf{X}(\mathbf{r}_0) d^3 \mathbf{r}_0 &= \mathbf{X}_T(\mathbf{r}); \\ \mathfrak{L} + \mathfrak{T} &= \mathfrak{I} \delta^3(\mathbf{r} - \mathbf{r}_0), \end{aligned} \quad (7.70)$$

for any vector field \mathbf{X} . Taking the inner product of Eq. (7.8) with \mathfrak{G}_T and that of Eq. (7.69) with $\mathbf{E}(\mathbf{r}_0)$, subtracting and integrating over the exterior cone volume V_0 , gives

$$\begin{aligned} \iiint_{V_0} [\mathbf{E}(\mathbf{r}_0) \cdot \nabla_0^2 \mathfrak{G}_T - \mathfrak{G}_T \cdot \nabla_0^2 \mathbf{E}(\mathbf{r}_0)] dV_0 & \quad (7.71) \\ = \mathbf{E}_T(\mathbf{r}) - \iiint_{V_0} \mathfrak{G}_T \cdot [\epsilon_0^{-1} \nabla_0 \rho(\mathbf{r}_0) - i\omega \mu_0 \mathbf{J}(\mathbf{r}_0)] dV_0, \end{aligned}$$

where Eq. (7.70) has been used. The left hand side of Eq. (7.71) can be written as the following integral over the cone surface A_0 using Green's second theorem [383]:

$$\begin{aligned} \iint_{A_0} [(\mathbf{n} \times \mathbf{E}_0) \cdot (\nabla_0 \times \mathfrak{G}_T) - (\mathbf{n} \times \mathfrak{G}_T) \cdot (\nabla_0 \times \mathbf{E}_0) & \quad (7.72) \\ + (\mathbf{n} \cdot \mathbf{E}_0) (\nabla_0 \cdot \mathfrak{G}_T) - (\mathbf{n} \cdot \mathfrak{G}_T) (\nabla_0 \cdot \mathbf{E}_0)] dA_0, \end{aligned}$$

in which $\mathbf{E}(\mathbf{r}_0)$ has been abbreviated as \mathbf{E}_0 . Since the boundary conditions (7.9) and (7.12) apply at the cone surface, and \mathfrak{G}_T satisfies Eq. (7.68), the first three terms in this surface integral vanish. Furthermore, using that $\nabla \cdot \mathbf{E} = \epsilon_0^{-1}\rho$, Gauss's theorem yields

$$\iint_{A_0} (\mathbf{n} \cdot \mathfrak{G}_T) (\nabla_0 \cdot \mathbf{E}_0) dA_0 = \epsilon_0^{-1} \iiint_{V_0} \mathfrak{G}_T \cdot \nabla_0 \rho(\mathbf{r}_0) dV_0,$$

so that the last term in Eq. (7.72) cancels identically the contribution of the charge density in Eq. (7.71). Therefore, Eq. (7.71) reduces to Eq. (7.13).

Appendix 7.C Green's function for conical geometry

The dyadic Green's function that satisfies

$$(\nabla^2 + k^2)\mathfrak{G} = (\nabla_0^2 + k^2)\mathfrak{G} = \mathfrak{I}\delta^3(\mathbf{r} - \mathbf{r}_0) \quad \text{for } 0 < \theta < \pi - \delta, \quad (7.73)$$

subject to the boundary condition

$$\mathfrak{G} \times \mathbf{e}_\theta = \mathfrak{D} \quad \text{at } \theta = \pi - \delta, \quad (7.74)$$

is [383, 384]

$$\mathfrak{G}(\mathbf{r}, \mathbf{r}_0) = -ik(\mathfrak{G}_L + \mathfrak{G}_M + \mathfrak{G}_N), \quad (7.75)$$

with

$$\mathfrak{G}_L = \sum_{\sigma} \sum_{m=0}^{\infty} \alpha_{\sigma m}^2 \begin{cases} \mathbf{L}_{\sigma m}^{(1)}(\mathbf{r}) \mathbf{L}_{\sigma m}^{(3)}(\mathbf{r}_0) \\ \mathbf{L}_{\sigma m}^{(1)}(\mathbf{r}_0) \mathbf{L}_{\sigma m}^{(3)}(\mathbf{r}) \end{cases}; \quad (7.76)$$

$$\mathfrak{G}_M = \sum_{\nu} \sum_{m=0}^{\infty} \frac{\alpha_{\nu m}^2}{\nu(\nu+1)} \begin{cases} \mathbf{M}_{\nu m}^{(1)}(\mathbf{r}) \mathbf{M}_{\nu m}^{(3)}(\mathbf{r}_0) \\ \mathbf{M}_{\nu m}^{(1)}(\mathbf{r}_0) \mathbf{M}_{\nu m}^{(3)}(\mathbf{r}) \end{cases}; \quad (7.77)$$

$$\mathfrak{G}_N = \sum_{\sigma} \sum_{m=0}^{\infty} \frac{\alpha_{\sigma m}^2}{\sigma(\sigma+1)} \begin{cases} \mathbf{N}_{\sigma m}^{(1)}(\mathbf{r}) \mathbf{N}_{\sigma m}^{(3)}(\mathbf{r}_0) \\ \mathbf{N}_{\sigma m}^{(1)}(\mathbf{r}_0) \mathbf{N}_{\sigma m}^{(3)}(\mathbf{r}) \end{cases}, \quad (7.78)$$

where the upper rows apply when $r < r_0$ and the lower rows apply when $r > r_0$. The scale factors α are given by [386]

$$(\alpha_{\sigma m})^{-2} = \int_0^{2\pi} \int_0^{\pi-\delta} |P_\sigma^m(\cos\theta)|^2 \sin\theta d\theta d\phi \quad (7.79)$$

$$= \frac{2\pi \sin\delta}{2\sigma+1} \left(\frac{\partial P_\sigma^m(\cos\theta)}{\partial\sigma} \frac{\partial P_\sigma^m(\cos\theta)}{\partial\theta} \right) \Big|_{\theta=\pi-\delta};$$

$$(\alpha'_{\nu m})^{-2} = \int_0^{2\pi} \int_0^{\pi-\delta} \left| \frac{d}{d\theta} P_\nu^m(\cos\theta) \right|^2 \sin\theta d\theta d\phi, \quad (7.80)$$

where P_σ^m denotes the associated Legendre function of the first kind, degree σ and order m . The vector functions constituting the dyadic products in Eqs. (7.76)-(7.78) are given in spherical components (e_r, e_θ, e_ϕ) by

$$\mathbf{L}_{\sigma m}^{(p)}(\mathbf{r}) = \begin{pmatrix} \frac{d}{dr} j_\sigma^{(p)}(kr) P_\sigma^m(\cos\theta) \\ \frac{j_\sigma^{(p)}(kr)}{r} \frac{d}{d\theta} P_\sigma^m(\cos\theta) \\ im \frac{j_\sigma^{(p)}(kr)}{r} \frac{P_\sigma^m(\cos\theta)}{\sin\theta} \end{pmatrix} e^{im\phi}; \quad (7.81)$$

$$\mathbf{M}_{\nu m}^{(p)}(\mathbf{r}) = \begin{pmatrix} 0 \\ im \frac{P_\nu^m(\cos\theta)}{\sin\theta} \\ -\frac{d}{d\theta} P_\nu^m(\cos\theta) \end{pmatrix} j_\nu^{(p)}(kr) e^{im\phi}; \quad (7.82)$$

$$\mathbf{N}_{\sigma m}^{(p)}(\mathbf{r}) = \begin{pmatrix} \sigma(\sigma+1) \frac{j_\sigma^{(p)}(kr)}{kr} P_\sigma^m(\cos\theta) \\ \frac{1}{kr} \frac{d}{dr} (r j_\sigma^{(p)}(kr)) \frac{d}{d\theta} P_\sigma^m(\cos\theta) \\ \frac{im}{kr} \frac{d}{dr} (r j_\sigma^{(p)}(kr)) \frac{P_\sigma^m(\cos\theta)}{\sin\theta} \end{pmatrix} e^{im\phi}, \quad (7.83)$$

in which $j_\sigma^{(p)}$ is the spherical Bessel function of the p -th kind and order σ . Because the functions are periodic in the azimuthal direction, $m = 0, 1, 2, \dots$. The sets of eigenvalues $\{\sigma\}$ and $\{\nu\}$ are such that the Green's function satisfies the boundary condition (7.74). Consequently, they are the solutions of

$$P_\sigma^m(-\cos\delta) = 0; \quad (7.84)$$

$$\frac{d}{d\theta} P_\nu^m(\cos\theta) \Big|_{\theta=\pi-\delta} = 0. \quad (7.85)$$

Miscellaneous properties of the vector functions are

$$\nabla \times \mathbf{L}_{\sigma m}^{(p)} = \mathbf{0}; \quad (7.86)$$

$$\nabla \cdot \mathbf{M}_{\nu m}^{(p)} = \nabla \cdot \mathbf{N}_{\sigma m}^{(p)} = 0; \quad (7.87)$$

$$k \mathbf{N}_{\sigma m}^{(p)} = \nabla \times \mathbf{M}_{\sigma m}^{(p)}. \quad (7.88)$$

Due to properties (7.86) and (7.87), the Green's function (7.75) can easily be split into a longitudinal part $\mathfrak{G}_{\text{long}}$ and transverse part \mathfrak{G}_T as

$$\mathfrak{G}_{\text{long}} = -ik\mathfrak{G}_L; \quad (7.89)$$

$$\mathfrak{G}_T = -ik(\mathfrak{G}_M + \mathfrak{G}_N). \quad (7.90)$$

Since the current densities considered in this chapter are independent of ϕ , terms having $m \neq 0$ in the expansion of \mathfrak{G}_T integrate to zero in Eq. (7.13). Moreover, the dyadic \mathfrak{G}_M makes no contribution to the integral since $\mathbf{M}_{\nu m} \cdot \mathbf{J} = 0$ for $m = 0$. Therefore, the relevant Green's function to be used in Eq. (7.13) is given by Eq. (7.17).

Appendix 7.D Electric field in the far zone

Substitution of Eqs. (7.16) and (7.17) in Eq. (7.13) yields

$$\begin{aligned} \mathbf{E}_T = & \frac{\mu_0 \omega k q}{\sqrt{2\pi}} \sum_{\sigma} \alpha_{\sigma}^2 \quad (7.91) \\ & \times \left(\mathbf{N}_{\sigma}^{(3)}(\mathbf{r}) \int_0^r \frac{j_{\sigma}(kz_0)}{kz_0} e^{-i\frac{k}{\beta}z_0} dz_0 + \mathbf{N}_{\sigma}^{(1)}(\mathbf{r}) \int_r^{\infty} \frac{h_{\sigma}^{(1)}(kz_0)}{kz_0} e^{-i\frac{k}{\beta}z_0} dz_0 \right), \end{aligned}$$

where the vector functions \mathbf{N}_{σ} are given by Eq. (7.83). In the far field $kr \rightarrow \infty$, the second term in large braces vanishes. Furthermore, the asymptotic form of the vector functions is

$$\mathbf{N}_{\sigma}^{(3)} \approx P_{\sigma}^1(\cos\theta) e^{-i\sigma\frac{\pi}{2}} \frac{e^{ikr}}{kr} \mathbf{e}_{\theta} \quad \text{for } kr \gg 1, \quad (7.92)$$

so that in the far zone the electric field reduces to Eq. (7.18), in which the integral

$$I_{\sigma}(\beta) = \int_0^{\infty} \frac{j_{\sigma}(kz_0)}{z_0} e^{-i\frac{k}{\beta}z_0} dz_0 \quad (7.93)$$

is tabulated [403] and given by Eq. (7.19).

Appendix 7.E Analysis of Q_{σ} in Eq. (7.52)

Using property (7.88) of the \mathbf{N} -functions and Stokes's theorem, integration in the plane $z = z_0$ yields

$$\int_0^{2\pi} \int_0^a \mathbf{e}_z \cdot \mathbf{N}_\sigma^{(1)}(\mathbf{r}_0) \rho_0 d\rho_0 d\phi_0 = \frac{2\pi a}{k} \mathbf{e}_\phi \cdot \mathbf{M}_\sigma^{(1)}(\mathbf{r}_1), \quad (7.94)$$

where the functions \mathbf{M}_σ are given by Eq. (7.82) with $m = 0$ and $\nu \equiv \sigma$, and \mathbf{r}_1 denotes the spherical coordinates

$$(r_1, \theta_1, \phi_1) = \left(\sqrt{z_0^2 + a^2}, \arccos \frac{z_0}{\sqrt{z_0^2 + a^2}}, \phi_1 \right). \quad (7.95)$$

Making use of the identity (7.94) and expression (7.82), Eq. (7.52) reduces to

$$Q_\sigma = \frac{2}{ka} \int_{-ka/\tan\delta}^{\infty} e^{-i\frac{s}{\beta}} P_\sigma^1\left(\frac{s}{R}\right) j_\sigma(R) ds \quad (7.96)$$

$$+ \frac{2 \tan \delta}{(ka)^2} P_\sigma^1(-\cos \delta) \int_{-ka/\tan \delta}^0 s e^{-i\frac{s}{\beta}} j_\sigma\left(\frac{-s}{\cos \delta}\right) ds;$$

$$R \equiv \sqrt{s^2 + (ka)^2}, \quad (7.97)$$

in which the substitution $s = kz_0$ has been applied. Note that the first line of this expression represents integration over a full semi-infinite cylinder, and the second line represents integration over the conical cut-out that is subtracted from the integration volume.

As a check on Eq. (7.96), the limit $ka \rightarrow 0$ will now be taken to obtain the equivalent expression for a point charge. From the power series of the Bessel function [388], the second line of Eq. (7.96) is proportional to $(ka)^\sigma$ as $ka \rightarrow 0$, so that it vanishes in the limit. In the first line, we use the identity [403]

$$P_\nu^{\mu+2}(x) + \frac{2(\mu+1)x}{\sqrt{1-x^2}} P_\nu^{\mu+1}(x) = (\nu-\mu)(\nu+\mu+1)P_\nu^\mu(x) \quad (7.98)$$

to rewrite

$$\frac{2}{ka} P_\sigma^1\left(\frac{s}{R}\right) = \frac{1}{s} \left[\sigma(\sigma+1) P_\sigma^0\left(\frac{s}{R}\right) - P_\sigma^2\left(\frac{s}{R}\right) \right]. \quad (7.99)$$

Making use of this identity, taking the limit $ka \rightarrow 0$ of Eq. (7.96) yields

$$\lim_{ka \rightarrow 0} Q_\sigma(\beta, ka) = \sigma(\sigma+1) I_\sigma(\beta), \quad (7.100)$$

where $I_\sigma(\beta)$ is given by Eqs. (7.93) and (7.19). With this, the electric field (7.51) generated by the charged disk correctly reduces to the field (7.18) generated by a point charge when $ka \rightarrow 0$.

Because the integrand in the first line of Eq. (7.96) is oscillatory, it is numerically beneficial to deform the integration path in the complex s -plane. Denote the integrand by $T_\sigma(s)$. The integration path is along the real line with a negative finite lower boundary and $T_\sigma(s)$ has cuts in the complex s -plane along the parts of the imaginary axis where $|s| > ka$, as shown in Fig. 7.14. Since $\lim_{A \rightarrow \infty} AT_\sigma(Ae^{i\phi}) = 0$ in the quadrant $-\pi/2 < \phi < 0$,

$$\int_0^\infty T_\sigma(s) ds = -i \int_C T_\sigma(s) ds, \quad (7.101)$$

where the contour C is shown in Fig. 7.14. Denoting the limit to the lower cut from the right by $s = -it + 0$, $t > ka$, expression (7.97) becomes

$$R = \sqrt{(-it + 0)^2 + (ka)^2} = -i\sqrt{t^2 - (ka)^2} \equiv -iR', \quad (7.102)$$

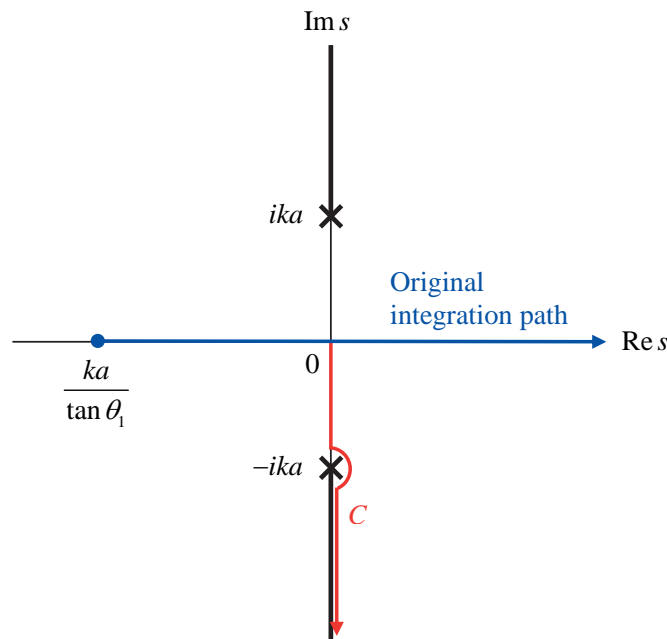


Figure 7.14: Original integration path in the first line of Eq. (7.96) and contour C in Eq. (7.101) in the complex s -plane. The cuts and poles of $T_\sigma(s)$ are shown as well.

while the Bessel function in Eq. (7.96) may be rewritten as [388]

$$j_\sigma(-iR') = e^{-i\sigma\frac{\pi}{2}} \sqrt{\frac{\pi}{2R'}} I_{\sigma+\frac{1}{2}}(R'), \quad (7.103)$$

where I denotes the modified cylindrical Bessel function of the first kind. Combining Eqs. (7.101)-(7.103), the integration along the positive real line in Eq. (7.96) equals

$$\int_0^\infty T_\sigma(s) ds = -ie^{-i\sigma\frac{\pi}{2}} \sqrt{\frac{\pi}{2}} \int_0^\infty e^{-\frac{t}{\beta}} P_\sigma^1\left(\frac{t}{R'}\right) \frac{I_{\sigma+\frac{1}{2}}(R')}{R'^{\frac{1}{2}}} dt, \quad (7.104)$$

by which the oscillatory behavior of the integrand is exchanged for exponentially damped behavior.

Appendix 7.F Peak field and pulse duration

The approximate electric field spectrum, indicated in the inset of Fig. 7.13, has the form

$$|E_{T\theta}(\omega)| \approx E_0 \begin{cases} 1 & \omega < \omega_1 \\ \sqrt{\frac{\ln \omega_2 - \ln \omega}{\ln \omega_2 - \ln \omega_1}} & \omega_1 < \omega < \omega_2 \\ 0 & \omega > \omega_2 \end{cases} \quad (7.105)$$

with E_0 given by Eq. (7.60). According to Eq. (7.58) the phase of the field equals

$$\arg E_{T\theta}(\omega) = kr + \phi(\omega), \quad (7.106)$$

where the term kr is equivalent to a time shift r/c in the time domain, and $\phi(\omega)$ is the phase of the sum in Eq. (7.58). A Taylor expansion of the time domain field $E_{T\theta}(t)$ around $t = r/c$ may now be obtained using the moments of the frequency domain field, since [404]

$$\left. \frac{d^n E_{T\theta}(t)}{dt^n} \right|_{t=r/c} = e^{-in\frac{\pi}{2}} \sqrt{\frac{2}{\pi}} \operatorname{Re} \int_0^\infty \omega^n e^{i\phi(\omega)} |E_{T\theta}(\omega)| d\omega. \quad (7.107)$$

Here, it has been used that $E_{T\theta}(-\omega) = E_{T\theta}^*(\omega)$ because $E_{T\theta}(t)$ is real. If $\phi(\omega)$ were zero, the field $E_{T\theta}(t)$ would be maximum at $t = r/c$, and its maximum value $E(t)_{\max}$ would be simply Eq. (7.107) with $n = 0$. Substituting Eq. (7.105), this would yield

$$E(t)_{\max} \approx \sqrt{\frac{2}{\pi}} E_0 \omega_2 \times \frac{\sqrt{\pi}}{2} \frac{\operatorname{erf}\left(\sqrt{\ln \frac{\omega_2}{\omega_1}}\right)}{\sqrt{\ln \frac{\omega_2}{\omega_1}}} \quad \text{for } \phi = 0. \quad (7.108)$$

The first factor on the right equals the amplitude that would result if the spectrum of Fig. 7.13 were fully coherent up to the frequency ω_2 and zero for $\omega > \omega_2$, while the second factor corrects for the slope in the spectrum. Analysis of the actual phase of $E_{T\theta}(\omega)$ shows that it is not zero; however, it is approximately constant at $\phi \approx -\pi/4$ for all three cases. Evaluating a few more orders of Eq. (7.107) and the resulting Taylor expansions of $E_{T\theta}(t)$ shows that this nonzero phase does alter the symmetry of the SPP pulse, but it does not affect the maximum value of field much. Therefore Eq. (7.108) is a good approximation for the maximum electric field amplitude in the time domain.

Finally, the duration τ of the time domain SPP pulse, which is defined by Eq. (7.61), is equal to

$$\tau \equiv \frac{1}{E(t)_{\max}} \int_{-\infty}^{\infty} E(t) dt = \frac{\sqrt{2\pi} E_0}{E(t)_{\max}}. \quad (7.109)$$

Bibliography

- [333] K. Wang and D. M. Mittleman, “Metal wires for terahertz wave guiding,” *Nature* **432**, 376–379 (2004).
- [334] T.-I. Jeon, J. Zhang, and D. Grischkowsky, “THz Sommerfeld wave propagation on a single metal wire,” *Appl. Phys. Lett.* **86**, 161904 (2005).
- [335] Q. Cao and J. Jahns, “Azimuthally polarized surface plasmons as effective terahertz waveguides,” *Opt. Express* **13**, 511–518 (2005).
- [336] K. Wang and D. M. Mittleman, “Dispersion of surface plasmon polaritons on metal wires in the terahertz frequency range,” *Phys. Rev. Lett.* **96**, 157401 (2006).
- [337] K. L. Wang and D. M. Mittleman, “Guided propagation of terahertz pulses on metal wires,” *J. Opt. Soc. Am. B* **22**, 2001–2008 (2005).
- [338] N. C. J. van der Valk and P. C. M. Planken, “Effect of a dielectric coating on terahertz surface plasmon polaritons on metal wires,” *Appl. Phys. Lett.* **87**, 071106 (2005).
- [339] S. A. Maier, S. R. Andrews, L. Martín-Moreno, and F. J. García-Vidal, “Terahertz surface plasmon-polariton propagation and focusing on periodically corrugated metal wires,” *Phys. Rev. Lett.* **97**, 176805 (2006).

- [340] L. Shen, X. Chen, Y. Zhong, and K. Agarwal, “Effect of absorption on terahertz surface plasmon polaritons propagating along periodically corrugated metal wires,” *Phys. Rev. B* **77**, 075408 (2008).
- [341] M. I. Stockman, “Nanofocusing of optical energy in tapered plasmonic waveguides,” *Phys. Rev. Lett.* **93**, 137404 (2004).
- [342] J. A. Deibel, N. Berndsen, K. Wang, D. M. Mittleman, N. C. van der Valk, and P. C. M. Planken, “Frequency-dependent radiation patterns emitted by THz plasmons on finite length cylindrical metal wires,” *Opt. Express* **14**, 8772–8778 (2006).
- [343] W. L. Barnes, A. Dereux, and T. W. Ebbesen, “Surface plasmon subwavelength optics,” *Nature* **424**, 824–830 (2003).
- [344] M. S. Sherwin, C. A. Schmuttenmaer, and P. H. Bucksbaum, eds., *Proc. DOE-NSF-NIH Workshop on opportunities in THz science, Arlington, VA.* (2004).
- [345] F. Keilmann, “Surface-polariton propagation for scanning near-field optical microscopy application,” *J. Microsc.* **194**, 567–570 (1999).
- [346] R. Hillenbrand and F. Keilmann, “Optical oscillation modes of plasmon particles observed in direct space by phase-contrast near-field microscopy,” *Appl. Phys. B* **73**, 239–243 (2001).
- [347] H.-T. Chen, R. Kersting, and G. C. Cho, “Terahertz imaging with nanometer resolution,” *Appl. Phys. Lett.* **83**, 3009–3011 (2003).
- [348] F. Buergens, R. Kersting, and H.-T. Chen, “Terahertz microscopy of charge carriers in semiconductors,” *Appl. Phys. Lett.* **88**, 112115 (2006).
- [349] D. Crawley, C. Longbottom, V. P. Wallace, B. Cole, D. Arnone, and M. Pepper, “Three-dimensional terahertz pulse imaging of dental tissue,” *J. Biomed. Opt.* **8**, 303–307 (2003).
- [350] R. M. Woodward, V. P. Wallace, D. D. Arnone, E. H. Linfield, and M. Pepper, “Terahertz pulsed imaging of skin cancer in the time and frequency domain,” *J. Biol. Phys.* **29**, 257–261 (2003).
- [351] K. Kneipp, Y. Wang, H. Kneipp, L. T. Perelman, I. Itzkan, R. Dasari, and M. S. Feld, “Single molecule detection using surface-enhanced Raman scattering (SERS),” *Phys. Rev. Lett.* **78**, 1667–1670 (1997).
- [352] S. Nie and S. R. Emory, “Probing single molecules and single nanoparticles by surface-enhanced Raman scattering,” *Science* **275**, 1102–1106 (1997).
- [353] R. H. Jacobsen, D. M. Mittleman, and M. C. Nuss, “Chemical recognition of gases and gas mixtures with terahertz waves,” *Opt. Lett.* **21**, 2011–2013 (1996).

- [354] M. Walther, M. R. Freeman, and F. A. Hegmann, “Metal-wire terahertz time-domain spectroscopy,” *Appl. Phys. Lett.* **87**, 261107 (2005).
- [355] T.-I. Jeon and D. Grischkowsky, “Direct optoelectronic generation and detection of sub-ps-electrical pulses on sub-mm-coaxial transmission lines,” *Appl. Phys. Lett.* **85**, 6092–6094 (2004).
- [356] G. Gallot, S. P. Jamison, R. W. McGowan, and D. Grischkowsky, “Terahertz waveguides,” *J. Opt. Soc. Am. B* **17**, 851–863 (2000).
- [357] R. Mendis and D. Grischkowsky, “Plastic ribbon THz waveguides,” *J. Appl. Phys.* **88**, 4449–4451 (2000).
- [358] H. Han, H. Park, M. Cho, and J. Kim, “Terahertz pulse generation in a plastic photonic crystal fiber,” *Appl. Phys. Lett.* **80**, 2634–2636 (2002).
- [359] R. Mendis and D. Grischkowsky, “Undistorted guided-wave propagation of sub-picosecond terahertz pulses,” *Opt. Lett.* **26**, 846–848 (2001).
- [360] F. Wang, D. Cheever, M. Farkhondeh, W. Franklin, E. Ihloff, J. van der Laan, B. McAllister, R. Milner, C. Tschalaer, D. Wang, D. F. Wang, A. Zolfaghari, T. Zwart, G. L. Carr, B. Podobedov, and F. Sannibale, “Coherent THz synchrotron radiation from a storage ring with high-frequency RF system,” *Phys. Rev. Lett.* **96**, 064801 (2006).
- [361] G. L. Carr, M. C. Martin, W. R. McKinney, K. Jordan, G. R. Neil, and G. P. Williams, “High-power terahertz radiation from relativistic electrons,” *Nature* **420**, 153–156 (2002).
- [362] G. L. Carr, M. C. Martin, W. R. McKinney, K. Jordan, G. R. Neil, and G. P. Williams, “Very high power THz radiation sources,” *J. Biol. Phys.* **29**, 319–325 (2003).
- [363] K.-L. Yeh, M. C. Hoffmann, J. Hebling, and K. A. Nelson, “Generation of 10 μ J ultrashort terahertz pulses by optical rectification,” *Appl. Phys. Lett.* **90**, 171121 (2007).
- [364] J. A. Deibel, K. Wang, M. D. Escarra, and D. M. Mittleman, “Enhanced coupling of terahertz radiation to cylindrical wire waveguides,” *Opt. Express* **14**, 279–290 (2006).
- [365] V. L. Ginzburg and V. N. Tsytovich, *Transition radiation and transition scattering* (Hilger, Bristol, 1990).
- [366] V. L. Ginzburg and I. M. Frank, “On the transition radiation theory,” *Sov. Phys. JETP* **16**, 15 (1946).

- [367] M. Ter-Mikaelian, *High-energy electromagnetic processes in condensed media* (Wiley, 1972).
- [368] W. K. H. Panofsky and M. Phillips, *Classical electricity and magnetism* (Dover, Mineola, 2005) 2nd ed.
- [369] A. Tremaine, J. B. Rosenzweig, S. Anderson, P. Frigola, M. Hogan, A. Murokh, C. Pellegrini, D. C. Nguyen, and R. L. Sheffield, “Observation of self-amplified spontaneous-emission-induced electron-beam microbunching using coherent transition radiation,” *Phys. Rev. Lett.* **81**, 5816–5819 (1998).
- [370] U. Happek, A. J. Sievers, and E. B. Blum, “Observation of coherent transition radiation,” *Phys. Rev. Lett.* **67**, 2962–2965 (1991).
- [371] Y. Shibata, T. Takahashi, T. Kanai, K. Ishi, M. Ikezawa, J. Ohkuma, S. Okuda, and T. Okada, “Diagnostics of an electron-beam of a linear-accelerator using coherent transition radiation,” *Phys. Rev. E* **50**, 1479–1484 (1994).
- [372] P. Kung, H.-C. Lihn, H. Wiedemann, and D. Bocek, “Generation and measurement of 50-fs (rms) electron pulses,” *Phys. Rev. Lett.* **73**, 967–970 (1994).
- [373] W. P. E. M. op ’t Root, P. W. Smorenburg, T. van Oudheusden, M. J. van der Wiel, and O. J. Luiten, “Theory of coherent transition radiation generated by ellipsoidal electron bunches,” *Phys. Rev. ST Accel. Beams* **10**, 012802 (2007).
- [374] Y. Shen, T. Watanabe, D. A. Arena, C.-C. Kao, J. B. Murphy, T. Y. Tsang, X. J. Wang, and G. L. Carr, “Nonlinear cross-phase modulation with intense single-cycle terahertz pulses,” *Phys. Rev. Lett.* **99**, 043901 (2007).
- [375] J. van Tilborg, C. B. Schroeder, Cs. Tóth, C. G. R. Geddes, E. Esarey, and W. P. Leemans, “Single-shot spatiotemporal measurements of high-field terahertz pulses,” *Opt. Lett.* **32**, 313–315 (2007).
- [376] C. Couillaud, “Production of X-ray transition radiation with relativistic electrons propagating at grazing incidence,” *Nucl. Instr. Meth. Phys. Res. A* **495**, 171–190 (2002).
- [377] O. J. Luiten, S. B. van der Geer, M. J. de Loos, F. B. Kiewiet, and M. J. van der Wiel, “How to realize uniform three-dimensional ellipsoidal bunches,” *Phys. Rev. Lett.* **93**, 094802 (2004).
- [378] O. J. Luiten, S. B. van der Geer, M. J. de Loos, F. B. Kiewiet, and M. J. van der Wiel, “Ideal waterbag electron bunches from an RF photogun,” in *Proc. Eur. Part. Acc. Conf.* (Lucerne, 2004) pp. 725–727.

- [379] S. B. van der Geer, M. J. de Loos, T. van Oudheusden, W. P. E. M. op 't Root, M. J. van der Wiel, and O. J. Luiten, "Longitudinal phase-space manipulation of ellipsoidal electron bunches in realistic fields," *Phys. Rev. ST Accel. Beams* **9**, 044203 (2006).
- [380] P. Musumeci, J. T. Moody, R. J. England, J. B. Rosenzweig, and T. Tran, "Experimental generation and characterization of uniformly filled ellipsoidal electron-beam distributions," *Phys. Rev. Lett.* **100**, 244801 (2008).
- [381] J. D. Jackson, *Classical electrodynamics* (Wiley, Chichester, 1999) 3rd ed.
- [382] F. L. Pedrotti, L. M. Pedrotti, and L. S. Pedrotti, *Introduction to optics* (Prentice-Hall, Englewood Cliffs, 2007) 3rd ed.
- [383] P. H. Morse and Feshbach H., *Methods of theoretical physics* (McGraw-Hill, New York, 1953).
- [384] C.-T. Tai, *Dyadic Green functions in electromagnetic theory* (IEEE Press, New York, 1994) 2nd ed.
- [385] L. B. Felsen, "Plane-wave scattering by small-angle cones," *IEEE Trans. Antennas Propagation* **5**, 121–129 (1957).
- [386] K. D. Trott, "Calculation of associated Legendre polynomials with non-integer degree," *Appl. Comp. Electromagnetics Soc. J.* **11**, 85–89 (1996).
- [387] H. M. McDonald, *Electric waves* (Cambridge university press, Cambridge, 1902).
- [388] M. Abramowitz and I. A. Stegun, *Handbook of mathematical functions* (Dover, Mineola, 1972) 9th printing.
- [389] R. G. Kouyoumjian, "Asymptotic high-frequency methods," *Proc. IEEE* **53**, 864–876 (1965).
- [390] K. M. Siegel, J. W. Crispin, and C. E. Schensted, "Electromagnetic and acoustical scattering from a semi-infinite cone," *J. Appl. Phys.* **26**, 309–313 (1955).
- [391] K. M. Siegel, H. A. Alperin, R. R. Bonkowski, J. W. Crispin, A. L. Maffett, C. E. Schensted, and I. V. Schensted, "Bistatic radar cross sections of surfaces of revolution," *J. Appl. Phys.* **26**, 297–305 (1955).
- [392] K. D. Trott, P. H. Pathak, and F. A. Molinet, "A UTD type analysis of the plane wave scattering by a fully illuminated perfectly conducting cone," *IEEE Trans. Antennas Propagation* **38**, 1150–1160 (1990).
- [393] R. E. Collin and F. J. Zucker, *Antenna theory* (McGraw-Hill, London, 1969) part 2.

- [394] C. H. Walter, *Traveling wave antennas* (Dover, New York, 1970).
- [395] M. Walther, G. S. Chambers, Z. Liu, M. R. Freeman, and F. A. Hegmann, “Emission and detection of terahertz pulses from a metal-tip antenna,” *J. Opt. Soc. Am. B* **22**, 2357–2365 (2005).
- [396] C. J. Hirschmugl, M. Sagurton, and G. P. Williams, “Multiparticle coherence calculations for synchrotron-radiation emission,” *Phys. Rev. A* **44**, 1316–1320 (1991).
- [397] O. D. Kellogg, *Foundations of potential theory* (Springer-Verlag, Berlin, 1926).
- [398] I. M. Kapchinskii and V. V. Vladimirkii, in *Proc. Int. Conf. High Energy Acc. Instr.* (Geneva, 1959) pp. 274–288.
- [399] W. P. E. M. Op ’t Root, *Generation of high-field, single-cycle terahertz pulses using relativistic electron bunches*, Ph.D. thesis, Eindhoven University of Technology (2009).
- [400] S. B. van der Geer, M. J. de Loos, W. P. E. M. Op ’t Root, W. van Dijk, W. van Hemmen, G. J. H. Brussaard, O. J. Luiten, W. Knulst, and M. J. W. Vermeulen, “Design, construction and operation of the Dutch RF-photoguns,” in *Proc. Part. Acc. Conf.* (Vancouver, Canada, 2009) pp. 569–571.
- [401] Q. Chen, M. Tani, Z. P. Jiang, and X. C. Zhang, “Electro-optic transceivers for terahertz-wave applications,” *J. Opt. Soc. Am. B* **18**, 823–831 (2001).
- [402] J. A. Stratton, *Electromagnetic theory* (McGraw-Hill, London, 1941).
- [403] I. S. Gradshteyn and I. M. Ryzhik, *Table of integrals, series, and products* (Elsevier, Amsterdam, 2007) 7th ed.
- [404] A. Papoulis, *The Fourier integral and its applications* (McGraw-Hill, London, 1962).

Concluding remarks

In this thesis, we have performed an analytical study of phenomena occurring in the interaction of bunches of charged particles with electromagnetic radiation. We thereby concentrated on bunches smaller than the wavelength of the radiation, for which coherent effects become significant. We identified novel physical phenomena and considered the feasibility of experimental observation and technological exploitation of them. In chapter 3, relativistic electron bunches in interaction with strong laser pulses were considered. Modeling the bunch as a point particle, it was shown that the radiation reaction force affects the bunch dynamics notably, even if this force can still be treated as a small perturbation. Considering larger bunches containing more charge, it was demonstrated that the radiation reaction effects may even become strong enough to yield considerably accelerated and collimated electron beams. In all cases, it proved essential to take into account the well-known ponderomotive force in order to obtain an accurate description of the electron bunch trajectories. In chapter 4, we studied this ponderomotive force in more detail. It was shown that the standard force expression is not valid in case there is a spatial direction present in which the field strength changes on the scale of the wavelength, i.e. a standing wave, and in addition the charged particle experiencing the force is relativistic. The ponderomotive description was generalized to cover this circumstance as well, yielding a polarization dependent ponderomotive force that may vanish or even change direction in certain field configurations.

Motivated by the usually rapid Coulomb expansion of electron bunches, and the correspondingly temporary nature of coherent effects, we then shifted attention towards subwavelength cold plasmas as non-expanding alternatives. Chapter 5 concerned heating mechanisms in ultracold plasmas driven by a radiofrequency field. We concluded that the process of collisional absorption, which involves Coulomb collisions with ions in the presence of the applied field, is the most important heating mechanism in such plasmas. However, this heating can be sufficiently mild so that the plasma remains ultracold for an extended period of time. In chapter 6, we concentrated on the electromagnetic aspect of the interaction of radiation with cold subwavelength plas-

mas, and studied the ponderomotive forces induced in the plasma by the radiation. Volume forces of a compressive or decompressive character were found depending on the density profile. Furthermore, the presence of a ponderomotive surface force was demonstrated, which proved to be essential to obtain results respecting conservation of momentum. The presented ponderomotive forces still exhibited the radiation reaction emphasized in chapter 3 on electron bunches, despite the fact that a completely different analytical approach was used. Similarly to electron bunches, therefore, considerable acceleration of ultracold plasmas due to radiation reaction is conceivable. Finally, in chapter 7 a system was studied in which subwavelength electron bunches act as a radiation source rather than a passive receiver of applied radiation. We proposed the generation of terahertz surface waves on a metal wire by launching electron bunches onto a tapered end of the wire. It was confirmed experimentally that this indeed yields very intense pulses of terahertz bandwidth.

A number of directions for further analytical work can be mentioned. A rigorous description of the self-consistent evolution of the bunch size and shape, including radiation reaction effects, would be very valuable in case of the laser-accelerated electrons of chapter 3, the driven subwavelength plasmas of chapters 5 and 6, and surface wave generating electrons of chapter 7 alike. However, it is questionable whether such a description is even possible without having to resort to a full 3D numerical integration of a system of fluid-like partial differential equations, in which case the benefits of an analytical treatment are largely lost. In chapter 3, we tentatively applied the common equation of motion including radiation reaction to the regime in which the radiation reaction force dominates, although this equation is normally used for situations in which this force can be considered a small perturbation. A more detailed investigation into the range of validity of the equation of motion would therefore be relevant. Regarding the standing wave ponderomotive force of chapter 4, generalization to fields with relativistic intensities or to relativistic transverse velocities would be interesting. Studying plasmas in chapters 5 and 6, we deliberately avoided the complication of plasma resonances by choosing sufficiently high driving frequencies, that is, underdense plasmas. It would be valuable to extend our results to overdense plasmas as well. In relation to ultracold plasmas, consideration of the heating mechanisms studied in chapter 5 under strongly coupled conditions would be of interest. The dielectric description adopted in chapter 6 may be generalized to magnetized plasmas [405] or relativistic quiver velocities [406]. The calculation of the obtainable terahertz surface waves in chapter 7 could be improved by inclusion of electron scattering by the atoms in the metal wire tip. Finally, an interesting alternative to proposed surface wave generation method, which involved electrons entering the wire material, may be offered by the reverse process. That is, extraction of electrons *out* of the wire tip, effected by photo-emission due to a subpicosecond laser pulse, would generate terahertz surface waves just as well. This idea is encouraged by a recent experiment demonstrating the propagation of an electric field transient along a wire

that was irradiated obliquely by a high-power laser pulse [407]. Chapter 7 provides the analytical framework to calculate the efficiency of such a scheme.

This thesis reported on completely analytical work. The benefits of such an approach are clear: analytical modeling allows for the identification of new physical effects, explicit distinction and separation of coexisting phenomena, and closed mathematical expressions exhibiting the scalings involved. All of these are essential in guiding both numerical simulations and the design of experiments. However, analytical treatment inherently involves the approximation of physical systems by idealized (but mathematically tractable) model systems, warranting subsequent numerical and experimental validation of the results obtained. The most substantial idealization adopted throughout this thesis has probably been the description of collections of discrete particles by continuous charged distributions. This neglect of granularity excludes important issues such as escape of particles from the bunch, the velocity distribution of the particles, and the study of interparticle processes like Coulomb collisions beyond presupposed statistical rates. In order to assess the significance of such processes, be it beneficial or detrimental, it would therefore be very valuable to numerically simulate the systems of discrete particles studied in this thesis. As mentioned, particularly important is the self-consistent evolution of the bunch size and shape in the studied processes. Preferably, numerical validation consists of single particle tracking simulations, since more macroscopic methods such as particle-in-cell codes still involve some degree of idealization and arbitrariness in the modeling assumptions. However, particle tracking simulation of the systems discussed in this thesis is extremely demanding for two reasons. First, the radiation reaction effects in chapter 3, the accelerating force in chapter 6, and the generation of surface waves in chapter 7 all involve the transfer of momentum between the particles and the radiation field. As we discussed in chapter 2, this transfer can only be consistently described in terms of the Lorentz forces experienced by the individual particles when these forces are based on the full retarded self-generated electromagnetic field. Most particle tracking codes, however, approximate the self-generated field by the electrostatic field [408, 409], which is insufficient for our purposes. Codes based on the full retarded field do exist [410], though. Second, the bunches we considered contain up to 10^{10} particles. It is currently forbiddingly time consuming to simulate all pairwise interactions of such a system, hence the bunch must be represented by one containing fewer particles. Naturally, the more particles can be simulated, the more accurate reality is simulated. A step in this direction is the use of graphics processing units (GPUs) to parallelize and thereby speed up the computations [411].

Naturally, next to numerical simulations, experimental verification will be needed in order to validate the results of this work. Throughout this thesis, we have taken special care to stay within the technologically possible when choosing experimental parameters in numerical examples. In chapter 3, for instance, we invoked optical

lasers with $\sim 10^{19}$ W/cm² intensity, CO₂ laser pulses with kJ energy content, and $\sim 10 - 100$ nm sized atomic clusters to predict measurable consequences of the coherently enhanced radiation reaction force. All of this technology is presently available. The electron trajectories through a standing wave presented in chapter 4 involved only lasers with moderate $\sim 10^{14}$ W/cm² intensities. The ultracold plasmas mentioned in the numerical examples of chapters 5 and 6 contained at most 5×10^{10} atoms, which number has already been achieved in atom traps, and these plasmas were subjected to available microwave fields. The electron bunches assumed in 7 can be presently obtained as well. At least in principle, therefore, all predictions made in this thesis could be experimentally verified. This has been done already for the terahertz surface wave generation described in chapter 7. However, the experimental parameters assumed in this work often corresponded to state-of-the-art technology, so that a full experimental reproduction would require an expensive list of equipment including high-power optical and CO₂ lasers, a well-controlled gas jet expanding in a vacuum chamber, a specially designed magneto-optical trap, and high-power custom-made klystrons. On the other hand, down-sized experiments designed to merely detect the presented effects, rather than produce technologically interesting beams etc., seem to be practically feasible. Nevertheless, these would still involve challenging issues such as subjecting an atomic cluster to a laser pulse in a controlled and reproducible configuration, timing and aligning a pulsed electron beam traveling through a pulsed standing wave, and feeding microwave power into an atom cooling setup.

In this thesis, we have identified a number of new technological possibilities that may be enabled by the studied physical phenomena. In chapter 3, we showed that the radiation reaction effects in dense electron bunches subjected to high-power laser pulses may partially suppress the instability that normally impedes laser-vacuum acceleration schemes [412], thereby enlarging the scope for effective bunch acceleration schemes. In addition, the coherently enhanced radiation reaction of high-density electron bunches offers the interesting possibility to study, within an experimentally accessible system, the fundamental topic of radiation reaction discussed in chapter 2. The modifications of the ponderomotive force derived in chapter 4 may have important implications for standing wave applications, such as existing electron bunch length measurements based on ponderomotive scattering of the electrons by a standing wave [413], and the proposed X-ray free electron laser relying on the wiggling motion of electrons in a standing wave [414]. Moreover, like the standing wave ponderomotive force, the related fundamental Kapitza-Dirac effect [415] may show polarization dependent features when generalized to relativistic electrons. In chapter 6, we established the existence of ponderomotive volume forces in homogeneous subwavelength dielectric objects, which may be used for manipulation of the object in contactless circumstances [416–418]. Furthermore, it was estimated that ultracold plasmas may be accelerated to keV ion energies, resulting in a neutralized beam with a brightness comparable to current high-performance ion sources [419]. Finally, in chapter 7 we showed that it

is possible to generate intense pulsed surface waves with terahertz bandwidth on a metal wire, which was confirmed experimentally. Subsequent focusing of such surface waves may yield intense and highly localized terahertz fields, enabling non-linear experiments with spatial resolution below the diffraction limit [420–422].

Bibliography

- [405] V. L. Ginzburg, *The propagation of electromagnetic waves in plasmas* (Pergamon, Oxford, 1964) sec. 10.
- [406] M. Brambilla, *Kinetic theory of plasma waves* (Oxford university press, Oxford, 1998) sec. 16.
- [407] K. Quinn, P. A. Wilson, C. A. Cecchetti, B. Ramakrishna, L. Romagnani, G. Sarri, L. Lancia, J. Fuchs, A. Pipahl, T. Toncian, O. Willi, R. J. Clarke, D. Neely, M. Notley, P. Gallegos, D. C. Carroll, M. N. Quinn, X. H. Yuan, P. McKenna, T. V. Liseykina, A. Macchi, and M. Borghesi, “Laser-driven ultrafast field propagation on solid surfaces,” *Phys. Rev. Lett.* **102**, 194801 (2009).
- [408] M. J. de Loos and S. B. van der Geer, “General Particle Tracer: a new 3D code for accelerator and beam line design,” in *Proc. Fifth Eur. Part. Acc. Conf.*, Vol. 2, edited by S. Myers, A. Pacheco, R. Pascual, Ch. Petit-Jean-Genaz, and J. Poole (Sitges, Spain, 1996) pp. 1241–1243, <http://www.pulsar.nl/gpt>.
- [409] L. Young and J. Billen, “The particle tracking code PARMELA,” in *Proc. Part. Acc. Conf.*, edited by J. Chew, P. Lucas, and S. Webber (Portland, USA, 2003) pp. 3521–3523, <http://laacg1.lanl.gov>.
- [410] L. Giannessi, P. Musumeci, and M. Quattromini, “TREDI: fully 3D beam dynamics simulation of RF guns, bendings and FELs,” *Nucl. Inst. Meth. Phys. Res. A* **436**, 443–444 (1999).
- [411] H.-Y. Schive, C. H. Chien, S.-K. Wong, Y.-C. Tsai, and T. Chiueh, “Graphic-card cluster for astrophysics (GraCCA) - Performance tests,” *New Astron.* **13**, 418–435 (2008).
- [412] G. V. Stupakov and M. S. Zolotarev, “Ponderomotive laser acceleration and focusing in vacuum for generation of attosecond electron bunches,” *Phys. Rev. Lett.* **86**, 5274–5277 (2001).
- [413] C. T. Hebeisen, G. Sciaini, M. Harb, R. Ernstorfer, T. Dartilongue, S. G. Kruglik, and R. J. D. Miller, “Grating enhanced ponderomotive scattering for visualization and full characterization of femtosecond electron pulses,” *Opt. Express* **16**, 3334–3341 (2008).

- [414] P. Balcou, “Proposal for a Raman X-ray free electron laser,” *Eur. Phys. J. D* **59**, 525–537 (2010).
- [415] P. L. Kapitza and P. A. M. Dirac, “The reflection of electrons from standing light waves,” *Proc. Cambridge Philos. Soc.* **29**, 297–300 (1933).
- [416] R. J. A. Hill and L. Eaves, “Vibrations of a diamagnetically levitated water droplet,” *Phys. Rev. E* **81**, 056312 (2010).
- [417] P. Stockel, I. M. Weidinger, H. Baumgartel, and T. Leisner, “Rates of homogeneous ice nucleation in levitated H₂O and D₂O droplets,” *J. Phys. Chem. A* **109**, 2540–2546 (2005).
- [418] S. E. Wolf, J. Leiterer, M. Kappl, F. Emmerling, and W. Tremel, “Early homogeneous amorphous precursor stages of calcium carbonate and subsequent crystal growth in levitated droplets,” *J. Am. Chem. Soc.* **130**, 12342–12347 (2008).
- [419] J. Orloff, M. Utlaut, and L. Swanson, *High resolution focused ion beams: FIB and its applications* (Kluwer Academic, New York, 2003).
- [420] M. Walther, M. R. Freeman, and F. A. Hegmann, “Metal-wire terahertz time-domain spectroscopy,” *Appl. Phys. Lett.* **87**, 261107 (2005).
- [421] S. Nie and S. R. Emory, “Probing single molecules and single nanoparticles by surface-enhanced Raman scattering,” *Science* **275**, 1102–1106 (1997).
- [422] H.-T. Chen, R. Kersting, and G. C. Cho, “Terahertz imaging with nanometer resolution,” *Appl. Phys. Lett.* **83**, 3009–3011 (2003).

Summary

Coherent phenomena in the interaction of pulsed particle beams and radiation

In this thesis, an analytical study is performed of phenomena occurring in the interaction of bunches of charged particles with electromagnetic radiation. The work concentrates on bunches smaller than the wavelength of the radiation, for which coherent effects become significant. Novel physical phenomena are identified and the feasibility of experimental observation and technological exploitation is considered.

The studied system of a subwavelength body of charge emerges in a variety of contexts in physics. The oldest one is probably that of classical electromagnetic models of charged particles. Derivations of the electromagnetic self-force of rigid charged objects, as have been developed in such models, are reviewed in this thesis. The mathematical equivalence of the various dissimilar self-force expressions is demonstrated explicitly. The position of the presented self-force calculations in the wider context of classical electrodynamic descriptions of charged particles is discussed, as well as their relevance to the description of macroscopic bunches of charged particles.

In modern high-power laser physics, phenomena associated with the electromagnetic self-force are referred to as radiation reaction effects. In this work, the coherent enhancement of such effects is considered and its influence on the motion of subwavelength electron bunches in interaction with intense laser pulses is analyzed. It is shown that the radiation reaction force behaves as a radiation pressure in the laser beam direction, combined with a damping force in the perpendicular direction. Due to Coulomb expansion of the electron bunch, coherent radiation reaction takes effect only in the initial stage of the laser-bunch interaction while the bunch is still smaller than the wavelength. However, this initial stage can have observable effects on the trajectory of the bunch. By scaling the system to larger bunch charges, the radiation reaction effects are strongly increased. On the basis of the usual equation of motion, this increase is shown to be such that radiation reaction may suppress the radial in-

stability normally found in ponderomotive acceleration schemes, thereby enabling the full potential of laser-vacuum electron bunch acceleration to GeV energies. However, the applicability of the used equation of motion still needs to be validated experimentally, which becomes possible using the presented experimental scheme.

In order to obtain an accurate description of electron bunch trajectories in a laser pulse, it proves to be essential to take into account the so-called ponderomotive force. This is the time-averaged Lorentz force experienced by a charged particle in an inhomogeneous, harmonically oscillating electromagnetic field. In this thesis, this force is studied in more detail for the special case of a relativistic charged particle entering an electromagnetic standing wave with a general three-dimensional field distribution and a nonrelativistic intensity. It is demonstrated that the standard ponderomotive force expression is not valid in this case, and the correct force is derived using a perturbation expansion method. The modified expression is still of simple gradient form, but contains additional polarization-dependent terms. These terms arise because the relativistic translational velocity induces a quiver motion in the direction of the magnetic force, which is the direction of large field gradients. Consistent perturbation expansion of the equation of motion leads to an effective doubling of this magnetic contribution. The derived ponderomotive force generalizes the polarization-dependent electron motion in a standing wave obtained earlier. Comparison with simulations in the case of a realistic, non-idealized, three-dimensional field configuration confirms the general validity of the analytical results.

Motivated by the usually rapid Coulomb expansion of electron bunches, and the correspondingly temporary nature of coherent effects, subwavelength quasi-neutral plasmas are considered in this thesis as alternatives in which the repulsive Coulomb force is absent. However, plasmas expand as well, although the expansion is driven by the thermal pressure. Therefore, several mechanisms by which an external electromagnetic field influences the temperature of a plasma are studied and specialized to the system of an ultracold plasma driven by a uniform radio frequency field. Heating through collisional absorption is reviewed and applied to ultracold plasmas. It is shown that the rf field modifies the three body recombination process by ionizing electrons from intermediate high-lying Rydberg states and upshifting the continuum threshold, resulting in a suppression of three body recombination. Heating through collisionless absorption associated with the finite plasma size is analyzed, revealing a temperature threshold below which collisionless absorption is ineffective.

In addition, also the electromagnetic aspect of the interaction of radiation with cold subwavelength plasmas is studied, and the ponderomotive forces induced in the plasma by the radiation are evaluated. To this end, the plasma is modeled as a sphere with a radially varying permittivity, and the internal electric fields are calculated by solving the macroscopic Maxwell equations using an expansion in Debye potentials. It

is found that the ponderomotive force is directed opposite to the plasma density gradient, similarly to large-scale plasmas. In case of a uniform density profile, a residual spherically symmetric compressive ponderomotive force is found, suggesting possibilities for contactless ponderomotive manipulation of homogeneous subwavelength objects. The presence of a surface ponderomotive force on discontinuous plasma boundaries is derived. This force is essential for a microscopic description of the radiation-plasma interaction consistent with momentum conservation. It is shown that the ponderomotive force integrated over the plasma is equivalent to the radiation pressure exerted on the plasma by the incident wave. The concept of radiative acceleration of subwavelength plasmas, proposed earlier, is applied to ultracold plasmas. It is estimated that these plasmas may be accelerated to keV ion energies, resulting in a neutralized beam with a brightness comparable to that of current high-performance ion sources.

Finally, in this thesis a system is studied in which subwavelength electron bunches act as a radiation source, rather than a passive receiver of applied radiation. A novel method is proposed to generate electromagnetic surface waves of terahertz bandwidth on a metal wire, by launching electron bunches onto a tapered end of the wire. To show the potential of this method, Maxwell's equations are solved for the appropriate boundary conditions. The metal wire tip is modeled as a perfectly conducting semi-infinite cone. It is shown that the surface waves can be recovered from the idealized fields by well-known perturbation techniques. The emitted radiation is strongly concentrated into a narrow solid angle near the cone boundary for cones with a small opening angle. It is found that sub-picosecond surface waves with peak electric fields of the order of MV/cm on a 1 mm diameter wire can be obtained using currently available technology, which has been confirmed experimentally.



Samenvatting

Coherente verschijnselen in de interactie van gepulste deeltjesbundels en straling

Atomen, waaruit materie is opgebouwd, zijn te scheiden in negatief geladen elektronen en positief geladen ionen. In dit proefschrift wordt een analytische studie gedaan naar de wisselwerking tussen wolkjes van zulke geladen deeltjes en straling. Straling bestaat uit zich voortplantende elektromagnetische golven, zoals zichtbaar licht en microgolven, welke zich onderscheiden in hun golflengte. Dit werk concentreert zich op wolkjes kleiner dan de golflengte (gewoonlijk kleiner dan een centimeter), waarin zogenaamde coherente effecten belangrijk zijn. Dit zijn effecten waarin de geladen deeltjes door hun onderlinge nabijheid elkaars invloed versterken. In dit proefschrift worden nieuwe fysische verschijnselen geïdentificeerd, en de haalbaarheid van experimentele observatie en technologische implementatie ervan worden overwogen.

Geladen objecten kleiner dan de golflengte komen voor in allerlei fysische contexten. De oudste is waarschijnlijk die van het klassieke model van geladen deeltjes, waarin men zich het deeltje, in tegenstelling tot de nu gangbare modellen, als een starre geladen bol voorstelt. Omdat lading zowel een kracht ondervindt van elektromagnetische velden, als zelf zulke velden genereert, oefent een geladen bol ook een kracht op zichzelf uit. In dit proefschrift worden eerder gemaakte afleidingen van deze zelfkracht beschouwd, en de wiskundige gelijkheid van de gevonden zelfkrachten aangetoond.

In de moderne fysica worden verschijnselen geassocieerd met de elektromagnetische zelfkracht aangeduid als stralingsreactie-effecten. In dit werk wordt de coherente versterking van zulke effecten behandeld, en wordt de invloed daarvan op de beweging van elektronenwolken in wisselwerking met intense laserpulsen geanalyseerd. Aange-toond wordt dat, als gevolg van stralingsreactie, de elektronen een kracht ondervinden in de voortplantingsrichting van de laserpuls, en dat bovendien hun beweging in de richting loodrecht daarop wordt gedempt. Echter, iedere elektronenwolk zal snel uit-

dijen omdat deeltjes met gelijke lading elkaar afstoten. Daarom zal de wolk niet lang kleiner dan de golflengte blijven, en is dus coherente versterking van stralingsreactie van zeer tijdelijke aard. Toch blijkt de eerste korte coherente periode voldoende om waarneembare effecten te veroorzaken. Voor wolkjes met een zeer grote hoeveelheid elektronen kan stralingsreactie zelfs zorgen voor stabilisatie van krachtige elektronenversnelling met een laserpuls, wat tot nu toe nog niet mogelijk is gebleken. Voor dit laatste geval is echter de geldigheid van de bewegingsvergelijking, waarmee deze stabilisatie wordt aangetoond, nog onderwerp van discussie.

Wanneer een geladen deeltje zich bevindt in een trillend elektromagnetisch veld, zal het zelf ook een trillende beweging gaan uitvoeren. Als bovendien de veldsterkte varieert met de positie, dan ondervindt het deeltje tijdsgemiddeld een kracht, die de ponderomotorische kracht wordt genoemd. In dit proefschrift wordt deze kracht onderzocht voor het speciale geval van een elektromagnetische staande golf. Zo'n staande golf bestaat uit een aaneenschakeling van posities met beurtelings een sterk veld (een buik) en geen veld (een knoop), en ontstaat wanneer twee elektromagnetische golven zich tegen elkaar in voortplanten. Algemeen wordt aangenomen dat de ponderomotorische kracht altijd in de richting van afnemende veldsterkte staat, hier dus richting de knopen. In dit werk wordt echter aangetoond dat dit voor geladen deeltjes, die zich voortbewegen met bijna de lichtsnelheid, niet altijd het geval is. Een gecorrigeerde uitdrukking voor de ponderomotorische kracht wordt afgeleid, die laat zien dat de kracht niet alleen afhangt van de sterkte van het veld, maar ook van de richting ervan. Als gevolg kan ponderomotorische kracht zich naar de buiken richten, of zelfs geheel verdwijnen.

Gemotiveerd door de snelle uitdijning van elektronenwolken, en de bijbehorende tijdelijkheid van coherente effecten, worden in dit proefschrift ook plasmawolken beschouwd. Een plasma bestaat namelijk uit zowel elektronen als ionen en is daardoor ongeveer neutraal, zodat geen sterke afstoting plaatsvindt. Echter, een plasmawolk dijt desondanks uit doordat de druk in de wolk hoger is dan daarbuiten, en de uitdijning is sneller naarmate het plasma warmer is. Daarom worden diverse mechanismen onderzocht via welke een elektromagnetische golf de temperatuur van een plasmawolk kan beïnvloeden, waarbij de nadruk op zogenaamde ultrakoude plasma's wordt gelegd. Dit zijn plasma's die sinds kort uit lasergekoelde atoomwolken kunnen worden gemaakt, en een temperatuur dichtbij het absolute nulpunt hebben.

Bovendien wordt ook het elektromagnetische aspect van de wisselwerking tussen straling en plasmawolken kleiner dan de golflengte onderzocht. Dit aspect komt tot uiting in de vorm van ponderomotorische krachten op de verschillende delen van de wolk. De optische eigenschappen van de plasmawolk worden gebruikt om het daarin heersende elektromagnetische veld in detail te berekenen, om zodoende deze ponderomotorische krachten af te leiden. Het blijkt dat de kracht meestal in de richting staat

van afnemende deeltjesdichtheid. Voor plasma's met een constante dichtheid comprimeert de kracht de wolk in alle richtingen. Omdat de dichtheid van met name ultrakoude plasma's goed experimenteel controleerbaar is, suggereren deze resultaten mogelijkheden voor doelbewuste ponderomotorische plasma-manipulatie met straling. Daarnaast wordt het bestaan van een ponderomotorische kracht werkend op het oppervlak van de wolk afgeleid. Aangetoond wordt dat deze oppervlaktekracht, tezamen met de krachten in het inwendige van het plasma, leiden tot voortstuwing in de voortplantingsrichting van de elektromagnetische golf, en wel dezelfde als eerder voor elektronenwolken in laserpulsen werd gevonden op basis van stralingsreactie. Het in het verleden voorgestelde concept om plasma's met deze voortstuwing te versnellen wordt toegepast op ultrakoude plasma's. Naar schatting zou dit een neutrale plasmabundel kunnen opleveren met vergelijkbare kwaliteiten als momenteel haalbare ionenbundels.

Tenslotte wordt in dit proefschrift een systeem bestudeerd waarin geladen deeltjes als een actieve stralingsbron fungeren, in tegenstelling tot bovengenoemde toepassingen waarin de deeltjes min of meer passieve objecten waren reagerend op van buiten opgelegde straling. Een nieuwe methode wordt voorgesteld waarmee elektromagnetische oppervlaktegolven op een metalen draad kunnen worden gegenereerd, door elektronenwolken met hoge snelheid op het gepunte uiteinde van de draad te schieten. De elektronen zullen dan in het metaal doordringen, en hun passage door het metaaloppervlak gaat gepaard met de productie van een sterke stralingspuls. Een deel van deze stralingspuls beweegt zich vervolgens als oppervlaktegolf langs de metalen draad voort. De geproduceerde straling wordt in detail berekend, waarmee de te verwachten sterkte en lengte van de oppervlaktegolf kunnen worden geschat. De voorspelde oppervlaktegolven zijn inmiddels ook experimenteel waargenomen.



Publications

P. W. Smorenburg, L. P. J. Kamp, and O. J. Luiten, "Classical formulations of the electromagnetic self-force of extended charged bodies" (submitted 2013).

P. W. Smorenburg, L. P. J. Kamp, and O. J. Luiten, "Ponderomotive manipulation of cold subwavelength plasmas", *Phys. Rev. E* **87**, 023101 (2013).

P. W. Smorenburg, L. P. J. Kamp, and O. J. Luiten, "Heating mechanisms in radio-frequency-driven ultracold plasmas", *Phys. Rev. A* **85**, 063413 (2012).

P. W. Smorenburg, J. H. M. Kanters, A. Lassise, G. J. H. Brussaard, L. P. J. Kamp, and O. J. Luiten, "Polarization-dependent gradient force in a standing wave", *Phys. Rev. A* **83**, 063810 (2011).

P. W. Smorenburg, J. H. M. Kanters, A. Lassise, G. J. H. Brussaard, L. P. J. Kamp, and O. J. Luiten, "Polarization-dependent gradient force in a standing wave", in *Proc. SPIE Conf. on Laser Acceleration of Electrons, Protons, and Ions and Medical Applications of Laser-Generated Secondary Sources of Radiation and Particles* (Prague, 2011).

B. Ersfeld, R. Bonifacio, S. Chen, M. R. Islam, P. W. Smorenburg, and D. A. Jaroszynski, "Steady-state description of an ion channel free-electron laser with varying betatron amplitude", in *Proc. SPIE Conf. on Laser Acceleration of Electrons, Protons, and Ions and Medical Applications of Laser-Generated Secondary Sources of Radiation and Particles* (Prague, 2011).

(Continued on next page)

P. W. Smorenburg, L. P. J. Kamp, G. A. Geloni, and O. J. Luiten, "Coherently enhanced radiation reaction effects in laser-vacuum acceleration of electron bunches", in *Proc. SPIE Conf. on Laser Acceleration of Electrons, Protons, and Ions and Medical Applications of Laser-Generated Secondary Sources of Radiation and Particles* (Prague, 2011).

P. W. Smorenburg, L. P. J. Kamp, G. A. Geloni, and O. J. Luiten, "Coherently enhanced radiation reaction effects in laser-vacuum acceleration of electron bunches", *Laser Part. Beams* **28**, 553-562 (2010).

P. W. Smorenburg, W. P. E. M. op 't Root, and O. J. Luiten, "Direct generation of terahertz surface plasmon polaritons on a wire using electron bunches", *Phys. Rev. B* **78**, 115415 (2008).

W. P. E. M. op 't Root, P. W. Smorenburg, T. van Oudheusden, M. J. van der Wiel, and O. J. Luiten, "Theory of coherent transition radiation generated by ellipsoidal electron bunches", *Phys. Rev. ST Accelerator Beams* **10**, 012802 (2007).

Curriculum vitae

- 2008-2013 **Ph.D. research Applied Physics,**
Eindhoven University of Technology.
- 2011 **Laser-plasma interactions and applications,**
Summer school, Strathclyde University, Glasgow, UK.
- 2010 **International research internship,**
Strathclyde University, Glasgow, UK.
- 2005-2008 **M.Sc. Applied Physics,**
Cum laude, Eindhoven University of Technology.
- 2005-2008 **Technology and development studies,**
Certificate program, Eindhoven Univ. of Technology.
- 2006 **Development worker,**
SASOL Foundation, Kitui, Kenya.
- 2006 **Industrial internship,**
NXP Semiconductors, Eindhoven.
- 2002-2005 **B.Sc. Applied Physics,**
Cum laude, Eindhoven University of Technology.
- 1996-2002 **VWO secondary education,**
Niftarlake College, Maarssen.



Dankwoord

Graag wil ik hier een aantal mensen bedanken die hebben bijgedragen aan de totstandkoming van dit proefschrift. In de eerste plaats ben ik mijn promotor *Jom Luiten* en copromotor *Leon Kamp* dankbaar voor een hele prettige en leerzame samenwerking. *Jom*, wij hebben elkaar leren kennen tijdens de BuEx Canada in 2004, de studiereis van studievereniging J.D. van der Waals waaraan ik als student en jij als wetenschappelijk begeleider deelnam. Ik herinner mij onze levendige discussie op een berghelling in Banff waarin wij uit ons hoofd de luchtdruk en het zuurstofgehalte op de top probeerden uit te rekenen. De gebleken gemeenschappelijke interesse vertaalde zich daarna achtereenvolgens in een interne stage, een afstudeerproject en tenslotte dit promotieonderzoek, alle bij jou in de vakgroep. Je wetenschappelijke richtinggevoel, overzicht, en vermogen om van elk denkbaar resultaat een positieve kant te zien, waren voor mij van onmisbare waarde. *Leon*, jouw aanwezigheid is zeer waardevol geweest in mijn promotie-onderzoek. Tijdens onze wekelijkse bespreking gaf jij mij de mogelijkheid om tot in detail de mathematisch-fysische aspecten van mijn werk te bediscussiëren. Je uitgebreide vakkennis heeft met regelmaat geleid tot de juiste keuze voor een succesvolle oplossingsmethode. *Jom* en *Leon* wil ik daarnaast bedanken voor de grondige, maar altijd prompte revisie van mijn artikelen, die toch in het algemeen bepaald niet kort van stof waren.

Willem op 't Root, in zekere zin mijn voorganger, ben ik dankbaar voor de prettige samenwerking tijdens mijn eerste jaren in de vakgroep. *Willem*, jouw onderzoek naar terahertz-straling bood mij een stimulerende context waarin ik mijn eigen stijl van werken kon ontwikkelen. Onze samenwerking heeft tot mooie wederzijdse resultaten geleid. Also I would like to thank *Dino Jaroszynski* for his formal and informal hospitality during my stay at Strathclyde University. *Joris Kanters*, die ik heb mogen begeleiden tijdens een deel van zijn afstudeerproject, wil ik bedanken voor zijn numerieke berekeningen van elektronenbanen door een staande golf, en voor zijn uitdagende vragen over de bijbehorende theorie. I would like to thank *Gianluca Geloni* for his thorough review of chapter 3 and his valuable suggestions. Stagiair *Maarten Sebregts* en afstudeerder *Koen van der Straten* ben ik dankbaar voor hun gedetailleerde numerieke simulaties van verhittingsmechanismen in plasmas.

Verder bedank ik alle collega's van de *vakgroep CQT* voor de leuke tijd. Ik heb altijd zeer gewaardeerd dat ik spontaan bij anderen kon binnenlopen voor hulp. Mijn mede-promovendi wil ik bedanken voor de gezellige momenten tussen de werkzaamheden door. In het bijzonder denk ik aan de hilarische momenten tijdens de vele uren die wij hebben samengewerkt bij het maken van persiflages van vertrekkende collega's.

Daarnaast wil ik de mensen in mijn persoonlijke omgeving bedanken. In het bijzonder dank ik mijn ouders *Jan* en *Diny Smorenburg*, die de keuzes in mijn nog korte carrière altijd volledig hebben gesteund. Ik ben hen zeer dankbaar voor alles wat zij voor mij mogelijk hebben gemaakt. Maar boven alles bedank ik mijn vrouw *Femke*. Meer nog dan dit proefschrift stonden de afgelopen jaren in het teken van onze opbloeiende relatie. *Fem*, jij doet mij beseffen welke zaken echt belangrijk zijn in het leven. Jouw warmte en vertrouwen zorgen voor een stevige thuisbasis van waaruit ik bijzaken, zoals een proefschrift, kan relativeren. Tenslotte: *Emma*, sinds jij er bent is thuiskomen na het werk leuker dan ooit!